Coupled Charge-Spin Transport and Spin–Orbit Phenomena in 2D Dirac Materials

Manuel Offidani

PhD

University of York

Physics

December 2018

Abstract

The advent of 2D layered materials, boasting high-crystal quality and rich electronic properties, has provided a unique arena for exploring exotic condensed-matter phenomena, including the emergence of ultra-relativistic Dirac fermions in graphene, topological insulating phases in WS_2, long-lived excitons in group-VI dichalcogenides and unconventional superconductivity in twisted bilayer graphene.

The enhancement of spin-orbit effects in heterointerfaces, built from the vertical stacking of different 2D layers, is recently attracting much attention. A series of crucial experiments have demonstrated the induction of strong spin-orbit effects in graphene sheets proximity-coupled to group-VI dichalcogenides. Owing to a combination of room-temperature spin transport over long distances and gate-tunable spin orbit interactions, such systems hold great promise for *all-electrical* generation and manipulation of spin currents, which is key to the realisation of the next generation of spintronics devices.

To fully unlock the potential of 2D Dirac materials for spintronics, these recent experimental findings call for the formulation of a solid theoretical framework which can underpin them, but also—and more importantly—predict novel phenomena. This thesis aims to develop the foundations of such a framework, with a focus on spin dynamics and coupled charge-spin transport in 2D Dirac materials with strong proximity-induced interactions.

A number of key results are established. We show that charge-to-spin interconversion in 2D Dirac materials can be understood in terms of exact symmetry relations (Ward identities). Depending on the specific spin-orbit interactions present in a 2D Dirac system, the symmetry relations dictate the relative contributions of the so-called *spin-Hall effect* (SHE) and *inverse spin Galvanic effect* (ISGE). In particular, for materials with interfacial breaking of mirror symmetry and unbroken (broken) sublattice symmetry, the SHE contribution is suppressed (sizable), whereas the ISGE contribution stays typically large and robust in both scenarios. The extrinsic SHE has its origin in a peculiar skew scattering mechanism—emerging from the non-coplanar spin texture of spin–orbit-coupled Dirac bands—and can be tuned by a gate voltage. We propose a diagrammatic approach to obtain the coupled charge/spin diffusion equations, as well as the spin relaxation times and the charge-to-spin interconversion rates. We supplement this study with a density matrix-based approach, allowing one to gain more insight into the delicate competition of the various energy scales present in realistic systems, and to calculate the spin relaxation time anisotropy of experimental relevance. Finally, we examine *ferromagnetic* 2D Dirac materials, through a unified theory of charge carrier transport combining semiclassical and fully-quantum mechanical approaches. We identify an experimental signature that characterises the crossover from the nonquantised anomalous Hall effect to the topologically-nontrivial *quantum anomalous Hall effect*, which can help future experimental efforts to unlock this fascinating quantum state of matter with Dirac fermions.

Contents

List of Figures

List of Tables

Acknowledgments

According to the Oxford dictionary, physics is 'the branch of science concerned with the nature and properties of matter and energy. The subject matter of physics includes mechanics, heat, light and other radiation, sound, electricity, magnetism, and the structure of atoms'. If you feel overwhelmed, and inspired, just by reading these few lines, you're probably a *physicist*. Such physicist is a weird breed, probably a unique profile within our society. Modern physics has had a huge impact on our culture, yet *the physicist* is quite often disregarded as a professional figure *per se.* Probably that's because physicists work in the background, far from the shining spotlight reserved for others. They actually necessitate intimacy. In the end, the role of the physicist is to make accessible to others some personal intuition about nature, struggling against the limitation of the (mathematical and/or spoken) language. Such a silent battle is a poetic-like creation process, which gets harder and harder as we delve deeper into the reality around us. One can discuss forever about the essence of this process, whether it is finite or endless, whether it leads to some ultimate truth or suffers from some intrinsic limitation. I don't want to discuss this here, for obvious reasons. In any case, here is the bottomline: it's nice to be a physicist. Presenting this PhD thesis, well, this probably makes me officially a physicist, which today I feel proud of.

Of course, nothing of this would have ever been possible without a strong self-motivation, and much more than that without other people by my side.

First, Aires, a young brilliant physicist and my supervisor. As cliché as it may sound, without him this thesis would not exist. He gave me the opportunity to work in his group, in first place, which has actually happened to be my first job. You've been a fantastic guide throughout my PhD, but also a friend. I wish you all the best for your academic career and a major breakthrough over the coming years!

Second, my collaborators: Roberto, Mirco, Miguel, Chunli. I learnt a lot from each interaction we have had in the past three (or so) years. You've made my life richer and I owe you the truest acknowledgments.

What about my friends in York? I think I owe them my apologies, in first place. When I started my PhD, I read many articles about how to successfully approach such an important stage of my career. Among those, I found particularly enlightening a note on a Nature blog, which sounded to me as a revelation, as a commandment to follow: *Devote your mind and soul to your PhD.* Well, I think I have followed that indication even too religiously, with my friends being those affected the most by that. Countless times I said no to Jacob's daily invitation to have a coffee, not too waste even thirty minutes of my work. Many times I left pub nights earlier than others, worrying about my pending calculations. I feel truly sorry about that! My greatest thanks to Jacob, Neville, Paul, Andrea, Marta, Jenny, Frederico, Razak, Cris, and all the others I am forgetting now due to the thesis write up-induced stress. You also made my life richer. A special thanks to Neville and Jenny for proofreading my thesis.

Thanks York (and thanks to the United Kingdom) for being my home for the past three years. My gratitude to you goes well beyond those simple words.

Thanks to all the people I interacted with over a coffee, in the corridor, on the football pitch, during conferences, on the thousands planes and trains I travelled with during this amazing period of my life.

Finally, the most important part of my acknowledgments. That's the part where words are

just not enough.

Thanks to my family.

Thanks to my mum. I owe everything to you and to your endless love.

Thanks to Serena, my love. I cannot imagine what my PhD would have been without you by my side. Despite the physical distance separating us most of the time, I have always felt you close, I have never felt alone. You have been my strength and my source of inspiration.

Declaration

I declare that this thesis is a presentation of original work and I am the sole author. This work has not previously been presented for an award at this, or any other, University. All sources are acknowledged as References. Parts of the work reported in this thesis have been adapted from articles published in the following scientific journals: Physical Review Letters, Physical Review B, MDPI Condensed Matter.

Chapter 4 and Chapter 6 (Sections 6 and 6) describe two collaborative works:

- *Covariant Conservation Laws and the Spin-Hall Effect in Dirac-Rashba Systems,* Mirco Milletarì, Manuel Offidani, Aires Ferreira, and Roberto Raimondi, Physical Review Letters **119,** 246801 (2017);
- *Optimal Charge-to-Spin Conversion in Graphene on Transition Metal Dichalcogenides,* Manuel Offidani, Mirco Milletarì, Roberto Raimondi, and Aires Ferreira, Physical Review Letters **119**, 196801 (2017);

that have been published in Physical Review Letters.

Chapter 5 describes collaborative work:

- *Microscopic Linear Response Theory of Spin Relaxation and Relativistic Transport Phenomena in Graphene*, Manuel Offidani, Roberto Raimondi, and Aires Ferreira, MDPI Condensed Matter **3**(2), 18 (2018);

published in MDPI Condensed Matter.

Chapter 6, Section 6 describes collaborative work

- *Microscopic Theory of Spin Relaxation Anisotropy in Graphene with Proximity-Induced Spin-Orbit Coupling*, Manuel Offidani, and Aires Ferreira, Physical Review B **98**, 245408 (2018);

published in Physical Review B.

Chapter 7 describes collaborative work:

- *Anomalous Hall Effect in 2D Dirac Materials with Broken Time-Reversal Symmetry,* Manuel Offidani, and Aires Ferreira, Physical Review Letter **121**, 126802 (2018);

which has been published in Physical Review Letters.

I declare that I fully participated in the formulation of the research, to the associated calculations and final interpretation of the results presented in all the above-mentioned papers, being also in most cases the author of the first draft of the papers.

Chapter 1

Introduction

Spin–orbit phenomena in solids

Spintronics and spin–orbitronics

In 1921, Arthur Compton first suggested that *"many magnetic phenomena find a satisfactory explanation on the hypothesis that matter contains a large number of minute elementary magnets"* [1]. The idea of *electrons' spin* however, took fully shape only after the pioneering works by Kronig, Uhlenbeck and Goudsmit, proposing an explanation to the anomalous Zeeman-effect with the introduction of a fourth quantum number in the Bohr-Sommerfeld atomic model [2,3]. Given the numerous subtleties a theoretical description of spin requires, including relativistic and quantum electrodynamic radiative corrections to its magnetic moment g_s [4–6], it is not surprising that, at the time of its origin, the existence of spin was considered highly controversial, being only fully accepted by the community a few years later.

After almost one century, electrons' spin lies at the centre of a conceptual and technological revolution. This success is to be explained with the dusk of traditional silicon-based electronic era; the downscaling of transistors below the "5 nm node" is limited by energy dissipation in the dormant state (ON/OFF leakage currents) and quantum effects [7], imposing a halt to the so-called Moore's law—a prediction by Intel co-founder Gordon Moore stating that the number of transistors in a semiconductor chip doubles roughly every year [8]. A call for disruptive technologies based on alternative building blocks to electrons' charge has emerged. In this context, the field of *spintronics* has arisen, aiming at leveraging the spin degree of freedom (DOF) of charge carriers to achieve that goal.

The principal advantage of promoting the spin DOF as the main carrier of information resides in its *non-volatile* nature. In spintronics devices, information is encoded into the orientation of a collection of spins, this having being fixed at a local minimum in the energy landscape. Leakage of information would be represented by a change in this particular configuration, e.g. a transition to another energy minimum due to thermal fluctuations. In magnets it is relatively easy to design energy barriers on the order of $\Delta_H \sim 10^{-18} J$ corresponding to an escape time of roughly ten years at room temperature and rendering spin-based information highly stable [9,10].

Despite its recent origin, spintronics research already numbers many breakthroughs. The discovery of the giant magnetoresistance [11,12] has led to an exponential increase in data storage capacity. Non-volatile magnetic memories based on magnetic tunnel junctions, exploiting the tunnel magnetoresistance and spin transfer torque (STT) effects, have offered lower power consumption and new paradigms for storage devices [13,14]. The applications mentioned so

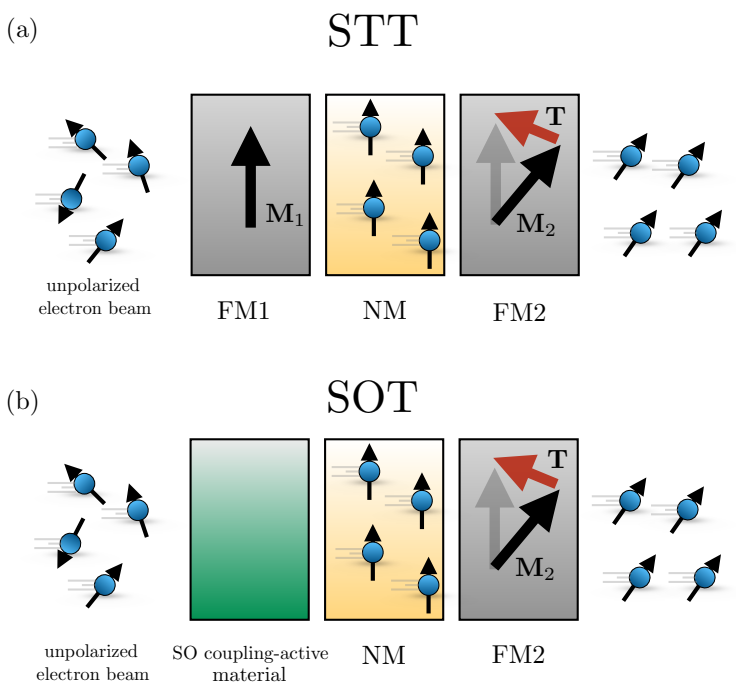

Figure 1.1: STT and spin–orbit torque (SOT) as methods to exchange angular momentum between different elements. (a) In a STT, an initially unpolarised electron beam is sent through a first ferromagnet FM1 with magnetisation $\mathbf{M}_1$, where spins get polarised. After having gone through a normal metal (NM), electrons with fixed spin polarisation pass through a second ferromagnet FM2 with magnetisation $\mathbf{M}_2$ not parallel to $\mathbf{M}_1$. This results in the exertion of a torque $\mathbf{T}$ on FM2. (b) In a SOT configuration, the initial beam of electrons acquires spin angular momentum by passing through a material with SO coupling, therefore without the need of $\mathbf{M}_1$. Successively spins exert a torque $\mathbf{T}$ on FM2, similarly to what happens in a STT device.

far fall into the so-called *classical* spintronics category, where the conversion from electrical to magnetic power—needed to interface the magnets with electrical input and output—is realised by means of exchange of angular momentum between itinerant spins and fixed local moments or magnetic components [see Fig. 1.1(a)]. The major limitation of these approaches is represented by their energy cost: typically for a single operation in a STT device, the required energy is about $\sim 10^{-13} J \gg \Delta_H$, which can potentially delete any non-volatile character of the spin DOF by closing the gap Δ_H [9,10].

Novel approaches are hence needed to realise the transfer of spin angular momentum between different components of a spintronics device. Amongst them, a particularly promising one aims at exploiting directly the relativistic coupling between *orbital and spin DOFs* enabled by the *spin–orbit (SO) interaction* [see Fig. 1.1(b)]. All-electrical control of spintronics devices by means of the SO interaction is set to add substantially more capability and performance to electronic devices [15].

Origin of spin–orbit interaction in solids

In atoms, the SO coupling is a *relativistic* correction to the electrons' energy levels of atomic spectra. To illustrate its origin however, it suffices to adopt semiclassical (SC) electrodynamics and non-relativistic quantum mechanics arguments. Let us consider a hydrogen atom, i.e. a two-body system made up of a positive charged nucleus and an orbiting electron. According to electrodynamics, in the presence of a radial electric field $\boldsymbol{\mathcal{E}}$ generated by the nucleus, electron's

perceive in their rest frame a effective magnetic field $\boldsymbol{\mathcal{B}}$

$$\boldsymbol{\mathcal{B}} = -\frac{\mathbf{v}\times\boldsymbol{\mathcal{E}}}{c^2}\,, \tag{1.1}$$

where $\mathbf{v}$ is the velocity of the electron and $c \simeq 3\times10^8$ m/s is the speed of light. Eq. (1.1) can be rewritten expressing the electric field in radial coordinates, i.e. $\boldsymbol{\mathcal{E}} = |\boldsymbol{\mathcal{E}}|\,\hat{\mathbf{r}} = -e^{-1}\partial_r V(r)\hat{\mathbf{r}}$, where $e = +1.6\times10^{-19}$ C is the elementary charge, $V(r)$ is the electrostatic energy of the electron in the central field. Also using $\mathbf{v} = \mathbf{p}/m_e$, where $\mathbf{p} = -\imath\hbar\boldsymbol{\nabla}$ is the momentum operator, $m_e = 9.11\times10^{-31}$ kg is the electron mass, and the definition of angular momentum $\mathbf{L} = \mathbf{r}\times\mathbf{p}$, we arrive at

$$\boldsymbol{\mathcal{B}} = \frac{1}{m_e\, e\, c^2}\frac{1}{r}\frac{\partial V(r)}{\partial r}\mathbf{L}\,, \tag{1.2}$$

stating that the effective magnetic field is parallel to the angular momentum of the electron. This enters the Hamiltonian of the system via the Larmor coupling to the spin magnetic moment $\boldsymbol{\mu}_s = g_s\mu_B\,\mathbf{S}/\hbar$, where $\mathbf{S} = \hbar\mathbf{s}/2$ is the spin operator, with $\mathbf{s} = (s_x, s_y, s_z)$ being Pauli matrices acting on the spinorial part of the wavefunction, $\mu_B = e\hbar/2m_e$ is the Bohr magneton and $g_s \simeq 2$ is the spin Landé factor (gyromagnetic ratio) of a free electron [6]. We have

$$H_{\mathrm{SOC}} = -\boldsymbol{\mu}_s\cdot\boldsymbol{\mathcal{B}} = \frac{-g_s\mu_B}{\hbar m_e\, e\, c^2}\frac{1}{r}\frac{\partial V(r)}{\partial r}\mathbf{S}\cdot\mathbf{L}\,. \tag{1.3}$$

Eq. (1.3) describes a coupling between spin and orbital DOFs, i.e. the SO coupling. Since the SO interaction is sensitive to the relative orientation of the spin polarisation to the angular momentum, orthogonal spin states are separated by a SO energy gap.

Let us now focus our attention on the SO interaction in condensed matter systems. The description of the motion of electrons in solids is usually given in terms of the energy bands $\epsilon_{n\mathbf{k}}$, where n is the band index and $\hbar\mathbf{k}$ the crystal momentum or quasimomentum [16]. The energy bands are spin degenerate if both time reversal Θ and inversion symmetry I are present. In fact, considering an additional spin index $s = \uparrow,\downarrow$ to $\epsilon_{n\mathbf{k}}$, one has

$$\Theta\,\epsilon_{ns\mathbf{k}} = \epsilon_{n\bar{s}\bar{\mathbf{k}}}\,, \tag{1.4}$$

$$I\,\epsilon_{ns\mathbf{k}} = \epsilon_{ns\bar{\mathbf{k}}}\,, \tag{1.5}$$

where $\bar{s} = -s$ and $\bar{\mathbf{k}} = -\mathbf{k}$, from which one easily derives

$$\epsilon_{ns\mathbf{k}} = \epsilon_{n\bar{s}\mathbf{k}}\,. \tag{1.6}$$

An interesting consequence is that nonmagnetic materials (time-reversal invariant systems) which lack a inversion centre can display a spin splitting at a given $\mathbf{k}$.

From a microscopic point of view, the SO Hamiltonian in solids can be obtained by considering a generalised version of Eq. (1.3) for arbitrary direction of V, reading[1]

$$H_{\mathrm{SOC}} = \frac{\hbar}{4\,m_e^2c^2}(\boldsymbol{\nabla}V\times\mathbf{p})\cdot\mathbf{s}\,. \tag{1.7}$$

$V(\mathbf{r}) = V_0(\mathbf{r}) + V_{\mathrm{imp}}(\mathbf{r})$ in this case is the result of the joint effect of the periodic crystal potential (V_0) and disorder potential V_{imp} stemming from the presence of impurities, lattice defects etc. In this thesis, we will be mainly interested in the first type of SO interaction, i.e. H^0_{SOC}. The

[1]The different numeric prefactor in Eq (1.7) with respect to Eq. (1.3) is due to the Thomas precession which is such that the effective magnetic field is half the value of Eq. (1.2), i.e. $\boldsymbol{\mathcal{B}} = -\mathbf{v}\times\boldsymbol{\mathcal{E}}/2c^2$ [4].

exact form for $H^0_{\rm SOC}$ ideally requires the full knowledge of $V_0(\mathbf{r})$, hence the matrix elements of the SO interaction between the Bloch states of the SO–free Hamiltonian: $\langle ns\mathbf{k}|H^0_{\rm SOC}|n's'\mathbf{k}\rangle$ [17]. In the description of the band structure of pristine materials $V_0(\mathbf{r})$ preserves the periodicity of the lattice potential, so that one can use symmetry arguments to obtain a representation of Eq. (1.7) in terms of known Bloch states. We provide a detailed derivation of the SO interaction in 2D honeycomb layers, which is of interest in this work, based on the symmetries of the lattice Hamiltonian in Appendix A . However, for a first visualisation of the effect of the SO interaction on the energy bands, we can consider a simple parabolic model, which in second quantised-form reads [17]

$$H_0 = H_{\rm kin} + H^0_{\rm SOC} = \sum_{\mathbf{k}} b^+_{\mathbf{k}}[\xi_{\mathbf{k}} + \gamma_{\mathbf{k}} \cdot \mathbf{s}] b_{\mathbf{k}} \,, \tag{1.8}$$

$$\xi_{\mathbf{k}} = \hbar^2\mathbf{k}^2/2m \,, \tag{1.9}$$

where $b^+_{\mathbf{k}}(b_{\mathbf{k}})$ is the fermionic creation (annihilation) operator, with anti-commutation rules $\{b_{\mathbf{k}}, b^\dagger_{\mathbf{k}'}\} = 1\,\delta_{\mathbf{k}\mathbf{k}'}$, $\{b_{\mathbf{k}}, b_{\mathbf{k}'}\} = \{b^\dagger_{\mathbf{k}}, b^\dagger_{\mathbf{k}'}\} = 0$. It can be seen that the SO coupling $\gamma_{\mathbf{k}}$, whose functional form depends on the specific details of the lattice, encodes the splitting of the energy bands into two spin-split subbands $s = \pm 1 (\equiv \uparrow, \downarrow)$

$$\epsilon_{s\mathbf{k}} = \xi_{\mathbf{k}} \pm |\gamma_{\mathbf{k}}| \,. \tag{1.10}$$

Nonequilibrium effects: manifestation of the spin–orbit interaction

The spin Hall effect

The SO interaction manifests in materials via a category of effects allowing an efficient conversion between charge and spin signals. The most famous example is the *spin Hall effect* (SHE) [18, 19].

In a spin analogy to its charge counterpart, i.e. the classical Hall effect [20], the SHE consists of a spin accumulation at the boundaries of a conductor, the "spin voltage" building up in orthogonal direction with respect to the applied current [cf. Fig. 1.2(a)]. In a sample with width L, this induces a spin-dependent shift of the chemical potential across the transverse direction [19]

$$\mu_{\uparrow,\downarrow}(y) = \pm \frac{\mu_s(2y - L)}{L} \,, \tag{1.11}$$

$$y \in [0, L] \,. \tag{1.12}$$

The SO interaction, which can be responsible for $\mu_s \neq 0$, plays a similar role to the Lorentz field in the classical Hall effect, such that no magnetic field is required for the SHE to happen. In fact, similarly to Mott scattering in vacuum [21], the "electron beam" is separated by the SO interaction present in the material into its spin components. Indeed this mechanism in normal metals was proposed by Dyakonov and Perel (DP) [18] as a solid-state realisation of Mott scattering. The SHE was first measured in semiconductors, with the spin accumulation at the boundaries of the samples probed by optical means [22, 23]. Onsager reciprocity [24], allows also the inverse effect to exist, i.e. the conversion of a spin-polarised current into a charge voltage. Such inverse spin Hall effect (ISHE) was discovered in semiconductors and in metals shortly after the reports on the discovery of the SHE [25–27].

It is curious that the experimental detection of SHE/ISHE was first made more than thirty years later than the theorisation of these phenomena. Their elusive nature stems from the dif-

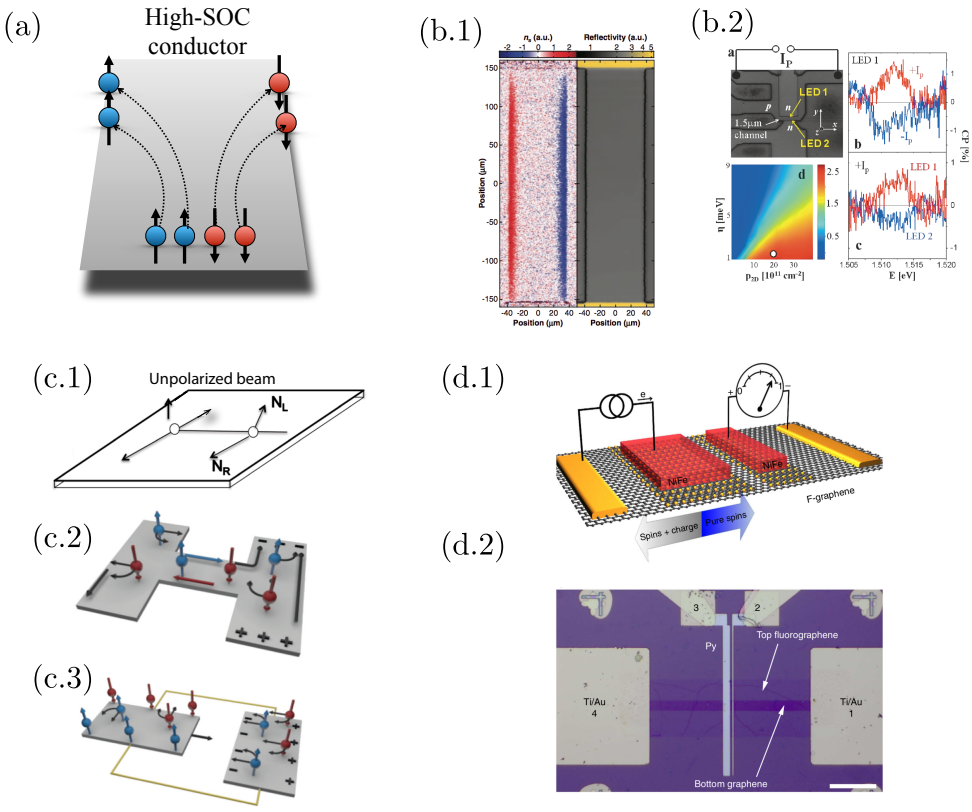

Figure 1.2: (a) In the SHE, a initially unpolarised electric current is separated into its spin components by some source of SO coupling (e.g. intrinsically present in the material or mediated by impurities). Different from the classical Hall effect, no magnetic field is needed. A spin accumulation of opposite signs builds up at the boundary of the sample. In (b.1) and (b.2) [respectively from Ref. [22] and [23]] the data obtained by optical means revealing this reversed spin accumulation. To observe the SHE by *electrical* means instead, recent proposals are based on the analogy with Mott scattering of electron beams in vacuum (c.1). Both the H-bar (c.2) and the Hirsch (c.3) geometry operate by combination of SHE and inverse SHE (ISHE). More recently, spin measurements mainly rely on non-local transport geometries ((d.1) and a scanning tunnelling microscopy image (d.2), both from Ref. [29]), where the spin accumulation generated by the SHE can be revealed far away from the source by inducing Larmor precession on itinerant spins (Hanle geometry).

ficulty of coupling pure spin currents to common electrical probes. To detect signatures of SO-coupled transport effects overcoming this barrier, different set-ups have been proposed, e.g. by Hirsch [19] and Hankiewicz *et al.* [28]. The former proposal borrows directly from the ordinary Hall effect, whereby a current flows in the closed circuit obtained by connecting the boundaries with opposite charge accumulation. In the spin equivalence envisioned in Ref. [19], the *spin Hall current*, carrying no charge, would be detected by means of a ISHE detector [see Fig. 1.2(c.3)]. The difficulties in realising Hirsch's device lie in the profound difference between a charge and a spin current. Whereas charge is a conserved quantity, implying the charge accumulation completely determines the induced *uniform* current, spin is not. The spin density vanishes on a length scale set by the *spin-relaxation time* (SRT) τ_s. The charge (spin) current satisfies the continuity(-like)

equation

$$\partial_t \rho + \boldsymbol{\nabla} \cdot \mathbf{J} = 0 \tag{1.13}$$

$$\partial_t S^a + \boldsymbol{\nabla} \cdot \mathbf{J}_s^a = -\frac{S^a}{\tau_s}\,, \tag{1.14}$$

where ρ is the charge density and $\mathbf{J}, \mathbf{J}_s$ are the charge and spin current respectively, $a = (x, y, z)$ is the spin index. From the arguments above, it can be understood that as the connecting wire in the Hirsch circuit is longer that a certain length scale $l_s = v\tau_s$, where v is the Fermi velocity, no difference exists between an open and a closed circuit [30].

In a complete analogy with Mott's vacuum chamber double scattering geometry, in the Hankiewicz's proposal a *H-bar device* had been put forward, where a charge current is applied along the first branch, is then converted into a perpendicular spin current by the SHE and finally reconverted into a detectable charge current by the ISHE in the second branch [see Fig. 1.2(c.2)]. Using this technique, the SHE was detected in ballistic semiconductors [31]. The H-bar technique falls into the class of *non-local* transport measurements, as there is a spatial separation between the injection and the detection point. Related to that and recently widely adopted is the non-local *spin valve* geometry originally discussed by Johnson and Silsbee [32], where two ferromagnetic electrodes (FM1 and FM2) are connected via a normal metal channel [see Fig. 1.2(d)]. Spin-polarised electrons are injected into the normal metal by passing a current into FM1. This creates a spin accumulation in the normal metal that acts as a source for a voltage V_{NL} building up on the far end of the samples and detectable via FM2. No charge current flows in the normal metal, hence the measured voltage is only sensitive to $\mathbf{S}$. A variation of this set-up has been proposed by Valenzuela and Tinkham to study the SHE/ISHE [26, 33]: a platform with CoFe magnetic electrodes and Al (normal metal channel), without the usage of a second ferromagnet (open circuit). In both geometries a magnetic field $\boldsymbol{\mathcal{B}}$ is applied, modulating the extracted spin signal by inducing Larmor precession. The extracted spin signal gives rise to the so-called Hanle curve [34,35]. The analysis and interpretation of the Hanle curve is of ultimate relevance for the extraction of important parameters such as the SRT, the spin diffusion length, but also providing more insightful information, e.g. the relative importance of the SHE/ISHE compared to other possible sources of the observed signal [36].

The inverse spin Galvanic effect

Despite its historical significance, the SHE is not the only possible charge-to-spin conversion (CSC) mechanism induced by SO effects. Broken structural inversion symmetry allows for the appearance of a *current-induced spin polarisation*, commonly known as inverse spin Galvanic effect[2] (ISGE) (see Fig. 1.3). Originally proposed by Ivchenko and Pikus [37], and observed by Vorobev *et al.* in Te [38], the ISGE was later theoretically studied by Lyanda-Geller, Aronov and Edelstein in a two-dimensional electron gas (2DEG) with SO coupling of the Bychkov-Rashba type[3] [39,40], whose Hamiltonian is (see also Section 4)

$$H_0^{\mathrm{2DEG}} = \frac{\mathbf{p}^2}{2m} + \lambda_{\mathrm{2DEG}}\,(\mathbf{p} \times \hat{z}) \cdot \mathbf{s}\,, \tag{1.15}$$

where $\mathbf{s} = (s_x, s_y)$ are Pauli matrices x, y acting on the spin DOF, m is the effective electron mass, and λ_{2DEG} is the Rashba parameter. The spin-Galvanic effect (SGE), the Onsager reciprocal of

[2] Also known as the *Edelstein effect*.

[3] For brevity, in the following we will adopt the common choice of referring to the 'Bychkov-Rashba interaction' as simply 'Rashba interaction'.

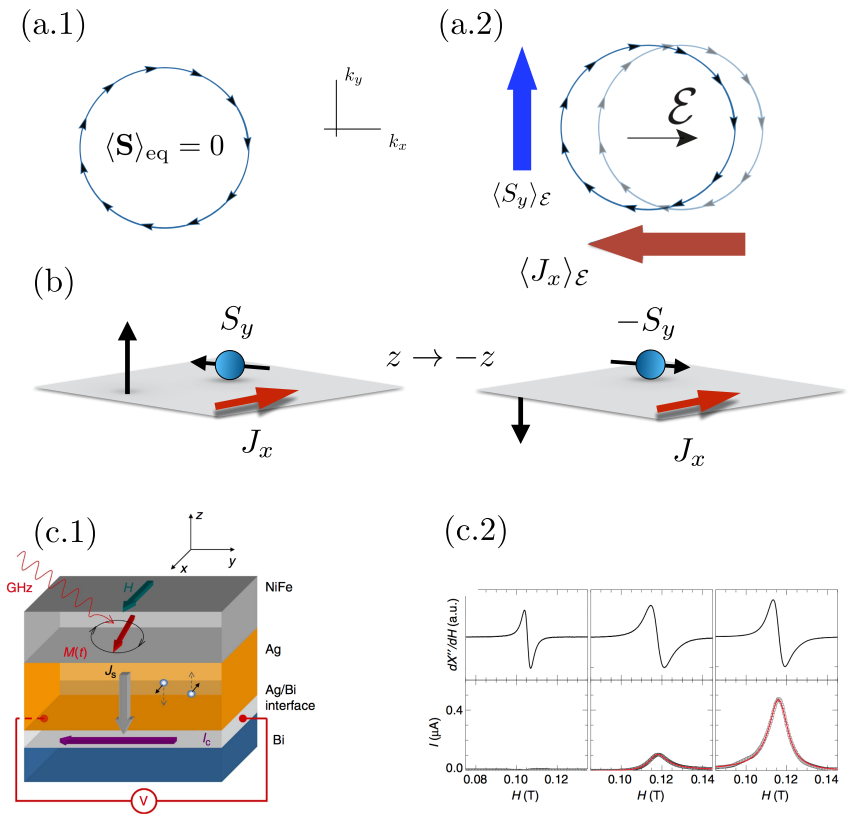

Figure 1.3: The ISGE. Due to the spin-momentum locking produced by the Rashba pseudomagnetic field (a.1), an out-of-equilibrium spin polarisation establishes orthogonally to the applied electric field $\boldsymbol{\mathcal{E}}$ (see Chapter 3); the distorted Fermi surface is represented in (a.2) by the shaded circle. (b) Such a spin-current coupling cannot occur under preserved $z \to -z$ symmetry conditions, since spin density and charge current transform differently under out-of-plane mirror reflection, the former (latter) being a axial (polar) vector. Breaking of this symmetry is hence required to have the ISGE. (c.1) and (c.2) (from Ref. [42]) show a recently-introduced method to measure the SGE in the 2DEG at Ag/Bi interface. A spin current is injected from a ferromagnet by magnetic resonance. The magnetic resonance signal is reported in the upper panels in (c.2). The three panels below refer to different systems, in order: NiFe(15)/Ag(10), NiFe(15)/Bi(8), and NiFe(15)/Ag(5)/Bi(8), of which only the latter realises a Rashba 2DEG. Accordingly, the charge current induced by the SGE is measured only when a 2DEG is formed (last panel)

the ISGE, has also been observed in GaAs semiconducting quantum wells [41].

The role of the ISGE for spintronics application is recently gaining strength, with experimental reports in Rashba 2DEG formed in Bi/Ag and $LaAlO_3/SrTiO_3$, as well as in topological insulator (TI) α-Sn thin films [42–44]. Moreover, novel techniques have been proposed to observe the effect. Rojas-Sanchez *et al.* [42] have recently put forward a set-up whereby probing the ferromagnet with magnetic-resonance technique, a spin current is injected to the 2DEG formed at the interface, which is then converted by the SGE into a detectable electric signal [see Fig. 1.3(c.1)]. Such signal is only measured when a 2DEG is effectively formed in the presence of both Bi and Ag, realising a Bi/Ag Rashba interface [see Fig. 1.3(c.2)].

The phenomenology of ISGE/SGE can be understood by symmetry arguments [45]. Electrical currents and spin polarisations are respectively polar and axial vectors. In centrosymmetric systems, where inversion symmetry is preserved, polar and axial vectors transform differently, hence no coupling between non-equilibrium spin density and charge current is allowed [see Fig. 1.3(b)]. However, in reduced symmetry conditions, polar and axial vectors components may

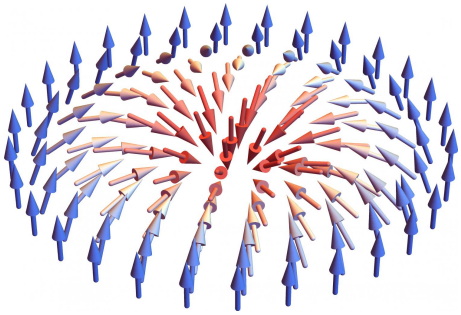

Figure 1.4: A spin skyrmion. The spin texture is such that inversion of the out-of-plane component is realised by varying some parameter, e.g. the position (real-space skyrmion) or the momentum (momentum-space skyrmion).

transform similarly. Consider, for instance, the case of electrons confined in the $x-y$ plane with mirror reflection about the $y-z$ plane (Σ^h_{yz}) preserved but with broken $z \to -z$ (Σ^v_{xy}) symmetry–e.g. induced by the presence of a substrate. Under the vertical plane reflection Σ^v_{xy}, the electrical current and spin polarisation transform as

$$\Sigma^v_{xy} : J_x, J_y \to -J_x, J_y \,, \tag{1.16}$$

$$\Sigma^v_{xy} : S_x, S_y \to S_x, -S_y \,. \tag{1.17}$$

A coupling between $J_i - S_j$ with $i \perp j$ is therefore allowed for broken Σ^v_{xy} symmetry. Microscopically, such a coupling is mediated by the SO interaction.

Other spin–orbit effects

The interplay of SO and magnetic exchange interactions is yet another research line attracting growing interest [46]. Ferromagnetic systems with broken inversion symmetry display a Dzyaloshinskii–Moriya interaction

$$H_{\mathrm{DM}} = \sum_{ij} \mathbf{D}_{ij} \cdot (\mathbf{S}_i \times \mathbf{S}_j) \,, \tag{1.18}$$

where $\mathbf{D}_{ij}$ is the Dzyaloshinskii–Moriya coupling for spins in lattice sites i, j. According to Eq. (1.18) , the energy of two neighbouring spins $\mathbf{S}_1, \mathbf{S}_2$ decreases (increases) if the respective orientation are connected by a clockwise (anti-clockwise) rotation around the Dzyaloshinskii–Moriya vector [47,48]. Such a term enables the formation of chiral spin structures, e.g. domain walls and magnetic skyrmions [49,50]. The latter are defined as spin textures displaying inverted out-of-plane magnetisation along the rotating pattern (see Fig. 1.4). Skyrmions are characterised by a topological number $S_{\mathrm{sk}} = \pm 1$, indicating the protection of the spin texture against smooth deformation and rendering them suitable for device applications [51]. Albeit originally proposed to exist in condensed matter systems as quasiparticles in real-space, skyrmionic band structures in *reciprocal space* can be established due to the interplay of SO coupling and magnetic exchange interaction [52,53]: in this thesis we will be interested in this latter case (see Chapter 7).

2D material-based spintronics

The advent of 2D materials

Atomically-thin material *sheets* have been for a long time only abstract objects, as they were thought not to exist as a stable state of matter. According to the so-called Mermin-Wagner theorem in fact, long wavelength fluctuations inevitably destroy the long-range order of 2D crystals [54]. Nevertheless, such 2D systems played an important role as theoretical platforms. For instance, most of the properties of carbon allotropes with complicated geometry, such as carbon nanotubes, were found to be captured by a simplified 2D graphite layer model [55]. Witness to the successful employment of those 2D models is the broad range of applications of carbon allotropes reached nowadays, ranging from antibiotics and flexible screens to solar cells [56–58].

The *physical isolation* of a carbon monolayer however has not been a reality until the discovery of graphene in 2004 [59], which truly initiated the field of *2D materials.* The contradiction between the 'birth' of graphene and the Mermin-Wagner theorem is resolved by considering that the thermodynamic fluctuations detrimental to the 2D crystal phase can be suppressed by anharmonic (nonlinear) coupling between bending and stretching modes, giving rise to *rippled* membranes embedded in the 3D space [60]. The low dimensionality is the key for unprecedentedly-known electrical, optical, structural and thermal properties [61]. Research on 2D materials is currently one of the most active areas in condensed matter physics; it is tempting to assume that 2D materials will soon be materials of choice across a range of applications. With Richard Feynman's 1959 prediction "There is plenty of room at the bottom" seeing its realisation [62], the family of 2D materials encompasses numerous and diverse compounds, including insulators (e.g. hexagonal boron-nitride), semiconductors [e.g. group-VI transition metals dichalcogenides (TMDs)], semimetals (graphene) and metals (e.g. NbS_2). The progress in exfoliation techniques (micromechanical cleavage, ion intercalation, surfactant-assisted ultrasonication, etc.) has allowed for the reduction of essentially any given layered bulk material into the monolayer limit [63–65]. Parallel to that, bottom-up approaches—such as chemical vapour deposition, where gaseous reactants are deposited onto a substrate to grow high quality 2D monolayers, also guarantee production of atomically thin compounds on a large scale [66].

Suitability of 2D materials for spintronics

Since their advent, 2D materials have been very attractive for spintronics purposes. To understand why, it is worth examining the prototype of a spin-logic device: the Datta-Das spin transistor [67] (see Fig. 1.5). In the device imagined by Datta and Das, spins injected from a ferromagnet (source) are free to propagate into a channel where they experience SO coupling (in Ref. [67] it is assumed to be of the Rashba type), its strength being tunable by gate voltage. The SO coupling is perceived by itinerant electrons as a pseudomagnetic field in their rest frame, controlling their precession period and allowing in turn selective extraction by a second ferromagnet (drain), e.g. collinear with the source. The maximum (minimum) extracted spin signal is obtained when the orientation of precessing spins coming in contact with the drain is parallel (antiparallel) to the drain magnetisation. The Datta-Das transistor assumes basically three operating principles: (1) spin-polarised carrier injection from the source into the device active channel, (2) large spin-propagation length and spin manipulation by the applied bias, and (3) spin-selective detection at the device drain [68].

In this respect, the idea of using the recently-discovered monolayer graphene as a spin chan-

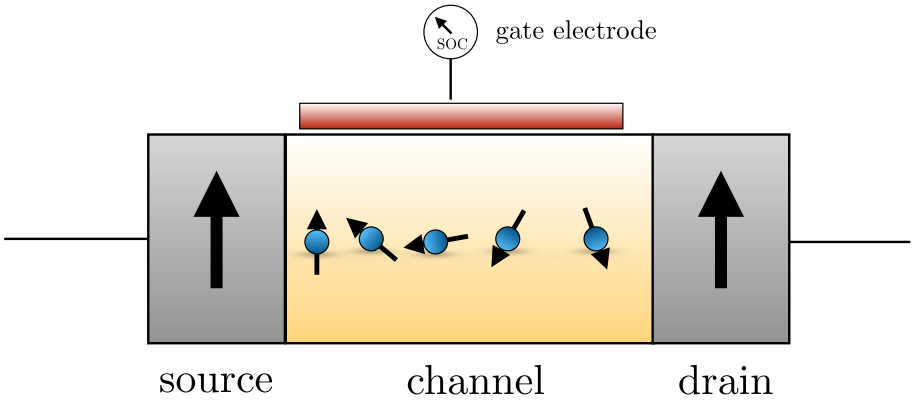

Figure 1.5: The Datta-Das transistor. A spin current is injected into the channel from a ferromagnetic source by passing through it a charge current. A gate electrode controls the strength of the SO coupling, which reflects in a different precession period of itinerant spins. Depending on the magnetisation direction of the drain electrode, the extracted spin signal can be modulated by the gate, with the spin current being at his maximum (minimum) if spins exiting the channel are parallel (antiparallel) to the drain magnetisation vector.

nel in the Datta-Das modulator emerged as natural. Firstly, due to the low dimensionality, it is intuitive to understand the advantages in interfacing graphene with source/drain ferromagnetic electrodes. Secondly, the large mean free path due to Dirac-like electron dispersion combined with low intrinsic SO coupling and hyperfine interaction [69–72], makes spin transport in this material virtually ballistic. On the other hand, the lack of sizable intrinsic SO coupling hinders spin manipulation by a gate: the Rashba parameter λ for typical electric fields $|\boldsymbol{\mathcal{E}}| \sim 0.15$ V/nm is estimated as

$$\lambda = A\,|\boldsymbol{\mathcal{E}}| = 0.01 \text{ meV}\,, \tag{1.19}$$

where A is a dimensional constant [73]. Here λ has to be compared with the typical kinetic energy of carriers in graphene, $\lambda \ll \epsilon_{\text{kin}} \simeq 4.6$ eV (see Appendix A).

A solution to this shortcoming of graphene might be found within the 2D-materials family. Many 2D systems present interesting spin-related properties [74]: for example, group-VI TMDs possess a unique spin-valley coupling (see Fig. 1.9), which we anticipate might serve—by exploiting *proximity effects*—as a key to manipulate the spin DOF of Dirac electrons; graphene/h-BN hybrids instead display enhanced spin-diffusion length with preserved high Dirac mobility, with also potential applications for spin filtering [75, 76]. From these considerations, it is clear how the variety inherent to the library of 2D materials render those systems particularly suitable to harnessing the spin DOF of electrons.

Van der Waals heterostructures: band-structure engineering and nonequilibrium effects

From the discussion above, it appears that the idea of combining different systems of reduced dimensionality into a new compound, which would ideally integrate the best properties of the single host materials, is very desirable. Such a route, concerning the vertical stacking of the 2D layers, is in fact already established experimentally. This Lego-approach give rise to so called *Van der Waals* (vdW) heterostructures, provided that vdW forces are responsible to keep the stack together [see Fig. 1.6(b)] [77]. Due to the reduced dimensionality, charge redistribution, structural changes and proximity effects—i.e. transfer of properties from one material to another

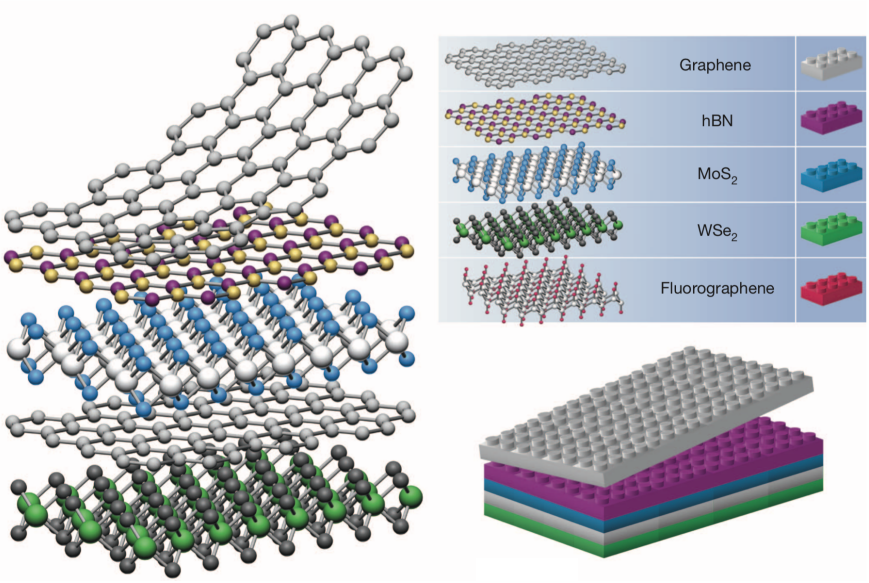

Figure 1.6: By vertically stacking 2D materials with different properties, one can potentially obtain new platforms with enhanced properties. This Lego-like approach goes under the name of vdW epitaxy. The figure is taken from Ref. [77].

via quantum tunnelling or Coloumb interaction—may occur in a very different way from usual 3D semiconducting heterostructures [78], opening a completely new venue for band structure engineering. Despite the recent origin of the research line, many successes have been reported by implementing vdW stacking. The emergence of superlattice Dirac points, surface reconstruction, gap opening and Hofstadter patterns are some examples of what have been observed in graphene on h-BN [79–81].

The rapid surge of vdW heterostructures has also offered unprecedented opportunities for exploration of nonequilibrium effects [82]. For instance, efficient phototransistors can be obtained by combining graphene high carrier mobility and TMDs sensitivity to light absorption [83, 84]. Long-living excitons could be created by using layered materials with different work functions, such as $MoSe_2/WSe_2$ [85]. Encapsulation of graphene with hBN has been shown to give rise to stable gate-controllable plasmonic modes, with low optical losses [86]. In this respect, vdW heterostructures represent a landmark for future technological advances.

Graphene-based spintronics

Spintronics (and valleytronics) with Dirac quasiparticles

Historically, graphene has been recognised as an attractive platform to be used in spintronics applications amongst the members of the ever-increasing family of 2D materials, as mentioned above. Low-energy excitations of its many-body ground state have a massless 2D Dirac character (for a detailed treatment see Appendix A), described by the continuum-limit Hamiltonian

$$H_{\mathrm{G}} = v\,(\tau_z \sigma_x p_x + \sigma_y p_y), \tag{1.20}$$

where the Fermi velocity $v \simeq 10^6$ m/s is an effective velocity of light. Above, σ_i, τ_i, with $i = x, y, z$ are Pauli matrices describing emergent effective *spin-like* DOFs of Dirac carriers associated

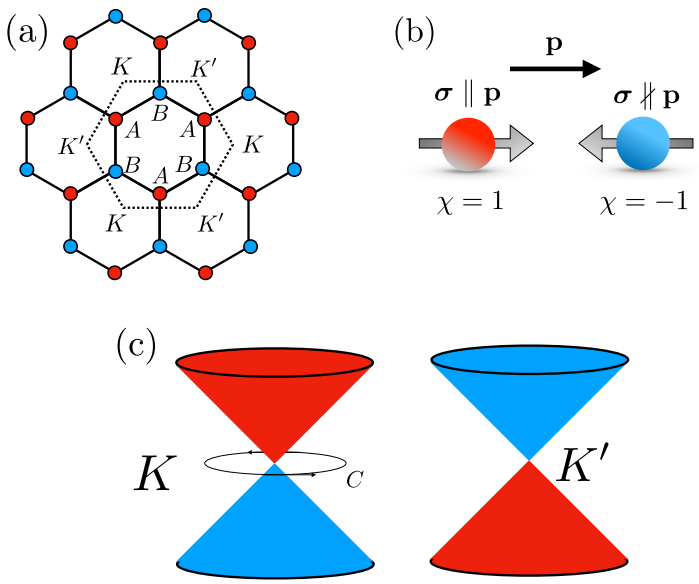

Figure 1.7: (a) The honeycomb lattice of graphene, with interpenetrating Bravais triangular sublattices A, B, respectively in red and blue. The first Brillouin zone is shown in dashed, with inequivalent corners K, K'. To describe electron dynamics in this particular crystal environment one adopts a massless Dirac 2D Hamiltonian. Carriers have here a spin-like DOF (pseudospin), stemming from the presence of two sublattices, which can be either parallel or antiparallel to the momentum vector, giving then a chiral characters to Dirac fermions. (c) The associated low-energy dispersion is linear, with two zero-energy points at the corners of the Brillouin zone K, K'. Carriers with positive energy at $K(K')$ have positive (negative) chirality, conversely for negative. The chirality of Dirac particles is also responsible for the acquisition of a nonzero Berry phase upon adiabatic loops around the Dirac points, which might result in nontrivial topological phases when a bandgap is opened in the spectrum.

with sublattice and valley spaces, as we discuss below.

The Hamiltonian Eq. (1.20) possesses many noteworthy properties. Firstly, the associate energy dispersion has a linear (massless) relativistic behaviour, with six zero-energy band crossing points (Dirac points) at the Brillouin zone corners (Fig. 1.7, see also Appendix A). Note, however, that the six bands can be grouped into two distinct categories due to rotational symmetry of the hexagonal honeycomb lattice—reducing the description to K or K' bands, obtainable from Eq. (1.20) by replacing τ_z with $\kappa = \pm 1$ respectively. Using the language of semiconductor physics, the double energy-degenerate extremal band points are referred to as *valleys*. We remark that the effective double degeneracy of the Dirac cones is guaranteed by the fermion doubling theorem [87]. Secondly, it is well known that in the massless limit, the Dirac equation is decoupled into two separate equations, describing *left- and right-handed chiral* particles [88]. Mathematically, the chirality of Dirac carriers is encoded in the presence in Eq. (1.20) of Pauli matrices σ_i associated to a spin-like DOF, commonly referred to as *pseudospin* [89]. To see that, one can rewrite Eq. (1.20) by introducing the chiral operator $\chi_\sigma = \boldsymbol{\sigma} \cdot \mathbf{p}/|\mathbf{p}|$, whose eigenstates are associated with eigenvalues ± 1. Thus, in analogy to the real spin of massless relativistic particles in the vacuum, the pseudospin of graphene's quasiparticles points in the parallel/antiparallel directions with respect to their momentum [see Fig. 1.7(b)]. Note that chiral symmetry in crystal structures coincides with sublattice symmetry. Indeed the chiral symmetry inherent to the Dirac Hamiltonian is due to the fact that the electron density is equally shared between A and B sublattice sites of the honeycomb structure. The ground state wavefunction is given then as an equal-weight

linear combination of orthogonal pseudospin "up/down" states (i.e. electrons living on A, B sites respectively) from which it follows that pseudospin of quasiparticles in graphene lies on the 2D plane, in agreement with our explanation above.

The chirality of Dirac carriers greatly contributes to the outstanding electronic properties of graphene and exotic phenomena such as the Klein tunnelling [90–92], crossover from weak antilocalisation to weak localisation [93, 94] and the chiral quantum Hall effect [95, 96]. Chiral symmetry is also behind the absence of backscattering [89] and the presence of completely delocalised critical zero-energy modes [97, 98].

A further signature of the chirality of graphene's quasiparticles manifests upon adiabatic evolution of the electron wavefunction along a closed loop C in $\mathbf{k}$ space [see Fig. 1.7(c)]. The acquired *Berry phase* is

$$\gamma_n = \oint_C \boldsymbol{\mathcal{A}}_{n\mathbf{k}}\, dl = \pi, \tag{1.21}$$

where $\boldsymbol{\mathcal{A}}_{n\mathbf{k}}$ is the *Berry connection* given in terms of the periodic part of the Bloch eigenstates $|u_{n\mathbf{k}}\rangle$ associated to Eq. (1.20), as $\boldsymbol{\mathcal{A}}_{n\mathbf{k}} = \imath \langle u_{n\mathbf{k}} | \boldsymbol{\nabla}_{\mathbf{k}} u_{n\mathbf{k}} \rangle$. This fact signifies the underlying nontrivial topology of this material. As such, by breaking chiral symmetry, graphene can be driven into different topological insulating phases, such as the quantum spin Hall (QSH) [99], quantum anomalous Hall (QAH) [100] or the quantum valley Hall phases.

Despite the Hamiltonian Eq. (1.20) describes spin degenerate quasiparticles, a SO term possessing the full point-group symmetry D_{6h} of the pristine honeycomb lattice is in principle allowed [99, 101]; the so-called *intrinsic* SO coupling is written as

$$H_{\mathrm{I}} = \lambda_{\mathrm{I}} \tau_z \sigma_z s_z \,. \tag{1.22}$$

The reason why H_{I} is usually neglected in Eq. (1.20) such that real spin only appears as a dummy DOF, is the smallness of the intrinsic SO strength λ_{I}. Early estimations by heuristic arguments in Ref. [99] yielded $\lambda_{\mathrm{I}} \sim 200\,\mu$eV, whereas later and more accurate tight-binding studies and first-principles results predicted values ranging from $1 - 50\,\mu\mathrm{eV} \sim 11 - 500$ mK [71, 73, 102–104], meaning $\lambda_{\mathrm{I}} \ll \hbar v/a \simeq 4.6$ eV, where $a = 0.142$ nm is the carbon-carbon bond length, justifying the negligence of the SO gap λ_{I} in the minimal Dirac model of graphene, Eq. (1.20).

If on the one hand, the low intrinsic SO coupling—in combination with the ultra-high mobility of chiral carriers—yields extremely long spin lifetimes, hence being desirable for utilising graphene as an exceptional spin channel, it would also, conversely, represent a shortcoming to harnessing the spin DOF of Dirac fermions, as discussed above. The extremely narrow intrinsic SO-gap region, which is unlikely to be accessed in realistic conditions, is in fact a very important limitation. Kane and Mele showed that the presence of such a SO term is associated with a $\mathbb{Z}_2$ QSH phase, manifesting with the appearance of topologically-protected edge states carrying a spin current winding around the boundary of a finite sample [99]. Hence, the excessively low intrinsic SO coupling poses an halt to the dream of utilising graphene as a perfect spintronic platform, allowing manipulation of multiple spin-like DOFs, with non-quantised long-lived spin currents at finite carrier density and quantised topologically-protected spin currents as the Fermi energy ϵ is tuned inside the QSH insulating gap.

In the light of the above considerations however, it is easy to understand how the gentle enhancement of SO coupling in graphene, preserving the Dirac structure, has become in recent years one of the most attractive experimental lines of research.

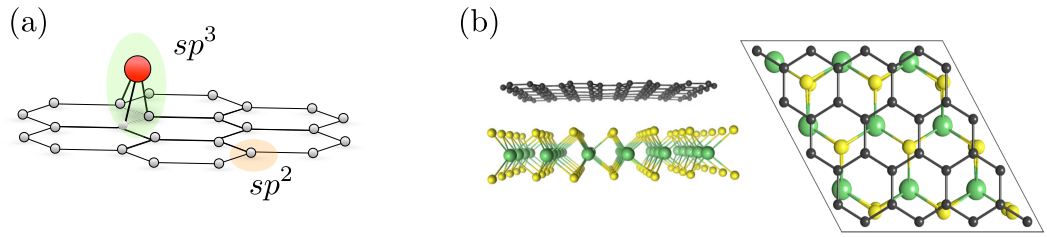

Figure 1.8: Adatom-decorated graphene and graphene-on-TMDs. (a) One-side decoration of graphene with external species, e.g. H, produces a modification of the chemical bonds $sp^2 \rightarrow sp^3$ (tetragonal structure). This induces a local enhancement of the SO coupling, as demonstrated in Ref. [105]. (b) Side view and top view of graphene/TMD bilayers, which have already been proven extremely successful to enhance the SO coupling experienced by Dirac fermions up to 1-10 meV.

Enhancing spin–orbit coupling in carbon layers: from spin–orbit coupling-active adatoms to graphene-on-a-substrate

One of the first proposals to enhance SO coupling in graphene [105] concerned adatom decoration. Even in the dilute limit $n_i \sim 0.01 - 0.05\%$, with n_i being the impurity density, adatoms, e.g. hydrogen, can produce giant local SO coupling $\lambda_{\text{adat}} = 1$ meV $\gg \lambda_{\text{I}}$ by locally introducing sp^3 bonding (see Fig. 1.8). Using heavier adatoms, e.g. indium or tantalum, can give rise to even larger SO coupling [106, 107], with a topological band gap in Ref. [106] predicted as large as 20 meV. However, experiments are facing difficulties to show a signature of the $\mathbb{Z}_2$ insulating phase [108–112], most likely due to strong valley mixing that takes place for the dilute adatom coverage of experimental relevance [113].

Graphene-based vdW systems with proximity-induced SO coupling offer good prospects in the circumvention of this situation. In particular, TMD monolayers have been recognised as an ideal matching to graphene. TMDs are compounds of the type MX_2, where M, X are respectively a transition metal and the chalcogen element; their crystal structure is such that an M layer is "sandwiched" between two X atomic layers in a trigonal prismatic or an octahedral phase [see Fig. 1.9(a)] [114–116]. Relevant to our purposes, we will mainly focus on group-VI semiconducting TMDs, e.g. M =Mo, W; X = S, Se. Henceforth we will refer to this subgroup when mentioning TMDs. Lack of inversion symmetry and the presence of a heavy metal atom in the lattice are responsible for a very large SO coupling splitting of the valence bands $\sim 150 - 450$ meV [117]. Time reversal symmetry forces the spin splitting to be opposite at different band edges (valleys) K, K' [see Fig. 1.9(a)]. A strong peculiar *spin-valley coupling* is hence present in TMDs [118]. Inversion-symmetry breaking is also responsible for circular dichroism in TMDs in different k-space regions, which takes the extreme form of optical selection rules at K, K' [119] [see Fig. 1.9(a)]. The spin-valley coupling can be then exploited to selectively create opposite spin-polarised populations at different valleys by optical means [120, 121].

The suitability of graphene on TMD bilayers for spintronics has been endorsed by recent theoretical and experimental results: electronic structure calculations show that relativistic effects in graphene on a TMD are greatly enhanced [122, 123] consistent with the SO coupling fingerprints in transport measurements [123–126]. These works point to a Rashba SO coupling in the range of 1–10 meV, up to four orders of magnitude larger than graphene on a standard substrate. A further advantage of these heterostructures stems from the optical selection rules characteristic of TMDs mentioned above, which would allow all-optical injection of spins into the graphene layer [84]. In fact, spin injection from a MoS_2 to an adjacent graphene layer has been recently

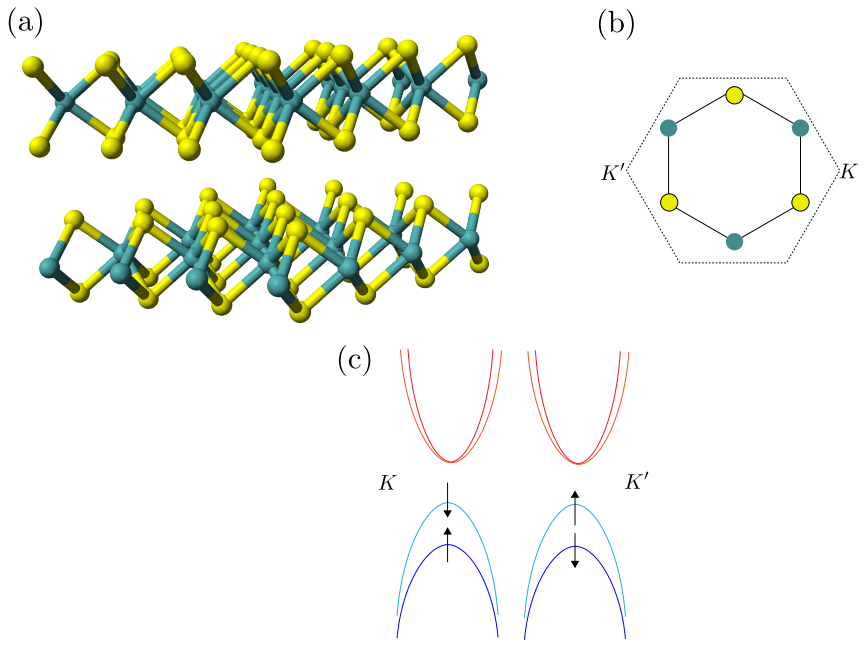

Figure 1.9: Transition metal dichalcogenides. (a) A 3D visualisation of typical MX_2 layered compounds. (b) Top view, showing the honeycomb structure with different species sitting on different corner of the hexagon. (c) Due to the structural inversion asymmetry, TMDs display spin-split bands at K, K' points, with a large [$\sim(0.1 - 0.5)$ eV] band gap. Time reversal symmetry guarantees that the spin polarisation is reversed at opposite valley, allowing selective spin excitation to the conduction bands by circularly polarised light (circular dichroism).

achieved [127], demonstrating the viability of the *optospintronics* route.

We briefly want to point out that more general graphene-on-a-substrate heterostructures, which strictly speaking do not fall into the vdW family—the substrate being a bulk, rather than a layer—are also attracting much attention. Proximity effects can be equally efficient, allowing the transfer of additional interactions to Dirac fermions beyond the SO coupling. For instance, the anomalous Hall effect (AHE) has been observed in graphene on YIG [128, 129], indicating the successful transfer of magnetic exchange coupling (MEC) to the carbon layer. The interest in magnetised graphene is also been fuelled by the expectation of accessing the topologically-protected regime of quantised transverse conductivity, i.e. the *quantum AHE*, as predicted few years ago [52, 130]. This sought-after regime has also been proposed in vdW heterostructures of graphene and layered ferromagnetic insulator $Cr_2Ge_2Te_6$ [131]. Another very interesting research line concerns induced superconductivity in graphene. The penetration of Cooper pairs from Nb contacts to graphene sheet has been recently obtained [132]. All these recent developments have paved the way to a new material-science era, having as protagonists atomically well-defined interfaces of materials with tailored on-demand properties.

Summary and outline: structure of this thesis

The scope of this thesis is to study theoretically coupled charge-spin transport and SO-related phenomena in 2D Dirac materials with proximity-induced SO interactions. As representative systems in this respect, particular focus will be devoted to graphene-on-TMD bilayers. This thesis is organised as follows: in Chapter 2 we will introduce the technical ingredients to present our work. In particular, we will revise the SC treatments commonly adopted to study trans-

port phenomena, and present our fully quantum mechanical (FQM) self-consistent formalism. The latter will allow for an accurate description of honeycomb layers with strong pseudospin-spin coupling, which takes into account on equal footing extrinsic (impurity-dependent) and intrinsic (band-structure driven) contributions to transport coefficients. In Chapter 3 we analyse thoroughly the electronic properties of the relevant models to study the dynamics of Dirac fermions subject to SO effects, i.e. the minimal (C_{6v} point symmetry group) and generalised (C_{3v} point symmetry group) 2D Dirac-Rashba models; the latter in particular encompasses all orbital and SO terms which are needed to capture the physics of realistic graphene/TMD heterostructures. In Chapter 4 we start to concentrate more specifically on transport effects in the nonequilibrium steady state, by considering the occurrence of the SHE and the ISGE in the C_{6v} model. We show the suppression (enhancement) of the SHE (ISGE), in a unified picture combining SC and quantum formalisms. We unveil the connection of the resulting nonequilibrium physics to the underlying conservation laws of the theory. In Chapter 5 we tackle the time-dependent description of charge-spin transport in the C_{6v} model; we establish a microscopic theory of coupled charge-spin dynamics starting from the diagrammatic FQM approach. The SRTs and the CSC rates will be then obtained. In Chapter 6 we extend our work to generalised 2D Dirac-Rashba systems. We examine the impact on the SHE and the ISGE of additional interactions present in realistic materials, exploring the conditions for the emergence of the SHE; then, we focus our attention on the description of spin relaxation in graphene/TMDs, based on a SC treatment of the density matrix. In particular, analytical formulas will be obtained for the spin dynamics and the SRTs in the strong SO regime, with interesting consequences in connection to on-going experiments. In Chapter 7 we broaden our horizon by applying our developed formalism to the case of graphene on a ferromagnetic substrate. We discuss the approaching of the quantum anomalous Hall state, identifying a robust experimental smoking gun forerunning this regime. Finally, Chapter 8 contains a final discussion and the conclusions of our work.

Chapter 2

Methods for Spin and Charge Transport in Disordered 2D Dirac Materials

Overview

In this Chapter we present the various formalisms adopted in the rest of this thesis to develop a unified theory of charge-spin transport phenomena in 2D Dirac materials. These formalisms can be categorised into two families: SC and FQM. The first class encompasses the SC Boltzmann transport theory and its quantum extensions based on the kinetic equation for the density matrix—we will briefly review both below. Their common SC trait is due to the average over some quantum DOF (e.g. spin) and the partial negligence of quantum coherence. This technical simplification allows for a more transparent physical interpretation of the results. However, lacking a rigorous treatment of the quantum nature of the electrons' wavefunction, its regime of validity is restricted to the situation where $k_F l \gg 1$, with k_F being the Fermi wavevector and l the mean-free path between collisions with impurity (or phonons). A more refined physical description can be obtained within the second class of FQM formalisms, based on a diagrammatic treatment of the Kubo linear response functions. Within the latter framework, one would in principle be able to capture not only leading SC contributions to the transport coefficients, but also quantum processes and interference effects, e.g. quantum side jump and diffractive skew scattering. However, we will mainly focus in this thesis on SC effects. Hence our approach aims at matching the FQM and SC results. We will find useful to adopt this strategy mainly for two reasons:

1. to benchmark our calculations by independent derivations within the two SC and FQM frameworks. This is of particular relevance in those cases where the physics is the result of the competition of several energy scales, especially when two or more of them are treated non-perturbatively;

2. to get a unified and more in-depth qualitative understanding of the results, along with a more transparent interpretation of them.

Finally, we note that the within the FQM-methods class, we also include the derivation and the analysis of the Ward identities (WIs). The latter, being exact symmetry relations based on the

underlying conservation laws of the model, represent a powerful tool, not only to benchmark the obtained results, but also—and more importantly—to directly predict the emergence of genuine relativistic transport effects.

Semiclassical formalisms

The 2D semiclassical Boltzmann transport theory

The Boltzmann transport equation (BTE) provides a statistical description of a system in terms of the function $f(\mathbf{r}, \mathbf{k}, t)$, i.e. the probability density of quasiparticles that can be found at time t in a very small region $d^d\mathbf{r}\, d^d\mathbf{k}$ of configuration space centred at ($\mathbf{r}$,$\mathbf{k}$), with d being the dimension of the system. The distribution function f is linked to the total number of particles N via

$$d^d\Omega\, f(\mathbf{r}, \mathbf{k}, t) = d^d\mathbf{r}\, d^d\mathbf{k}\, f(\mathbf{r}, \mathbf{k}, t) = dN\,, \tag{2.1}$$

where dN is the number of particle in the small volume $d^d\Omega$. Knowing f, the macroscopic observables describing the system can be obtained, as we shall see below. We will consider from now on the case $d = 2$, which is relevant to the work in this thesis. By introducing a momentum distribution function with a precise value at each point in space, the Boltzmann approach clearly violates Heisenberg uncertainty principles, which poses limits to its validity. However the usage of the BTE is justified in terms of wavepackets with well-defined average momentum *or* centre of mass coordinates, spin, etc. [133, 134]. In a solid, f is also labeled by a band index n. We will omit that for a while and discuss its inclusion below.

The BTE is derived on the assumption of Hamiltonian dynamics for the centre of mass and the average momentum of the wavepacket [135]. Under the SC equations of motion, the assumption of incompressible fluid holds, which means an external electromagnetic force $\mathbf{F} = -e(\boldsymbol{\mathcal{E}} + \mathbf{v} \times \boldsymbol{\mathcal{B}})$, where $\boldsymbol{\mathcal{E}}, \boldsymbol{\mathcal{B}}$ are the electric and magnetic field respectively, only produces a shift in position and momentum of the wavepacket, respectively $\mathbf{r}' = \mathbf{r} + \mathbf{v}dt$, $\mathbf{k}' = \mathbf{k} + \mathbf{F}\, dt/\hbar$, where $\mathbf{v}$ is the velocity. Instead, the number of particles in $d^d\Omega$ can only be altered by collisions. For later convenience we use the notation $f(\mathbf{r}, \mathbf{k}, t) = f_{\mathbf{k}}(\mathbf{r}, t)$. Taking the total time derivative of the distribution function, we get

$$\frac{df_{\mathbf{k}}(\mathbf{r}, t)}{dt} = \frac{\partial f_{\mathbf{k}}(\mathbf{r}, t)}{\partial t} + \mathbf{v} \cdot \boldsymbol{\nabla}_{\mathbf{r}} f_{\mathbf{k}}(\mathbf{r}, t) + \frac{1}{\hbar}\mathbf{F} \cdot \boldsymbol{\nabla}_{\mathbf{k}} f_{\mathbf{k}}(\mathbf{r}, t) = I[f]\,, \tag{2.2}$$

where on the right-hand side (RHS) of Eq. (2.2) we have the collision integral $I[f]$. To find an analytic form for $I[f]$ we consider transitions between states with different momenta $\mathbf{k} \to \mathbf{k}'$ induced by a static potential V. In this thesis we will consider point-like random potentials generated by N_i impurities located at position $\mathbf{r}_i$

$$V(\mathbf{r}) = u_0 \sum_i^{N_i} \delta(\mathbf{r} - \mathbf{r}_i)\,, \tag{2.3}$$

where u_0—dimension of energy $\times$ area—measures the scattering strength. We have taken here for simplicity a *scalar* impurity potential, i.e. a potential diagonal in all internal DOFs. We generalise our treatment later to more realistic forms, including intervalley and spin-dependent scattering. Standardly, the random potential is treated by means of a disorder-average procedure over all the possible impurity configurations [136]. After having performed disorder average and having taken the thermodynamic limit $N, \Omega \to \infty$, it can be shown that, rather than involving

a sum of scattering terms from different centres, the collision integral is reduced to a *single-impurity* term, scaling with the impurity concentration $n_i = N/\Omega$ [136, 137]. The probability of the elastic collision event can be obtained by invoking the Fermi's golden rule [138]

$$W_{\mathbf{k}\mathbf{k}'} = \frac{2\pi n_i}{\hbar} |\langle \mathbf{k}'|\mathrm{T}|\mathbf{k}\rangle|^2 \delta(\epsilon_{\mathbf{k}} - \epsilon_{\mathbf{k}'}) \,, \tag{2.4}$$

where the Dirac delta function ensures conservation of energy in the scattering event. In Eq. (2.4) T is the single-impurity T-matrix defined in terms of V as

$$\mathrm{T}_{\mathbf{k}\mathbf{k}'} = \langle \mathbf{k}'|V|\Psi_{\mathbf{k}}\rangle \,, \tag{2.5}$$

where $\Psi_{\mathbf{k}}$ is an eigenstate of the full Hamiltonian of the system $H = H_0 + V$ that satisfies the Lippman-Schwinger equation[1] [136]

$$|\Psi_{\mathbf{k}}\rangle = |\mathbf{k}\rangle + \frac{V}{\epsilon_{\mathbf{k}} - H_0 + \imath 0^+} |\Psi_{\mathbf{k}}\rangle \,, \tag{2.6}$$

and $|\mathbf{k}\rangle$ represents a plane wave. The collision integral will then be written as [$f_{\mathbf{k}} \equiv f_{\mathbf{k}}(\mathbf{r}, t)$]

$$I[f] = -\frac{1}{\Omega} \sum_{\mathbf{k}'} (W_{\mathbf{k}\mathbf{k}'} f_{\mathbf{k}} - W_{\mathbf{k}'\mathbf{k}} f_{\mathbf{k}'}) \,. \tag{2.7}$$

In addition to a sum over all scattered waves with different momenta $\mathbf{k}'$, collision events also produce a coordinate shift of the centre of mass of the wavepacket, known as *side-jump* [140–142], which is not included in Eq. (2.7). However it is of secondary importance in this thesis, as we are interested in dominant contributions to transport coefficient in the dilute limit, as we explain in more detail in the following. Note that number conservation imposes [143–145]

$$\int d^2\mathbf{r} \frac{1}{\Omega} \sum_{\mathbf{k}} I[f(\mathbf{r}, \mathbf{k}, t)] = 0 \,. \tag{2.8}$$

The Fermi-Dirac distribution function

$$f^0_{\mathbf{k}} = \frac{1}{1 + e^{(\epsilon_{\mathbf{k}} - \mu)/k_B T}} \,, \tag{2.9}$$

where μ, k_B, T are the chemical potential, Boltzmann constant and temperature respectively, is a space- and time-independent solution to the BTE, i.e. an equilibrium solution. However, in the presence of weak external forces $\mathbf{F}$ the system is driven out of equilibrium and the electron density is redistributed. A solution to the BTE can be found on the assumption that the system only slightly departs from the local equilibrium, i.e.

$$f_{\mathbf{k}} = f^0_{\mathbf{k}} + \delta f_{\mathbf{k}} \,, \tag{2.10}$$

where $\delta f_{\mathbf{k}}$ is a correction linear in the external field. The corresponding *linearised* BTE is written as [137]

$$\frac{\partial\, \delta f_{\mathbf{k}}}{\partial t} + \mathbf{v} \cdot \boldsymbol{\nabla}_{\mathbf{r}}\, \delta f_{\mathbf{k}} + \frac{1}{\hbar} \mathbf{v} \cdot \mathbf{F} \left(-\frac{\partial f^0_{\mathbf{k}}}{\partial \mu} \right) = I[\delta f_{\mathbf{k}}] \,. \tag{2.11}$$

To study the dynamics of electrons in solid-state systems, a label for the electronic bands needs

[1] The sign of the imaginary, small addend $\imath 0^+$ is selected to describe the physical scattering problem (outgoing wave) [139].

to be added to the distribution function, beyond additional quantum indices including the spin and other quantum DOFs, i.e. $f_{\mathbf{k}} \to f_{\alpha\mathbf{k}}$ with $\alpha = \{n, s, ...\}$. $\mathbf{v}$ in Eq. (2.11) is replaced by the band velocity $\mathbf{v}_{\alpha\mathbf{k}}$. The displacement of the physical observables $\mathcal{O}$ with respect to their equilibrium value are obtainable from the solution of the BTE as

$$\delta\mathcal{O}(\mathbf{r}, t) = \sum_{\alpha} \sum_{\mathbf{k}} \langle \mathcal{O} \rangle_{\alpha\mathbf{k}} \, \delta f_{\alpha\mathbf{k}}(\mathbf{r}, t) \,, \tag{2.12}$$

where $\langle \mathcal{O} \rangle_{\alpha\mathbf{k}} = \langle \alpha\mathbf{k}|\mathcal{O}|\mathbf{k}\alpha\rangle$ is the average value of $\mathcal{O}$ on the eigenstate of the system $|\mathbf{k}\alpha\rangle$. For example, the nonequilibrium part of the charge current is given by

$$\delta\mathbf{J}(\mathbf{r}, t) = \sum_{\alpha} \sum_{\mathbf{k}} \langle \mathbf{J} \rangle_{\alpha\mathbf{k}} \, \delta f_{\alpha\mathbf{k}}(\mathbf{r}, t) = -e \sum_{\alpha} \sum_{\mathbf{k}} \mathbf{v}_{\alpha\mathbf{k}} \, \delta f_{\alpha\mathbf{k}}(\mathbf{r}, t) \,. \tag{2.13}$$

In its simplest form, the BTE presented in this section for electrons in solids completely neglects quantum coherence effects. In the following we will introduce refinements to the SC formalism allowing one to partially capture quantum coherence.

Time-dependent perturbation theory for the density matrix: a Boltzmann-like equation

A "quantum upgrade" to the SC Boltzmann equation can be obtained by replacement of the classical distribution function with the density matrix of the system ρ obeying the quantum Liouville equation [146]

$$\frac{\partial \rho}{\partial t} + \frac{\imath}{\hbar}[H^{\text{tot}}, \rho] = 0 \,. \tag{2.14}$$

The total Hamiltonian includes the bare part (H_0), the interaction with the electromagnetic field, and the impurity potential V. In principle Eq. (2.14) takes fully into account the quantum nature of the electronic wavefunctions. In practice, however, it is difficult to solve it in its full generality. To simplify the treatment, one usually adopts the diffusive limit $k_F l \gg 1$ and integrates out some DOF, while keeping the quantum coherence for some other. To give a concrete example, one may think about neglecting interband transitions (pseudospin coherence) in graphene, while preserving real spin coherence. We will adopt a similar prescription in Chapter 6. Following the procedure put forward in Ref. [147], Eq. (2.14) can be projected onto a set of time-independent states with definite wavevector $\{|\mathbf{k}\alpha\rangle\}$. We will chose them, later on, as the eigenstates of the 2D Dirac Hamiltonian of graphene. We use the notation $\rho_{\mathbf{k}\mathbf{k}'} \equiv \rho^{\alpha\alpha'}_{\mathbf{k}\mathbf{k}'} = \langle \mathbf{k}\alpha|\rho|\mathbf{k}'\alpha'\rangle$. The density matrix is then decomposed into its diagonal and off-diagonal parts in momentum space i.e. $\rho_{\mathbf{k}\mathbf{k}'} = f_{\mathbf{k}}\delta_{\mathbf{k}\mathbf{k}'} + g_{\mathbf{k}\mathbf{k}'}$, where for $g_{\mathbf{k}\mathbf{k}'}$ we take $\mathbf{k} \neq \mathbf{k}'$. As implicitly assumed when writing Eq. (2.12), the majority of observables are diagonal in momentum, hence we are mainly interested in the form of $f_{\mathbf{k}}$. As discussed in detail in Refs. [147,148], a closed equation for $f_{\mathbf{k}}$ can be derived upon assuming a Gaussian-noise statistics for the configurational average of the weak random scattering potential V in Eq. (2.3), i.e.

$$\langle V_{\mathbf{k}\mathbf{k}'} \rangle_{\text{dis}} = 0 \,, \tag{2.15}$$

$$\langle V_{\mathbf{k}\mathbf{k}'} V_{\mathbf{k}'\mathbf{k}''} \rangle_{\text{dis}} = \delta_{\mathbf{k},\mathbf{k}''} n_i u_0^2 \,, \tag{2.16}$$

where the disorder average for a generic operator A is defined as [136]

$$\langle A \rangle_{\rm dis} = \lim_{N_i,\Omega\to\infty} \prod_{i=1}^{N_i} \int_\Omega \frac{d\mathbf{r}_i}{\Omega} A(\mathbf{r}_1, \mathbf{r}_2, .., \mathbf{r}_{N_i}) \Big|_{\frac{N_i}{\Omega}=n_i} . \tag{2.17}$$

Note the Eqs. (2.15)-(2.16) are obtained on the assumption of a scalar scattering potential. As anticipated above, we will discuss in Chapter 3 and in subsequent Chapters a more general case. After lengthy calculations [148–150], the final equation is found as

$$\frac{\partial f_{\mathbf{k}}}{\partial t} + \frac{\imath}{\hbar}[H_0, f_{\mathbf{k}}] - \frac{e}{\hbar}(\boldsymbol{\mathcal{E}} + \mathbf{v}\times\boldsymbol{\mathcal{B}})\cdot\boldsymbol{\nabla}_{\mathbf{k}} f_{\mathbf{k}} = I[f] \tag{2.18}$$

with

$$I[f] = -\frac{\pi}{\hbar}\langle \sum_{\mathbf{k}'} \delta(\epsilon_{\mathbf{k}} - \epsilon_{\mathbf{k}'}) \left[V_{\mathbf{k}\mathbf{k}'} V_{\mathbf{k}'\mathbf{k}} f_{\mathbf{k}} + f_{\mathbf{k}} V_{\mathbf{k}\mathbf{k}'} V_{\mathbf{k}'\mathbf{k}} - 2 V_{\mathbf{k}\mathbf{k}'} f_{\mathbf{k}'} V_{\mathbf{k}'\mathbf{k}}\right]\rangle_{\rm dis} . \tag{2.19}$$

The latter represents the matrix generalisation of the collision integral in the RHS of Eq. (2.2). Also note that Eq. (2.18) contains on the left-hand side (LHS) a Larmor term $[H_0, f_{\mathbf{k}}]$ describing coherent precession of electrons' spin or pseudospin DOFs: we will focus our attention on its effect in Chapter 6. The Kubo formalism, which we are about to present, allows very naturally to go beyond the limitations of SC Boltzmann-like descriptions.

Fully quantum mechanical formalisms

Kubo linear response theory

The SC formalism presented above describes how the electron distribution, and thus the observables, responds to the application of weak external forces. An analogous FQM approach is given by the Kubo formula [151]. We present here a short derivation. For simplicity, we restrict our focus to the zero temperature formalism. Let us consider an external spatially homogenous perturbation[2]

$$H_\mu^{\rm ext}(t) = \phi_\mu(t)\mathcal{O}_\mu(t) , \tag{2.20}$$

which drives a system with Hamiltonian H out of equilibrium. Above, ϕ_μ is a source field coupled to some operator $\mathcal{O}_\mu$, μ being a index related to the spatial orientation of the fields and/or their associated matrix structure (see Chapter 5). In the linear response spirit, the expectation value of any other generic observable $\mathcal{O}_\nu$ is linear in the perturbing source, i.e.

$$\langle \mathcal{O}_\nu(t)\rangle_\phi = \langle \mathcal{O}_\nu(t)\rangle_{\rm eq} + \int dt'\, \chi_{\nu\mu}(t,t')\,\phi_\mu(t') , \tag{2.21}$$

where $\langle ...\rangle_{\rm eq}$ and $\langle ...\rangle_\phi$ denote respectively quantum average over a basis set of many-body quantum states $\{n^{\rm eq}\}, \{n^{\rm int}\}$ respectively in the absence (equilibrium) or presence of the external field. Explicitly

$$\langle \mathcal{O}_\nu\rangle_\phi = \frac{1}{Z}\sum_{\{n^{\rm int}\}} e^{-\beta E_n^{\rm int}} \langle n^{\rm int}|\mathcal{O}_\nu|n^{\rm int}\rangle = \frac{\sum_{\{n^{\rm int}\}} e^{-\beta\epsilon_n^{\rm int}}\langle n^{\rm int}|\mathcal{O}_\nu|n^{\rm int}\rangle}{\sum_{\{n^{\rm int}\}} e^{-\epsilon_n^{\rm int}/k_BT}} , \tag{2.22}$$

where $\epsilon_n^{\rm int}$ is the energy of the interacting state $|n^{\rm int}\rangle$. Eq. (2.22) holds in a similar fashion for the equilibrium average $\langle ...\rangle_{\rm eq}$. $\chi_{\nu\mu}(t,t')$ is the so-called *response function*, whose explicit form can

[2] We work here in the Heisenberg picture, so that operators are time dependent.

be derived by means of the Kubo formula [152]. Suppose the external perturbation is switched on at some time $t = t_0$, i.e.

$$H^{\text{tot}} = H + H^{\text{ext}}_{\mu}(t)\,\theta(t-t_0) = H + \phi_{\mu}(t)\mathcal{O}_{\mu}(t)\,\theta(t-t_0)\,, \tag{2.23}$$

where $\theta(.)$ is the Heaviside step function. The time evolution of the perturbed states is described by

$$H^{\text{tot}}(t)\,|n^{\text{int}}(t)\rangle = \imath\hbar\frac{\partial}{\partial t}|n^{\text{int}}(t)\rangle\,. \tag{2.24}$$

It is convenient to switch from the Heisenberg to the interaction picture considering

$$\begin{aligned}|n^{\text{int}}(t)\rangle &= e^{-\frac{\imath}{\hbar}Ht}|\hat{n}^{\text{int}}(t)\rangle = e^{-\frac{\imath}{\hbar}Ht}\hat{U}_{\mu}(t,t_0)|\hat{n}^{\text{int}}(t_0)\rangle \\ &= e^{-\frac{\imath}{\hbar}Ht}\hat{U}_{\mu}(t,t_0)|n^{\text{eq}}\rangle\,,\end{aligned} \tag{2.25}$$

where the hat $\hat{\cdot}$ denotes a quantity taken in the interaction picture, and we have used that the states at $t = t_0$ coincide with those of the unperturbed system $\{|n^{\text{eq}}\rangle\}$. We have introduced above the evolution operator

$$\hat{U}_{\mu}(t,t_0) = \mathscr{T}\exp\left(-\imath/\hbar\int_{t_0}^{t}\hat{H}^{\text{ext}}_{\mu}(t')\,dt'\right)\,, \tag{2.26}$$

with $\mathscr{T}$ denoting time-ordering. Substituting Eqs. (2.25), (2.26) into Eq. (2.22) and expanding to linear order in $\phi_{\mu}(t)$, one arrives at the celebrated *Kubo formula* [151]

$$\chi_{\nu\,\mu}(t,t') = \chi_{\nu\,\mu}(t-t') = -\frac{\imath}{\hbar}\theta(t-t')\langle[\langle\hat{\mathcal{O}}_{\nu}(t),\hat{\mathcal{O}}_{\mu}(t')]\rangle_{\text{eq}}\,. \tag{2.27}$$

Eq. (2.27) is generally valid for any operators $\mathcal{O}_{\mu,\nu}$. For pedagogical purposes here, we now continue the presentation considering the 2D conductivity tensor σ_{ij} of disordered electron systems, neglecting many-body effects. σ_{ij} describes how a charge current—precisely, the paramagnetic part) $\langle J_i\rangle = -e\langle v_i\rangle$, v_i being the velocity along $\hat{i}$—builds up in the system in a parallel or transverse direction to an applied electric field, homogeneous in space

$$\langle J_i(t)\rangle = \int_{-\infty}^{+\infty}dt'\,\sigma_{ij}(t-t')\mathcal{E}_j(t')\,. \tag{2.28}$$

It can be shown [153] that in Fourier space one finds

$$\begin{aligned}\sigma_{ij}(\omega) &= \int_{-\infty}^{+\infty}dt\,e^{\imath\,(\omega+\imath 0^+)t}\sigma_{ij}(t) \\ &= \imath\hbar\Omega\sum_{n^{\text{eq}}\neq m^{\text{eq}}}\langle m^{\text{eq}}|J_i|n^{\text{eq}}\rangle\langle n^{\text{eq}}|J_j|m^{\text{eq}}\rangle\left(\frac{f^0(\epsilon^{\text{eq}}_m)-f^0(\epsilon^{\text{eq}}_n)}{(\epsilon^{\text{eq}}_n-\epsilon^{\text{eq}}_m)(\epsilon^{\text{eq}}_n-\epsilon^{\text{eq}}_m-\hbar\omega+\imath 0^+)}\right)\,,\end{aligned} \tag{2.29}$$

where $f^0(\epsilon)$ is the Fermi distribution function. Beyond the charge conductivity tensor, in this thesis we will also be concerned with spin-dependent responses. Whereas those are meant in response to an electric field, the corresponding formulas to Eq. (2.29) are obtained upon replacement of $J_i \to \mathcal{O}(\mathbf{S})$, where $\mathcal{O}(\mathbf{S})$ is some spin-dependent operator, e.g. spin-density or spin-current.

In the static case $\omega = 0$, i.e. the DC response of the system, a more transparent form of Eq. (2.29)—commonly referred to as Kubo-Streda formula [154]—can be obtained by introducing the single-particle Green's functions in the retarded/advanced (R/A) sectors (see Sec. 2 for a

more complete presentation)

$$G^{R/A}_{\epsilon}(\omega=0)\equiv G^{R/A}(\epsilon)=\frac{1}{\epsilon-H\pm\imath 0^{+}}=\frac{1}{\epsilon-(H_0+V)\pm\imath 0^{+}}=\sum_{\{n^{\rm eq}\}}\frac{|n^{\rm eq}\rangle\langle n^{\rm eq}|}{\epsilon-\epsilon_n^{\rm eq}\pm\imath 0^{+}}\,. \quad (2.30)$$

We now assume the zero-temperature limit $T=0$; thermal effects will be discussed in the next Chapters. In Ref. [153] it is shown that $\sigma_{ij}(\omega\to 0)$ can be split into two terms: a first one σ^{I}_{ij} carrying information about the contribution of electrons at the Fermi level ϵ, and a second one, σ^{II}_{ij}, taking into account off-Fermi surface processes

$$\sigma^{I}_{ij}(\epsilon)=\frac{e^2\hbar}{4\pi\Omega}\mathrm{Tr}\left[v_i(G^R(\epsilon)-G^A(\epsilon))v_jG^A(\epsilon)-v_iG^R(\epsilon)v_j(G^R(\epsilon)-G^A(\epsilon))\right]\,, \quad (2.31)$$

$$\sigma^{II}_{ij}(\epsilon)=\frac{e^2\hbar}{4\pi\Omega}\int_{-\infty}^{+\infty}d\epsilon' f^0(\epsilon')\,\mathrm{Tr}\left[v_iG^R(\epsilon')v_j(\partial_{\epsilon'}G^R(\epsilon'))-v_i(\partial_{\epsilon'}G^R(\epsilon'))v_jG^R(\epsilon')+\text{h.c.}\right]\,, \quad (2.32)$$

where the Tr is meant on motional (position or momentum) and quantum indices. In Chapter 5, we discuss the generalisation to time-dependent dynamics, i.e. the case of finite ω.

It is worth anticipating here that the type-I contribution of generic response functions includes in principle the SC-like part of the response, scaling as $\propto n_i^{-1}$. More generally, resulting from the contribution of Green's functions with analyticity in opposite halves of the complex plane, simple complex-analysis considerations show that it is the dominant term in the diffusive limit $k_F l\sim\epsilon\,\tau\gg 1$, where τ is the effective relaxation time of bare eigenstates at the Fermi level ϵ introduced by disorder (see discussion below) [136, 155].

Diagrammatic treatment of the response function for disordered materials

The equilibrium Hamiltonian H generally contains a bare and a disordered part

$$H=H_0+V\,. \quad (2.33)$$

The presence of a random potential V requires additional care for Eqs. (2.31)-(2.32). Those are modified by introducing disorder average over all possible impurity configurations as defined in Eq. (2.17). For instance, σ^{I}_{ij} is given by

$$\sigma^{I}_{ij}(\epsilon)=\frac{e^2\hbar}{4\pi\Omega}\mathrm{Tr}\left[\overline{v_i(G^R(\epsilon)-G^A(\epsilon))v_jG^A(\epsilon)-v_iG^R(\epsilon)v_j(G^R(\epsilon)-G^A(\epsilon))}\right]\,, \quad (2.34)$$

where the bar $\overline{A}\equiv\langle A\rangle_{\rm dis}$ is an alternative notation to indicate disorder average, Eq. (2.17). The internal Green's functions in Eq. (2.34) are associated to the total Hamiltonian H_0+V, see Eq. (2.30). To work out an explicit form for Eq. (2.34) (and generically any disorder-dependent response) a possibility is to adopt a *diagrammatic technique*, which we illustrate below. It is more instructive to first visualise this prescription for the two-point (Green's) function, upper part of Fig. 2.1. The standard procedure requires a Feynman expansion of the two-point function in Eq. (2.30) in terms of interaction lines with the scattering potential V [136]. This produces a series of diagrams with an arbitrary number of interaction vertices (first line of Fig. 2.1). These diagrams are then averaged over all possible impurity configurations, which yields contractions of scattering potential legs V with impurity density n_i crosses (to all orders in n_i and V), as shown in Fig. 2.1, second-fourth lines. In mathematical terms, the Green's functions satisfy a

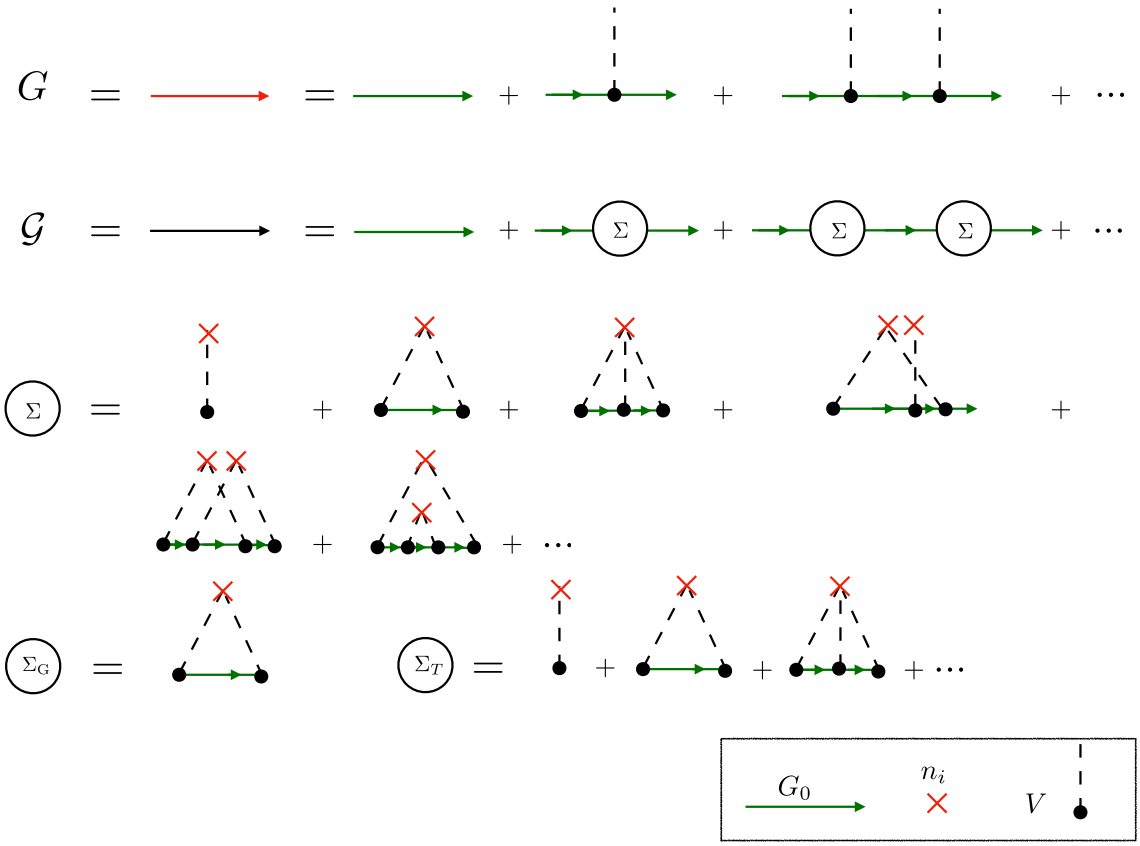

Figure 2.1: Diagrammatic representation of the disordered Green's functions and of the self-energy. In the first line, the Dyson expansion of the total Green's function (red arrow) in terms of the bare propagators (green arrow) and the scattering potential V (dashed legs with dots). When performing disorder average (second line) one obtains the disorder-averaged Green's function (black arrow), which can be represented as a function of the self-energy Σ. The latter (third/fourth lines) contains in principle all irreducible diagrams with an arbitrary number of impurity legs, which after disorder average are contracted in pairs, triplets, etc. with an impurity density cross n_i (red cross). In practice one performs some approximation. For instance, in the Gaussian approximation, one only consider Σ_{G} with the "triangle diagram" [LHS of fifth line). In the T-matrix approximation (RHS of fifth line) all diagrams to all powers in V but with just one impurity density insertion are taken into account.

Dyson equation of the type

$$G^a = G_0^a + G_0^a\, V\, G_0^a + \ldots = G_0^a + G_0^a\, V\, G^a\,, \tag{2.35}$$

which after impurity average yields

$$\mathcal{G}^a(\epsilon) \equiv \overline{G^a}(\epsilon) = \frac{1}{(G_0^a(\epsilon))^{-1} - \Sigma^a(\epsilon)} = \frac{1}{\epsilon - H_0 - \mathrm{Re}\Sigma^a(\epsilon) \mp \imath\,\mathrm{Im}\Sigma^a(\epsilon)}\,. \tag{2.36}$$

In the above, the *self-energy* Σ^a can be seen as a shift of the Fermi energy (real part)[3] ϵ, plus a broadening of spectral lines (imaginary part), endowing the eigenstates of H_0 with a finite lifetime. Σ^a contains in principle the sum of all possible irreducible diagrams without external bare-propagators lines. In practice, one usually adopts some approximation to reduce the complexity of Σ^a to a subset of all these possible diagrams. To understand the hierarchy of these

---

[3] We discuss this point in more detail in Sec. 3.

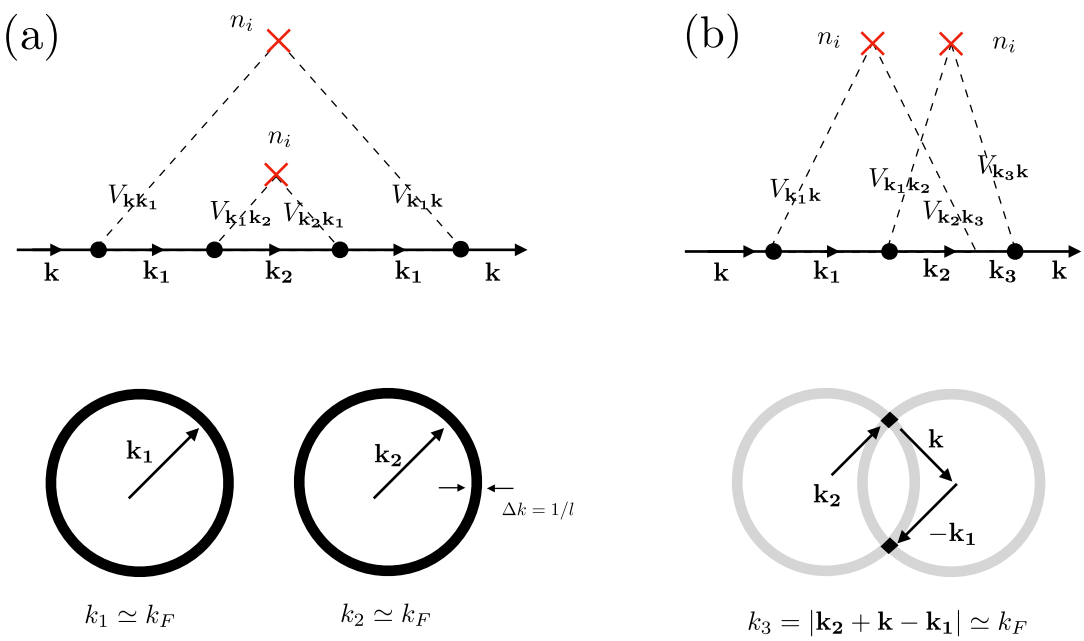

Figure 2.2: Crossing self-energy diagrams (b) are subdominant with respect to noncrossing ones (a). Under the constraint of momentum conservation (elastic scattering), the available phase-space volume for momentum relaxation is reduced in processes described by crossing diagrams (b) by a factor $(k_F l)^{-1}$, which in metals is usually very small $(k_F l)^{-1} \ll 1$. It has to be noted that $(k_F l)^{-1}$ approaching the unity indicates the crossover to the quantum regime, as quantum interference effects become non-negligible. This justifies the usage of the noncrossing approximation for the description of SC transport effects. The figure is adapted from Ref. [156].

diagrams, let us compare non-crossing and crossing *wigwam* diagrams, of the same order in n_i, V (Fig. 2.2) [156]. To illustrate this we take a simple parabolic system [Eq. (1.15) without SO coupling]

$$H_{0\mathbf{k}} = \langle \mathbf{k}|H_0|\mathbf{k}\rangle = \frac{\hbar^2 k^2}{2m}, \tag{2.37}$$

and assuming $\mathrm{Re}\,\Sigma^a = 0\,, \mathrm{Im}\,\Sigma^a = \hbar/\tau$. This can also be seen as a spreading of the wavepacket in $\mathbf{k}$ space: $\mathbf{k}_F \to \mathbf{k}_F + \Delta\mathbf{k}$. The modulus of the wavevector spreading is found by imposing

$$\frac{\hbar^2(k_F+\Delta k)^2}{2m} - \frac{\hbar^2 k_F^2}{2m} = \frac{\hbar}{\tau} \implies \Delta k \simeq \frac{1}{v_F \tau} = \frac{1}{l}, \tag{2.38}$$

where v_F is the Fermi velocity. Therefore the phase-space volume available for electron-states relaxation at the Fermi level after scattering is given by

$$\Omega_{\text{scatt}} = \pi[(k_F+\Delta k)^2 - k_F^2] = 2\pi k_F \Delta k = \frac{2\pi k_F}{l}. \tag{2.39}$$

We consider elastic scattering from impurities, so that conservation of momentum is obeyed and all internal and external propagator lines in the diagrams Fig. 2.2 are associated with a momentum $k \simeq k_F$. For the diagram Fig. 2.2(a) we see the internal momenta $k_1, k_2 \simeq k_F$ relax independently so that the total phase-space volume is given by $\Omega_{\text{scatt}}|_a = (2\pi k_F/l)^2$. On the other hand for the wigwam diagram Fig. 2.2(b) a further constraint needs to be fulfilled, i.e. $k_3 = |\mathbf{k} + \mathbf{k}_2 - \mathbf{k}_1| \simeq k_F$. This bounds the available phase-space volume to a ring with radius k_F

and cross section $(1/l)^2$, meaning $\Omega_{\text{scatt}}|_b = (2\pi k_F/l)(\pi/l^2)$, see Fig. 2.2(b). Therefore

$$\frac{\Omega_{\text{scatt}}|_b}{\Omega_{\text{scatt}}|_a} = \frac{\pi/l^2}{2\pi k_F/l} \simeq \frac{1}{k_F l}\,. \tag{2.40}$$

In metals $(k_F l)^{-1} \ll 1$ so that neglecting crossing diagrams is justified [156]. The latter parameter $(k_F l)^{-1}$ is indeed, according to Ioffe and Regel, what controls the validity of the SC Boltzmann-Drude theory for metals, as for $(k_F l)^{-1} \sim 1$ quantum interference effects become important [157]. Therefore it can be used to control the diagrammatic expansion, in that leading order diagrams in $(k_F l)^{-1}$ are associated to SC processes, whereas higher-order terms encode quantum corrections. As in this thesis we are mainly interested in SC effects, we will adopt the noncrossing approximation for the self-energy; we shall discuss in more detail in the following.

We discuss now the generalisation of the diagrammatic treatment to the four-point disordered response function, of the type of Eq. (2.34). According to the Feynman rules, the disorder average procedure here can be understood in two steps: a first partial resummation of diagrams to all orders produces Green's function renormalisation $G \to \mathcal{G}$, for each of the two fermionic lines; secondly, the renormalised upper and lower lines are further connected by scattering potential legs. In the noncrossing approximation—i.e. neglecting diagrams where these potential legs intersect each other—this produces the so-called *ladder series* (see Fig. 2.3, second line). Those diagrams can be resummed in a self-consistent equation [Bethe-Salpeter (BS)] for one of the vertices. For instance, for the leading terms involving propagators with analyticity in opposite semi-halves of the complex ϵ-plane (R/A sectors) of the conductivity σ^I_{ij} Eq. (2.34) one can consider renormalisation of the velocity vertex (third line of Fig. 2.3). Mathematically, Eq. (2.34) becomes

$$\sigma^I_{ij}(\epsilon) = \frac{e^2\hbar}{4\pi\Omega}\text{Tr}[\overline{v_i G^R(\epsilon) v_j G^A(\epsilon)}] = \frac{e^2\hbar}{4\pi\Omega}\text{Tr}[v_i \mathcal{G}^R(\epsilon)\tilde{v}_j(\epsilon)\mathcal{G}^A(\epsilon)]\,, \tag{2.41}$$

where the renormalised vertex $\tilde{v}_j$ solution to the BS equation is represented diagrammatically in Fig. 2.3 third line, and it is written, for a scalar potential with Gaussian statistics Eqs. (2.15)-(2.16) as

$$\tilde{v}_j(\epsilon) = v_j(\epsilon) + n_i u_0^2\,\text{Tr}\left[\mathcal{G}^R(\epsilon)\tilde{v}_j(\epsilon)\mathcal{G}^A(\epsilon)\right]\,. \tag{2.42}$$

Finally, let us note an important point. The treatment just discussed, where vertex renormalisation is given by Eq. (2.42) (and diagrammatic version in Fig. 2.3), is customary for parabolic systems. This is consistent with the assumption of weak scattering, i.e. the Born Approximation (BA), where usually also a Gaussian white-noise statistics [Eqs. (2.15)-(2.16)] is taken into account. However, as put forward in Refs. [158,159] the latter approach is generally not suitable for 2D massless fermions, where perturbation introduced by impurities can fall into the resonant regime of very strong scattering [160]. Therefore we will work within the T-matrix approximation for the self-energy and the ladder series, as shown in Fig. 2.4. We can notice simple potential insertions (dots) are replaced with T-matrix insertions. We will discuss when it is required in the following Chapters of this thesis, how the different approaches provide different results.

Conservation laws and Ward Identities

The response functions introduced above generally obey some constraints, encoding the conservation laws of the physical systems under study. Another formulation of this sentence involves Noether's theorem [161]: if a system possesses some symmetry then there is an associated con-

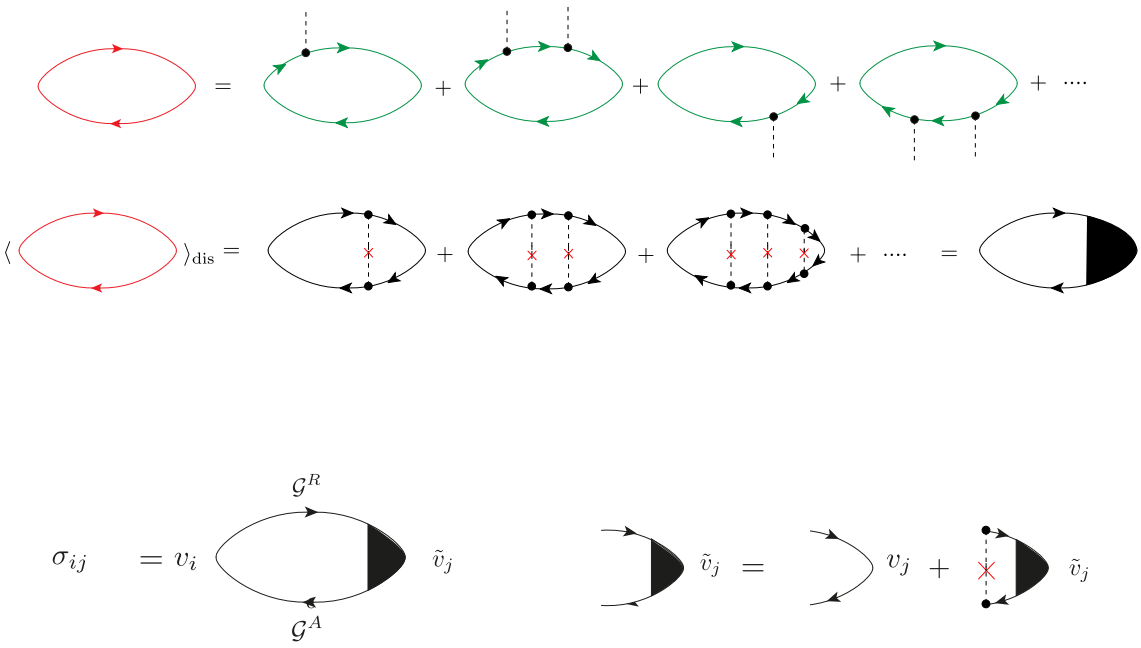

Figure 2.3: Diagrammatic representation of the disordered responses. The full disordered response [bubble with full (red) propagators] is first expanded in a product of Feynman series for the two fermionic lines, as shown in the first line. Disorder averaging (second line) produces single Green's function renormalisation (black lines) as shown in Fig. 2.1 but also a series of diagrams where the propagators are connected. This gives rise, in the noncrossing approximation, to *the ladder* series, which can be viewed as a self-consistent equation (BS) for the renormalised vertex. For instance, for the leading σ^I_{ij} contribution to the conductivity, one of the two charge current vertices is renormalised.

served quantity.

Gauge invariance, i.e. the invariance of a theory under certain Lie groups of local transformations, is of fundamental importance in modern field theories. In the field-theory language, charge conservation, i.e. the continuity equation Eq. (1.13) introduced above

$$\partial_t \rho(x) + \boldsymbol{\nabla}\mathbf{J}(x) \equiv \partial^\mu J_\mu(x) = 0\,, \tag{2.43}$$

with $x \equiv (t, \mathbf{x})$, $\partial^\mu \equiv (\partial_t, \boldsymbol{\nabla})$, $J_\mu \equiv (J_0, \mathbf{J})$ where $J_0 = \rho$ is the charge density, can be understood as a consequence of the $U(1)$ gauge invariance of quantum electrodynamics. Under local gauge transformations, the electromagnetic potential $A_\mu(x) = (\phi(x), \mathbf{A}(x))$ *and* the fermionic fields transform as

$$A_\mu(x) \to A'_\mu(x) = A_\mu(t, \mathbf{x}) + \partial_\mu \chi(t, \mathbf{x})\,, \tag{2.44}$$

$$\Psi(x) \to \Psi'(x) = e^{\imath\, e\, \chi(x)} \Psi(x)\,. \tag{2.45}$$

where $\chi(x)$ is a local phase and $\partial_\mu = g_{\mu\nu}\partial^\nu = (-\partial_t, \boldsymbol{\nabla})$, with $g_{\mu\nu} = \mathrm{diag}(-1, +1, +1)$ being the Minkowski (2+1)D metric tensor [6].

In a system with $SU(2)$-invariant SO interaction, the companion equation to Eq. (1.13), i.e. the spin continuity-like Eq. (1.14) can also be understood as a consequence of the gauge invariance of the theory [162]. Under $SU(2)$ local rotations, the vector potential and the (spinorial) fermionic

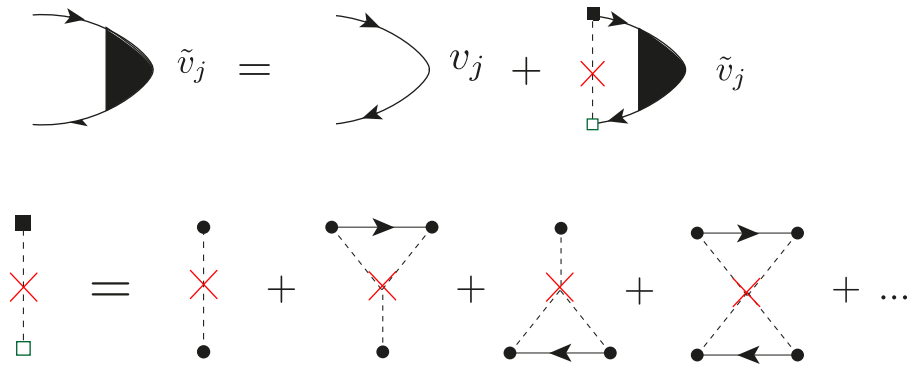

Figure 2.4: T-matrix ladder. In the T-matrix ladder each simple impurity potential insertion, represented by a simple dot as shown in Fig. 2.3, is replaced by a T-matrix insertion (black and green-bordered white square, indicating respectively the T-matrix in the R/A sectors), whose diagrammatic expansion is shown in the second line.

fields transform as

$$A_\mu(x) \to A'_\mu(x) = e^{\frac{\imath}{2}\sum_a \theta_a(x) s_a} A_\mu(x)\, e^{-\frac{\imath}{2}\sum_a \theta_a(x) s_a} - \imath(\partial_\mu e^{\frac{\imath}{2}\sum_a \theta_a(x) s_a})\, e^{-\frac{\imath}{2}\sum_a \theta_a(x) s_a}, \tag{2.46}$$

$$\Psi(x) \to \Psi'(x) = e^{\frac{\imath}{2}\sum_a \theta_a(x) s_a} \Psi(x), \tag{2.47}$$

where $\theta_a(x) = \theta_a(t, \mathbf{x})$, $a = (x, y, z)$ are the components of the non-Abelian gauge field.

We will see below in detail a field-theoretical derivation of the conservation laws for the Dirac-Rashba model of our interest. Once the conservation laws are obtained, they can be exploited to establish a connection between the two-points and the four-points functions, i.e. the Green's and the response functions respectively. The resulting equations are known as WIs [152]. We limit ourselves in this introductory paragraph to saying that formally the WIs are obtained by defining a vertex function

$$\Lambda^\mu(x, y, z) = \langle \mathscr{T}(J^\mu(x)\Psi(y)\Psi^\dagger(z)) \rangle\,, \tag{2.48}$$

and evaluating the space-time derivative $\partial_\mu \Lambda^\mu$. Below we make use of this further theoretical ingredient to show how in the minimal 2D Dirac-Rashba model, an evaluation of the WIs leads to a complete determination of the spin Hall response of the disordered system. Going beyond the minimal model, such a complete determination of the SHE is not generally possible. Still, the WIs provide strong constraints on the spin Hall response, being then a powerful tool to understand the nonequilibrium physics of systems with SO interaction.

Chapter 3

2D Dirac Materials with Broken Mirror Symmetry: Electronic Structure and Disorder Effects

Overview

To set the stage for our study of SO phenomena in honeycomb layers, we discuss the fundamental electronic properties of 2D Dirac materials with broken mirror symmetry $z \to -z$, starting from low-energy continuum models. In this respect, the starting point is the minimal 2D Dirac-Rashba model, where the bare graphene Hamiltonian [Eq. (1.20)] is supplemented with a Rashba interaction resulting from the interfacial breaking about the 2D plane (e.g. in the presence of a substrate), see discussion in Sec. 1. From a symmetry standpoint, this is described by the C_{6v} group of the hexagonal lattice [163]. Honeycomb layers with C_{6v} symmetry are invariant under 6-fold rotations about the $\hat{z}$ axis, such that A, B sublattice sites remain equivalent; however asymmetric spin-flip hopping among nearest- and next-nearest neighbours is allowed [see Fig. 3.1(b)].

Another important class is represented by honeycomb layers which are invariant under the C_{3v} point symmetry group. This is the case, e.g., for semihydrogenated graphene—i.e. *graphone*, where only one sublattice is affected by hybridisation with intercalated hydrogen atom [164]—or graphene/TMD heterostructures, where the small lattice mismatch produces different effective fields on A, B carbon atoms sitting closer to either the chalcogen or the metal element (see also Fig. 1.8). In the continuum limit, this is reflected in the appearance of additional orbital and SO terms in the Hamiltonian.

In the following, we discuss the properties of the minimal 2D Dirac-Rashba model in the presence of disorder, which will serve as a testbed to explore SO effects for Dirac fermions. In Sec. 3 we extend the discussion to the class of C_{3v} invariant Hamiltonians, which faithfully describe the electronic structure of graphene/TMD heterostructures of our interest. In particular, we will see how the *spin texture* of the energy states is dramatically affected by the broken sublattice symmetry, which lies at the heart of the novel physics uncovered in this thesis.

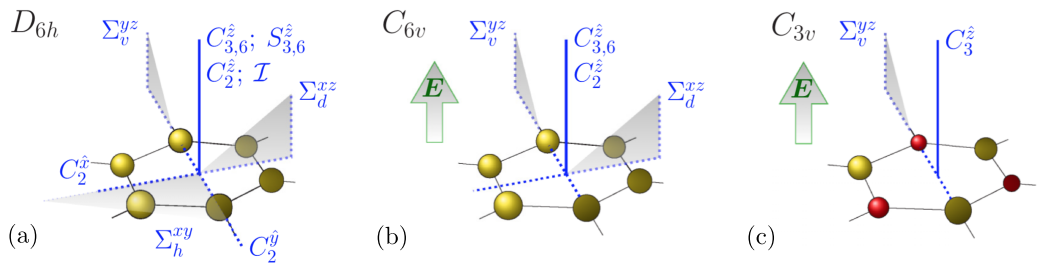

Figure 3.1: Point-group symmetries of the honeycomb lattice. (a) The bare hexagonal plaquette is characterised by the D_{6h} point-symmetry group. (b) Breaking of inversion symmetry about the 2D plane (e.g. by application of perpendicular electric field, or a substrate) reduces the point symmetry group $D_{6h} \to C_{6v}$. (c) If the sublattice symmetry is also broken, the symmetry group is further reduced $C_{6v} \to C_{3v}$. The latter model is representative of graphene/TMD hybrids we are interested in. Figure adapted from Ref. [163].

The minimal Dirac-Rashba model: from D_{6h} to C_{6v}

The effective low-energy Hamiltonian describing the electronic properties of 2D Dirac fermions subject to a uniform Rashba interaction[1] is

$$H = \int d\mathbf{x}\, \Psi^\dagger(\mathbf{x})\, \mathscr{H}\, \Psi(\mathbf{x})\,, \tag{3.1}$$

$$\mathscr{H} = \tau_z \left(\hbar\, v\, \boldsymbol{\sigma}\cdot\mathbf{p} + \lambda\ (\boldsymbol{\sigma}\times\mathbf{s})\cdot\hat{z}\right) + V(\mathbf{x})\,, \tag{3.2}$$

where v is the bare velocity of massless Dirac fermions, $\mathbf{p} = -\imath\boldsymbol{\nabla}$ is the 2D kinematic momentum operator, λ is the SOC strength and τ_i, σ_i, s_i $(i = x, y, z)$ are Pauli matrices associated respectively with valley, sublattice (pseudospin) and spin DOFs. $\Psi^\dagger\,(\Psi)$ are fermionic field creation (annihilation) operators. To simplify the presentation in the following we use natural units $(\hbar \equiv 1 \equiv e)$.

It is convenient to define the Hamiltonian density on a given valley $K\,(K')$ associated with index $\kappa = +1(-1)$, as

$$H_\kappa = \int d\mathbf{x}\, \Psi_\kappa^\dagger(\mathbf{x})\, \mathscr{H}_\kappa\, \Psi_\kappa(\mathbf{x}) \tag{3.3}$$

$$\mathscr{H}_\kappa = \kappa\left(v\,\boldsymbol{\sigma}\cdot\mathbf{p} + \lambda\ (\boldsymbol{\sigma}\times\mathbf{s})\cdot\hat{z}\right) + V(\mathbf{x})\,. \tag{3.4}$$

Here, $V(\mathbf{x})$ is a disorder potential describing elastic scattering from nonmagnetic short-range impurities (see below). For the moment, to simplify the presentation, we also neglect intervalley scattering processes.

Bare system

We fix the valley index for the moment to be $\kappa = 1$. The energy dispersion relation associated with the free part of Hamiltonian Eq. (3.3) is

$$\epsilon_{\mu\nu\mathbf{k}} = \mu\lambda + \nu\sqrt{\lambda^2 + v^2|\mathbf{k}|^2}\,, \tag{3.5}$$

[1] In the *magic-basis* representation $(KA\uparrow, KA\downarrow, KB\uparrow, KB\downarrow, K'B\uparrow, K'B\downarrow, K'A\uparrow, K'A\downarrow)^t$ [see Eq. (A.16)].

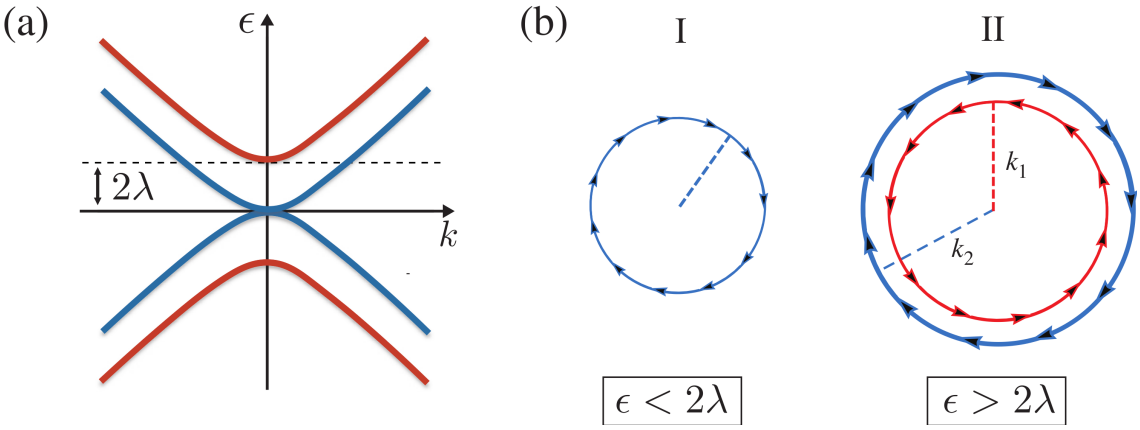

Figure 3.2: (a) Energy dispersion of the Dirac-Rashba model around the K point. The splitting of the Dirac bands leads to a spin gap or *pseudogap* of width 2λ. (b) Tangential winding of the spin texture in regimes I and II.

where $\mu, \nu = \pm 1$ represents the various subbands [Fig. 3.2(a)]. While the quantum index ν is associated to the carrier polarity, $\nu = 1\,(\nu = -1)$ for electrons (holes), μ is related to the spin chirality of energy states, as we explain below. To write the associated eigenstates in compact form, it is convenient to introduce the quantity $\varpi_\mu = \text{arcsinh}(-\mu\,\lambda/vk)$

$$\Psi_{0\mu\nu\mathbf{k}}(\mathbf{x}) \equiv \Phi_{0\mu\nu\mathbf{k}} e^{\imath \mathbf{k}\cdot\mathbf{x}} = \frac{1}{2\sqrt{\cosh \varpi_\mu}} \begin{pmatrix} -\imath\,\mu\,\nu\, e^{-\imath\phi_\mathbf{k}}\, e^{\nu\varpi_\mu/2} \\ e^{-\nu\varpi_\mu/2} \\ -\imath\,\mu\, e^{-\nu\varpi_\mu/2} \\ \nu\, e^{\imath\,\phi_\mathbf{k}}\, e^{\nu\varpi_\mu/2} \end{pmatrix} e^{\imath \mathbf{k}\cdot\mathbf{x}}, \tag{3.6}$$

and $\phi_\mathbf{k}$ is the angle formed by the wavevector with $\hat{k}_x$.

Given Eq. (3.6), it can be seen, by direct evaluation, that the Rashba interaction aligns the electron spin at right angles to the wavevector, the so-called spin–momentum locking configuration [Fig. 3.2(b)], i.e.

$$\langle \Phi_{\mu\nu\mathbf{k}} | \mathbf{s} | \Phi_{\mu\nu\mathbf{k}} \rangle \equiv \langle \mathbf{s} \rangle_{\mu\nu\mathbf{k}} = \mu\nu(\sin\phi_\mathbf{k}, -\cos\phi_\mathbf{k}, 0)\,. \tag{3.7}$$

The latter equation suggests to define a spin helicity index $\chi = \mu\nu = \pm 1$, which will in turn be useful in the following. For Fermi energy $|\epsilon| > 2|\lambda|$ (region II), the split Fermi surface displays counter-rotating spin textures reminiscent of (nonchiral) 2DEGs with Rashba interaction [165]. A regime (pseudogap or region I) where the Fermi energy intersects a single subband, with electronic states having well-defined spin helicity, extends for energies $|\epsilon| < 2|\lambda|$, which is strictly similar to the situation for surface states of TIs [166, 167]. In the conventional 2DEG this circumstance only happens at a single point i.e., the intersection between the parabolic bands [168]. Importantly, the spin texture of energy bands in the 2D Dirac–Rashba model is modulated by the band velocity, which can be seen by recasting Eq. (3.7) as

$$\langle \mathbf{s} \rangle_{\mu\nu\mathbf{k}} = -\mu \langle \boldsymbol{\sigma} \rangle_{\mu\nu\mathbf{k}} \times \hat{z}\,, \tag{3.8}$$

where $\langle \boldsymbol{\sigma} \rangle_{\mu\nu\mathbf{k}} = (1/v)\nabla_\mathbf{k} \epsilon_{\mu\nu\mathbf{k}}$ is the pseudospin polarisation vector. As we show in the following Chapters, the entanglement between pseudospin and spin DOFs in the model is responsible for a rich energy dependence of the spin texture which in turn will be shown to impact the behaviour of the transport coefficients [169, 170]. For brevity of notation, we assume $\epsilon, \lambda > 0$ in

the remainder of this Chapter.

The real-space bare R/A single-particle Green's function ($a = A, R \equiv -, +$) is

$$G_0^a(\mathbf{x}, t) = \mp \imath \left\langle 0 | \mathscr{T} \left[\Psi_0(0,0), \Psi_0^\dagger(\mathbf{x}, t) \right] | 0 \right\rangle \theta(\pm t), \tag{3.9}$$

where $\mathscr{T}$ is the time-ordering operator, $\theta(.)$ is the Heaviside step function, $\langle 0|...|0\rangle$ is the quantum average over the many-body (noninteracting) ground state, and $\Psi_0^\dagger, \Psi_0$ are field operators for the disordered-free part of the Hamiltonian $H_0 = H_D + H_R$ in Eq. (3.3). Fourier transforming Eq. (3.9) in energy and momentum domains we obtain

$$G_{0\mathbf{k}}^a(\epsilon) = \int d\mathbf{x} \int dt \, e^{\imath(\epsilon + \imath a 0^+)t} e^{-\imath \mathbf{k}\mathbf{x}} G_0^a(\mathbf{x}, t) = \frac{1}{\epsilon - H_{0\mathbf{k}} + \imath a 0^+}, \tag{3.10}$$

where

$$H_{0\mathbf{k}} = v \, \boldsymbol{\sigma} \cdot \mathbf{k} + \lambda (\boldsymbol{\sigma} \times \mathbf{s})_z, \tag{3.11}$$

is the momentum representation of the bare Hamiltonian. Explicit calculation of $G_{0\mathbf{k}}^a$ requires to define the projectors $P_{\mu\nu\mathbf{k}} = |\Phi_{\mu\nu\mathbf{k}}\rangle\langle\Phi_{\mu\nu\mathbf{k}}|$ onto the eigenstates of Eq. (3.6), which are found as

$$P_{\mu\nu\mathbf{k}} = \frac{1}{4\cosh\varpi_\mu} \Big\{ \cosh\varpi_\mu \, \sigma_0 s_0 + \nu \, \sinh\varpi_\mu \, \sigma_z s_z + \nu \, \sigma_i s_0 \, \hat{k}_i + \mu \, \nu \, (\sigma_0 s_x \sin\phi_{\mathbf{k}} + \sigma_0 s_y \, \cos\phi_{\mathbf{k}}) \tag{3.12}$$

$$+ \mu \, (e^{\nu \varpi_\mu} \, \cos 2\phi_{\mathbf{k}} + e^{-\nu\varpi_\mu} \frac{\sigma_x s_y - \sigma_y s_x}{2}) - \mu \, e^{\nu\varpi_\mu} \, \sin 2\phi_{\mathbf{k}} \frac{\sigma_x s_x - \sigma_y s_y}{2} \Big\}, \tag{3.13}$$

and summation over repeated index $i = (x, y)$ is implied. In terms of the projectors, the momentum propagators are now given as

$$G_{0\mathbf{k}}^a(\epsilon) = \sum_{\mu,\nu=\pm 1} \frac{P_{\mu\nu\mathbf{k}}}{\epsilon - \epsilon_{\mu\nu\mathbf{k}} + \imath \, a \, 0^+}, \tag{3.14}$$

with the full calculation reported in Appendix B.

Disorder effects

Including disorder, the propagator in Eq. (3.9) is generalised to

$$G^a(\mathbf{x}, \mathbf{x}'; t - t') = \mp \imath \left\langle 0 | \mathscr{T} \left[\Psi(\mathbf{x}, t), \Psi^\dagger(\mathbf{x}', t') \right] | 0 \right\rangle \theta(\pm t \mp t'). \tag{3.15}$$

A first Fourier transform in the energy domain yields

$$G^a(\mathbf{x}, \mathbf{x}'; \epsilon) = \langle \mathbf{x}' | \frac{1}{[G_0^a(\epsilon)]^{-1} - V} | \mathbf{x} \rangle, \tag{3.16}$$

where $G_0^a(\epsilon) = (\epsilon + \imath v \boldsymbol{\sigma} \cdot \boldsymbol{\nabla} + \lambda \, (\boldsymbol{\sigma} \times \mathbf{s}) \cdot \hat{z} \pm \imath 0^+)^{-1}$ is the Green's function of free 2D Dirac–Rashba fermions introduced above. In the presence of disorder randomly distributed across the material, translation invariance is broken and the Green's function depends on both $\mathbf{x}, \mathbf{x}'$. After the disorder average procedure over all possible impurity configurations, as discussed in Sec. 2, translational invariance is restored and the averaged Green's function only depends on the difference $\mathbf{x} - \mathbf{x}'$: $\mathcal{G}^a(\mathbf{x} - \mathbf{x}', \epsilon) = \overline{G^a(\mathbf{x}, \mathbf{x}'; \epsilon)}$. The latter—whose diagrammatic representation is reported in Fig. 2.1(a)—is in fact the central quantity in our approach. Its momentum

representation is

$$\mathcal{G}^a_{\mathbf{k}}(\epsilon) = \frac{1}{[G^a_{0\mathbf{k}}(\epsilon)]^{-1} - \Sigma^a_{\mathbf{k}}(\epsilon)}\,, \tag{3.17}$$

where

$$\Sigma^a_{\mathbf{k}}(\epsilon) = \int d(\mathbf{x}-\mathbf{x}')\, e^{-\imath \mathbf{k}(\mathbf{x}-\mathbf{x}')}\, \overline{\langle \mathbf{x}'|V\frac{1}{1-G^a_0(\epsilon)V}|\mathbf{x}\rangle}\,, \tag{3.18}$$

is the disordered averaged self-energy within the noncrossing approximation. For illustration purposes, let us consider for the moment short-range spin-transparent (scalar) impurities[2], e.g. vacancies [cf. Eq. (2.3)]

$$V(\mathbf{x}) = u_0 \sum_i^{N_i} \delta(\mathbf{x}-\mathbf{x}_i)\,, \tag{3.19}$$

where u_0—with units $[u_0]$ = Energy × Area—parameterises the scattering strength of the impurities. In this case, the associated self-energy is $\mathbf{k}$-independent, $\Sigma^a_{\mathbf{k}}(\epsilon) \equiv \Sigma^a(\epsilon)$, and hence we drop this index in what follows. To account for the characteristic resonant (unitary) scattering regime of graphene with relaxation time $\tau \propto \epsilon$ [160,171,172], we will adopt a T-matrix approach by evaluating the self-energy $\Sigma^a(\epsilon)$ at all orders in V. We obtain

$$\Sigma^a(\epsilon) = n_i \frac{u_0}{1-u_0\, g^a_0(\epsilon)} + O(n_i^2) = n_i \mathrm{T}^a(\epsilon) + O(n_i^2)\,, \tag{3.20}$$

where n_i is the impurity areal density and $\mathrm{T}^a(\epsilon)$ is the single-impurity T-matrix. Note that neglecting multiple impurity scattering diagrams $\propto O(n_i^2)$ is justified in the diffusive regime with $k_F l \sim \epsilon\tau \gg 1$, i.e., away from the Dirac point [158]. We have also introduced

$$g^a_0(\epsilon) = g^a_{0,0}(\epsilon)\gamma_0 + g^a_{0,zz}(\epsilon)\,\gamma_{zz} + g^a_{0,r}(\epsilon)\,\gamma_r\,, \tag{3.21}$$

as the momentum integrated Green's function of the clean system [cf. Eq. (3.14)]

$$g^a_0(\epsilon) = \frac{1}{\Omega}\sum_{\mathbf{k}} G^a_{0\mathbf{k}}(\epsilon)\,, \tag{3.22}$$

and where[3]

$$\gamma_0 = \sigma_0 s_0\,, \tag{3.23}$$

$$\gamma_{zz} = \sigma_z s_z\,, \tag{3.24}$$

$$\gamma_r = (\boldsymbol{\sigma}\times\mathbf{s})\cdot\hat{z}\,. \tag{3.25}$$

Explicit calculation yields

$$g^a_{0,0}(\epsilon) = -\frac{1}{8\pi v^2}\left[\epsilon\left(\mathcal{L}_{\mathrm{II}}(\epsilon) + a\imath\pi\,\theta_{\mathrm{II}}(\epsilon)\right) + \lambda\left(\mathcal{L}_{\mathrm{I}}(\epsilon) + a\imath\pi\,\theta_{\mathrm{I}}(\epsilon)\right)\right]\,, \tag{3.26}$$

$$g^a_{0,zz}(\epsilon) = -\frac{\lambda}{8\pi v^2}\left(\mathcal{L}_{\mathrm{I}}(\epsilon) + a\imath\pi\,\theta_{\mathrm{I}}(\epsilon)\right)\,, \tag{3.27}$$

$$g^a_{0,r}(\epsilon) = +\frac{\epsilon}{16\pi v^2}\left(\mathcal{L}_{\mathrm{I}}(\epsilon) + a\imath\pi\,\theta_{\mathrm{I}}(\epsilon)\right)\,. \tag{3.28}$$

[2]We will present a generalisation including intervalley and spin-dependent scattering potentials (in some cases) in the following Chapters.

[3]We are treating here the single-valley problem. When generalising the following matrix structures to include the valley $SU(2)$ DOF we have: $\gamma_0 = \tau_0\sigma_0 s_0$, $\gamma_{zz} = \tau_0\sigma_z s_z$, $\gamma_r = \tau_z\,(\boldsymbol{\sigma}\times\mathbf{s})\cdot\hat{z}$.

In the above, $\theta_{\mathrm{I(II)}}(\epsilon) = \theta(\epsilon + 2\lambda) \mp \theta(\epsilon - 2\lambda)$ selects the energy regime (regime I, II in Fig. 3.2) and

$$\mathcal{L}_{\mathrm{I(II)}}(\epsilon) = \ln\left|\frac{\Lambda^2}{\epsilon(\epsilon+2\lambda)}\right| \mp \ln\left|\frac{\Lambda^2}{\epsilon(\epsilon-2\lambda)}\right|, \tag{3.29}$$

with Λ denoting the ultraviolet cutoff of the low-energy theory [160].

The self-energy simplifies in two important limiting cases: (i) weak Gaussian disorder ($|u_0| \ll |g_0^a|^{-1}$) and (ii) unitary disorder ($u_0 \to \pm\infty$). In the weak-Gaussian scattering regime, it suffices to only take into account the 'rainbow' diagram with two impurity lines in the Dyson expansion; see Fig. (2.1). For scalar disorder this approximation is tantamount to assuming that the disorder potential satisfies white-noise statistics introduced above [cf. Eqs. (2.15)-(2.16)] [136]

$$\langle V(\mathbf{x})\rangle = 0\,, \tag{3.30}$$

$$\langle V(\mathbf{x})V(\mathbf{x}')\rangle = n_i u_0^2\,\delta(\mathbf{x}-\mathbf{x}')\,. \tag{3.31}$$

In this case we have

$$\Sigma^a(\epsilon)|_{\mathrm{Gauss.}} \equiv \Sigma^a_{\mathrm{G}}(\epsilon) = n_i u_0^2\, g_0^a(\epsilon)\,. \tag{3.32}$$

The real part of the self-energy provides a parametrically small renormalisation of the band structure (see discussion below) and a shift of the chemical potential, which can be safely neglected in the diffusive regime of interest [169]. We thus find

$$\Sigma_G^{R/A}(\epsilon) = \mp\imath\, n_i(\eta_0(\epsilon)\gamma_0 + \eta_r(\epsilon)\,\gamma_r + \eta_{zz}(\epsilon)\,\gamma_{zz})\,, \tag{3.33}$$

where the functions $\eta_0, \eta_r, \eta_{zz}$, are proportional to the imaginary parts of Eqs. (3.26)-(3.28), have different forms depending on the Fermi level position. In the following it will be convenient to express those quantities in terms of the quasiparticle broadening outside the pseudogap

$$\frac{1}{2\tau(\epsilon)} \equiv n_i\eta_0(\epsilon)|_{\epsilon>2\lambda}. \tag{3.34}$$

Explicitly, considering Eqs. (3.26)-(3.28) and Eq. (3.32), for $\epsilon > 2\lambda$ we have

$$n_i\eta_0(\epsilon) = n_i\, u_0^2\,\frac{\epsilon}{4v^2} = \frac{1}{2\tau(\epsilon)}\,, \tag{3.35}$$

$$n_i\eta_{zz}(\epsilon) = 0\,, \tag{3.36}$$

$$n_i\eta_r(\epsilon) = 0\,, \tag{3.37}$$

whereas for $0 < \epsilon < 2\lambda$ we find

$$n_i\eta_0(\epsilon) = \frac{n_i u_0^2}{8v^2}(\epsilon+\lambda) = \frac{1}{4\tau}(1+\frac{\lambda}{\epsilon})\,, \tag{3.38}$$

$$n_i\eta_{zz}(\epsilon) = \frac{n_i u_0^2}{8v^2}\lambda = \frac{1}{4\tau(\epsilon)}\frac{\lambda}{\epsilon}\,, \tag{3.39}$$

$$n_i\eta_r(\epsilon) = -\frac{1}{2}\frac{n_i u_0^2}{8v^2}\epsilon = -\frac{1}{8\tau(\epsilon)}\,. \tag{3.40}$$

Within the full the T-matrix approximation, considering again Eqs. (3.26)-(3.28) and Eq. (3.20) we can still formally write $\Sigma^a(\epsilon)$ as Eq. (3.33), with (we omit the energy dependence to allow an

easier readability)

$$\eta_0, \eta_{zz} = \frac{u_0}{2} \, \mathrm{Im} \left[\frac{1}{1 - u_0 \left(g^+_{0,0} + g^+_{0,zz} \right)} \pm \frac{1 - u_0 \left(g^+_{0,0} - g^+_{0,zz} \right)}{\left[1 - u_0 \left(g^+_{0,0} - g^+_{0,zz} \right) \right]^2 - \left(2 u_0 \, g^+_{0,r} \right)^2} \right] , \tag{3.41}$$

and

$$\eta_r = \mathrm{Im} \left[\frac{u_0 g^+_{0,r}}{\left[1 - u_0 \left(g^+_{0,0} - g^+_{0,zz} \right) \right]^2 - \left(2 u_0 \, g^+_{0,r} \right)^2} \right] . \tag{3.42}$$

Particularly important is the unitary limit of strong scattering $u_0 \to \infty$ (e.g. as given from vacancies). In regime II and at large Fermi energy one still finds a scalar self-energy ($\eta_{zz} \simeq 0 \simeq \eta_r$) where $\tau(\epsilon)$ is given by

$$\frac{1}{2\tau(\epsilon)} \bigg|_{\mathrm{TMA}, u_0 \to \infty} = \frac{n_i}{\epsilon} \frac{4\pi v^2}{\pi^2 + \mathcal{L}^2_{\mathrm{II}}(\epsilon)} . \tag{3.43}$$

Once the self-energy has been obtained it is possible to explicitly calculate the disorder-averaged Green's function in Eq. (3.17). To this end, we note that in both the Gaussian and T-matrix approximation Eqs. (3.32),(3.20), the self-energy acquires an additional matrix structure γ_{zz} which is not included in the original model Eq. (3.3). To obtain the disorder-averaged propagators explicitly it is convenient to define an effective model [169]

$$H_{\mathrm{eff}} = H_0 + \int d\mathbf{x} \, \Psi^\dagger_0(\mathbf{x}) \lambda_{zz} \gamma_{zz} \Psi_0(\mathbf{x}) , \tag{3.44}$$

and calculate the associated bare Green's functions similarly to what has been presented above. The connection to the disorder-averaged propagators is realised by means of an analytic continuation procedure, as shown in Appendix B.

Scattering cross section in the minimal Dirac-Rashba model: absence of skewness

A crucial feature of the minimal C_{6v} Dirac-Rashba model is the absence of skewness in the impurity cross sections. In other words, scattering probabilities possess left-right symmetry at all orders in the impurity potential associated with Eq. (3.19). This implies that skew scattering is not realised in this class of systems.

To see this, an easier yet significant evaluation of the scattering cross section can be done in regime I—we take positive energies $\nu = 1$, with simply-connected Fermi surface, hence no scattering between Fermi surfaces with different chirality is allowed. The Fermi golden rule, Eq. (2.4) for the states $(\mu, \nu) = (-1, 1)$ is written as

$$W_{\mathbf{k}\mathbf{k}'} \equiv W(\phi) = 2\pi n_i |\langle \Phi_{-1,1,\mathbf{k}'} | \mathrm{T}^R | \Phi_{-1,1,\mathbf{k}} \rangle|^2 \, \delta(\epsilon_{-1,1\mathbf{k}} - \epsilon_{-1,1\mathbf{k}'}), \tag{3.45}$$

where $\phi = \phi_{\mathbf{k}'} - \phi_{\mathbf{k}}$. Here it is sufficient to keep terms up to second order in u_0

$$\mathrm{T}^R = \frac{u_0}{1 - u_0 g^R_0} \simeq u_0 + u_0 g^R_0 u_0 + O(u_0^3) . \tag{3.46}$$

In the C_{6v} model, using the eigenstates of Eq. (3.6), we find

$$W(\phi) = 2\pi n_i |\mathrm{T}_\phi^R|^2 \, \delta(\epsilon_{-1,1\mathbf{k}} - \epsilon_{-1,1\mathbf{k}'}) \,, \tag{3.47}$$

$$|\mathrm{T}_\phi^R|^2 = |2\pi n_i \left[(u_0 + \eta_0)\mathrm{T}_0 + \eta_{zz}\mathrm{T}_{zz} + \eta_r \mathrm{T}_r\right]|^2 \,, \tag{3.48}$$

with

$$\mathrm{T}_{0,zz} = \frac{\lambda \cos\phi + \frac{\epsilon}{2}(\cos\phi \pm 1)}{\epsilon + \lambda} \,, \tag{3.49}$$

$$\mathrm{T}_r = \frac{-\epsilon}{\epsilon + \lambda} \,, \tag{3.50}$$

and the parameters η_0, η_r, η_{zz} as reported in Eqs. (3.38)-(3.40). At lowest order in u_0 we have

$$W(\phi) = 2\pi n_i \left[u_0^2 \frac{\epsilon(1+\cos\phi) + 2\lambda\cos\phi}{4(\epsilon+\lambda)^2} + u_0^3 f(\cos(\phi)) \right] \,, \tag{3.51}$$

where $f(\cos\phi)$ is a cumbersome function of ϵ, λ. The important result is the evenness of W as a function of ϕ: $W(\phi) = W(-\phi)$, i.e. the cross section is left-right symmetric, as we wanted to demonstrate. This result stems from the fact that scalar impurities preserve left-right symmetry. We remind that this result holds at all order in the impurity potential strength.

The generalised Dirac-Rashba model: from C_{6v} to C_{3v}

Bare model

We now focus on the C_{3v} model. In broken sublattice-symmetry conditions, the bare Hamiltonian in Eq. (3.1) has to be supplemented by sublattice-resolved intrinsic SO terms $\lambda_{zz}^{A,B}$, plus an orbital mass Δ. Re-instating here for convenience the valley index, the associated Hamiltonian density reads

$$\mathscr{H}_{0,\kappa} = \kappa \left(v\, \boldsymbol{\sigma} \cdot \mathbf{p} + \lambda \, (\boldsymbol{\sigma} \times \mathbf{s}) \cdot \hat{z} + \Delta \sigma_z \right) + \frac{(\sigma_z + \kappa\sigma_0)s_z}{2} \lambda_{zz}^A + \frac{(\sigma_z - \kappa\sigma_0)s_z}{2} \lambda_{zz}^B \,. \tag{3.52}$$

It is convenient to define here the following parameters

$$\frac{\lambda_{zz}^A \pm \lambda_{zz}^B}{2} = \{\lambda_{zz}, \lambda_{\mathrm{sv}}\} \,. \tag{3.53}$$

Whereas the average of $\lambda_{zz}^A, \lambda_{zz}^B$ yields the intrinsic SO coupling—compatible already with C_{6v} symmetry, a non-vanishing difference between them encodes the broken sublattice symmetry, with the associated term commonly referred to as spin-valley interaction. Making use of these newly-defined parameters, Eq. (3.1) takes the following form

$$\mathscr{H}_{0,\kappa} = \kappa \left(v\, \boldsymbol{\sigma} \cdot \mathbf{p} + \lambda \, (\boldsymbol{\sigma} \times \mathbf{s}) \cdot \hat{z} + \Delta\, \sigma_z + \lambda_{\mathrm{sv}} s_z \right) + \lambda_{zz} \sigma_z s_z \,. \tag{3.54}$$

The intrinsic-like SO coupling λ_{zz} [cf. Eq. (1.22)] however is typically very small in graphene-based heterostructures of interest for this thesis and can therefore be ignored here [122].

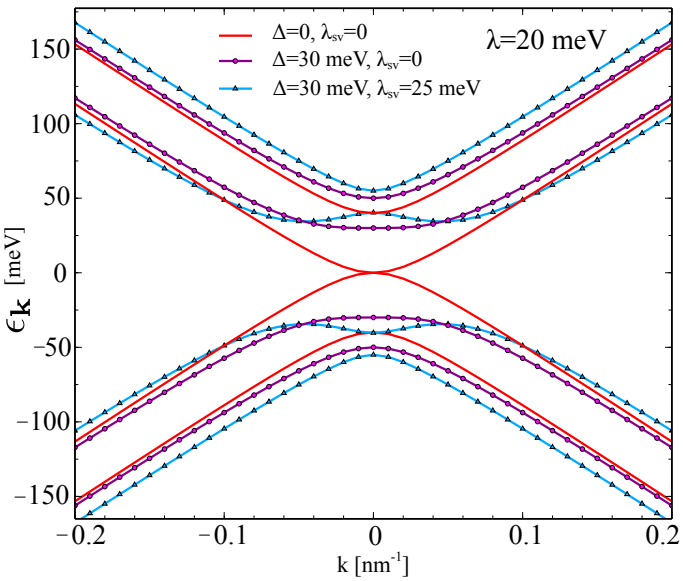

Figure 3.3: Evolution of the 2D Dirac-Rashba band structure in the C_{3v} model. A band gap is only opened when the Rashba interaction is combined with any of the other terms in Eq. (3.54).

The spectrum associated with Eq. (3.54), in the case $\lambda_{zz} = 0$, admits a close form given by

$$\epsilon_{\nu\chi\kappa\mathbf{k}} = \nu\sqrt{v^2k^2 + \Delta_\chi^2(k)}\,, \tag{3.55}$$

$$\Delta_\chi^2(k) = \Delta^2 + \lambda_{\rm sv}^2 + 2\lambda^2 + 2\chi\sqrt{(\lambda^2 - \Delta\lambda_{\rm sv})^2 + v^2k^2(\lambda^2 + \lambda_{\rm sv}^2)}\,, \tag{3.56}$$

where we recall that $\chi = \pm 1$ is the spin helicity index encountered before for anti-clockwise and clockwise-rotating in-plane spin textures respectively[4]. A typical band structure for the Hamiltonian Eq. (3.54) is reported in Fig. 3.3. A band gap can only be opened if the Rashba SOC is in combination with any of the other terms in Eq. (3.54). The Rashba pseudogap at $k = 0$ is easily computed as

$$2\tilde{\lambda} = \min\{|\Delta + \lambda_{\rm sv}|,\, \sqrt{4\lambda^2 + (\Delta - \lambda_{\rm sv})^2}\}, \tag{3.57}$$

while the bottom of the spin majority conduction band is

$$\epsilon_m = \frac{|\lambda(\Delta + \lambda_{\rm sv})|}{\sqrt{\lambda^2 + \lambda_{\rm sv}^2}}\,. \tag{3.58}$$

For energies $\epsilon_m < \epsilon < 2\tilde{\lambda}$ the spectrum develops a small "Mexican hat" feature [122]. In Fig. 3.3 we show the evolution of the spectrum for finite Rashba effect as one turns on the proximity couplings $\Delta, \lambda_{\rm sv}$. We note that the energy spectrum is gapless in the following particular cases: (i) $\lambda = 0$ and $|\lambda_{\rm sv}| > |\Delta|$ and (ii) $\lambda_{\rm sv} = -\Delta$.

The breaking of sublattice symmetry dramatically impacts the spin texture. With either $\lambda_{\rm sv} \neq 0$ or $\Delta \neq 0$ an out-of-plane component is allowed [170]

$$\langle \mathbf{s} \rangle_{\kappa\chi\mathbf{k}} = \chi\, \varrho(k)\, (\hat{k} \times \hat{z}) + m^z_{\kappa\chi}(k)\hat{z}\,. \tag{3.59}$$

The first term describes the spin winding generated by the Rashba effect, cf. Eq. (4.37) and Fig. (3.2), while the second is its out-of-plane tilting due to broken sublattice symmetry (see

[4]The relation $\chi = \nu\mu$ where μ is the index used previously in Eq. (3.5) is readily obtained by taking the limit $\Delta, \lambda_{\rm sv} \to 0$,

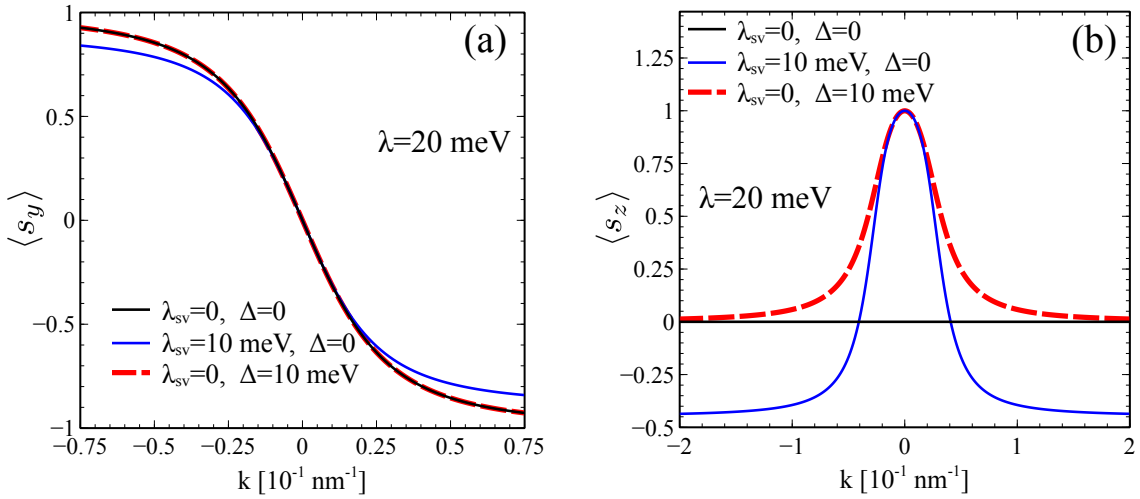

Figure 3.4: Spin texture of the $\chi = -1$ band in the C_{3v} model along the path $\mathbf{k} = (k, 0)$. The Fermi velocity is taken as $v = 10^6$m/s. (a) The in-plane texture of the minimal C_{6v} model is only mildly affected by the introduction of the spin-valley and the mass term. (b) On the other hand, the breaking of sublattice symmetry give rise to an out-of-plane spin component, typically very large in the vicinity of the Dirac point.

Fig. 3.4).

The full form of the bare Green's function for this model is reported in Appendix (B).

Disorder effects

Let us consider the introduction of scalar disorder in Eq. (3.54). Interestingly, the matrix structures associated with different terms appearing in Eq. (3.54) form a closed Clifford algebra, so that we do not need to consider any effective model–contrary to what done in the C_{6v} case, see Eq. (3.44)—to write down the disordered averaged Green's function. It suffices then to perform directly the analytical continuation of Eq. (B.13) as

$$\mathcal{G}^a_{\mathbf{k}}(\epsilon, \lambda, \lambda_{\rm sv}, \Delta, \lambda_{zz}) = G^a_{0\mathbf{k}}(\epsilon + \imath\, n_i\, a\, \eta_0, \lambda - \imath\, n_i\, a\, \eta_r, \lambda_{\rm sv} - \imath\, n_i\, a\, \eta_{\rm sv}, \Delta - \imath\, n_i\, a\, \eta_\Delta, \lambda_{zz} - \imath\, n_i\, a\, \eta_{zz})\,, \tag{3.60}$$

where we have denoted with η_ς the component of the self-energy associated to each of the parameters of the Hamiltonian, ς being an index for any matrix structure in Eq. (3.54). Concretely, in the full $3 \times SU(2)$ representation: $\gamma_\varsigma = \{\gamma_0, \gamma_r, \gamma_{zz}, \gamma_{\rm sv}, \gamma_\Delta\}$ with $\gamma_{\rm sv} = \tau_z\, s_z\, \gamma_\Delta = \tau_z\, \sigma_z$. To have a concrete visualisation, in the Gaussian approximation we have

$$\eta_\varsigma = -n_i u_0^2 {\rm Im} \frac{|{\rm tr}[g_0^R \gamma_\varsigma]|}{|{\rm tr}[\gamma_\varsigma^2]|}, \tag{3.61}$$

g_0^R being the retarded momentum-integrated propagator for this model (see Appendix D).

The presence of additional structures in the propagators of the C_{3v} model with respect to the simpler Dirac-Rashba case reflects the activation of *skewness*, i.e. left-right asymmetry upon impurity scattering, modifying the result of Eq. (3.51). This hints to the establishment of non-zero transverse responses (e.g. Hall and/or SHEs). We will analyse this problem in greater detail in the following Chapters, where we start the presentation of our results concerning transport in Dirac-Rashba systems.

For completeness, we want to conclude this Chapter by examining a further effect of disorder,

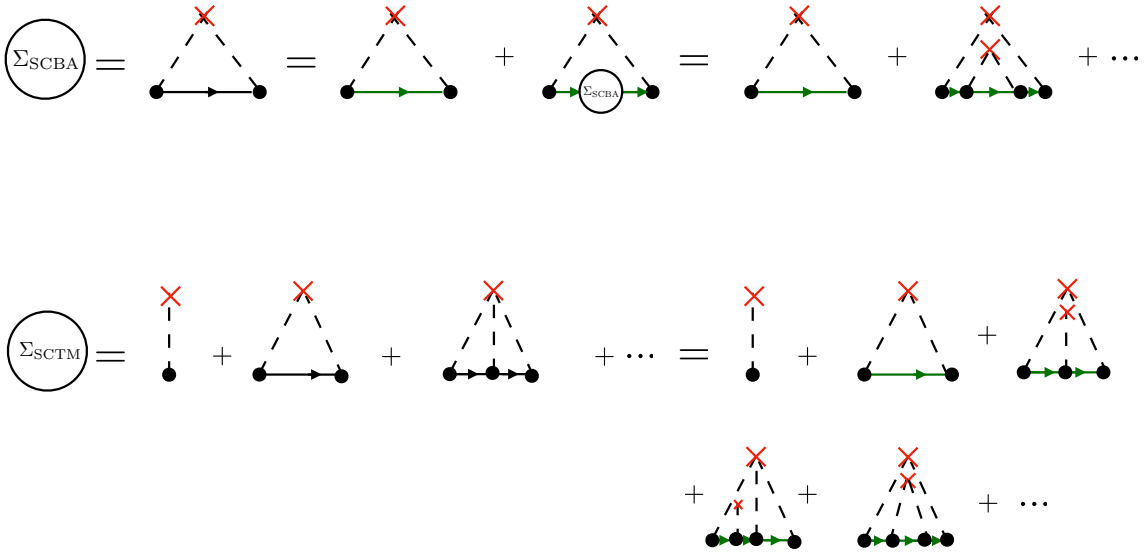

Figure 3.5: The self-consistent BA and T-matrix self-energies are diagrammatically obtained from Σ_G, Σ_T respectively in Fig. 2.2 by replacing the bare internal propagators (green lines) with *renormalised* propagators (black lines). This generates the series of diagrams after the second equalities in the equations for $\Sigma_{\rm SCBA}$ and $\Sigma_{\rm SCTM}$.

as anticipated above [see discussion after Eq. (2.36)], i.e. a renormalisation of the band structure by the *real part* of the self-energy. This can be easily understood by looking at the form of the renormalised Green's function (2.36), which we rewrite here

$$\mathcal{G}^a(\epsilon) = \frac{1}{(G_0^a(\epsilon))^{-1} - \Sigma^a(\epsilon)} = \frac{1}{\epsilon - H_0 - \mathrm{Re}\Sigma^a(\epsilon) \mp \imath\, \mathrm{Im}\Sigma^a(\epsilon)} \tag{3.62}$$

$$= \frac{1}{\epsilon - \tilde{H}_0 \mp \imath\, \mathrm{Im}\Sigma^a(\epsilon)}\,, \tag{3.63}$$

where we have defined $\tilde{H}_0 = H_0 + \mathrm{Re}\Sigma^a$. In our presentation above, with the self-energy treated at Gaussian or T-matrix level, we have ignored this effect. To justify this, for simplicity, let us return for a moment to the C_{6v} pure Rashba model and look at the renormalisation of the Rashba strength for energies $\epsilon > 2\lambda > 0$ (regime II). In the Gaussian approximation $\Sigma^a = n_i u_0^2 g_0^a$, it is found as [cf. Eq. (3.28)]

$$\frac{\delta\lambda}{\lambda} = -\frac{1}{\lambda}\mathrm{Re}\frac{\mathrm{tr}[\Sigma^a \gamma_r]}{\mathrm{tr}[\gamma_r^2]} = \frac{n_i u_0^2}{16\pi v^2}\frac{\epsilon}{\lambda}\ln\left|\frac{\Lambda^2}{\epsilon(\epsilon+2\lambda)}\right| \simeq 1.8\times 10^{-3}\,, \tag{3.64}$$

where we have used typical experimental values for the parameters $n_i = 10^{-12}\mathrm{cm}^{-2}$, $u_0 = 1\,\mathrm{eV}\times\mathrm{nm}^2$, $\lambda = 0.1\epsilon = 0.01\,\mathrm{eV}$. An estimate according to the T-matrix scheme yields the same order of magnitude for $\delta\lambda$. A similar argument applies for the other parameters $\delta\epsilon, \delta\lambda_{zz}$. Therefore, in the dilute limit of our interest, we conclude the renormalisation of the band structure is safely negligible.

The self-energy however, can be treated according to more refined schemes. For instance, a first improvement with respect to the simple Gaussian-BA is the *self-consistent Born approximation* (SCBA) where one considers the series of interpenetrating rainbow diagrams to all orders, see Fig. 3.5 [173]. Similarly, one can adopt a *self-consistent T-matrix* (SCTM) approach, second equation in Fig. 3.5. In both cases, how sizable is in principle this disorder-induced effect is a question far from being obvious.

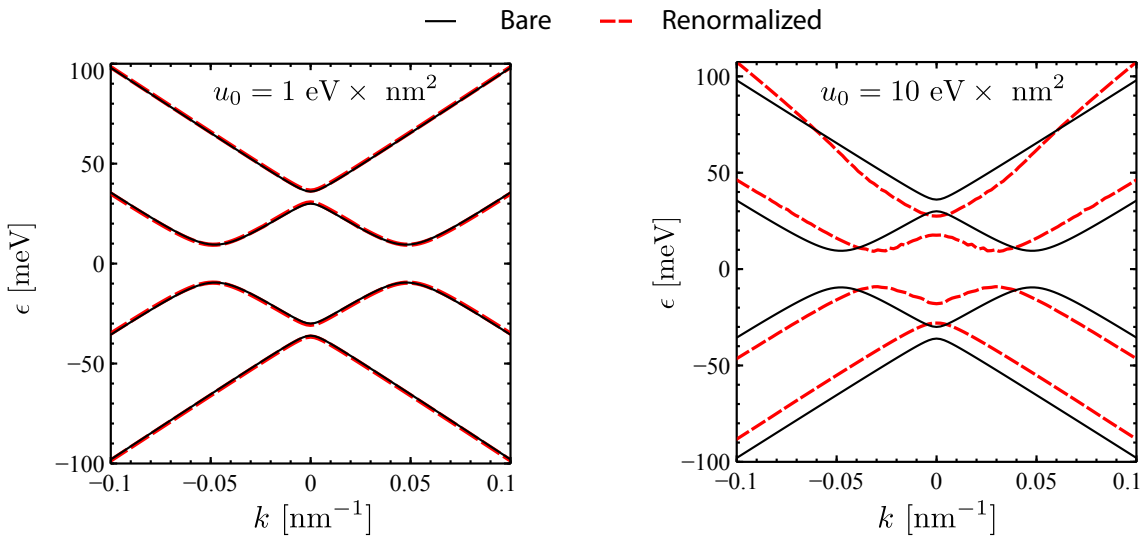

Figure 3.6: Band structure of the C_{3v} model with $\lambda_{\rm sv} = 3\lambda = 30$ meV and $\Delta = \lambda_{zz} = 0$ meV, in the bare case (solid black curves) and renormalised by disorder (dashed red), for scattering strength $u_0 = (1, 10)$ eV $\times$ nm^2, respectively in panel (a) and (b). The impurity concentration is chosen as $n_i = 10^{-12}$cm^{-2}.

To give a concrete example, let us perform a calculation in the C_{3v} model within the SCTM scheme. According to this prescription, the set of self-consistent equations associated with the diagrammatic representation in Fig. 3.5 is

$$\Sigma^a_{\rm SCTM} = n_i \mathrm{T}(\Sigma^a_{\rm SCTM}) = n_i \frac{u_0}{1 - u_0 g^a_{\rm SC}(\Sigma^a_{\rm SCTM})}\,, \tag{3.65}$$

$$g^a_{\rm eff}(\Sigma^a_{\rm SCTM}) = g^a(\tilde{\epsilon}^{\rm SCTM}, \tilde{\lambda}^{\rm SCTM}, \tilde{\lambda}^{\rm SCTM}_{\rm sv}, \tilde{\Delta}^{\rm SCTM}, \tilde{\lambda}^{\rm SCTM}_{zz})\,. \tag{3.66}$$

Above, the notation with superscript SCTM indicates renormalisation by the self-consistent $\Sigma^a_{\rm SCTM}$, i.e.

$$\tilde{\epsilon}^{\rm SCTM} \equiv \epsilon + [\delta\epsilon + \imath\, a\, \eta_0]_{\rm SCTM}\,, \tag{3.67}$$

and similarly for the other parameters. We illustrate in Fig. 3.6 the result for $n_i = 10^{-12}$cm^{-2}, $\lambda_{\rm sv} = 3\lambda = 30$ meV, $\Delta = \lambda_{zz} = 0$ meV and for the two choices of scattering strength $u_0 = (1, 10)$ eV $\times$ nm^2. The band renormalisation becomes more prominent for increasing disorder strength.

Chapter 4

Spin Hall effect and Inverse Spin Galvanic Effect in the Dirac-Rashba model

Overview

In this Chapter we start our study of SO-related transport phenomena in 2D Dirac systems. We thus present a detailed theoretical analysis of the SHE and the ISGE in the minimal Dirac–Rashba model, in the presence of disorder and external perturbations.

First, we unveil a set of *exact* symmetry relations, i.e the WIs, that impose strong constraints on the spin dynamics of Dirac fermions subject to SO fields. In the minimal 2D Dirac-Rashba model, the existence of a covariant conservation law for the spin current—stemming from the $SU(2)$ gauge invariance of the Hamiltonian—allows us to obtain the analytic form of the two-particle spin-current vertex function directly from the self-energy of the Dirac fermions. From that, we show that the spin Hall conductivity in the minimal model [Eq. (3.3)] is *zero* in the presence of an arbitrary dilute concentration of scalar nonmagnetic impurities, *irrespective of the position of the Fermi level*. The closeness to the Rashba 2DEG case—for which the SHE is also absent—in this respect (see Refs. [174–178]) is remarkable but far from being trivial, as we discuss below.

On the upside, while spin Hall currents are not supported, a robust current-driven spin polarisation, i.e. the ISGE (see Sec. 1) can establish in this particular system. We show the efficiency of the CSC achieves the maximum attainable value, i.e. unity (in units of the charge conductivity) in the regime with only one populated subband. Remarkably, at high electronic density where both bands with opposite helicity are occupied, the efficiency decays only algebraically with the Fermi energy, therefore staying sizable in a large window of experimentally accessible energies. Finally, we also show that the giant ISGE predicted for graphene with Rashba SO coupling is robust against disorder strength.

Spin Hall effect in the Dirac-Rashba model

We have remarked how, in 2D systems with broken mirror symmetry, the Rashba interaction H_{R} mixes orbital states with opposite spins, leading to spin-split bands with counter-rotating

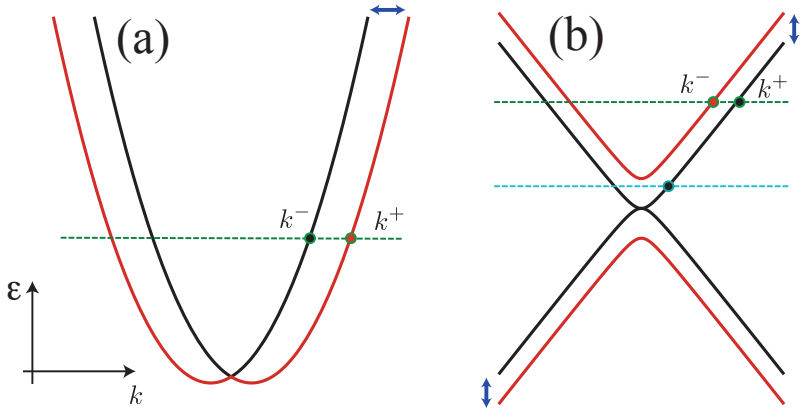

Figure 4.1: Schematic of the splitting of electronic states due to Rashba effect in a 2DEG (a) and graphene (b). The Fermi surface consists of two branches in a 2DEG. In graphene, for energies in the Rashba pseudogap $|\epsilon| < 2|\lambda|$ the Fermi surface is simply connected. Arrows indicate the type of splitting.

spin textures [165] (see also Fig. 3.2). For the 2DEG it has been demonstrated how the very helical nature of these states enforces a *vanishing* SHE in the presence of (scalar) impurity scattering [174–178]. Yet, a non-zero SHE in the 2DEG model can be achieved by extrinsic skew scattering mechanisms, in the presence of SO-active impurities or of terms breaking time-reversal symmetry (e.g., by magnetic impurities) [179–181].

Given the universality of the Rashba effect (also observed in ultra-thin metals [182, 183], quantum wells [184, 185] and surfaces of TIs [186–188]), it is of the utmost importance to understand whether the absence of SHE is a general property of nonmagnetic surfaces with broken inversion symmetry, or rather a peculiarity of the 2DEG. The interfacial enhancement of SO coupling in graphene has been recently demonstrated [123–125, 128, 189, 190], making it a promising model system to explore this fundamental question. The departure from the standard Rashba effect in a 2DEG can be readily appreciated for a minimal model of graphene subject to $z \to -z$ asymmetric SO coupling, as discussed in Chapter 3. In the long-wavelength limit, the relevant SO Rashba interaction for Dirac particles is obtained from the 2DEG form Eq. (1.15) by replacing momentum with pseudospin operator $\mathbf{p} \to \boldsymbol{\sigma}$ in $H_{\rm R}$ [99, 191], see also Eq. (3.1). This model possesses two noteworthy features. First, in contrast to the 2DEG case, the band splitting occurs along the energy axis (Fig. 4.1). Secondly, the Dirac helical spin texture is momentum dependent, i.e., $|\langle \mathbf{s} \rangle|$ is not conserved [191] [see Eq. (3.8)]. Moreover, the Dirac-Rashba Hamiltonian admits a straightforward generalisation by adding further interactions preserving the inherent $SU(2)$ spin structure (cf. Chapter 3), such as a spin–valley coupling [see Eq. (3.54)]. Such unique features make the Dirac–Rashba model an ideal testbed to re-examine the absence of SHE in interfaces with spin-split states.

A parenthesis: spin Hall effect in the Rashba 2DEG

The suppression of SHE in 2DEGs subject to uniform Rashba interactions occurs in the presence of an arbitrary small concentration of scalar impurities. Formally, the disorder corrections resulting from the resummation of ladder diagrams exactly cancel the "clean" spin Hall conductivity [174–178, 192]. In Ref. [177] it was shown that this puzzling cancellation has its origin in the existence of a covariant conservation law for the spin current. For example, the spin-y component satisfies

$$\partial_t J^y_0(\mathbf{x}, t) + \partial^i J^y_i(\mathbf{x}, t) = -2\,\lambda_{\rm 2DEG}\, m\, J^z_y(\mathbf{x}, t), \tag{4.1}$$

where J_0^a ($a = x, y, z$) is the spin density, J_i^a is the pure spin current flowing in the $i = x, y$ direction (see below), m is the effective electron mass, and $\lambda_{\rm 2DEG}$ is the 2DEG Rashba parameter. The main difference with respect to the charge continuity equation Eq. (1.13) originates from the non-Abelian nature of spin, which results in the additional contribution on its RHS. Eq. (4.1) suggests that in the steady state of a homogeneous system, J_y^z is zero irrespective of the underlying relaxation mechanism. Below we show that a similar covariant conservation law exists for Dirac materials and discuss its consequences.

Conservation laws I: clean system

A peculiarity of Dirac theories is the possible existence of quantum anomalies due to the joint effect of an infinite Dirac sea of filled electron states and an external field [88,193]. Let us consider the minimal coupling of the 2D Dirac-Rashba model to a $U(1)$ gauge field $A_\mu \equiv (A_0, A_i)$

$$\mathscr{H}_{0,\kappa}^{\rm min} = \Psi_{0,\kappa}^\dagger \left\{ \kappa \left[v\, \sigma^i \left(-\imath \partial_i - A_i \right) - A_0 + \lambda \left(\boldsymbol{\sigma} \times \mathbf{s} \right)_z \right] \right\} \Psi_{0,\kappa} \,. \tag{4.2}$$

To simplify the presentation we have taken the valley index as $\kappa = +1$ and will omit it hereafter, including a valley degeneracy factor $g_v = 2$ when required. We use the compact notation $\partial^\mu \equiv (\partial_t, \partial_i)$ with summation over dummy indices. The Dirac spin and charge currents are, respectively

$$J_\mu^a(x) = \Psi_0^\dagger(x)\, \mathcal{J}_\mu^a / 2\, \Psi_0(x) = \Psi_0^\dagger(x)\, s^a v_\mu / 2\, \Psi_0(x) \,, \tag{4.3}$$

$$J_\mu(x) = \Psi_0^\dagger(x) v_\mu \Psi_0(x) \,, \tag{4.4}$$

where $v^\mu \equiv (1, v\,\boldsymbol{\sigma})$ and $x \equiv (t, \mathbf{x})$. The Heisenberg equation of motion for the spin density reads

$$\partial_t J_0^a = \imath [\mathscr{H}_0^{\rm min}, J_0^a] \,, \tag{4.5}$$

which after some algebra becomes

$$\partial^\mu J_\mu^a(x) = -\frac{2\lambda}{v} \epsilon_{bc}^a\, \epsilon^{bl} J_l^c(x) + \imath \int dy [J_0^a(x), J_\mu(y)] A^\mu(y), \tag{4.6}$$

where ϵ^{bl} (ϵ_{bc}^a) is the Levi-Civita symbol of second (third) rank. The term on the LHS and the first on the RHS result from the commutator of J_0^a respectively with the kinetic and the Rashba term, and give a contribution identical to the one found in the 2DEG upon identification of $m \to 1/v$, c.f. Eq. (4.1). Both terms can be combined as the covariant derivative D_μ

$$D_\mu \mathcal{O}^a = \partial_\mu \mathcal{O}^a + 2\, \epsilon_{bc}^a\, \mathcal{A}_\mu^b \mathcal{O}^c \,, \tag{4.7}$$

where the $SU(2)$ gauge field due to the homogeneous Rashba interaction is $\mathcal{A}_0^a = 0$, $\mathcal{A}_i^a = -\lambda / v\, \epsilon^{ai}$. Without the last term on the RHS, Eq. (4.6) would take the form of a $SU(2)$ covariant conservation law for the spin density $D^\mu J_\mu = 0$. The current commutator in the last term (Schwinger term) defines the anomaly. However, a careful analysis shows that this commutator is identically zero [169], as we show in detail in Appendix C. We thus find

$$D^\mu J_\mu^a(x) = 0 \,. \tag{4.8}$$

Eq. (4.6), and hence Eq. (4.8), states that in the steady state ($\partial^\mu = 0$) the spin Hall current must vanish, in agreement with the argument in Ref. [177].

Let us now try to derive the same result by direct diagrammatic inspection. Fixing, e.g., the y direction for the flowing of the spin current (z polarised) we need to evaluate

$$J^z_y\Big|_{\text{clean}} = \sigma^z_{yx}\Big|_{\text{clean}} \mathcal{E}_x \equiv \sigma_{\text{SH}}|_{\text{clean}}\, \mathcal{E}_x \,. \tag{4.9}$$

The calculation of spin Hall response (type I and II), is obtained from Eqs. (2.31)-(2.32) upon replacement $v_i \to \mathcal{J}^z_y = v\, s_z \sigma_y/2$, i.e.

$$\sigma_{\text{SH}}(\epsilon)|_{\text{clean}} = \sigma^I_{\text{SH}}(\epsilon)\Big|_{\text{clean}} + \sigma^{II}_{\text{SH}}(\epsilon)\Big|_{\text{clean}} \,, \tag{4.10}$$

$$\sigma^I_{\text{SH}}(\epsilon)\Big|_{\text{clean}} = \frac{1}{4\pi\Omega}\text{Tr}\left[\mathcal{J}^z_y(G^R(\epsilon) - G^A(\epsilon))v_x G^A(\epsilon) - \mathcal{J}^z_y G^R(\epsilon) v_x (G^R(\epsilon) - G^A(\epsilon))\right] \,, \tag{4.11}$$

$$\sigma^{II}_{\text{SH}}(\epsilon)\Big|_{\text{clean}} = \frac{1}{4\pi\Omega}\int_{-\infty}^{+\infty} d\epsilon' f(\epsilon')\, \text{Tr}\left[\mathcal{J}^z_y G^R(\epsilon') v_x (\partial_{\epsilon'} G^R(\epsilon')) - \mathcal{J}^z_y (\partial_{\epsilon'} G^R(\epsilon')) v_x G^R(\epsilon') + \text{h.c.}\right] \,, \tag{4.12}$$

where $v_x = v\,\sigma_x$. In the clean limit $G^{R/A} \to G^{R/A}_{0\mathbf{k}}$, where the clean propagators of the 2D Dirac Rashba model are reported in Eq. (3.14). We find

$$J^z_y = \left(-\frac{\epsilon}{16\pi\lambda}\left[\frac{2\lambda+\epsilon}{\epsilon+\lambda} + \theta(\epsilon - 2\lambda)\frac{2\lambda-\epsilon}{\epsilon-\lambda}\right]\right)\mathcal{E}_x \neq 0 \,, \tag{4.13}$$

in agreement with Ref. [194]. Here we assumed $\epsilon, \lambda > 0$. Eq. (4.13) seems to contradict the result of Eq. (4.8). However the contradiction is only apparent, and it is resolved by recalling that, without a relaxation mechanism, there is no true stationary state, which does not allow, therefore, to consider the limit $\partial^\mu = 0$ of Eq. (4.8). In the following we show that Eq. (4.13) misses important physics related to scattering-induced relaxation that leads to $\sigma_{\text{SH}} = 0$.

Conservation laws II: disorder effects

Broadly speaking, the Fermi surface contribution to σ_{SH} (type I) is dominated by incoherent multiple scattering off impurities, which can be viewed as a series of skew scattering and side jump events [153, 158, 159, 195]. To determine how such effects change the naive picture presented above, we consider the full disordered Hamiltonian [cf. Eq. (3.3)], by adding to the bare Dirac-Rashba Hamiltonian the random scalar potential $V(\mathbf{x})$, which we will assume to be Gaussian distributed with zero mean, as discussed above, Eqs. (2.15)-(2.16). This approximation is accurate in the limit of weak potential scattering provided cross sections are right–left symmetric, as it is the case for the pure Rashba model [see Eq. (3.51)]. We note that short-range impurities lead to scattering potentials that are off-diagonal in both sublattice and valley spaces. The intervalley scattering (with matrix structure $\propto \tau_{x,y}$) produced by such disorder affects the charge conductivity σ_{xx} [196], but it does not change the covariant conservation law for the spin current, as the commutator of $\tau_{x,y}$ with any of the spin operators is zero.

From a diagrammatic viewpoint, disorder enters the evaluation of the response functions both in the propagators (as a self-energy) and the interaction vertex [155], see Chapter 2. These two quantities are *not* independent of each other but they are related by the WIs [88, 193]. Here we will show that the non-Abelian WIs associated to the spin current vertex completely determines the spin current J^z_y in the DC limit and therefore it can be used to directly evaluate the spin

Hall conductivity. To see this, consider the three-legged spin vertex function [cf. Eq. (2.48)]

$$\Lambda^{y}_{\mu}(x,x',x'') = \langle \mathscr{T}\, J^{y}_{\mu}(x)\, \Psi(x')\, \Psi^{\dagger}(x'')\rangle\,. \tag{4.14}$$

Above the fermionic fields create/annihilate states associated to the *full* Hamiltonian $H = H_0 + V$. To obtain the WIs we take the spacetime derivative with respect to x, i.e. $\partial^{\mu}_{(x)}\Lambda^{y}_{\mu}$. Making explicit the form of the time-ordering operator, one finds

$$\partial^{\mu}_{(x)}\Lambda^{y}_{\mu} = \partial^{\mu}_{(x)}\left\{\theta(t-t')\theta(t'-t'')\langle J^{y}_{\mu}(x)\Psi(x')\Psi^{\dagger}(x'')\rangle + ...\text{permutations...}\right\} \tag{4.15}$$

$$= \delta(t-t')\theta(t'-t'')\langle J^{y}_{0}(x)\Psi(x')\Psi^{\dagger}(x'')\rangle + ... + \langle \mathscr{T}\partial^{\mu}_{(x)} J^{y}_{\mu}(x)\Psi(x')\Psi^{\dagger}(x'')\rangle\,. \tag{4.16}$$

At this point one can make use of the conservation law for J^{y}_{μ} Eq. (4.6) and of the fermionic anti-commutation rules. Identifying the single-particle Green's function as $G(x,x') = -\imath\langle\mathscr{T}\Psi(x)\Psi(x')\rangle$ (cf. Eq. (3.15)), after a few lines of calculation we arrive at

$$\partial^{\mu}\Lambda^{y}_{\mu}(x,x',x'') = \frac{\imath}{2}\left[G(x',x)\, s^{a}\delta(x-x'') - s^{a}G(x,x'')\delta(x-x')\right] - 2\epsilon_{yab}\mathcal{A}^{b}_{\mu}\Lambda^{c}_{\mu yb}(x,x',x'')\,. \tag{4.17}$$

We can now move to frequency-momentum space considering $(qx = q_0 t - \mathbf{q}\cdot\mathbf{x})$

$$\Lambda^{y}_{\mu}(x,x',x'') = \int dk \int dq\, e^{-\imath(k+q/2)(x'-x)} e^{-\imath(k-q/2)(x-x'')}\Lambda^{y}_{\mu}(k,q), \tag{4.18}$$

in terms of which the WIs reads

$$q_{\mu}\Lambda^{y}_{\mu} = G(k+q/2)\frac{s^{y}}{2} + \frac{s^{y}}{2}G(k-q/2) - 2\imath\frac{\lambda}{v}\Lambda^{c}_{\mu}\,. \tag{4.19}$$

The connection to the diagrammatic calculation is made by making explicit the form of the three-legged function in terms of the truncated vertices Γ^{a}_{μ}, which are nothing but the vertices appearing in the response functions [155]

$$\Lambda^{a}_{\mu}(k,q) = G(k+q/2)\Gamma^{a}_{\mu}(k,q)G(k-q/2)\,. \tag{4.20}$$

Performing the $q\to 0$ limit and analytical continuation $k_0 \pm q_0/2 \to \omega \pm \imath 0^{+}$, we obtain

$$q_{\mu}\Gamma^{y}_{\mu}(\mathbf{k},0) = \frac{1}{2}\left[s^{y}\left(G^{A}_{\mathbf{k}}\right)^{-1} - \left(G^{R}_{\mathbf{k}}\right)^{-1}s^{y}\right] - 2\imath\frac{\lambda}{v}\mathcal{J}^{z}_{y}\,, \tag{4.21}$$

where we have identified the spin Hall vertex $\Gamma^{z}_{y} \equiv \mathcal{J}^{z}_{y}$. Note the latter equation includes the effect of disorder *to all orders*. At this stage, we can easily perform disorder average $\langle ...\rangle_{\text{dis}}$ to both sides [Eq. (2.17)], and considering the formal definition of the disordered averaged Green's functions $\mathcal{G}^{a}_{\mathbf{k}}(\epsilon) = \left[\epsilon - H_{0\mathbf{k}} - \Sigma^{a}(\epsilon)\right]^{-1}$, we finally obtain the uniform DC ($q\to 0$) limit

$$\tilde{\mathcal{J}}^{z}_{y} = \imath\frac{v}{4\lambda}\left\{[s_y,\tilde{H}_0]_{-} + \imath\,[s_y,\text{Im}\,\Sigma^{R}]_{+}\right\}\,, \tag{4.22}$$

where $\pm$ stands for the (anti-)commutator, $\tilde{H}_0 = H_0 + \text{Re}\,\Sigma$ is the bare Hamiltonian renormalised by the real part of the self-energy, and $\tilde{\mathcal{J}}^{z}_{y} = \langle\mathcal{J}^{z}_{y}\rangle_{\text{dis}}$ is the renormalised spin Hall vertex. We see that owing to the non-Abelian nature of the WIs, Eq. (4.19) completely determines the effective spin Hall current vertex in the minimal model.

The obtained result provides an *exact* relation between the spin Hall current vertex and the self-energy, and as such it is independent of the particular approximation scheme used to evalu-

ate disorder effects. Let us adopt here the Gaussian approximation; using the expression of the self-energy in Eqs. (3.35)-(3.40) we arrive at

$$\tilde{\mathcal{J}}^z_y(\epsilon) = \frac{v}{2} \times \begin{cases} \sigma_y s_z - \frac{1}{2\lambda\tau}\sigma_0 s_y & , \epsilon > 2\lambda \\ \sigma_y s_z - \frac{1}{4\lambda\tau}\left(1+\frac{\lambda}{\epsilon}\right)\sigma_0 s_y & \\ +\frac{1}{8\lambda\tau}\sigma_x s_0 + \frac{1}{4\pi\tau\lambda}\sigma_z s_x. & , \epsilon \leq 2\lambda \end{cases} \tag{4.23}$$

In both cases $\epsilon \lessgtr 2\lambda$, the first term is just the bare spin current vertex $J^z_y = \frac{v}{2}\sigma_y s_z$. For $\epsilon > 2\lambda$, the second term, generated by the disorder, is the bare spin density vertex $\sigma_0 s_y/2$ without the factor $-v/2\lambda\tau$. The parameter $\lambda\tau$, in fact, plays a fundamental role in determining the importance of disorder. At first sight one could be tempted to think that within the weak disorder limit ($\epsilon\tau \gg 1$) and for strong SO coupling ($\lambda\tau \gg 1$), all disorder corrections can be neglected. However, it turns out that the spin polarisation response is of order $\lambda\tau$ (see below), whereas the bare spin current response, due to the first term in Eq. (4.23) is of order $(\lambda\tau)^0$. Hence, the two terms in the first line of Eq. (4.23) are of the same order irrespective of the disorder strength. Similar considerations apply also for $\epsilon < 2\lambda$.

Ward identities

Using Eq. (4.23), we evaluate the Fermi surface contribution [cf. Eq. (4.11)]

$$\sigma^{\mathrm{I}}_{\mathrm{SH}}(\epsilon) = \int \frac{d\mathbf{k}}{(2\pi)^2}\, \mathrm{tr}\left[\tilde{\mathcal{J}}^z_y(\epsilon)\, \mathcal{G}^R_{\mathbf{k}}(\epsilon)\, v_x\, \mathcal{G}^A_{\mathbf{k}}(\epsilon)\right] \tag{4.24}$$

$$= \bar{\sigma}_{\mathrm{SH}}(\epsilon) + \bar{\sigma}_{SG}(\epsilon) + \bar{\sigma}_{xx}(\epsilon) + \bar{\sigma}_{zx}(\epsilon)\,, \tag{4.25}$$

where $v_x = v\,\sigma_x s_0$ is the bare charge current vertex. Moreover, $\bar{\sigma}_{\mathrm{SH}}$, $\bar{\sigma}_{\mathrm{SG}}$, $\bar{\sigma}_{xx}$, and $\bar{\sigma}_{zx}$ are the conductivity "bubbles" corresponding to the various terms in Eq. (4.23), respectively, a spin Hall ($\sigma_y s_z$), spin galvanic ($\sigma_0 s_y$), longitudinal ($\sigma_x s_0$) and "staggered" ($\sigma_z s_x$) conductivities. Outside the pseudogap, where the Fermi surface splits into two branches (Fig. 4.1), we find $\bar{\sigma}_{xx} = \bar{\sigma}_{zx} = 0$ and $\bar{\sigma}_{\mathrm{SH}} = -\bar{\sigma}_{\mathrm{SG}}$, where

$$\bar{\sigma}_{\mathrm{SH}}(\epsilon) = -\frac{1}{8\pi}\left(\frac{\epsilon^2}{\epsilon^2-\lambda^2} - \frac{1}{1+4\lambda^2\tau^2}\right), \tag{4.26}$$

and thus the type I contribution to the spin Hall conductivity is zero, $\sigma^{\mathrm{I}}_{\mathrm{SH}} = 0$. This result deserves a few comments: First, in the $\lambda\tau \gg 1$ limit, one recovers Eq. (4.13). Second, the "empty bubble" spin Hall conductivity ($\bar{\sigma}_{\mathrm{SH}}$) is precisely counteracted by the corresponding "empty bubble" for spin density-charge current response function ($\bar{\sigma}_{\mathrm{SG}}$). This indicates that the absence of SHE is linked to the onset of a current-induced, in-plane spin polarisation, i.e. the ISGE, as we demonstrate in the following sections. The remaining (type II) contribution [cf. Eq. (4.12)]

$$\sigma^{\mathrm{II}}_{\mathrm{SH}}(\epsilon) = -\frac{1}{2\pi}\int \frac{d\mathbf{k}}{(2\pi)^2}\int_{-\infty}^{0} dk_0\, \mathrm{Re}\,\mathrm{tr}\left[\left[\partial_{k_0}\mathcal{G}^R_k(\epsilon)\right]\mathcal{J}^z_y\,\mathcal{G}^R_k(\epsilon)\,v_x - \mathcal{G}^R_k(\epsilon)\,\mathcal{J}^z_y\left[\partial_{k_0}\mathcal{G}^R_k(\epsilon)\right]v_x\right], \tag{4.27}$$

accounts for processes away from the Fermi surface, as we have discussed in Eq. (2.32). Explicit evaluation shows that $\sigma^{\mathrm{II}}_{\mathrm{SH}} = 0$ and thus $\sigma_{\mathrm{SH}} = \sigma^{\mathrm{I}}_{\mathrm{SH}} + \sigma^{\mathrm{II}}_{\mathrm{SH}}$ is zero, in agreement with our earlier argument, see Eqs. (4.1)-(4.6). Interestingly, in the 2DEG–Rashba model, the type II term is only zero in the formal limit $\epsilon\tau \to \infty$ and can attain large values for $\lambda\tau \approx 1$ [197]. The exact vanishing

of the off-Fermi surface contribution in this regime $\epsilon > 2\lambda$ is a *unique feature* of the Dirac theory. We now move gears to the regime $\epsilon < 2\lambda$, where only one subband is occupied. We note that this regime has no analogy in the 2DEG model, for which the Fermi surface always consists of two disconnected rings (Fig. 4.1), except for the intersection point between the spin-split bands. The mechanism leading to $\sigma_{\rm SH} = 0$ is thus far from obvious. To investigate this issue, we evaluate the Fermi surface contribution making use of the WIs [see Eq. (4.23)] and the type II contribution using Eq. (4.27). After a lengthy calculation, we find for both contributions

$$\sigma^{\rm I}_{\rm SH}(\epsilon) = \frac{\epsilon}{16\pi\lambda} \quad , \quad \sigma^{\rm II}_{\rm SH}(\epsilon) = -\sigma^{\rm I}_{\rm SH}(\epsilon)\,. \tag{4.28}$$

so that $\sigma_{\rm SH} = 0$. Note that since $\sigma^{\rm I}_{\rm SH}$ is of order 1, we can evaluate the type II contribution [Eq. (4.27)] directly in the absence of disorder. The suppression of the SHE in the regime $0 < \epsilon \leq 2\lambda$ therefore results from a compensation between scattering corrections to the "clean" spin Hall conductivity and off-Fermi surface processes.

Diagrammatic evaluation

We now show the consistency of our results with a standard diagrammatic evaluation. To account also for other electric-field dependent out-of-equilibrium responses (e.g. charge conductivity), it is convenient to consider the renormalised charge current vertex instead of the spin Hall current one. The renormalised charge current vertex satisfies the following BS coupled equations (see Fig. 2.3)

$$\tilde{v}_{x,\mu a} = v\,\delta_{\mu x}\,\delta_{a0} + Y^{\nu b\lambda c}_{\mu a\rho d}\,I_{\nu b\lambda c}\,\tilde{v}^{\rho d}_{x}\,, \tag{4.29}$$

$$Y^{\nu b\lambda c}_{\mu a\rho d} = {\rm tr}\left[\sigma_\mu\, s_a\, \sigma_\nu\, s_b\, \sigma_\rho\, s_d\, \sigma_\lambda\, s_c\right]\,, \tag{4.30}$$

$$I_{\nu b\lambda c} = \frac{n_i\,u_0^2}{4}\int \frac{d\mathbf{k}}{(2\pi)^2}\,\mathcal{G}^R_{\mathbf{k},\nu b}(\epsilon)\,\mathcal{G}^A_{\mathbf{k},\lambda c}(\epsilon). \tag{4.31}$$

In principle, I spans the entire Clifford Algebra generated by $\sigma_\mu \otimes s_a$. However, not all matrix elements contribute to the renormalisation of the charge vertex. It is convenient to consider the effect of a single impurity density insertion, i.e. solving Eq. (4.29) by replacing $\tilde{v}_x \to v_x$ on the RHS. The corresponding solution $\bar{v}_x$ is found of the form: $\bar{v}_x = \delta v_{x0}\,\sigma_x\,s_0 + \delta v_{yz}\,\sigma_y\,s_z + \delta v_{0y}\,\sigma_0\,s_y + \delta v_{zx}\,\sigma_z\,s_x$, with δv_{ij} some non-zero matrix elements. This result suggests the form of the ansatz for $\tilde{v}_x$ to use in Eq. (4.29)

$$\tilde{v}_x = \tilde{v}_{x0}\,\sigma_x\,s_0 + \tilde{v}_{yz}\,\sigma_y\,s_z + \tilde{v}_{0y}\,\sigma_0\,s_y + \tilde{v}_{zx}\,\sigma_z\,s_x\,. \tag{4.32}$$

Since no new matrix element is generated in this procedure, the ansatz closes the system. Therefore, in addition to the renormalised charge vertex $\tilde{v}^{x0}_x$, we find that disorder induces an effective spin Hall ($\tilde{v}^{yz}_x$), spin galvanic ($\tilde{v}^{0y}_x$) and "staggered" ($\tilde{v}^{zx}_x$) interaction. Their explicit form reads (for $\epsilon > 2\lambda$): $\tilde{v}^{x0}_x = 2\,v$, $\tilde{v}^{0y}_x = -2\,v(\lambda/\epsilon)$, $\tilde{v}^{zx}_x = 0$ and $\tilde{v}^{yz}_x = 0$. In order to evaluate the spin Hall conductivity we use now Eq. (4.25), with the ladder series now included in the charge vertex (i.e. $\tilde{\mathcal{J}}^z_y \to \mathcal{J}^z_y$ and $v_x \to \tilde{v}_x$). Using Eq. (4.29), it is now easy to relate the renormalised vertex

directly to the spin Hall and Drude conductivity

$$\sigma_{\rm SH} = \frac{1}{2\pi}\left(\frac{2\,v}{n_i\,u_0^2}\right)\tilde{v}_x^{yz} = 0, \tag{4.33}$$

$$\sigma_{xx} = \frac{1}{2\pi}\left(\frac{4\,v}{n_i\,u_0^2}\right)(\tilde{v}_x^{x0} - v) = \frac{2\,\epsilon\,\tau}{\pi}. \tag{4.34}$$

We mentioned earlier that higher-order scattering contributions to the self-energy (and ladder series) could generate important corrections. This happens when impurities in the system lead to skew scattering. In the 2DEG, it is well known that skew scattering is absent (unless other ingredients, such as SO-active impurities are considered), and we demonstrated in Section 3 that is also the case for Dirac fermions. The absence of skewness has in fact an intuitive explanation: the spin of Rashba eigenstates is locked in-plane, so that in a given scattering event quasiparticles cannot distinguish left and right. We verified this by means of the self-consistent diagrammatic approach introduced in Ref. [159] at T-matrix level, together with the WIs [Eq. (4.22)].

We note in passing that random spatial fluctuations in the Rashba coupling (e.g., due to corrugations or impurities) can provide an alternative source of SHE [198, 199]. This can be understood by introducing a space-dependent part to the $SU(2)$ gauge field

$$A_i^a \to A_i^a + \delta A_i^a(\mathbf{x})\,, \tag{4.35}$$

which generates an additional term in the spin equation of motion[1], i.e.

$$\partial^\mu J_\mu^a(x) = \epsilon_{bc}^a[A_\mu^b + \delta A_\mu^b(\mathbf{x})]J_\mu^c(x). \tag{4.36}$$

In the equation above, one still needs to perform disorder average. Should it be non-vanishing, such an additional term $\langle \epsilon_{bc}^a\,\delta A_\mu^b(\mathbf{x})\,J_\mu^c(x)\rangle_{\rm dis}$ sets the steady-state value of the spin Hall current.

Inverse spin Galvanic effect in the Dirac-Rashba model

In the search for novel spintronic materials, the role of the ISGE (see Sec. 1), together with its Onsager reciprocal—the SGE—is gaining strength. Experimental detection of both effects has been recently reported in spin-split 2DEGs formed in Bi/Ag and $LaAlO_3/SrTiO_3$ and TI α-Sn thin films [42–44]. For what concerns graphene, the enhancement of non-equilibrium spin polarisation has been proposed in ferromagnetic TMDs and magnetically-doped TI/graphene [200, 201].

In this Section we study the occurrence of this effect in the Dirac-Rashba model.

Semiclassical analysis

The starting point is the Dirac-Rashba Hamiltonian of Eq. (3.3), with the spectrum shown in Fig. 3.2. Similarly to what was done above, we focus on positive energies $\epsilon > 0$. The spin texture associated with each band, reads [cf. Eq. (3.8)]

$$\langle \mathbf{s}\rangle_{\alpha\mathbf{k}} = -\chi\,\varrho(k)\,(\hat{k}\times\hat{z})\,, \tag{4.37}$$

[1]Note here operators are meant in the presence of disorder, associated with field operators $\Psi^\dagger, \Psi$.

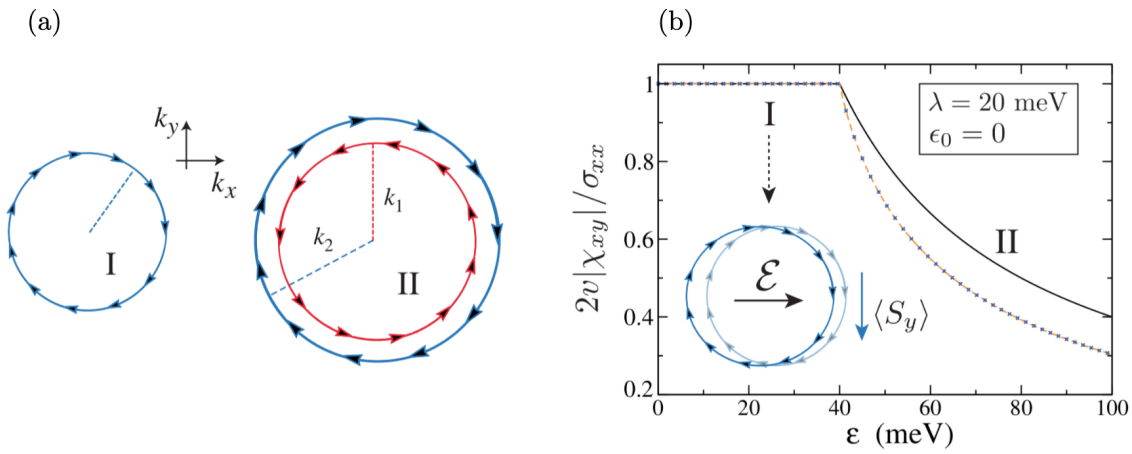

Figure 4.2: (a) Tangential winding of spin texture in regimes I and II (cf. Fig. 3.2). (b) Ratio between the static spin–charge susceptibility and charge conductivity (in units of $2v$) [thick line (Born limit); dashed line (strong scattering limit, $u_0 \to \infty$)].

where $\alpha \equiv (\kappa\chi)$ and $\chi = \pm 1$ is the spin-helicity index. The latter equation describes spin winding generated by the Rashba effect [Fig. 4.2(a)], with the spin texture being fully in-plane [191].

The entanglement between spin and sublattice DOFs generates a nontrivial k-dependence in the spin texture, $\varrho(k)$ coinciding with the band velocity (in units of v)

$$\varrho\,(k) = \frac{vk}{\sqrt{\lambda^2 + v^2k^2}} = \frac{v_{\chi=-1,k}}{v}\,, \tag{4.38}$$

$$v_{\alpha k} = \partial_k \epsilon_{\alpha \mathbf{k}}\,, \tag{4.39}$$

The low-energies regime $\epsilon < 2\lambda$ [regime I, Fig. 4.2(b-c)] is particularly interesting: here electronic states at a given $\mathbf{k}$ have *well-defined spin helicity*. This feature is reminiscent of spin–momentum locking in topologically protected surface states [166], which suggests that this system supports robust CSC.

The efficiency of CSC can be demonstrated using a simple SC argument, i.e. within the BTE formalism presented in Sec. 2 [cf. Eq. (2.11)]. Under a DC electric field, say $\vec{\mathcal{E}} = \mathcal{E}\,\hat{x}$, the $\hat{y}$-polarised spin density in the steady state reads [cf. Eq. (2.12)]

$$\langle S_y \rangle = \sum_\alpha \int \frac{d\mathbf{k}}{(2\pi)^2} \frac{1}{2} \langle s_y \rangle_{\alpha \mathbf{k}}\, \delta f_{\alpha \mathbf{k}}\,, \tag{4.40}$$

where $\delta f_{\alpha \mathbf{k}}$ is the deviation of the quasiparticle distribution function with respect to equilibrium. In general, an ansatz to $\delta f_{\alpha \mathbf{k}}$ can be given in terms of two terms, respectively parallel and perpendicular to the applied electric field [171]. Owing to the tangential winding of the in-plane spin texture however, only the longitudinal component of the quasiparticle distribution function $\delta f^{\parallel}_{\alpha \mathbf{k}} \equiv g_\alpha(k)\, \hat{k} \cdot \hat{k}_x$ contributes to the integral. At zero temperature one can write

$$g_\alpha(k) = -\mathcal{E} v_{\alpha k}\, \tau_{*\alpha k}\, \delta(\epsilon_{\alpha k} - \epsilon), \tag{4.41}$$

where $\tau_{*\alpha k}$ is the longitudinal transport time. For energies inside the Rashba pseudogap (regime I), one easily finds

$$\langle S_y \rangle_{\mathrm{I}} = -\frac{\mathcal{E}}{4\pi}\, \varrho(k_F)\, k_F \tau_* = -\frac{\mathcal{E}}{4\pi}\, \frac{v_F}{v}\, k_F \tau_* \tag{4.42}$$

where k_F is the Fermi momentum and $\tau_* = \tau_{*(\kappa-)k_F}$. The charge current density,

$$\langle J_x \rangle = -v \sum_{\alpha} \int \frac{d\mathbf{k}}{(2\pi)^2} \langle \sigma_x \rangle_{\alpha\mathbf{k}} \, \delta f_{\alpha\mathbf{k}} \,, \tag{4.43}$$

can be computed following identical steps. We obtain

$$\langle J_x \rangle_{\mathrm{I}} = \frac{\mathcal{E}}{2\pi} \, v_F \, k_F \, \tau_* \,, \tag{4.44}$$

where $v_F = |v_{\chi=-1,k}|$. We thus find $\langle S_y \rangle_{\mathrm{I}} = -\langle J_x \rangle_{\mathrm{I}}/(2v)$. Figure 4.2 (d) shows the ratio of $\langle S_y \rangle / \langle J_x \rangle$ in the linear response regime computed according to the Kubo formula, confirming the linear proportionality $\langle S_y \rangle_{\mathrm{I}} \propto \langle J_x \rangle_{\mathrm{I}}$ in regime I. The well-defined spin winding direction in regime I, responsible for the SC form of the non-equilibrium spin polarisation [Eq. (4.42)], automatically implies a large ISGE in the dilute limit. As we show later, in the regime $|\epsilon| > 2\lambda$ the CSC tends to diminish due to opposite contributions from the two bands with counter-rotating spin textures (see Fig. 4.2). However we will show below that the efficiency only exhibits an *algebraic* decay law with the Fermi energy, enabling a remarkably robust ISGE in typical experimental conditions.

Quantum treatment

To evaluate the full energy dependence of the ISGE, we generalise the self-consistent diagrammatic approach developed in Ref. [159], to incorporate SO coupling non-perturbatively at all orders, and solving the BS equations for the renormalised vertex in T-matrix ladder approximation. This will provide us with exact results in the limit $\epsilon\,\tau \sim k_F v_F \tau_* \gg 1$. The leading-order and zero-temperature spin density–charge current response function we are interested in (A/R sectors of type I contribution) reads as a modification of the spin Hall response in Eq. (4.11) with $\mathcal{J}^z_y \to S_y = s_y/2$, i.e.

$$\chi_{yx}\,(\omega = 0) = \frac{1}{2\pi\Omega} \langle \mathrm{Tr} \left[S_y \, G^R \, J_x \, G^A \right] \rangle_{\mathrm{dis}} \,. \tag{4.45}$$

For practical purposes, we consider the model of short-range scalar impurities, Eq. (3.19), used above. This choice will enable us to establish key analytical results across weak (Born) and strong (unitary) scattering regimes by treating disorder at T-matrix level.

The self-energy is given by [cf. Eq. (3.20)]

$$\Sigma^a = n_i \, \mathrm{T}^a = \frac{1}{u_0^{-1} - g_0^a} \,, \tag{4.46}$$

where g_0^a is given by Eq. (3.22). Neglecting the real part of Σ^a which can be shown not to enter the leading order response, we can formally write Eq. (3.33) as

$$\Sigma^{\pm} = \mp \imath n_i \left(\eta_0 \gamma_0 + \eta_{zz} \, \gamma_{zz} + \eta_r \, \gamma_r \right) \,, \tag{4.47}$$

with the explicit form of the parameters in the latter equation reported in Eqs. (3.41)-(3.42). The rich matrix structure in Eq. (4.47) stems from the chiral (pseudospin) character of quasiparticles. In contrast, in the 2DEG with Rashba SO interaction, the self-energy due to spin-independent impurities is a scalar function across all regimes [202]. We take the disorder averaged Green's functions consistently with the T-matrix approximation, as obtained previously, with the associ-

ated analytical continuation prescription (see Eq. (B.5)). The last step consists of evaluating the vertex corrections. The renormalised charge current vertex satisfies the following BS equation

$$\tilde{v}_x = v_x + n_i \int \frac{d\mathbf{k}}{(2\pi)^2} \left\{ \mathrm{T}^R \, \mathcal{G}^R_{\mathbf{k}} \, \tilde{v}_x \, \mathcal{G}^A_{\mathbf{k}} \, \mathrm{T}^A \right\} . \tag{4.48}$$

The infinite set of noncrossing diagrams generated by the T-matrix ladder describes incoherent multiple scattering events *at all orders* in the scattering strength u_0 (Fig. 2.4), yielding an accurate description of SO-coupled transport phenomena in the dilute regime [159]. Exploring the properties of the Clifford algebra, one can show that the nonzero vertex components have a one-to-one correspondence to their associated non-equilibrium response functions [170], similarly to what was presented in the Gaussian approximation Eqs. (4.33)-(4.34). This allows us to express χ_{yx} in terms of the spin density component *only*, $\tilde{v}^{0y}_x$, i.e., $\chi_{yx} = F_s(u_0)\, \tilde{v}^{0y}_x$, where

$$\tilde{v}^{0y}_x = -\frac{v}{\epsilon} \frac{\epsilon^2 \left(\epsilon + 2\lambda\right) + \theta(\epsilon - 2\lambda) \left(8\lambda^3 - \epsilon^3\right)}{\epsilon^2 + 4\lambda^2} + \varepsilon_\Lambda . \tag{4.49}$$

Here, ε_Λ is a weak correction logarithmic in the ultraviolet cutoff Λ set by the inverse of the lattice scale [160]. Finally, $F_s(u_0)$ is a complicated function, which in the Gaussian and unitary scattering limits takes the form

$$F_s(u_0) = \frac{1}{2\pi n_i} \times \begin{cases} \frac{4}{u_0^2} & , |g^R_0 u_0| \ll 1 \\ \left(\frac{\epsilon}{2\pi v^2} \ln \left| \frac{\Lambda^2}{\epsilon \sqrt{\epsilon^2 - 4\lambda^2}} \right| \right)^2 & , |u_0| \to \infty \end{cases} \tag{4.50}$$

respectively.

Analogously, we can determine the expression for the charge conductivity $\sigma_{xx} = F_c(u_0)\tilde{v}^{x0}_x$, with $\tilde{v}^{x0}_x$. We can finally write the CSC rate as

$$\frac{2v|\chi_{yx}|}{\sigma_{xx}} = \theta(2\lambda - \epsilon) + \frac{2\lambda}{\epsilon} g(u_0, \epsilon)\, \theta(\epsilon - 2\lambda) , \tag{4.51}$$

where $g(u_0, \epsilon = 2\lambda) = 1$ and deviates only slightly from this value when u_0 is large and for $\epsilon > 2\lambda$ [see Fig. 4.2(d)]. The central result Eq. (4.51) puts our earlier SC argument on firm grounds, and shows that the CSC is slightly affected by the disorder strength outside the Rashba pseudogap.

Impact of random spin–orbit coupling

We finally comment on the rippling of the graphene surface and imperfections which can cause local variations in the Rashba pseudogap [203–205]. Inhomogeneities in the SO energy scales can be important even in samples with strong interfacial effect [190]. We analyse here the impact of *random* Rashba fields on the CSC efficiency. In graphene without proximity SO, random Rashba fields lead to current-driven spin polarisation via asymmetric spin precession [172]. In graphene on TMDs, small fluctuations in the Rashba coupling ($|\lambda(\mathbf{x}) - \lambda| \ll \lambda$) cannot disturb the spin helicity of eigenstates. This directly implies that the CSC rate in regime I remains unaffected. To investigate the impact of random SO coupling in regime II, we model it as short-range disorder potential with Rashba matrix structure:

$$V_{\mathrm{RRF}}\left(\mathbf{x}\right) = u_r \gamma_r \sum_{i=1}^{N} \delta\left(\mathbf{x} - \mathbf{x}_i\right) , \tag{4.52}$$

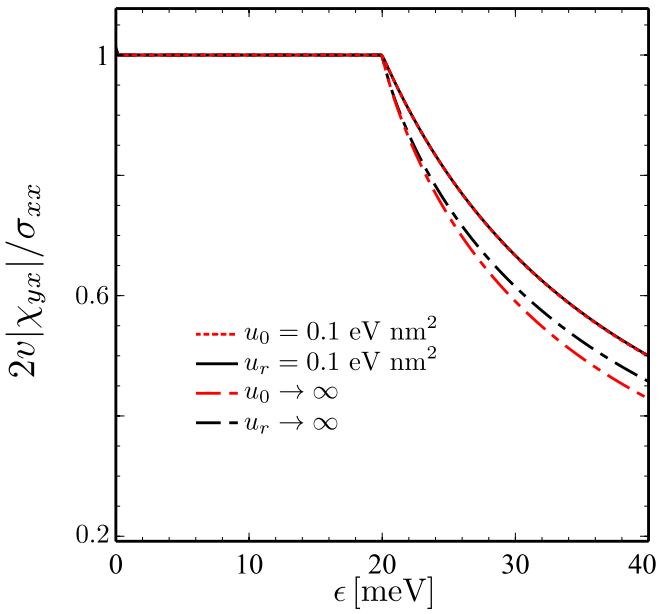

Figure 4.3: Comparison between pure scalar (u_0) and pure Rashba disorder (u_r). We set $\lambda = 10$ meV. While in the weak scattering limit the results coincide, Rashba impurities manifest their impact more clearly in the unitary limit. However, even in this case, the impact is very small and the spin susceptibility is dominated by the uniform Rashba term.

Neglecting its real part, the self-energy Σ^a preserves the structure of Eq. (3.33)

$$\Sigma^{R,A}(\epsilon) = \mp \imath\, n_i \left(\eta_0(\epsilon)\gamma_0 + \eta_{zz}(\epsilon)\,\gamma_{zz} + \eta_r(\epsilon)\,\gamma_r\right) , \tag{4.53}$$

with the specific form of the parameters ($\epsilon > 0$)

$$\begin{cases} \eta_0(\epsilon) = -\eta_r(\epsilon) = \frac{u_r^2}{2v^2}\epsilon\,, \eta_r(\epsilon) = 0\,, & \epsilon > 2\lambda \\ \eta_0(\epsilon) = -\eta_r(\epsilon) = -\eta_3(\epsilon) = \frac{u_r^2}{4v^2}\epsilon\,, & \epsilon \leq 2\lambda \end{cases} . \tag{4.54}$$

We find that at leading order in the impurity areal density, Eq. (4.51) still holds with a slightly different functional form for $g\,(u_r, \epsilon)$. In Fig. 4.3 we plot the ratio $|\chi_{yx}|/\sigma_{xx}$ for Rashba-like and scalar impurities. As considered above, the CSC ratio in the two cases is virtually identical in the Born scattering regime. This confirms that as long as the proximity effect is well developed in the band structure of graphene, the CSC mechanism is robust against random fluctuations in the energy scales of the model.

Conservation laws: connection of the large inverse spin Galvanic effect to the vanishing spin Hall effect

To conclude this Chapter, we would like to highlight the connection of the *vanishing* SHE in the Dirac-Rashba systems to the *large* ISGE. We show that they have a common stem in the $SU(2)$-conservation laws of the model we have discussed in this Chapter. To simplify the presentation here we restrict our focus to the Gaussian case, although a similar result can be obtained within the T-matrix approach, following the same steps.

Let us revisit the conservation law (equation of motion) Eq. (4.6), which here we rewrite

directly for the homogeneous case

$$\partial_t S_y = \frac{2\lambda}{v} J_y^z \,. \tag{4.55}$$

Also we make use of Eq. (4.33), which relates the spin Hall response directly to the associated component of the renormalised charge vertex, and the corresponding equation for out-of-equilibrium spin polarisation

$$J_y^z = \sigma_{\rm SH}\mathcal{E}_x = \frac{1}{2\pi}\left(\frac{2\,v}{n_i\,u_0^2}\right)\tilde{v}_x^{yz}\mathcal{E}_x\,, \tag{4.56}$$

$$S_y = \chi_{yx}\mathcal{E}_x = \frac{1}{2\pi}\left(\frac{2}{n_i\,u_0^2}\right)\tilde{v}_x^{0y}\mathcal{E}_x \tag{4.57}$$

Considering the BS equation in the Gaussian approximation for $\tilde{v}_x$ Eq. (4.29), by defining $M_{\mu a\rho d} \equiv Y^{\nu b\lambda c}_{\mu a\rho d}\, I_{\nu b\lambda c}$, we have

$$\tilde{v}_x^{yz} = M_{yz\rho d}\tilde{v}_x^{\rho d} = M_{yzx0}\tilde{v}_x^{x0} + M_{yz0y}\tilde{v}_x^{0y} + + M_{yzyz}\tilde{v}_x^{yz} + + M_{yzzx}\tilde{v}_x^{zx}\,. \tag{4.58}$$

We can now neglect the terms proportional to $\tilde{v}_x^{yz}, \tilde{v}_x^{zx}$ as the associated coefficient can be shown, by direct inspection, to contribute at next order in the parameter $\epsilon\,\tau \gg 1$ [169]. Therefore we have

$$\tilde{v}_x^{yz} = M_{yzx0}\tilde{v}_x^{x0} + M_{yz0y}\tilde{v}_x^{0y}\,, \tag{4.59}$$

which substituted in Eq. (4.56) gives

$$J_y^z = \frac{1}{2\pi}\frac{2\,v}{n_i\,u_0^2}(M_{yzx0}\tilde{v}_x^{x0} + M_{yz0y}\tilde{v}_x^{0y})\mathcal{E}_x \tag{4.60}$$

$$= \frac{1}{2\pi}\frac{2\,v}{n_i\,u_0^2}M_{yzx0}\tilde{v}_x^{x0}\mathcal{E}_x + vM_{yz0y}S_y\,, \tag{4.61}$$

where we have exploited Eq. (4.57). From the latter equation we have

$$S_y = \frac{1}{2\pi v}\frac{2}{n_i\,u_0^2}\frac{1}{M_{yz0y}}(v\tilde{v}_x^{x0}\mathcal{E}_x - J_y^z)\,. \tag{4.62}$$

The first term in the latter equation, which contains $\tilde{v}_x^{x0}$ is the part proportional to $J_x = \sigma_{xx}\mathcal{E}_x$ [see Eq. (4.34)]. Given that (in the correct units) the spin signal—being obtained by means of the CSC mechanism—cannot exceed the charge current, it follows from Eq. (4.62) that $J_y^z \geq 0$. The *optimal* out-of-equilibrium spin polarisation along $\hat{y}$ is obtained then when $J_y^z = 0$. We conclude that the two effects (the SHE and the ISGE) in this model are mutually determined: the vanishing SHE implies the largest possible ISGE.

Conclusions

In this Chapter we have studied the response to weak external perturbations of honeycomb layers described by the C_{6v} point group symmetry. By means of a diagrammatic approach for the charge conductivity and the spin susceptibility in the presence of dilute disorder, we have demonstrated how the resulting steady state in response to externally applied electric fields, is characterised by the absence of the SHE and the production of a robust ISGE. We have unveiled the underlying $SU(2)$ conservation laws of the theory, showing how the out-of-equilibrium phe-

nomena mentioned above can be understood within the framework of these exact symmetry relations.

The formalisms developed here sets the basis for the study of more realistic systems of honeycomb layers with broken sublattice symmetry (C_{3v} point symmetry group), which we tackle in the following Chapters of this thesis.

Chapter 5

Microscopic Theory of Spin Diffusion in Dirac Rashba Materials

Overview

In the previous Chapter we have introduced the theory of SO-coupled transport in graphene with uniform Rashba SO coupling, focusing on the nonequilibrium phenomena in the *DC limit*. To recapitulate, it was shown that disorder-induced corrections exactly balance the intrinsic generation of a spin Hall current[1] $\langle J_{\rm SH}\rangle_{\boldsymbol{\mathcal{E}}} = 0$, where $\boldsymbol{\mathcal{E}}$ is the external DC electric field [169]. The vanishing of the SHE in the pure Rashba model was connected to the establishment of a robust nonequilibrium in-plane spin polarisation $\langle \mathbf{S}\rangle_{\boldsymbol{\mathcal{E}}} \neq 0$ with $\mathbf{S}\perp\boldsymbol{\mathcal{E}}$, i.e. the large ISGE [170]. In this Chapter we develop a *time-dependent* framework to unveil how the steady state of the 2D Dirac-Rashba model described in the previous Chapter is reached, and capturing in particular charge-to-spin interconversion rates and SRTs.

This topic is of particular interest in the light of recent developments in graphene/TMD heterostructures. Understanding the microscopic origin and the magnitude of the SRTs in such materials is clearly a problem of central importance; however the breaking of inversion symmetry in honeycomb layers couples different *SU(2)* subspaces [spin and sublattice, see Eq. (3.1)], making the determination of the SRTs a challenging task. In fact, the identification of the main source of the relatively fast spin relaxation in graphene samples with high-mobility has been a controversial puzzle for many years [206]. Hanle precession measurements found a large spread in τ_s from tens of picoseconds up to a few nanoseconds [75, 207–216] (see also Fig. 5.1), reflecting the different sample preparation and device fabrication methods. On the other hand early theoretical estimates hinted at ultra-long spin lifetime in graphene ($\tau_s \approx 1$–$100\,\mu$s), mainly due to weak hyperfine interactions and intrinsic SO coupling [218]. To resolve this discrepancy, theoretical studies have explored a number of possible spin relaxation sources, including magnetic impurities, SO-active adatoms, ripples and other substrate effects [105, 219–225]. Numerical approaches have provided further insight into the relaxation mechanisms, enriching the scenario to include the impact of electron-hole puddles and pseudospin-spin coherence near the Dirac point [226, 227].

Extending previous theoretical descriptions of spin relaxation based on SC approximations [228, 229], we derive here the coupled spin-charge drift-diffusion equations for nonmagnetic disorder and generic homogeneous perturbations by means of the diagrammatic technique for

[1] The statement is true for spin-independent disorder.

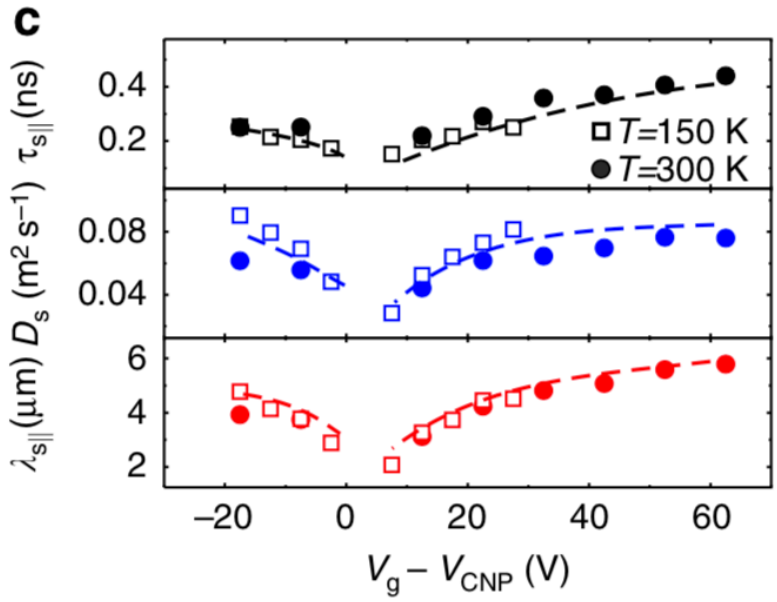

Figure 5.1: In-plane SRT $\tau_s^{\|}$, spin-diffusion coefficient D_s and spin-relaxation length $\lambda_s^{\|}$ in pristine graphene, obtained from the spin precession measurements (Hanle) in Ref. [217]. The SRT is found at room temperature ~$0.1 - 0.5$ ns, with a characteristic V-shape as a function of the gate potential, with a minimum at the Dirac point $V_{\rm CNP}$ (Figure from Ref. [217]).

disordered electrons. Such a FQM treatment able to capture self-consistently CSC effects and SRTs in graphene induced by both uniform and random SO coupling, is still overdue. We note that a similar approach has been adopted very recently in the context of 2DEGs with both Rashba and Dresselhaus interactions [45], where it was shown perfect agreement between the Kubo diagrammatic formalism and the Keldysh theory [230]. Here, we focus on the C_{6v} 2D Dirac-Rashba model Eq. (3.1), as being a paradigmatic model for studies of spin relaxation in graphene. We extend the standard quantum diagrammatic formalism to accommodate the enlarged 2 (spin) $\otimes$ 2 (pseudospin) Clifford structure of the 2D Dirac–Rashba model. This leads to a 16-dimensional diffuson operator in the absence of intervalley scattering. We find that the typical DP relation connecting the SRT and the momentum lifetime in the weak SO coupling regime, that is $\tau_s \propto \tau^{-1}$ for $\lambda\tau \ll 1$ holds at all orders in the scattering potential strength. In particular, we provide the analytical expression of τ_s in the unitary limit of very strong potential scattering. We finally show that the meaning and interpretation of our results for the SRTs can be also clarified by the $SU(2)$ covariant conservation laws inherent to the diagrammatic structure.

Microscopic linear response theory for spin relaxation

General formalism

Our starting point is the Dirac-Rashba Hamiltonian of Eq. (3.1) supplemented by a impurity potential of the form Eq. (3.19). The corresponding bare (disorder-averaged) Green's functions $G^a_{0\mathbf{k}}$ ($\mathcal{G}^a_{\mathbf{k}}$) are reported in Eq. (3.14) [and full disordered form in (B.12)].

Let us consider a generic external perturbation of the type

$$H^{\rm ext}_{\alpha\beta}(\mathbf{x},t) = -\mathcal{J}_{\alpha\beta}\mathcal{A}_{\alpha\beta}(\mathbf{x},t)\,, \tag{5.1}$$

where $\mathcal{J}_{\alpha\beta} \propto \sigma_\alpha s_\beta$ ($\alpha, \beta = 0, i$) is the current density operator ($\alpha = x, y$) or density operator ($\alpha = 0, z$) and $\mathcal{A}_{\alpha\beta}$ is a generalised vector potential [169]. We will consider in detail two important cases: (i) an electric field perturbation *e.g.*, $H^{\rm ext}_{x0}(\mathbf{x}, t) = -v\sigma_x s_0 A_x(\mathbf{x}, t)$ and (ii) a spin density fluctuation $H^{\rm ext}_{0i}(\mathbf{x}, t) = -\frac{1}{2}\sigma_0 s_i B_i(\mathbf{x}, t)$. The induced spin polarisation density

$$S_i(\mathbf{x}, t) = \frac{1}{2}\langle \Psi^\dagger(\mathbf{x}, t)\, \sigma_0 s_i\, \Psi(\mathbf{x}, t)\rangle\,, \tag{5.2}$$

is evaluated within the framework of the linear response theory. This approach has been applied to derive charge–spin diffusion equations describing spin dynamics and magnetoelectric effects in 2DEGs [45, 231, 232]. As shown below, a suitable extension of this approach to accommodate the enlarged (spin $\otimes$ pseudospin) Clifford algebra $\gamma_{\alpha\beta} = \sigma_\alpha s_\beta$ will allow us to obtain a rigorous microscopic theory of diffusive transport and spin relaxation for 2D Dirac materials.

The linear response of the i-component of the spin polarisation vector at zero temperature reads as

$$S_i(\mathbf{x}, t) = -\int d\mathbf{x}' \int_{-\infty}^{\infty} dt'\, \chi_{i,\alpha\beta}(\mathbf{x} - \mathbf{x}', t - t')\, \partial_{t'} \mathcal{A}_{\alpha\beta}(\mathbf{x}', t')\,, \tag{5.3}$$

where $\chi_{i,\alpha\beta}(\mathbf{x} - \mathbf{x}', t - t')$ is the generalised spin susceptibility associated to the external perturbation *i.e.*, an electric field $\mathcal{E}_x(\mathbf{x}, t) = -\partial_t A_x(\mathbf{x}, t)$ or a 'spin injection field' $\phi_i(\mathbf{x}, t) = -\partial_t B_i(\mathbf{x}, t)$ [233]. Expressing the response function in Fourier space, in the long-wavelength limit $\mathbf{q} \to 0$ we have the type of structure for the response function encountered before [cf. Eq. (4.45)]

$$\chi_{i,\alpha\beta}(0, \omega) = \frac{c}{2} \lim_{\mathbf{q}\to 0} \int \frac{d(\mathbf{x} - \mathbf{x}')}{(2\pi)^2}\, e^{-\imath(\mathbf{x}-\mathbf{x}')\mathbf{q}} \left[\mathrm{Tr} \left\langle \gamma_{0i}\, G^R(\mathbf{x}, \mathbf{x}'; \epsilon + \omega)\, \gamma_{\alpha\beta}\, G^A(\mathbf{x}', \mathbf{x}; \epsilon) \right\rangle_{\rm dis} \right]\,, \tag{5.4}$$

where $c = v$ ($c = 1/2$) for a electric (spin injection) field and Tr is the trace over all DOFs. $\chi_{i,\alpha\beta}$ above describes the spin dynamics generated by uniform perturbation. The SRTs are encoded in the singularities of this response function. As we show below, owning to the unique Dirac structure of the theory, this response function already contains all the information about CSC and SRTs, differently from the 2DEG where charge/spin coupling can only be captured for $\mathbf{q} \neq 0$ [231, 232]. This motivates our choice to consider uniform perturbations from the outset, as we discuss in greater detail below. Note that terms involving products of Green's functions on the same sector (RR and AA) are smaller by a factor of $(\epsilon\tau)^{-1}$ and thus can be safely neglected [see discussion after Eq. (2.32)].

The disorder average in Eq. (5.4) is evaluated by means of the diagrammatic technique introduced in Chapter 2 (Fig. 5.2, cf. Figs. 2.3-2.4). For brevity of notation, we first present the formalism within the Gaussian approximation for the self-energy, Eqs. (3.35)-(3.40). In Sec. 5, we provide the connection with the full T-matrix result. We point out that we will restrict our focus here to diffusive systems with weak SO coupling $\lambda\tau \ll 1$ and $\epsilon \gg \lambda$.

A summation of noncrossing two-particle (ladder) diagrams leads to the type of formula used before, with renormalised Green's functions and a dressed vertex

$$\chi^{(\rm NC)}_{i,\alpha\beta}(0, \omega) = \frac{\kappa}{2} \sum_{\mathbf{k}} \mathrm{tr} \left\{ \gamma_{0i}\, \mathcal{G}^R_{\mathbf{k}}(\epsilon + \omega)\, \tilde{\gamma}_{\alpha\beta}(\omega)\, \mathcal{G}^A_{\mathbf{k}}(\epsilon) \right\}\,, \tag{5.5}$$

where tr is the trace over internal DOF (spin and sublattice). The dressed vertex $\tilde{\gamma}_{\alpha\beta}$ satisfies the BS equation

$$\tilde{\gamma}_{\alpha\beta}(\omega) = \gamma_{\alpha\beta} + \frac{4}{2\pi\tau N_0} \sum_{\mathbf{k}} \mathcal{G}^R_{\mathbf{k}}(\epsilon + \omega)\, \tilde{\gamma}_{\alpha\beta}(\omega)\, \mathcal{G}^A_{\mathbf{k}}(\epsilon)\,, \tag{5.6}$$

where $N_0 \equiv \epsilon/\pi v^2$ (for the T-matrix extension see Eq. (5.40) and text therein). Projecting onto

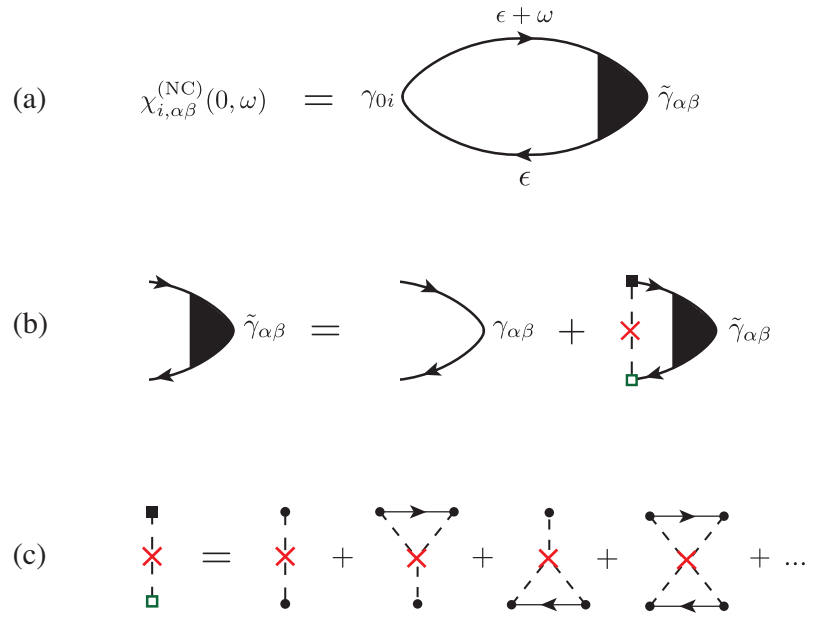

Figure 5.2: Diagrammatic technique for evaluation of generalised spin susceptibilities (cf. Figs. 2.3-2.4). (a) Two-particle ladder diagram. (b) BS equation for the vertex renormalisation. (c) Skeleton expansion of the ladder diagram in terms of an infinite series of two-particle, noncrossing diagrams. Full (open) square denotes a T($T^\dagger$) matrix insertion.

the elements of the Clifford algebra

$$\tilde{\gamma}_{\alpha\beta\varrho\varsigma}(\omega) = \frac{1}{4}\mathrm{tr}[\tilde{\gamma}_{\alpha\beta}(\omega)\,\sigma_\varrho s_\varsigma]\,, \tag{5.7}$$

we recast the BS equation into the form

$$\tilde{\gamma}_{\alpha\beta\varrho\varsigma}(\omega) = \delta_{\alpha\varrho}\delta_{\beta\varsigma} + \sum_{\mu,\nu=0,x,y,z} M_{\mu\nu\varrho\varsigma}(\omega)\tilde{\gamma}_{\alpha\beta\mu\nu}(\omega)\,, \tag{5.8}$$

where

$$M_{\mu\nu\varrho\varsigma}(\omega) = \frac{1}{2\pi\tau N_0}\sum_{\mathbf{k}}\mathrm{tr}\left[\mathcal{G}^R_{\mathbf{k}}(\epsilon+\omega)\gamma_{\mu\nu}\mathcal{G}^A_{\mathbf{k}}(\epsilon)\gamma_{\varrho\varsigma}\right]\,. \tag{5.9}$$

Introducing the 16-dimensional vectors

$$\tilde{\gamma}_{\alpha\beta}(\omega) = (\tilde{\gamma}_{\alpha\beta00}(\omega),...,\tilde{\gamma}_{\alpha\beta zz}(\omega))^{\mathrm{t}}\,, \tag{5.10}$$

$$\gamma_{\alpha\beta} = (0,0,....,\gamma_{\alpha\beta\alpha\beta},...,0)^{\mathrm{t}}\,, \tag{5.11}$$

a more compact matrix form for Eq. (5.6) is given in terms of the *diffuson operator* $\mathcal{D}^{-1}$ as

$$\mathcal{D}^{-1}\tilde{\gamma}_{\alpha\beta}(\omega) \equiv (\mathbf{1}_{16\times16} - M^{\mathrm{t}}(\omega))\tilde{\gamma}_{\alpha\beta}(\omega) = \gamma_{\alpha\beta}\,. \tag{5.12}$$

The spin relaxation rates are simply identified as the poles of the generalised susceptibility in the complex ω-plane. The determination of the SRTs is thus reduced to the analysis of the behaviour of $\mathcal{D}^{-1} = \mathcal{D}^{-1}(\omega)$ [136].

The formal result Eq. (5.12) deserves a few comments. Firstly, $\mathcal{D}^{-1}$ spans in principle the entire Clifford algebra, which physically encodes the coupled dynamics of spin and other observables associated with the elements $\gamma_{\alpha\beta}$. However, by exploiting symmetries, $\mathcal{D}^{-1}$ can be

reduced into block diagonal form, such that only some observables are coupled to the spin polarisation along the three spatial directions. Secondly, a distinct feature of Dirac systems is that spin densities are coupled to charge currents even in the case (considered here) of spatially uniform external perturbations $\mathbf{q}$=0. The linear Dirac dispersion of graphene is reflected in the form of the charge current $J_i = v\,\sigma_i$ and spin current $\mathcal{J}_i^a = v\,\sigma_i s_a/2$ vertices, which do not depend explicitly on momentum; by virtue of that they can be directly identified (apart from constants) as elements of the Clifford algebra. Therefore all the relevant information about coupling between currents and densities *is built-in* to the 16×16 diffusion operator Eq. (5.12) in our formalism. This will allows us to obtain a unified description of both nonequilibrium spin dynamics and relativistic transport phenomena within our $\mathbf{q}$=0 formalism. We analyse the implications below.

The coupling of the electrons' spin to currents or other observables in the long wavelength limit also suggests two equivalent scenarios to study spin relaxation. The first natural choice is to consider spin injection and investigate the relaxation of the spin density profile (density–density response); alternatively, one can probe the spin response indirectly by exciting an observable coupled to the spin density through $\mathcal{D}^{-1}$. For instance, as we have already seen, one can drive a charge current via application of an electric field to obtain a in-plane spin polarisation of carriers (ISGE). In that case, the information about the in-plane SRTs is readily accessible by examining how the steady state (Edelstein) polarisation is achieved (density–current response).

Before moving on, let us remind that within the Gaussian approximation, a useful relation can be derived connecting the generalised susceptibility Eq. (5.5) and the renormalised vertex

$$\chi^{(\mathrm{NC})}_{i,\alpha\beta}(0,\omega) = \frac{c}{2\Gamma}\sum_{\mu\nu} M_{\mu\nu 0i}(\omega)\tilde{\gamma}_{\alpha\beta\mu\nu}(\omega) = \frac{c}{2\Gamma}\left(\tilde{\gamma}_{\alpha\beta 0i}(\omega) - \delta_{\alpha 0}\delta_{\beta i}\right)\,, \tag{5.13}$$

where $\Gamma \equiv (2\pi\tau N_0)^{-1}$ and we have used Eq. (5.8). The above equation states the spin response can be *solely* obtained from the associated component of the renormalised vertex $\tilde{\gamma}_{\alpha\beta 0i}$. A similar relation holds for other response functions, see Eqs. (4.33)-(4.34). Therefore Eq. (5.13) and similar relations allow one to identify the components of a renormalised vertex with the associated observables, and will turn useful in the following.

In Eq. (4.32) we made explicit the structure of the renormalised charge vertex, chosen along $\hat{x}$, which—beyond the expected velocity renormalisation—was found to have nonzero components along additional matrix structures. Those additional terms encode all the possible responses of the system to the application of an electric field along $\hat{x}$, such as the ISGE (associated to matrix structure $\sigma_0 s_y \equiv \gamma_{0y}$). Due to Onsager reciprocity, one expects a similar structure to Eq. (4.32) for the renormalised *spin density* vertex along $\hat{y}$: $\tilde{\gamma}_{0y}/2$, which guarantees that inverse CSC phenomena are also captured, e.g. the *direct* SGE $S_y \to J_x$. The different couplings amongst the various operator associated to physical observables can be in fact captured by exploring symmetry arguments. We want to show this here, generalising the discussion to all spin polarisations $S_{x,y,z}$. The model of Eq. (3.1) is invariant under the group $C_{\infty v}$, which is an emergent symmetry of the continuum (long-wavelength) theory. As rotations in the continuum do not describe the sublattice symmetry $A \leftrightarrow B$ of the graphene system, a representation O for the relevant set of discrete operations has to be considered. Relevant to us are C_2, the rotation of π around the $\hat{z}$-axis exchanging sublattice (and valleys), and R_x, the reflection over the $\hat{x}$-axis. We have

$$O(C_2) = \tau_x s_z\,, \tag{5.14}$$

$$O(R_x) = \tau_z \sigma_x s_y r_x, \tag{5.15}$$

with $r_x : (\mathbf{x},\mathbf{y}) \to (\mathbf{x},-\mathbf{y})$ and we recall $\tau_{i=x,y,z}$ are Pauli matrices acting on the valley DOF. We

also make use of isospin rotations $\Lambda_{x,y,z}$ [173, 234]

$$\Lambda_{x,y} = \tau_{x,y}\sigma_z\,, \tag{5.16}$$

$$\Lambda_z = \tau_z\,. \tag{5.17}$$

For scalar disorder, as no additional matrix structures are generated compared to the ordered case, it suffices to examine the form of the clean-system susceptibility at $\omega = 0$

$$\chi^{RA,\text{clean}}_{i,\alpha\beta} \equiv \frac{1}{4}\text{Tr}\left[\gamma_{0i}\, G^R_0(\epsilon)\, \gamma_{\alpha\beta}\, G^A_0(\epsilon)\right]. \tag{5.18}$$

For any of the symmetries $\mathcal{S}$ listed above, we have $\mathcal{S}^{-1}G^{R/A}_0\mathcal{S} = G^{R/A}_0$, and inserting resolutions of the identity in the form $\mathcal{S}^\dagger\mathcal{S}$ into Eq. (5.18) we find

$$\chi^{RA,\text{clean}}_{i,\alpha\beta} = \frac{p_{\alpha\beta}p_{0i}}{4}\text{Tr}\left[\gamma_{0i}\, G^R_0(\epsilon)\gamma_{\alpha\beta}\, G^A_0(\epsilon)\right] = p_{\alpha\beta}p_{0i}\,\chi^{RA,\text{clean}}_{i,\alpha\beta}\,, \tag{5.19}$$

where $p_{\alpha\beta}(p_{0i}) = \pm 1$ is the parity of $\gamma_{\alpha\beta}(\gamma_{0i})$ under $\mathcal{S}$. From this result, we see that a nonzero response requires the operator $\gamma_{\alpha\beta}$ to have the same parity of the spin vertex under the action of any of $\mathcal{S}$. The allowed couplings and parities under $\mathcal{S}$ are shown in the Tab. 5.1. As anticipated above, the in-plane components $S_{x(y)}$ are coupled to orthogonal charge currents $\sigma_{y(x)}$, as well as spin Hall currents $\gamma_{xz}(\gamma_{yz})$ and staggered magnetisations $\gamma_{zy}(\gamma_{zx})$ [169, 170]. The out-of-plane component S_z is instead coupled to a mass term σ_z and in-plane spin currents γ_{xx}, γ_{yy}.

Polarisation	C_2	R_x	$\Lambda_{x,y,z}$	Couplings
S_x	-1	-1	+1	σ_y, γ_{xz}, γ_{zy}
S_y	-1	+1	+1	σ_x, γ_{yz}, γ_{zx}
S_z	+1	-1	+1	σ_z, γ_{xx}, γ_{yy}

Table 5.1: Table summarising the allowed couplings to the spin polarisation in the 2D Dirac–Rashba model with nonmagnetic scalar disorder.

Diffusive equations and spin relaxation times

In the following, we choose to consider the in-plane spin response to an AC electric field $H^{\text{ext}}_\parallel = -v\sigma_i A_i(\omega) = -(i\omega)^{-1}v\sigma_i\mathcal{E}_i(\omega)$, $i = x, y$. This choice, as discussed above, is equivalent to considering in-plane spin injection, but has the advantage to allow for a unified description of spin dynamics and charge-spin interconversion, e.g. to capture the ISGE or other similar effects [36, 235]. For the out-of-plane spin dynamics, we take a spin-density perturbation $H^{\text{ext}}_\perp = \frac{1}{2}s_z B_z(\omega)$ (see Tab. 5.1).

In-plane spin dynamics

Without loss of generality, let us consider the dynamics of the $\hat{y}$ polarization. According to Tab. 5.1, s_y is coupled to three operators: σ_x, $\sigma_y s_z$ and $\sigma_z s_x$. However, leading terms in the $(\epsilon\tau)^{-1}$ expansion are only contained in the s_y/σ_x sub-block. Hence, to capture the SRTs it suffices to restrict the focus to this 2×2 algebra. As anticipated above, we consider here the response to an AC electric field $\mathcal{E}_x(\omega)$, associated with the vertex $c\gamma_{x0} = v\sigma_x \equiv v_x$ (details of the calculation and the full form of the 4×4 diffuson operator are reported in Ref. [236]). To capture purely diffusive

processes, we expand $\mathcal{D}^{-1}(\omega)$ in the low-frequency and small SO coupling limits, $\omega\tau \ll 1$ and $\lambda\tau \ll 1$, respectively. In this regime, Eq. (5.12) is written then as

$$\begin{pmatrix} \frac{1}{2}(1-\imath\omega\tau) & \frac{\lambda}{\epsilon}\Gamma_s(1+3\imath\omega\tau) \\ \frac{\lambda}{\epsilon}\Gamma_s(1+3\imath\omega\tau) & \Gamma_s - \imath\omega\tau \end{pmatrix} \begin{pmatrix} \tilde{\gamma}_{x0x0} \\ \tilde{\gamma}_{x00y} \end{pmatrix} = \begin{pmatrix} 1 \\ 0 \end{pmatrix}, \tag{5.20}$$

where $\Gamma_s = \tau/\tau_s = 2\lambda^2\tau$. In light of the previous discussion below Eq. (5.13), $\tilde{v}_{x0}$ and $\tilde{v}_{0y}$ are connected by a linear transformation to the steady-state charge current and the spin polarisation.

Off-diagonal elements of Eq. (5.20) carry in relation to diagonal ones an extra order of smallness λ/ϵ, suggesting spin and charge to be weakly coupled in this limit. Their inclusion however encodes charge-to-spin interconversion and it is essential to get a correct physical description. The eigenvalues $-\imath\omega_\pm$ of the matrix in Eq. (5.20) are found as

$$-\imath\omega_+ \simeq \frac{1}{\tau}\left(1+16\frac{\Gamma_s^3}{\epsilon^2\tau}\right), \tag{5.21}$$

$$-\imath\omega_- \simeq \frac{1}{\tau_s}\left(1-\frac{\Gamma_s^3}{\epsilon^2\tau}\right), \tag{5.22}$$

and can be associated with charge current and SRTs, respectively. We see then the SRT can be identified as the mass ($\omega = 0$) term of the spin-spin part of the diffuson

$$\frac{1}{\tau_s} \equiv \frac{1}{\tau_s^{\parallel}} \simeq 1 - M_{0y0y}(\omega=0) \simeq 2\lambda^2\tau\,. \tag{5.23}$$

Inverting Eq. (5.20), we find

$$\tilde{\gamma}_{x0x0} \simeq \frac{1}{\tau}\frac{2}{-\imath\omega+\frac{1}{\tau}}, \tag{5.24}$$

$$\tilde{\gamma}_{x00y} \simeq 2\frac{\lambda}{\epsilon}\frac{1}{\tau}\frac{\Gamma_s}{-\imath\omega+\frac{\Gamma_s}{\tau}}, \tag{5.25}$$

from which, by using Eq. (5.13) and the corresponding relation for the charge-current component, upon Fourier transform, to derive the diffusive equation of motion for coupled charge-spin dynamics as

$$\partial_t J_x(t) = -\frac{1}{2\tau}(J_x(t) - J_x^0(t))\,, \tag{5.26}$$

$$\partial_t S_y(t) = -\frac{1}{\tau_s^{\parallel}}(S_y(t) - S_y^0(t))\,, \tag{5.27}$$

where $J_x^0(t) \equiv 2v^2\mathcal{E}_x(t)/\Gamma$ and $S_y^0(t) \equiv -\lambda\mathcal{E}_x(t)/\epsilon\alpha$. Note that charge current relaxation is regulated by the transport time $\tau_{\rm tr} \equiv 2\tau$, indicating the absence of backscattering for scalar impurities [237, 238].

Out-of-plane spin dynamics

For the out-of-plane spin dynamics we consider the renormalised vertex $c\tilde{\gamma}_{0z} = \frac{1}{2}\tilde{s}_z$. The off diagonal components of the associated 4×4 diffuson block contains sub-leading terms in the $(\epsilon\tau)^{-1}$ expansion [236], such that the out-of-plane SRTs can be calculated similarly to Eq. (5.23) as

$$\frac{1}{\tau_s^{\perp}} \simeq 1 - M_{0z0z}(\omega) \simeq 4\lambda^2\tau\,. \tag{5.28}$$

The generalisation of the equations of motion Eqs. (5.26),(5.27) in this case is written as

$$\partial_t S_z(t) = -\frac{1}{\tau_s^{\perp}}(S_z(t) - S_z^0(t))\,, \tag{5.29}$$

where $S_z^0(t) = \dot{B}_z(t)/4\Gamma$ is the effect of the external perturbation (spin-injection field). The in-plane and out-of-plane SRTs are in the following relation

$$\frac{1}{\tau_s^{\parallel}} = \frac{1}{2}\frac{1}{\tau_s^{\perp}}\,, \tag{5.30}$$

which is nothing but the well-known DP ratio for 2DEGs [231]. The above result has also been obtained for graphene within the time-dependent perturbation theory for the density matrix [228]. The agreement between graphene and the Rashba 2DEG results is expected at high electronic density $\epsilon \gg \lambda$.

Obtaining the spin relaxation times from the conservation laws in the DC limit

In this section, we demonstrate how the SRTs we have obtained above can be equivalently extracted in the *static limit* $\omega = 0$. This remarkable result is rooted in the conservation laws associated to the disordered Dirac–Rashba Hamiltonian Eq. (4.8) [169]. Let us re-write here the Heisenberg equation of motion for the spin polarisation

$$\partial_t S_i = \imath[H, S_i] = \frac{2\lambda}{v}\epsilon_{lj}\,\epsilon^c_{li}\,J^c_j\,, \tag{5.31}$$

where $\epsilon_{lj}, \epsilon^c_{li}$ are the second and third rank Levi-Civita tensors and $J^c_j = \langle \mathcal{J}^c_j \rangle$ is the $\hat{j}$-component of the pure spin current (with polarisation "c"). As before, we consider an electric field applied along the $\hat{x}$ direction. We find

$$\partial_t S_y = \frac{2\lambda}{v} J^z_y\,, \tag{5.32}$$

where J^z_y is identified as the spin Hall current according to the chosen geometry. The spin Hall current is written in response to the electric field

$$J^z_y = \sigma^z_{yx}\mathcal{E}_x\,, \tag{5.33}$$

where σ^z_{yx} is the DC spin Hall conductivity calculated according to Eq. (5.5) with $\tilde{\gamma}_{0y} \to v\tilde{\gamma}_{yz}$. As for now no assumption has been made for the self-energy approximation associated to the scalar impurities field. Let us start from the more transparent Gaussian case. Using the corresponding version of Eq. (5.13) for σ^z_{yx} [i.e. Eq. (4.33)], together with Eq. (5.8) we have

$$\sigma^z_{yx} = \frac{v^2}{2\alpha}\tilde{\gamma}_{x0yz} = \frac{v^2}{2\Gamma}\left(M_{x0yz}\tilde{\gamma}_{x0x0} + M_{0yyz}\tilde{\gamma}_{x00y}\right)\,. \tag{5.34}$$

In the latter we have neglected the terms M_{yzyz} and M_{zxyz} which, as said above, provide higher order corrections in the $(\epsilon\tau)^{-1}$ expansion. Multiplying both sides of Eq. (5.34) by the electric field $\mathcal{E}_x$, and using $S_y = \chi_{y,x0}\,\mathcal{E}_x$ together with Eq. (5.13), we find

$$J^z_y = \frac{v^2}{2\alpha}M_{x0yz}\tilde{\gamma}_{x0x0}\,\mathcal{E}_x + v\,M_{0yyz}S_y\,. \tag{5.35}$$

Despite the Dirac character of fermions, the steady-state case of the continuity equation Eq. 5.31 imposes the latter spin Hall current to vanish, analogously to the 2DEG case [169]. This implies the establishment of the out-of-equilibrium value for the spin polarization as

$$S_y^0 = -\frac{\tilde{\gamma}_{x0x0}}{2\,\Gamma\,v}\frac{M_{x0yz}}{M_{0yyz}}\mathcal{E}_x\,. \tag{5.36}$$

Evaluating the above quantities explicitly $\tilde{\gamma}_{x0x0} = 2$, $M_{x0yz}/M_{0yyz} = \lambda/\epsilon$ and we recover the ISGE obtained in Ref. [170]. Using Eq. (5.32) we finally arrive at

$$J_y^z = v\,M_{0yyz}\left(S_y - S_y^0\right)\,, \tag{5.37}$$

and therefore

$$\partial_t S_y \equiv -\frac{1}{\tau_s^{\parallel}}\left(S_y - S_y^0\right)\,, \tag{5.38}$$

where we have identified the SRT

$$\frac{1}{\tau_s^{\parallel}} = -2\lambda\,M_{0yyz} = 2\lambda^2\tau\,, \tag{5.39}$$

in perfect accordance with the result obtained above, Eq. (5.23). The bubble M_{0yyz} is therefore what completely determines the in-plane spin relaxation.

We now ask how the above result is modified when treating the self-energy within the T-matrix approximation. The BS equation Eq. (5.6) now reads

$$\tilde{\gamma}_{x0}(\epsilon) = \gamma_{x0} + n_i\sum_{\mathbf{k}}\mathrm{T}^R(\epsilon)\,\mathcal{G}^R_{\mathbf{k}}(\epsilon)\,\tilde{\gamma}_{x0}(\epsilon)\,\mathcal{G}^A_{\mathbf{k}}(\epsilon)\,\mathrm{T}^A(\epsilon)\,, \tag{5.40}$$

where $\mathrm{T}^{R/A}(\epsilon)$ is the single-impurity T-matrix in the R/A sectors introduced in Eq. (3.20). Projecting onto the Clifford algebra, similarly to Eq. (5.8), we have

$$\tilde{\gamma}_{x0\varrho\varsigma} = \delta_{x\varrho}\delta_{0\varsigma} + \sum_{\mu\nu\zeta\xi=0,x,y,z} Y_{\varrho\varsigma\zeta\xi}N_{\mu\nu\zeta\xi}\tilde{\gamma}_{x0\mu\nu}\,, \tag{5.41}$$

where we have defined

$$N_{\mu\nu\zeta\xi} = \frac{n_i}{4}\sum_{\mathbf{k}}\mathrm{tr}\left(\mathcal{G}^R_{\mathbf{k}}\,\gamma_{\mu\nu}\,\mathcal{G}^A_{\mathbf{k}}\,\gamma_{\zeta\xi}\right), \tag{5.42}$$

$$Y_{\varrho\varsigma\zeta\xi} = \frac{1}{4}\mathrm{tr}[\mathrm{T}^A\,\gamma_{\varrho\varsigma}\,\mathrm{T}^R\,\gamma_{\zeta\xi}]\,. \tag{5.43}$$

Recasting Eq. (5.41) in vector notation, in the same spirit of Eq. (5.12), we have

$$\tilde{\boldsymbol{\gamma}}_{x0} = \boldsymbol{\gamma}_{x0} + Y\,N^{\mathrm{t}}\tilde{\boldsymbol{\gamma}}_{x0}\,, \tag{5.44}$$

and consequently

$$Y^{-1}(\tilde{\boldsymbol{\gamma}}_{x0} - \boldsymbol{\gamma}_{x0}) = N^{\mathrm{t}}\tilde{\boldsymbol{\gamma}}_{x0}\,. \tag{5.45}$$

The latter equation allows again to find a connection with the observables. For example, the generalisation of Eq. (5.13) is written as

$$\chi_{y,x0} = \frac{2v}{n_i}\sum_{\mu\nu}N_{\mu\nu0y}\tilde{\gamma}_{x0\mu\nu} = \frac{2v}{n_i}\sum_{\mu\nu}Y^{-1}_{0y\mu\nu}\tilde{\gamma}_{x0\mu\nu}\,. \tag{5.46}$$

The spin Hall conductivity instead is found as

$$\sigma^z_{yx} = \frac{2v^2}{n_i} \sum_{\mu\nu} Y^{-1}_{yz\mu\nu} \tilde{\gamma}_{x0\mu\nu} \,. \tag{5.47}$$

Differently to the Gaussian case, where we were able to relate the response of an observable uniquely to the associated component of the renormalised vertex, in the T-matrix limit in principle all components of $\tilde{\gamma}_{x0}$ would contribute, each of them with weight given by Y^{-1}. In the limiting case of unitary limit $u_0 \to \infty$, where $\lim_{u_0\to\infty} \mathrm{T}^{R/A} = -\frac{1}{g_0^{R/A}}$, we find a simplification as

$$Y^{-1}_{\varrho\varsigma\zeta\xi} = |g^R_{0,0}|^2 \delta_{\varrho\zeta}\delta_{\varsigma\xi} \,. \tag{5.48}$$

This implies that for Eq.(5.47) a relation similar to the Gaussian case is obtained

$$J^z_y = \sigma^z_{yx}\mathcal{E}_x = \frac{2v^2}{n_i}|g^R_{0,0}|^2 \tilde{\gamma}_{x0yz}\,\mathcal{E}_x = \frac{2v^2}{n_i} N_{x0yz}\tilde{\gamma}_{x0x0}\mathcal{E}_x + v\, N_{00yz}|g^R_{0,0}|^{-2} S_y \,, \tag{5.49}$$

where we have restricted our focus again to the dominant subspace σ_x/s_y. After standard algebra, we arrive at

$$\partial_t S_y = \frac{2\lambda}{v}\sigma^z_{yx}\mathcal{E}_x = \frac{2\lambda}{v} v\, N_{0yyz}(S_y - S^0_y) \,, \tag{5.50}$$

and the SRT defined as

$$\frac{1}{\tau^{\parallel}_s} = 2\lambda\, |g^R_{0,0}|^{-2} N_{00yz} = 2\lambda \frac{1}{\epsilon^2}\frac{16\pi^2 v^4}{\pi^2 + \mathcal{L}^2_{\Pi}} N_{00yz} = 2\lambda^2\tau \,, \tag{5.51}$$

where we have used the definition of τ in the unitary limit, Eq. (3.43). We conclude that the formal expression connecting τ_s and τ (the DP relation) is the same as that found in the Gaussian limit for the self-energy. However, given the different dependence of τ on the Fermi level in the two approximations—cf. Eq. (3.35) and Eq. (3.43)—one has

$$\frac{\tau(\epsilon)}{\tau^{\parallel}_s(\epsilon)} = \begin{cases} \frac{2\lambda^2}{\epsilon^2}\left(\frac{2v^2}{n_i u_0^2}\right)^2 & \text{Gaussian,} \\ \epsilon^2 \frac{\lambda^2}{2}\left(\frac{\pi^2+\mathcal{L}^2_{\Pi}}{4\pi^2 n_i v^2}\right)^2 & \text{Unitary.} \end{cases} \tag{5.52}$$

The SRT associated to the out-of-plane component can be derived along the same lines. The relevant Heisenberg equation now reads

$$\partial_t S_z = -\frac{2\lambda}{v}(J^x_x + J^y_y) \,, \tag{5.53}$$

and a similar reasoning that lead to Eq, (5.39), allows us to conclude

$$\frac{1}{\tau^{\perp}_s} = 2\lambda(M_{0zxx} + M_{0zyy}) = 4\lambda^2\tau \,, \tag{5.54}$$

in the Gaussian limit, and a similar relation for the unitary limit.

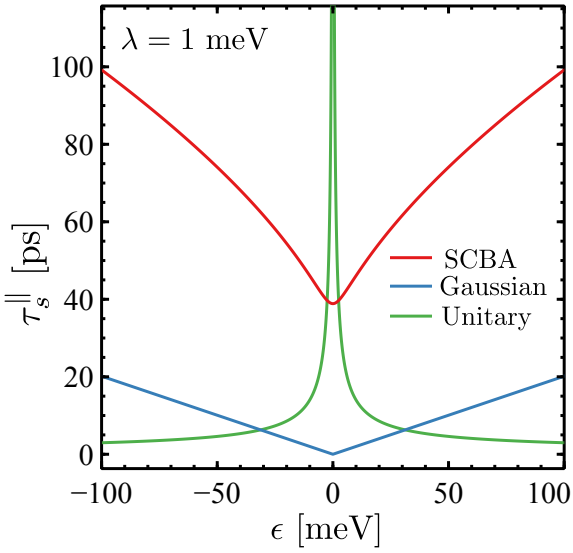

Figure 5.3: DP in-plane SRT calculated according different schemes for the self-energy: SCBA (red line), Gaussian (blue line) and unitary limit (green line). The most important feature obtained within the SCBA is a strong renormalisation of $\tau_s^{\parallel}$ in the vicinity of the Dirac point, reflecting a disorder-induced finite density of states in that region. In the plot $\lambda = 1$ meV and $\Gamma = 60$ meV.

Discussion

Here, we discuss the range of validity of the DP relation obtained in Eq. (5.52) within the Gaussian and unitary limits of potential scattering. The energy dependence of the spin lifetime for fixed impurity concentration is shown in Fig. 5.3. Away from the Dirac point, within the Gaussian approximation, the spin lifetime increases linearly since $\tau \propto \epsilon^{-1}$ (see Eq. (3.35)). In the unitary limit, instead, one has a linear dependence $\tau \propto \epsilon$ (see Eq. (3.43)), leading to vanishing spin lifetime at high electron doping. On the other hand, near the Dirac point, the noncrossing approximation breaks down. It is not surprising that the spin lifetime dependences near the Dirac point are found to be nonphysical as $\epsilon \to 0$ (see Fig. 5.1). Here we are mostly interested in the diffusive regime away from the Dirac point $\epsilon\tau \gg 1$, thus neglecting interference effects that can correct the standard DP relation [227, 239, 240]. As discussed in Chapter 3, an important refinement is possible within the noncrossing formalism used here by evaluating the $O(n_i^2)$ terms in Eq. (3.43). Such higher-order terms encode the strong renormalisation of the single-particle propagators by incoherent multiple scattering approaching the Dirac point. To show this, it suffices to resum the infinite class of 'rainbow' diagrams, i.e. the SCBA (see Fig. 3.5). The SCBA self-energy is given by the solution of the following self-consistent equation [173]

$$\frac{1}{2\tau}\bigg|_{\text{SCBA}} = -\Im\Sigma_{\text{SCBA}}(\epsilon) = -\Im\left[\frac{n_i}{4\pi v^2}(\epsilon - \Sigma_{\text{SCBA}}(\epsilon))\ln\left(\frac{-\Lambda^2}{(\epsilon - \Sigma_{\text{SCBA}}(\epsilon))^2}\right)\right]. \tag{5.55}$$

In Fig. 5.3 we show that the SCBA provides a physical (finite, nonzero) τ_s approaching the Dirac point. To obtain a representative curve, we take $\lambda = 1$ meV and we choose the impurity density and the scattering strength such that the SCBA nonperturbative energy scale $\Gamma = \Lambda\, e^{-2\pi v^2/(n_i u_0^2)}$ [173] is a few tens meV. The in-plane SRT is then found to lie in the range 50-100 ps. The magnitude of $\tau_s^{\parallel}$ is compatible with previous reports where the (uniform or random) Rashba SO coupling is treated by SC or numerical approaches [227, 228], see also Fig. 5.1.

Finally we comment briefly on the apparently different asymptotic behaviour of the SCBA vs

the BA result (respectively red and blue solid lines in Fig. 5.3). The SCBA and the BA provides the same result only for $|\epsilon| \gg \Gamma$ [173]. For our choice of $\Gamma = 60$ meV, it can be shown by direct inspection that an agreement is restored for energies $\epsilon \sim 10^3$ meV.

Conclusions

In this Chapter, we laid out the foundations of a general microscopic theory of coupled charge/spin transport and spin dynamics in the diffusive limit of 2D Dirac systems subject to SO interactions. Our work represents the logical extension of the previously-developed diagrammatic treatments [231, 232] to all orders in the scattering potential, for disordered electron systems with an enlarged pseudospin $\otimes$ spin Clifford algebra [169,170]. We applied the formalism to the paradigmatic case of 2D Dirac fermions with Rashba SO coupling considering the purely diffusive regime $\lambda\tau \ll 1 \ll \epsilon\tau$. We demonstrated how the DP relation between momentum and spin lifetime $\tau \propto \tau_s^{-1}$ holds in both the Gaussian (weak short-range scatterers) and the unitary (strong short-range scatterers) limits, despite the drastically different energy dependence of the momentum scattering times $\tau = \tau(\epsilon)$ in the two regimes. We derived the same result both by direct diagrammatic resummation (in the noncrossing approximation) and by exploiting the conservation laws of the theory in the zero-frequency limit. Under the diffusive regime $\lambda\tau \ll 1 \ll \epsilon\tau$ it is not possible to study the dynamics in the region of Fermi energies comparable to the Rashba pseudogap region $\epsilon \sim 2\lambda$, which is predicted to display interesting out-of-equilibrium phenomena, as we have shown in Chapter 4. The strong spin-momentum locking peculiar of this regime lets us infer a modification of the relation between τ_s and τ towards the Elliot-Yafet type $\tau_s \propto \tau$. Our theory sets the stage to study the spin dynamics in that regime. This topic has become of renewed great interest due to recent progresses in graphene-based heterostructures, where Hanle precession experiments in oblique fields have been recognised as a viable tool to estimate the induced large SO effects [241–243]. We tackle this topic in greater detail in the following Chapter.

Chapter 6

Spin-orbit Effects in Realistic Systems: Graphene–Transition Metal Dichalcogenide Heterostructures

Overview

In Chapter 4 we have analysed theoretically the SHE and ISGE in the pure 2D Dirac-Rashba model. The vanishing SHE and the robust ISGE were shown to originate from the underlying $SU(2)$ covariant spin-conservation laws of the theory. We also suggested how this result can be understood in terms of the spin texture of electron bands, where, for spin lying completely in plane, the SHE (ISGE) is suppressed (enhanced).

Although the Dirac-Rashba model represents an excellent testbed to study SO effects for Dirac fermions, it relies on the assumption of unbroken sublattice symmetry (point group symmetry C_{6v}, see discussion in Chapter 3). This approximation fails to capture many graphene-on-a-substrate systems, including graphene/TMD hybrids of our interest. To capture the physics of this wider class of honeycomb-layered materials, a description beyond the pure Dirac-Rashba model is required.

In this Chapter we re-examine the SHE and ISGE in the full C_{3v} model representative of graphene/TMD bilayers. We demonstrate that a finite spin Hall conductivity is restored in the presence of a spin–valley interaction, which endows the bands with a finite component of out-of-plane spin polarisation. More generally, by making use of the WIs, we provide a systematic way to predict the emergence of the SHE in this class of Dirac-Rashba systems of experimental relevance. As for the ISGE, we generalise our previous results in Sec. 4 by introducing a proper figure of merit to quantify the CSC efficiency, taking into account the momentum-dependence of the spin texture. We show that the giant ISGE predicted in the pure Rashba model is robust upon the introduction of additional proximity-induced interactions and remains large at room temperature.

Finally we study the nonequilibrium spin dynamics. A time-dependent perturbative treatment is employed to derive the spin Bloch equations governing the spin dynamics at high electronic density $\epsilon \gg \lambda_{\rm SOC}$ for arbitrary ratio $\lambda_{\rm SOC}/\eta$, where $\eta \propto \tau^{-1}$ is the disorder-induced quasiparticle broadening and $\lambda_{\rm SOC}$ is the largest amongst the present SO energy scales. Rich scenarios are predicted, depending on a delicate competition between interface-induced Rashba and spin–valley interactions. We study the spin anisotropy ratio of out-of-plane to in-plane spin

lifetimes $\zeta = \tau_s^{\perp}/\tau_s^{\parallel}$. Different formulas for ζ are obtained in the motional-narrowing regime of weak SO coupling ($\lambda_{\text{SOC}} \ll \eta$), and for well-resolved SO coupling ($\lambda_{\text{SOC}} \gtrsim \eta$), which can be useful to model spin transport in ultra-clean vdW heterostructures.

Spin Hall Effect in graphene on transition metal dichalcogenides

In the pure Dirac-Rashba model, the Heisenberg equation for the spin density along y reads (cf. Eq. 4.55)

$$\partial_t S_y = \frac{2\lambda}{v} J_y^z \,. \tag{6.1}$$

The latter equation implies that the spin Hall current is vanishing in the steady state $\partial_t = 0$, as dictated by the $SU(2)$ covariant conservation laws of the theory. Note that Eq. 6.1 to be physically realised, i.e. for the steady state to be reached, a relaxation mechanism—e.g. scattering from impurities—is necessary.

We explore here the possibility to induce a SHE in Dirac-Rashba systems. Note that if an additional addend were present in Eq. 6.1, a finite spin Hall current would be restored in the steady state, cf. for a similar situation Eq. (4.36) valid in the presence of a random Rashba interaction. We demonstrate that this situation is actually the case for graphene/TMD heterostructures. To see this, we briefly review the derivation of the $SU(2)$ conservation laws in the pure Dirac-Rashba model from a different perspective, and then extend the reasoning to the C_{3v} case with Hamiltonian Eq. (3.54). We work in the valley $\kappa = 1$ and omit the valley index for simplicity of the presentation.

The starting point is Eq. (4.2), which we recast in a more compact and general form

$$\mathscr{H}_0^{\text{min}} = \Psi_0^{\dagger} \left(v\, \sigma^i \left(-\imath\, \partial_i - \boldsymbol{\mathcal{A}}_i - A_i \right) - \boldsymbol{\mathcal{A}}_0 - A_0 \right) \Psi_0 . \tag{6.2}$$

Here $\mu = (0, x, y)$, and summation over repeated indices $i = (x, y)$ is implicit. We also have

$$\boldsymbol{\mathcal{A}}_\mu = \sum_{a=\{x,y,z\}} \mathcal{A}_\mu^a s^a \,. \tag{6.3}$$

In the spirit of Eq. (6.2), disordered Dirac fermions can be seen as minimally coupled to both the conventional electromagnetic 3D vector potential $A_\mu = (A_0, \mathbf{A})$ *and* to a *SU(2)* gauge field $\boldsymbol{\mathcal{A}}_\mu$. The pure Rashba-model is obtained by setting

$$\mathcal{A}_x^y = -\mathcal{A}_y^x = \lambda / v \,, \tag{6.4}$$

and all the other components equal to zero. The action S associated with the Hamiltonian Eq. (6.2) reads

$$S = \int dt \, [\int d\mathbf{x}\, \Psi_0^{\dagger}(\mathbf{x}) \left(\imath \partial_t - \mathscr{H}_0^{\text{min}}(\mathbf{x}) \right) \Psi_0(\mathbf{x})] \tag{6.5}$$

$$= \int dx\, \Psi_0^{\dagger}(\mathbf{x}) \left[\imath\, \partial_t + v \sigma^i (\imath\, \partial_i + \boldsymbol{\mathcal{A}}_i + A_i) + \boldsymbol{\mathcal{A}}_0 + A_0 \right] \Psi_0(\mathbf{x}) \,. \tag{6.6}$$

In the Noether sense, a conservation law for the theory can be derived by considering the sta-

tionarity of S under infinitesimal $SU(2)$ gauge transformation [cf. Eq. (2.46)]

$$\mathcal{U} = e^{\frac{\imath}{2}\sum_a \theta_a(x) s_a}\,. \tag{6.7}$$

At linear order in $\theta_a(x)$ and $\partial_\mu\theta_a(x)$, the non-Abelian nature of the rotation produces the following transformation rules for the fermionic spinors and the $SU(2)$ gauge fields [88]

$$\Psi_0 \to \Psi_0' = \mathcal{U}\Psi_0 \simeq \Psi_0 + \delta\Psi_0 = \Psi_0 + \frac{\imath}{2}\sum_a \theta_a(x) s^a\,, \tag{6.8}$$

$$\boldsymbol{\mathcal{A}}_\mu \to \boldsymbol{\mathcal{A}}_\mu' = \mathcal{U}\,\boldsymbol{\mathcal{A}}_\mu\,\mathcal{U}^{-1} + (\partial_\mu\mathcal{U})\mathcal{U}^{-1} \tag{6.9}$$

$$= \boldsymbol{\mathcal{A}}_\mu + \delta\boldsymbol{\mathcal{A}}_\mu = \boldsymbol{\mathcal{A}}_\mu + \frac{\imath}{2}\sum_a [\theta_a s^a, \boldsymbol{\mathcal{A}}_\mu] + \sum_a [\partial_\mu\theta_a(x)] s^a\,. \tag{6.10}$$

The total variation of the action is given by

$$\Delta S = \sum_\mu \left[\frac{\delta S}{\delta\Psi_0}\delta\Psi_0 + \frac{\delta S}{\delta(\partial_\mu\Psi_0)}\delta(\partial_\mu\Psi_0) + \frac{\delta S}{\delta\Psi_0^\dagger}\delta\Psi_0^\dagger + \frac{\delta S}{\delta(\partial_\mu\Psi_0^\dagger)}\delta(\partial_\mu\Psi_0^\dagger) + \sum_a \frac{\delta S}{\delta\mathcal{A}_\mu^a}\delta\mathcal{A}_\mu^a \right]. \tag{6.11}$$

By making use of Eqs. (6.8)-(6.10) and the Euler-Lagrange equations for the action Eq. (6.5), after few lines of calculations we find

$$\Delta S = \sum_\mu\sum_a \Delta S^a = \sum_\mu\sum_a \partial_\mu\left(\theta_a j_\mu^a\right) + J_\mu^a\left\{\partial_\mu\theta_a + \frac{\imath}{4}\mathrm{tr}\left[s^a[\sum_b \theta_b s^b, \boldsymbol{\mathcal{A}}_\mu]\right]\right\} \tag{6.12}$$

$$= \sum_\mu\sum_a \left\{\partial_\mu j_\mu^a + \imath\,[\boldsymbol{\mathcal{A}}_\mu, \boldsymbol{J}_\mu]_a\right\}\theta_a + (j_\mu^a + J_\mu^a)\partial_\mu\theta_a\,, \tag{6.13}$$

with

$$j_\mu^a = \frac{\imath}{2}\frac{\delta S}{\delta(\partial_\mu\Psi)} s^a\Psi\,, \tag{6.14}$$

$$J_\mu^a = \frac{\delta S}{\delta\mathcal{A}_\mu^a}\,, \tag{6.15}$$

$$\boldsymbol{J}_\mu = \frac{1}{2}\sum_a J_\mu^a s^a\,. \tag{6.16}$$

For ΔS to vanish for arbitrary variation of $\theta_a, \partial_\mu\theta_a$, the following conditions must hold true [162]

$$j_\mu^a = -J_\mu^a\,, \tag{6.17}$$

$$D_\mu \boldsymbol{J}_\mu \equiv \partial_\mu \boldsymbol{J}_\mu - \imath[\boldsymbol{\mathcal{A}}_\mu, \boldsymbol{J}_\mu] = 0\,. \tag{6.18}$$

Note the the Noether current j_μ^a is connected to the physical current J_μ^a simply by a minus sign. Eq. (6.18) is exactly the generalisation of the covariant conservation law for the spin-current found in Eq. (4.6), which can be more easily seen by expanding it into its components

$$\partial_t J_0^a + \partial_i J_i^a + 2\epsilon^{abc}(\mathcal{A}_0^b J_0^c + \mathcal{A}_i^b J_i^c) = 0\,. \tag{6.19}$$

For the pure Rashba case, identifying the spin density $J_0^a \equiv S_a$, given Eq. (6.4) one recovers Eq. (6.1). However, from Eq. (6.19) more general conclusion can be drawn. In particular, the spin valley term present in the C_{3v} model Eq. (3.54) induces a non-zero component of the gauge $SU(2)$ potential

$$\mathcal{A}_0^z = \lambda_{\mathrm{sv}} s_z\,. \tag{6.20}$$

Considering Eq. (6.19) then, the following conservation law is found

$$\partial_t S_y = \frac{2\lambda}{v} J_y^z - 2\lambda_{\rm sv}\, S_x\,, \tag{6.21}$$

which implies that in the steady state

$$J_y^z = v\frac{\lambda_{\rm sv}}{\lambda} S_x\,. \tag{6.22}$$

Notice at the opposite valley $\kappa = -1$, the sign of the RHS of the last equation is reversed due to the spin-valley coupling, so that ultimately the spin Hall current is proportional to the *valley-filtered* spin polarisation along $\hat{x}$ [169]. Keeping our convention for the orientation of the electric field ($\boldsymbol{\mathcal{E}} \parallel \hat{x}$), such a term can be observed in principle, due to the spin-momentum locking, upon *transverse* shifting of the Fermi surface in response to the applied $\boldsymbol{\mathcal{E}}$, i.e. in the presence of skew scattering. In terms of the WIs for the truncated vertex Γ^a_μ, a similar procedure leading us to Eq. (4.21) gives

$$q_\mu \Gamma^y_\mu(\mathbf{k},0) = \frac{1}{2}\left[s^y \left(G^A_{\mathbf{k}}\right)^{-1} - \left(G^R_{\mathbf{k}}\right)^{-1} s^y\right] - 2\imath\frac{\lambda}{v}\mathcal{J}^z_y + 2\imath\lambda_{\rm sv}\Gamma^x_0\,. \tag{6.23}$$

Disorder is not yet included in the treatment. Considering scalar impurities [Eq. (2.3)] however only requires performing disorder average of both sides of Eq. (6.23), which results into the following relation between the renormalised spin Hall vertex and the "staggered" spin-x vertex

$$\tilde{\mathcal{J}}^z_y = v\frac{\lambda_{\rm sv}}{\lambda}\tilde{\Gamma}^x_0 + \imath\frac{v}{4\lambda}\left\{[s_y,\tilde{H}]_- + \imath\,[s_y,\mathrm{Im}\,\Sigma^R]_+\right\}\,. \tag{6.24}$$

In the presence of a spin-valley term then, the WI does not fully determine the spin Hall vertex. However the exact symmetry relation Eq. (6.24)—and obviously its analogy for the associated response functions Eq. (6.22), represents a strong constraint for the observables under considerations in realistic models. In particular, Eq. (6.24) is expected to hold for the C_{3v} model Eq. (6.29). In fact λ_{zz} is neglected due to its smallness as explained before [122], and the additional orbital mass Δ does not enter at all the conservation law for spin polarisation S_y, which we can easily understand by noting that $[S_y, \Delta\,\tau_z\sigma_z] = 0$.

Diagrammatic calculation of the spin Hall effect

We now perform a direct diagrammatic calculation of the spin Hall current. Let us focus on the leading-order $\sigma^I_{\rm SH}$ contribution

$$\sigma^I_{\rm SH}(\epsilon) = \int \frac{d\mathbf{k}}{(2\pi)^2}\,\mathrm{tr}\,\left[\mathcal{J}^z_y\,\mathcal{G}^R_{\mathbf{k}}(\epsilon)\,\tilde{v}_x\,\mathcal{G}^A_{\mathbf{k}}(\epsilon)\right]\,. \tag{6.25}$$

The matrix $M_{\mu a\rho d} \equiv Y^{\nu b\lambda c}_{\mu a\rho d}\, I_{\nu b\lambda c}$ entering the BS equation for the renormalised charge vertex [cf. Eq. (4.29)]

$$\tilde{v}_{x,\mu a} = v\,\delta_{\mu x}\,\delta_{a0} + Y^{\nu b\lambda c}_{\mu a\rho d}\, I_{\nu b\lambda c}\,\tilde{v}^{\rho d}_x\,, \tag{6.26}$$

acquires now four extra additional non-vanishing components

$$\mu a = \{x0, 0y, yz, zx, 0x, y0, zy, xz\}\,, \tag{6.27}$$

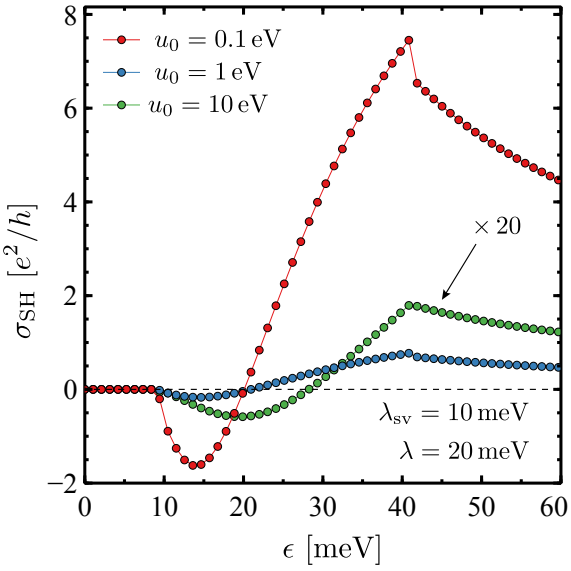

Figure 6.1: The black dashed line $\sigma_{\mathrm{SH}} = 0$ represents the result obtained in the pure Dirac-Rashba model (see Chapter 4). When a spin-valley coupling is introduced in the model, the associated spin conservation laws impose the emergence of a non-vanishing SHE. In the plot, for $\lambda = 2\lambda_{\mathrm{sv}} = 20\,\mathrm{meV}$ we report the obtained result for the Fermi surface contribution (σ^I_{SH}) for different value of the scalar-disorder strength u_0. The impurity concentration is set as $n_i = 10^{12}\,\mathrm{cm}^{-2}$.

where the first four were already non-zero in the C_{6v} pure Dirac-Rashba case, whereas the last four are a consequence of broken sublattice symmetry. Because of the higher dimensionality of $M_{\mu\alpha\rho d}$, inverting Eq. (6.26) and hence an analytical expression for the spin Hall current, is a difficult task. Nevertheless we can obtain simple analytical results in some particular case. Neglecting Δ for a while, we find the spin Hall conductivity reads, for energy above the Rashba pseudogap $\epsilon > 2\tilde{\lambda}$ [cf. Eq. (3.57)] and in the weak scattering limit $|u_0 g_0^R| \ll 1$ as

$$\sigma^I_{\mathrm{SH}}(\epsilon > 2\tilde{\lambda}) = \frac{1}{n_i u_0^2} \frac{4\epsilon\lambda^4\lambda_{\mathrm{sv}}(\lambda - \lambda_{\mathrm{sv}})(\lambda + \lambda_{\mathrm{sv}})^2}{[\epsilon^2\lambda_{\mathrm{sv}}(\epsilon - \lambda_{\mathrm{sv}})^2 + \lambda^2(\epsilon^4 + 3\lambda_{\mathrm{sv}})]^2}\,. \tag{6.28}$$

Note here $\sigma^I_{\mathrm{SH}} \propto n_i^{-1}$, which is signature of the dominant (SC) contribution in the dilute limit we are interested in. $\sigma^{II}_{\mathrm{SH}}$ [Eq. (4.27)] only provides corrections $O(1)$ which we can therefore neglect, yielding $\sigma_{\mathrm{SH}} \equiv \sigma^I_{\mathrm{SH}}$. In Fig. 6.1 we report a plot of the σ^I_{SH} across all energy regimes.

In accordance to the arguments above based on the conservation laws, we have hence confirmed by direct calculation the non-vanishing SHE in generalised Dirac-Rashba systems.

Our findings for the C_{3v} model constitute an important step towards a unified theory of spin and charge dynamics for Dirac-Rashba materials in generic non-stationary conditions. Real-space methodologies for evaluation of transverse conductivities have been recently proposed [244, 245], which can help to tackle more complex scenarios. The exact symmetry relations presented here provide a stringent test for real-space numerical approaches, for which the achievable energy resolutions still represent a major limiting factor.

Inverse spin Galvanic effect

One intuitive reason behind the large CSC presented in Chapter 4 was the peculiar spin-momentum locking configuration of Rashba states: spins lying completely in the plane maximise the conver-

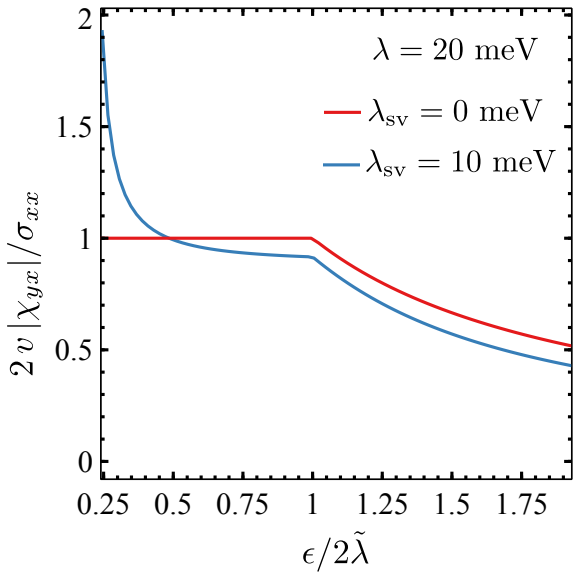

Figure 6.2: Comparison of the "naive" CSC efficiency in the presence/absence of a spin-valley term. The plot is produced by considering the definition of Eq. (6.30). The efficiency inside the Rashba pseudogap attains a value larger than 1 (for $\lambda_{\rm sv} = 10$ meV), due to a faster decrease of the band velocity with respect to the spin polarisation S_y. This motivates our alternative definition of the CSC efficiency with respect to Eq. (6.30).

sion of an externally-driven charge current upon displacement of the Fermi surface within the 2D plane (see Fig. 4.2). On the other hand, we have seen that as soon as other terms beyond the Rashba SO interaction enter the full C_{3v} Hamiltonian Eq. (3.1), reading in $\mathbf{k}$-space as

$$H_{0\mathbf{k}} = v\,\tau_z \boldsymbol{\sigma}\cdot\mathbf{k} + \lambda\,\tau_z\,(\boldsymbol{\sigma}\times\mathbf{s})\cdot\hat{z} + \lambda_{\rm sv}\tau_z s_z + \lambda_{zz}\sigma_z s_z + \Delta\tau_z\sigma_z\,, \tag{6.29}$$

electrons' spins are tilted out-of-the-plane (see Fig. 3.4). This leads to a finite SHE as we have seen above. What is the picture for the CSC ISGE efficiency of the Rashba model? In this section we discuss this issue.

The result obtained in Chapter 4, where the CSC was found for the minimal Rashba model as [cf. Eq. (4.51)]

$$\gamma(\epsilon) \equiv \left|\frac{2\,v\,\chi_{yx}(\epsilon)}{\sigma_{xx}(\epsilon)}\right| = \theta(2\lambda-\epsilon) + \frac{2\lambda}{\epsilon}g(u_0,\epsilon)\,\theta(\epsilon-2\lambda)\,, \tag{6.30}$$

where g is a function interpolating between the weak ($g=1$) and strong ($g\lesssim 1$) scattering case. In particular in regime I, the following relations hold true [cf. Eqs. (4.42),(4.44)]

$$\langle S_y\rangle_{\rm I} = \chi_{yx}\mathcal{E} = -\frac{\mathcal{E}}{4\pi}\,\varrho(k_F)\,k_F\tau_*\,, \tag{6.31}$$

$$\langle J_x\rangle_{\rm I} = \sigma_{xx}\mathcal{E} = \frac{\mathcal{E}}{2\pi}\,v_F\,k_F\,\tau_*\,, \tag{6.32}$$

which result in the first term on the RHS of Eq. (6.30). τ_* is the transport time calculated at the Fermi wavevector, as defined in Eq. (4.41). The definition of γ as for Eq. (6.30) deserves some comments. Firstly, at the Dirac point $k=0$ where the spin texture is not established yet, the CSC should vanish accordingly. Secondly, when introducing additional terms in the Hamiltonian, the band velocity close to the Dirac point tends to zero faster than χ_{yx}, producing $\gamma > 1$, which

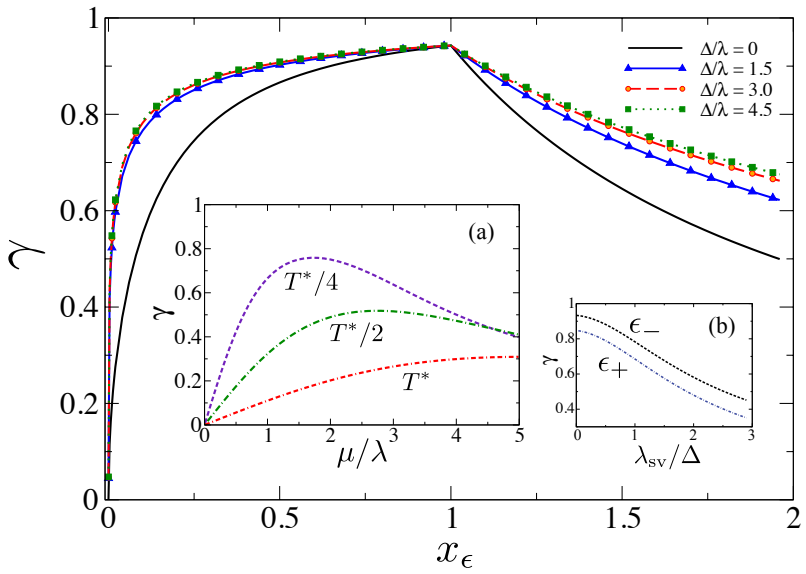

Figure 6.3: Main: Fermi energy dependence of the ISGE efficiency at selected values of Δ for $\lambda = 15$ meV and $\lambda_{sv} = 0$. The x-axis is rescaled as $x_\epsilon = |\epsilon - \epsilon_0| / |2\tilde{\lambda} - \epsilon_0|$ for clarity. Insets: (a) γ as function of chemical potential (μ) at selected temperatures for a prototypical heterostructure with $\lambda = 10$ meV, $\lambda_{sv} = \Delta = 0$ (Ref. [125]); $k_B T^* = 25$ meV (room temperature). (b) Variation of γ with λ_{sv} for a Fermi energy slightly below (above) the Rashba pseudogap's edge [$\epsilon_\pm = 2\tilde{\lambda} \times (1.0 \pm 0.1)$] for $\Delta = \lambda/2$ and $\lambda = 15$ meV. All calculations performed in the weak scattering limit.

is counterintuitive for a measure of the CSC efficiency (see Fig. 6.2). An alternative and more appropriate figure of merit must then be sought.

Generally speaking, the CSC is expected to be larger in regime I, as the detrimental contribution of the higher energy-band due to its counter-rotating spin texture is inhibited. Therefore it is easier to define a proper figure of merit by analysing this energy range. Here the CSC *is only limited by the electronic mobility*, i.e., $|\langle S_y \rangle|_{\mathrm{I}} \approx \langle J_x \rangle_{\mathrm{I}} / (2v_F) \propto (k_F \tau_*)\, \mathcal{E}$. This suggests that $\gamma \equiv |\varrho| = |\langle S_y \rangle| / (2v_F \langle J_x \rangle)$ is the proper figure of merit in regime I. Generalising Eq. (4.38) by including Δ, λ_{sv} interactions in the Hamiltonian—we neglect the intrinsic SO coupling λ_{zz}, typically very small in graphene on TMDs [122]—cf. discussion after Eq. (3.54)—we have

$$\varrho\,(k) = \frac{vk\lambda}{\sqrt{\left(\Delta\lambda_{sv} - \lambda^2\right)^2 + v^2k^2\left(\lambda^2 + \lambda_{sv}^2\right)}}\,. \tag{6.33}$$

For the pure Rashba model we find the efficiency is *nearly saturated*

$$\gamma_{\max} = \max_{\epsilon \in \mathrm{I}} |\varrho(k(\epsilon))| = 2\sqrt{2}/3 \approx 0.94. \tag{6.34}$$

Note $|\varrho(k=0)| = 0$, so that our figure of merit correctly takes into account the shrinking of the Fermi surface and the vanishing of the associated spin texture. In regime II, both spin helicities $\chi = \pm 1$ contribute to the non-equilibrium spin density, resulting into a decay of the CSC rate. Here the figure of merit is not uniquely defined. To analyse this regime, we define γ heuristically, satisfying: (i) $0 \leq \gamma \leq 1$ for all parameters, (ii) γ decays for $\epsilon \gg 2\tilde{\lambda}$ due to collapsing of spin-split Fermi rings and (iii) γ is continuous across the Rashba pseudogap. Since the band velocity saturates quickly to its upper bound ($= v$), we use its value at the Rashba pseudogap edge as

representative for the regime II, which leads us to the following definition

$$\gamma(\epsilon) = \frac{2|\chi_{yx}(\epsilon)|}{\sigma_{xx}(\epsilon)} \times \begin{cases} v_F(\epsilon) & , \epsilon < 2\tilde{\lambda} \\ v_F(2\tilde{\lambda}) & , \epsilon \geq 2\tilde{\lambda} \end{cases} . \tag{6.35}$$

where $v_F(\epsilon) \equiv |v_{\chi=-}(k(\epsilon))|$. Consistently with the rate derived for the minimal model [Eq. (4.51)], the asymptotic behaviour of γ is of power-law type, and thus the CSC remains robust in the accessible range of electronic densities. We show our results in Fig. 6.3. In realistic graphene/TMD heterostructures, Δ and $\lambda_{\rm sv}$ can be comparable to the Rashba coupling [122], leading to major modifications in the band structure. Our thorough analysis, summarised in Fig. 6.3, shows that the ISGE remains robust. For instance, for $|\lambda_{\rm sv}| \ll \lambda, |\Delta|$, the k-dependence of the in-plane spin texture is virtually unaffected [Eq. ((6.33))]. Thus, according to the SC results the CSC efficiency should be high at the Rashba pseudogap edge. This is confirmed by a numerical inversion of the BS equations in the full model. The figure of merit γ plotted in Fig. 6.3 reaches its predicted optimal value [Eq. (6.34)]. When the spin–valley coupling is significant, the in-plane spin texture shrinks, however the CSC efficiency remains sizable [Fig. 6.3(b)].

Temperature dependence

A relevant question is how much efficiency is lost due to thermal fluctuations. Figure 6.3(a) shows the CSC figure of merit at selected temperatures in the weak scattering limit, calculated by employing the following definition

$$\gamma(\mu, T) = \frac{\int_{-\infty}^{+\infty} d\epsilon \, \frac{\partial f(\epsilon,\mu,T)}{\partial \epsilon} \, 2|\chi_{yx}(\epsilon, T=0)| \left[\theta(|\epsilon| - 2\tilde{\lambda}) v_F(2\tilde{\lambda}) + \theta(2\tilde{\lambda} - |\epsilon|) v_F(\epsilon)\right]}{\int_{-\infty}^{+\infty} d\epsilon \, \frac{\partial f(\epsilon,\mu,T)}{\partial \epsilon} \, \sigma_{xx}(\epsilon, T=0)} , \tag{6.36}$$

where $f(\epsilon, \mu, T) = \{1 + \exp\left[(\epsilon - \mu)/k_B T\right]\}^{-1}$ is the Fermi–Dirac distribution function.

Since the $T = 0$ ratio decays slowly in regime II, the smearing caused by thermal activation is ineffective, allowing a giant ISGE at room temperature, e.g., $\gamma_{\rm room} \approx 0.3$ for a chemical potential $\mu \approx 5\lambda \approx 50$ meV.

Microscopic theory of spin relaxation in graphene on transition metal dichalcogenides

Having presented a comprehensive framework concerning the steady-state response of graphene on TMD hybrids, in this Section we want to tackle the time-dependent dynamics of electrons' spin. Allowing for an easier analytical treatment, we consider here the highly-doped regime $\epsilon \gg \lambda_{\rm SOC}$, where $\lambda_{\rm SOC}$ is any of the SO interactions present in the Hamiltonian. How does the presence of multiple SO terms affect the dynamics of spins? An interesting competition is expected to establish between the *in-plane* Rashba SO coupling, which directly couples to the velocity of electrons, hence acting as a Lorentz pseudomagnetic field [169], and the spin-valley SO coupling, which conversely couples to the *out-of-plane* spin components S_z, being in other words a Zeeman-like pseudomagnetic field. In fact, interface-induced Rashba and spin-valley interactions in graphene/TMD bilayers can in principle be large as tens of meV [125]. For this reason, the spin dynamics associated to in-plane and out-of-the-plane channels in samples with sizable $\lambda, \lambda_{\rm sv}$ is set by distinct time scales. Such a possible anisotropy of the spin dynamics can be quantified by the *spin relaxation time anisotropy* (SRTA) ratio, $\zeta = \tau_s^{\perp}/\tau_s^{\parallel}$. The SRTA in graphene

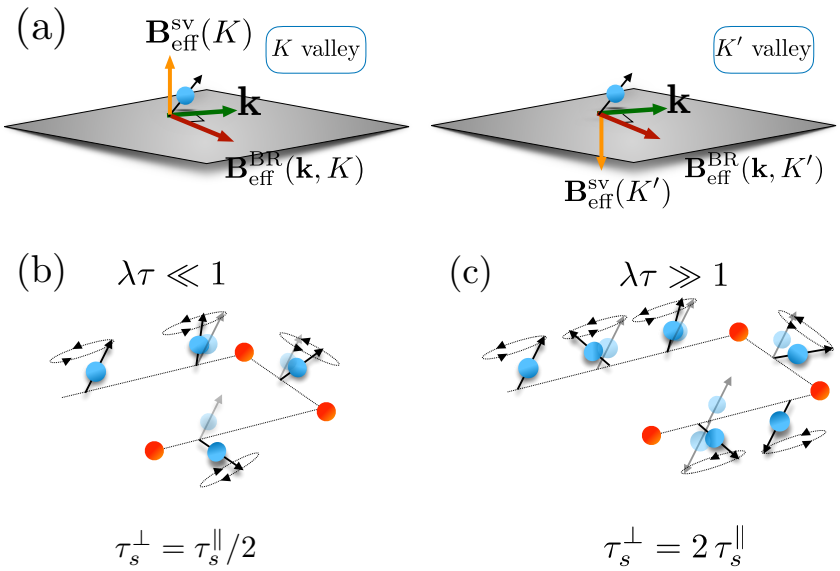

Figure 6.4: Spin relaxation in the C_{3v} model. (a) The Rashba pseudomagnetic field $\mathbf{B}_{\rm eff}^{\rm BR}$ is always orthogonal to the direction of motion $\hat{\mathbf{k}}$ and lies in the plane. On the other hand the spin-valley pseudomagnetic field $\mathbf{B}_{\rm eff}^{\rm sv}$ (independent of $\mathbf{k}$) has opposite signs in inequivalent valleys: $\mathbf{B}_{\rm eff}^{\rm sv}(\kappa) = -\mathbf{B}_{\rm eff}^{\rm sv}(\bar{\kappa})$, where $\kappa = -\bar{\kappa} = (K, K')$. Spin relaxation regimes: (b) in the pure Rashba model ($\lambda_{\rm sv} = 0$) spin lifetimes satisfy $\tau_s^\perp = \tau_s^\parallel/2$ for $\lambda\tau \ll 1$; (c) the relation is reversed in the strong SO coupling limit $\lambda\tau \gg 1$ where $\tau_s^\perp = 2\tau_s^\parallel$. This picture is affected by the spin-valley coupling and intervalley scattering, as discussed in the main text [cf. Eqs. (6.86)-(6.91)]

on TMD monolayers has been found to attain giant values on the order of $\zeta \sim 10 - 100$ [241,242], testifying to the important role played by the spin-valley SO coupling. A simple SRTA model has been proposed in Ref. [246], which assumes that the electronic motion of bare quasiparticles is affected by a weak SO field with a precession axis randomly changing due to scattering events. This framework provides the dependence of ζ on two important dimensionless parameters, $\lambda_{\rm sv}/\lambda$ and $\tau/\tau_{\rm iv}$, where $\tau_{\rm iv}$ is the sample-specific intervalley correlation time [243]. However, the formalism presented there is limited to the weak SO coupling regime, $\lambda_{\rm SOC}\tau \ll 1$ with $\lambda_{\rm SOC} = \max\{|\lambda|, |\lambda_{\rm sv}|\}$, whereas ultra-clean samples can display strong SO coupling on the order of (or larger than) the disorder broadening [125,126,247]. Meanwhile, the development of a *microscopic* approach capable of providing an intuitive, unified description of spin relaxation processes for arbitrary values of $\lambda_{\rm SOC}\tau$ and $\lambda_{\rm SOC}\tau_{\rm iv}$ would be highly desirable. Here, we address this problem by means of the single-particle density matrix formalism. We obtain a set of coupled spin Bloch equations governing the spin dynamics in the effective C_{3v} Hamiltonian in the presence of common sources of intravalley and intervalley disorder. The treatment employed here is strictly valid in the SC transport regime of experimental relevance, $|\epsilon| \gg \lambda_{\rm SOC}$. However, the qualitative features of the different spin relaxation regimes predicted here are also expected to manifest at low electronic densities. Rich scenarios are shown to emerge, from simple exponentially-decaying spin polarisation density to fast damped modes, depending on the relative magnitude of the main energy scales of the problem: λ, $\lambda_{\rm sv}$, $1/\tau$ and $1/\tau_{\rm iv}$. Finally, we derive analytic expressions for the SRTA ratio ζ in both weak SO coupling regime (compatible with Ref. [243]) and the strong SO coupling regime of ultra-clean samples ($\lambda_{\rm SOC}\tau \gtrsim 1/2$).

Formalism: spin Bloch equations

It is convenient to perform our treatment in the highly-doped regime. In this limit, we can rewrite the C_{3v} Hamiltonian Eq. (3.54), supplemented with generic disorder $V(\mathbf{x})$, by separating the bare graphene part to the uniform SO part $V_{\rm SO}$

$$H = \int d\mathbf{x}\, \Psi^\dagger(\mathbf{x})\, [\tau_z\, v\, \boldsymbol{\sigma}\cdot\mathbf{p} + V_{\rm SO} + V(\mathbf{x})\,]\, \Psi(\mathbf{x})\,. \tag{6.37}$$

The starting point of our approach is the quantum Liouville equation for the single-particle density matrix operator [147–150, 248]

$$\frac{\partial \rho}{\partial t} + \imath[\, H_0 + V_{\rm SO} + V, \rho\,] = 0\,. \tag{6.38}$$

As said above, the interaction V describes uncorrelated disorder

$$V(\mathbf{x}) = V_{\rm intra}(\mathbf{x}) + V_{\rm inter}(\mathbf{x})\,, \tag{6.39}$$

$$= \sum_{\alpha=0,z}\sum_{\beta=0,x,y,z} [\tau_0\sigma_\alpha u_{\alpha\beta}(\mathbf{x})]s_0 + \sum_{\alpha=x,y}\sum_{\beta=0,x,y} [\tau_\alpha\sigma_\beta u_{\alpha\beta}(\mathbf{x})]s_0\,, \tag{6.40}$$

with Gaussian (white-noise) statistics[1]

$$\langle u_{\alpha\beta}(\mathbf{x}) u_{\alpha'\beta'}(\mathbf{x}')\rangle_{\rm dis} = u^2_{\alpha\beta}\,\delta_{\alpha\alpha'}\,\delta_{\beta\beta'}\,\delta(\mathbf{x}-\mathbf{x}')\,. \tag{6.41}$$

All types of non-magnetic disorder are included in $V(\mathbf{x})$. Interactions $\propto \sigma_{0,z}$ describe on-site potentials and terms $\propto \sigma_{x,y}$ encode fluctuations in the hopping between neighbouring sites (e.g., due to adatoms and ripples) [173]. The terms in the second addend [Eq. (6.40)] mix states on inequivalent valleys leading to a finite intervalley scattering time.

In order to derive the general spin Bloch equations governing the spin dynamics for high electronic density, we follow closely the treatment by Culcer and Winkler [147,148]. The first step is to project Eq. (6.38) onto plane-wave eigenstates of the unperturbed graphene Hamiltonian, namely (see Appendix A)

$$\langle \mathbf{x}|\mathbf{k}\sigma\kappa s\rangle = \frac{1}{\sqrt{2}}\, e^{i\mathbf{k}\cdot\mathbf{x}}|\kappa\rangle \otimes \begin{pmatrix} \kappa\,\sigma\, e^{-\imath\phi_{\mathbf{k}}/2} \\ e^{\imath\phi_{\mathbf{k}}/2} \end{pmatrix} \otimes |s\rangle\,, \tag{6.42}$$

where $\kappa,\sigma,s = \pm 1$ are indices for valley, sublattice and spin DOFs, respectively. The free graphene eigenvalues read as $\epsilon^{\sigma\kappa s}_{\mathbf{k}} = \sigma v k$, where $k = |\mathbf{k}|$. ρ is then a matrix of dimension $2^3 = 8$, whose matrix elements are written as $\rho^{\varsigma\varsigma'}_{\mathbf{k}\mathbf{k}'} = \langle \mathbf{k}'\varsigma'|\rho|\mathbf{k}\varsigma\rangle$ and $\varsigma = \{\sigma,\kappa,s\}$ is a short-hand for the set of quantum indices (we use a similar notation for V). $V_{\rm SO}$ has non-zero matrix elements between conduction and valence states leading to interband transitions. However, we focus here on the large Fermi energy regime $\epsilon/\lambda_{\rm SOC} \gg 1$, where interband coherence effects are strongly suppressed[2]. In what follows, we take $\langle \mathbf{k}'\sigma'|\rho|\mathbf{k}\sigma\rangle = \delta_{\sigma\sigma'}\rho_{\mathbf{k}\mathbf{k}'}$ and fix the Fermi level in the conduction band, dropping the sublattice index ($\sigma = 1$) from the expressions.

Following Refs. [147, 148], we write $\rho_{\mathbf{k}\mathbf{k}'} = f_{\mathbf{k}\mathbf{k}}\delta_{\mathbf{k}\mathbf{k}'} + g_{\mathbf{k}\mathbf{k}'}$, where for $g_{\mathbf{k}\mathbf{k}'}$ it is assumed $\mathbf{k} \neq \mathbf{k}'$. We neglect valley coherence, $\langle \kappa'|\rho|\kappa\rangle = \delta_{\kappa\kappa'}$, since typical valley-coherence times are

[1] To simplify the notation here, we omit the explicit dependence on the impurities areal density n_i, rescaling the scattering potential strength as $u^2 \to u^2/n_i$ [cf. Eq. (2.16)].

[2] Since the spin-valley interaction is proportional to the identity matrix in sublattice space σ_0, it cannot mediate interband transitions. Thus, strictly speaking, it suffices to consider $\epsilon/|\lambda| \gg 1$ to neglect interband effects.

much shorter than the relevant spin-precession and relaxation timescales [249]. We have

$$\frac{\partial f_{\mathbf{k}}}{\partial t} + \imath[H_0 + V_{\mathrm{SO}}, f]_{\mathbf{kk}} = -\imath[V, g]_{\mathbf{kk}}\,, \tag{6.43}$$

$$\frac{\partial g_{\mathbf{kk}'}}{\partial t} + \imath[H_0 + V_{\mathrm{SO}}, g]_{\mathbf{kk}'} = -\imath[V, g]_{\mathbf{kk}'}\,. \tag{6.44}$$

We are ultimately interested in the diagonal part $f_{\mathbf{kk}}$, as the spin observables are defined as

$$\mathbf{S} = \frac{1}{2}\mathrm{Tr}[\rho \cdot \mathbf{s}] = \frac{1}{2}\sum_{\mathbf{k},\kappa} \mathrm{tr}[f^{\kappa}_{\mathbf{kk}} \cdot \mathbf{s}] = \frac{1}{2}\sum_{\mathbf{k},\kappa} \mathbf{S}^{\kappa}_{\mathbf{k}}\,. \tag{6.45}$$

We hence solve Eq. (6.44) and substitute the solution into the RHS of Eq. (6.43), which gives the collision integral. After a somewhat lengthy but straightforward calculation, where Eqs. (6.43)- and (6.44) are expressed in the interaction picture and the evolution operator is expanded to second order in V, one arrives at the following equation for the spin components

$$\partial_t \mathbf{S}^{\kappa}_{\mathbf{k}} + L^{\kappa}_{\mathbf{k}} \mathbf{S}^{\kappa}_{\mathbf{k}} = -\pi \sum_{\mathbf{k}'\kappa'} \delta(\epsilon_{\mathbf{k}} - \epsilon_{\mathbf{k}'}) \left\langle \mathbf{S}^{\kappa}_{\mathbf{k}}\, V^{\kappa\kappa'}_{\mathbf{kk}'}\, V^{\kappa'\kappa}_{\mathbf{k}'\mathbf{k}} + V^{\kappa\kappa'}_{\mathbf{kk}'}\, V^{\kappa'\kappa}_{\mathbf{k}'\mathbf{k}}\, \mathbf{S}^{\kappa}_{\mathbf{k}} - 2\, V^{\kappa\kappa'}_{\mathbf{kk}'}\, \mathbf{S}^{\kappa'}_{\mathbf{k}'}\, V^{\kappa'\kappa}_{\mathbf{k}'\mathbf{k}} \right\rangle_{\mathrm{dis}}\,, \tag{6.46}$$

with a Larmor precession term

$$L^{\kappa}_{\mathbf{k}} = 2 \begin{pmatrix} 0 & -\kappa\lambda_{\mathrm{sv}} & \lambda\cos\phi_{\mathbf{k}} \\ \kappa\lambda_{\mathrm{sv}} & 0 & \lambda\sin\phi_{\mathbf{k}} \\ -\lambda\cos\phi_{\mathbf{k}} & -\lambda\sin\phi_{\mathbf{k}} & 0 \end{pmatrix}. \tag{6.47}$$

A comment is in order. Central to our derivation of the quantum kinetic equation is the assumption of Gaussian disorder. Strictly speaking, the latter is equivalent to the first BA [236] and thus it neglects (i) skew scattering (allowed in the C_{3v} model [169], albeit suppressed in the limit $\epsilon/\lambda_{\mathrm{SOC}} \gg 1$ [53]) and (ii) modifications to the energy dependence of the collision integral for realistic (non-Gaussian) disorder with typical momentum scattering time $\tau(\epsilon) \propto \epsilon$ (as opposed to $\tau(\epsilon) \propto \epsilon^{-1}$ for Gaussian disorder) [250].

Importantly, the collision integral [RHS of Eq. (6.46)] retains its form at all orders in the Born series, with V formally replaced by the single-impurity T-matrix [172]. For this reason, our final expressions for the spin lifetimes (written in terms of transport scattering times, see below) remain accurate for general types of non-magnetic static disorder.

Next, we use the quantum kinetic equation [Eq. (6.46)] to obtain the Bloch equations governing the spin dynamics. Firstly, we separate the collision integral $I[\mathbf{S}^{\kappa}_{\mathbf{k}}]$ into intravalley and intervalley parts, $\kappa' = \{\kappa, \bar{\kappa}\} = \{\kappa, -\kappa\}$. For uncorrelated matrix disorder [Eq. (6.41)], we find

$$\langle |V^{\kappa\kappa}_{\mathbf{kk}'}|^2 \rangle_{\mathrm{dis}} = \sum_{p=\pm} \left[\tilde{u}_p^2 + (u_p^2 - \tilde{u}_p^2) F^p_{\mathbf{kk}'} \right], \tag{6.48}$$

$$\langle |V^{\kappa\bar{\kappa}}_{\mathbf{kk}'}|^2 \rangle_{\mathrm{dis}} = \sum_{p=\pm} \left[\tilde{w}_p^2 + (w_p^2 - \tilde{w}_p^2) F^p_{\mathbf{kk}'} \right], \tag{6.49}$$

where $F^{\pm}_{\mathbf{k}\mathbf{k}'} = \cos^2[(\phi_{\mathbf{k}} \pm \phi_{\mathbf{k}'})/2]$ and

$$u_+^2 = u_{0x}^2 + u_{zx}^2\,, \quad u_-^2 = u_{00}^2 + u_{z0}^2\,, \tag{6.50}$$

$$\tilde{u}_+^2 = u_{0y}^2 + u_{zy}^2\,, \quad \tilde{u}_-^2 = u_{0z}^2 + u_{zz}^2\,, \tag{6.51}$$

$$w_+^2 = u_{xx}^2 + u_{yx}^2\,, \quad w_-^2 = u_{x0}^2 + u_{y0}^2\,, \tag{6.52}$$

$$\tilde{w}_+^2 = u_{xy}^2 + u_{yy}^2\,, \quad \tilde{w}_-^2 = u_{xz}^2 + u_{yz}^2\,. \tag{6.53}$$

Since Gaussian disorder preserves parity $F^{\pm}_{\mathbf{k}\mathbf{k}'} = F^{\pm}_{\mathbf{k}'\mathbf{k}}$, the dynamics of spin polarisation density is governed by only three microscopic relaxation rates, which are simple functions of the disorder couplings (see Appendix D). To illustrate the various spin relaxation regimes, it suffices to consider a pair of couplings leading to a finite intervalley scattering time. Without loss of generality, we choose

$$u \equiv u_- = \sqrt{u_{00}^2 + u_{z0}^2}\,, \tag{6.54}$$

$$w \equiv w_- = \sqrt{u_{x0}^2 + u_{y0}^2}\,. \tag{6.55}$$

Within the subset of disorder couplings, we can recast the collision integral into the form

$$I^{\text{intra}}[\mathbf{S}^{\kappa}_{\mathbf{k}}] = -2\pi\, u^2 \sum_{\mathbf{k}'} F_{\mathbf{k}\mathbf{k}'}(\mathbf{S}^{\kappa}_{\mathbf{k}} - \mathbf{S}^{\kappa}_{\mathbf{k}'})\,\Delta_{\mathbf{k}\mathbf{k}'}\,, \tag{6.56}$$

$$I^{\text{inter}}[\mathbf{S}^{\kappa}_{\mathbf{k}}] = -2\pi\, w^2 \sum_{\mathbf{k}'} (1 - F_{\mathbf{k}\mathbf{k}'})\,(\mathbf{S}^{\kappa}_{\mathbf{k}} - \mathbf{S}^{\bar{\kappa}}_{\mathbf{k}'})\,\Delta_{\mathbf{k}\mathbf{k}'}\,, \tag{6.57}$$

where $\Delta_{\mathbf{k}\mathbf{k}'} \equiv \delta(\epsilon_{\mathbf{k}} - \epsilon_{\mathbf{k}'})$. To solve the coupled system of 6 equations (3 polarisation $\times$ 2 valleys), Eq. (6.46), we expand $\mathbf{S}^{\check{}}_{\mathbf{k}}$ in cylindric harmonics

$$\mathbf{S}^{\kappa}_{\mathbf{k}} = \sum_{m=-\infty}^{\infty} \mathbf{S}^{\kappa,m}_{k}\, e^{\imath\, m\, \phi_{\mathbf{k}}}\,. \tag{6.58}$$

Substituting Eq. (6.58) into Eq. (6.46), and retaining only the lowest-order harmonics $m = 0, \pm 1$, we finally obtain (see Appendix D for details)

$$\partial_t S^0_x = -\frac{2r^2}{\tau}(S^0_x - \bar{S}^0_x) - 2\lambda_{\text{sv}} S^0_y + \lambda \sum_{m=\pm 1} S^m_z\,, \tag{6.59}$$

$$\partial_t S^0_y = -\frac{2r^2}{\tau}(S^0_y - \bar{S}^0_y) + 2\lambda_{\text{sv}} S^0_x + \imath\lambda \sum_{m=\pm 1} m S^m_z\,, \tag{6.60}$$

$$\partial_t S^0_z = -\frac{2r^2}{\tau}(S^0_z - \bar{S}^0_z) - \lambda \sum_{m=\pm 1} \left(S^m_x + \imath m S^m_y\right)\,, \tag{6.61}$$

and

$$\partial_t S^{\pm 1}_x = \lambda S^0_z - 2\lambda_{\text{sv}} S^{\pm 1}_y - h(S^{\pm 1}_x, \bar{S}^{\pm 1}_x)\,, \tag{6.62}$$

$$\partial_t S^{\pm 1}_y = \mp\imath\lambda S^0_z + 2\lambda_{\text{sv}} S^{\pm 1}_x - h(S^{\pm 1}_y, \bar{S}^{\pm 1}_y)\,, \tag{6.63}$$

$$\partial_t S^{\pm 1}_z = -\lambda(S^0_x \mp \imath S^0_y) - h(S^{\pm 1}_z, \bar{S}^{\pm 1}_z)\,, \tag{6.64}$$

where

$$h(S^{\pm 1}_i, \bar{S}^{\pm 1}_i) = \frac{1}{\tau}[(1 + 2r^2) S^{\pm 1}_i + r^2 \bar{S}^{\pm 1}_i]\,, \tag{6.65}$$

with $(\mathbf{S}^{\kappa=\pm 1,m}_k)_i \equiv (S^m_i, \bar{S}^m_i)$. We have introduced the ratio of intervalley to intravalley disorder

couplings

$$r = w/u\,, \tag{6.66}$$

and[3]

$$\tau = (u^2\epsilon/4v^2)^{-1}\,, \tag{6.67}$$

$$\tau_{\rm iv} = \tau/3r^2\,, \tag{6.68}$$

the intravalley and intervalley transport scattering times, respectively. The spin Bloch equations [Eqs. (6.59)-(6.64)] and the corresponding expressions for the barred component at $\kappa = -1$, obtained by the formal replacement $S \to \bar{S}$ and $\lambda_{\rm sv} \to -\lambda_{\rm sv}$, are the central result of this section. These equations highlight the crucial role played by intervalley scattering ($r > 0$); first term on the RHS of Eqs. (6.59)-(6.61) for $m = 0$ and last two terms inside brackets in Eq. (6.65) for $m = \pm 1$. The spin Bloch equations for the full disorder model have the same structure as Eqs. (6.59)-(6.64) with an additional intervalley relaxation rate. The remaining couplings ($u_+, w_+, \tilde{u}_\pm$ and $\tilde{w}_\pm$) are found to (i) renormalise the total τ and $\tau_{\rm iv}$ and (ii) open an additional intervalley channel. For brevity, in what follows we assume $\lambda, \lambda_{\rm sv} > 0$.

Results

We are primarily interested in the zeroth harmonics of the various spin components, which according to Eq. (6.45) completely determine the spin density observables [4]. Below, we derive closed formulas for the time dependence of the spin polarisation density in two limiting cases, $\lambda \gg \lambda_{\rm sv}$ and $\lambda \ll \lambda_{\rm sv}$.

Intravalley scattering only: $w = 0$

The calculations are carried out explicitly for the out-of-plane component $S_z \equiv S^0_z + \bar{S}^0_z$. The spin Bloch equations are recast in the following form

$$\begin{pmatrix} \partial_t & \lambda & 0 \\ -4\lambda & \partial_t + \frac{1}{\tau} & 2\lambda_{\rm sv} \\ 0 & -2\lambda_{\rm sv} & \partial_t + \frac{1}{\tau} \end{pmatrix} \begin{pmatrix} S_z \\ y \\ z \end{pmatrix} = \begin{pmatrix} 0 \\ 0 \\ 0 \end{pmatrix}\,, \tag{6.69}$$

where we introduced the following admixtures of in-plane spin harmonics

$$y = \sum_{m=\pm 1} (S^m_x + \bar{S}^m_x) + \imath\, m\, (S^m_y + \bar{S}^m_y)\,, \tag{6.70}$$

$$z = \sum_{m=\pm 1} (S^m_y + \bar{S}^m_y) - \imath\, m\, (S^m_x + \bar{S}^m_x)\,. \tag{6.71}$$

The eigenfunctions can be written as

$$\begin{pmatrix} S_z(t) \\ y(t) \\ z(t) \end{pmatrix} = \sum_{i=1}^{3} c_i{}'_i e^{\omega_i t}\,, \tag{6.72}$$

[3] Note that τ is defined with an extra factor of 2 with respect to Eq. (3.35) derived within Kubo formalism. This is an artefact of limiting our ansatz to a finite number of harmonics. The physics described in the following is not affected by this choice.

[4] Harmonics with $m = \pm 1$ contain information about spin currents, which couple to the spin density in Eqs. (6.59)-(6.64) via the Rashba interaction.

where ω_i are the the solution of the algebraic equation

$$\omega^3 + \frac{2}{\tau}\omega^2 + \left[4(\lambda^2 + \lambda_{\rm sv}^2) + \frac{1}{\tau^2}\right]\omega + \frac{4\lambda^2}{\tau} = 0\,, \tag{6.73}$$

and φ_i are the corresponding eigenvectors. The coefficients c_i are determined by imposing the Cauchy boundary conditions $S_z^0(t=0) = 1/2$, $y(t=0) = z(t=0) = 0$. The analytical solution to Eq. (6.73) is rather cumbersome. It is more transparent instead to find a solution perturbatively by expanding

$$\omega = \omega^{(0)} + \beta\,\omega^{(1)} + \beta^2\omega^{(2)} + O(\beta^3)\,, \tag{6.74}$$

where $\beta = \lambda_{\rm sv}/\lambda$ ($\beta = \lambda/\lambda_{\rm sv}$) representing the case of dominant Rashba (spin-valley) interaction. We find

$$S_z(t) = \frac{1}{4}\sum_{s=\pm1}\left(1 - \frac{s}{\sqrt{1-c_z^2}}\right)e^{-\omega_s t}\,,\ \text{for}\,\lambda \gg \lambda_{\rm sv}\,, \tag{6.75}$$

where $c_z = 4\lambda\tau$ and

$$\omega_s = \frac{(1 + s\sqrt{1-c_z^2})}{2\tau}\left(1 - \frac{\lambda_{\rm sv}^2}{2\lambda^2}\frac{c_z^2}{c_z^2 - 1 + s\sqrt{1-c_z^2}}\right). \tag{6.76}$$

In the particular case $\lambda_{\rm sv} = 0$, we obtain $\omega_s = 1/\tau_s^{\perp}$ with

$$\tau_s^{\perp} = (4\lambda^2\tau)^{-1}, \tag{6.77}$$

which is the familiar DP relation [236]. In this regime, the spin relaxation is governed by motional narrowing, yielding its characteristic dependence $\tau_s \propto \tau^{-1}$ [150, 246]. On the other hand, for well-resolved SO coupling, the electron's spin completes full Larmor precession cycles in between scattering events, which induces spin-memory loss with a characteristic law $\tau_s \approx 2\tau$ (see Fig. 6.4 and discussion below) [251–253].

Combining the two limiting cases, we have

$$S_z(t)|_{\lambda\gg\lambda_{\rm sv}} = \frac{1}{2}\begin{cases}\exp[-4\,\lambda^2\tau\,t\,(1 - 4\lambda_{\rm sv}^2\tau^2)]\,, & \lambda\tau \ll 1\\ e^{-t/2\tau}\cos(2\,\lambda\,t(1 + \lambda_{\rm sv}^2/\lambda^2))\,, & \lambda\tau \gg 1\end{cases} \tag{6.78}$$

The damped oscillatory mode appears when $\lambda \gtrsim 1/2\tau$ similarly to non-chiral 2DEGs subject to strong Rashba effect [251–253]. For the in-plane component, we find

$$S_x(t)|_{\lambda\gg\lambda_{\rm sv}} = \frac{1}{2}\begin{cases}\cos(2\lambda_{\rm sv}t)\times & \\ \exp[-2\,\lambda^2\tau\,t(1 - 4\lambda_{\rm sv}^2\tau^2)]\,, & \lambda\tau \ll 1\,,\\ \cos(\lambda t)^2\,e^{-\frac{t}{\tau}}\,, & \lambda\tau \gg 1\,.\end{cases} \tag{6.79}$$

where the solution in the strong SO coupling limit includes the higher-order harmonics $m = \pm 2$ [see Eq. (6.58)]. In samples with dominant spin–valley SO coupling ($\lambda_{\rm sv} \gg \lambda$), we find instead

$$S_z(t)|_{\lambda_{\rm sv}\gg\lambda} = \frac{1}{2}\exp\left[-\frac{4\lambda^2\tau\,t}{1 + 4\lambda_{\rm sv}^2\tau^2}\right], \tag{6.80}$$

which provides the asymptotic behaviour

$$S_z(t)|_{\lambda_{\rm sv}\gg\lambda} = \frac{1}{2}\begin{cases} \exp[-4\,\lambda^{\,2}\tau\, t(1-4\lambda_{\rm sv}^2\tau^2)]\,, & \lambda_{\rm sv}\tau \ll 1\,, \\ e^{-\frac{t}{\tau}\frac{\lambda^2}{\lambda_{\rm sv}^2}}\,, & \lambda_{\rm sv}\tau \gg 1\,. \end{cases} \tag{6.81}$$

For the in-plane component, we have

$$S_x(t)|_{\lambda_{\rm sv}\gg\lambda} = \frac{1}{2}\begin{cases} \cos\left(2\lambda_{\rm sv}t\right)\times \\ \exp[-2\,\lambda^{\,2}\tau\, t(1-4\lambda_{\rm sv}^2\tau^2)]\,, & \lambda_{\rm sv}\tau \ll 1 \\ \cos\left[2\lambda_{\rm sv}t\left(1+\frac{\lambda^2}{\lambda_{\rm sv}^2}\right)\right] e^{-\frac{t}{2\tau}\frac{\lambda^2}{\lambda_{\rm sv}^2}}\,, & \lambda_{\rm sv}\tau \gg 1 \end{cases} \tag{6.82}$$

with the transition between overdamped and damped oscillatory modes occurring for $\lambda_{\rm sv} \gtrsim 1/\tau$.

These results deserve some comments. For strong Rashba interaction ($\lambda_{\rm sv} \ll 1/\tau \ll \lambda$), second line of Eqs. (6.78) and (6.79), the spin polarisation density includes an oscillatory component. Note, however, that only in-plane spins experience spin-valley–modulated precession, with small frequency $\omega = 2\lambda_{\rm sv} \ll \lambda$ in this particular regime; see Eq. (6.79), first line. The lack of spin-valley-driven precession for out-of-plane spins can be understood from simple commutator algebra, $\partial_t S_z \propto \imath[H_{\rm sv}, S_z] = 0$. In the limiting case of strong spin-valley interaction ($\lambda \ll 1/\tau \ll \lambda_{\rm sv}$), this reflects in a purely decaying (overdamped) mode for S_z—second line of Eq. (6.81)—and underdamped behaviour for S_x with a large frequency $\omega = 2\lambda_{\rm sv} \gg \lambda$; second line of (6.82). As we show in the following section, the spin dynamics in clean samples with long $\tau_{\rm iv}$ display similar behaviour (see Fig. 6.5). In systems with $\lambda \gg \lambda_{\rm sv}, 1/\tau$, the spin lifetimes are given by $\tau_s^{\parallel} = \tau$ and $\tau_s^{\perp} = 2\tau$. Here, a single scattering event suffices to randomise the electron's spin. The faster decay rate of in-plane spin polarisation component indicates the dominant role of $|m| = 2$ contributions in the harmonic expansion Eq. (6.58), yielding a SRTA ratio $\zeta = 2$. For dominant spin–valley interaction ($\lambda_{\rm sv} \gg \lambda$), the spin lifetime is extremely long and, as such, in-plane spins can precess coherently. As pointed out in Ref. [243], this behaviour is dramatically changed when intervalley scattering is included in the picture (see below). For weak SO coupling, namely, $\lambda \ll \lambda_{\rm sv} \ll 1/\tau$ and $\lambda_{\rm sv} \ll \lambda \ll 1/\tau$, the spin dynamics is of the DP type i.e., $\tau_s \propto \tau^{-1}$, as reported in the first lines of Eqs. (6.78)-(6.79) and (6.81)-(6.82). In the former case, the spin-valley interaction leads to a correction of order $\propto \lambda_{\rm sv}^2/\lambda^2$ to the well-known DP spin relaxation law of Rashba models [228, 236, 246]. In the weak SO coupling regime (for finite λ), the spin lifetimes satisfy the standard ratio, $\zeta \simeq 1/2$. On the other hand, the limiting case of vanishingly small Rashba interaction $\lambda \ll \lambda_{\rm sv} \ll 1/\tau$ is very different in this respect. The valley-Zeeman-like interaction does not couple to electrons' velocity and, at a given valley, its direction is fixed ($\pm\hat{z}$). Thus, in this case, no randomisation of the precession axis can occur and the spin relaxation is efficiently suppressed as $\lambda \to 0$. Yet, a small Rashba interaction is sufficient to relax the spins via motional narrowing, as reported in our equations.

From these results, the SRTA ratio for *intravalley disorder* is readily obtained

$$\zeta|_{\tau_{\rm iv}\to\infty} = \begin{cases} 2\,, & \lambda\tau \gg \{1, \lambda_{\rm sv}\tau\} \\ 1/2\,, & \text{all other cases} \end{cases}\,. \tag{6.83}$$

In samples with strong Rashba interaction $\lambda \gg \lambda_{\rm sv}, 1/\tau$, the quantum kinetic theory predicts a SRTA ratio, $\zeta = 2$. This difference with respect to the standard DP regime, $\zeta = 1/2$, stems from the distinct role of the $SU(2)$ gauge field in the two cases $\lambda\tau \ll 1$ and $\lambda\tau \gg 1$. It can be

readily verified by inspecting Eq. (6.47) that the precession period for in-plane and out-of-plane spins must satisfy $T_\perp = T_\parallel/2$ across all regimes. In the spin motional-narrowing limit (random dynamics) mentioned above, with $\lambda\tau \ll 1$, the faster precession of out-of-plane spins reflects in a different step of the random walk $\delta\varphi_\perp = 2\delta\varphi_\parallel$, hence $\tau_s^\perp = \tau_s^\parallel/2$ [Fig. 6.4(b)]. On the other hand, for $\lambda\tau \gg 1$, spins relax on the timescale of a single-impurity scattering event. Here, the in-plane spin dynamics is driven by the higher-order harmonics $S_x^{\kappa,\pm 2}$ and the inverse relation is found $\tau_s^\perp = 2\tau_s^\parallel$.

Intervalley scattering case: $w \neq 0$

Atomically-sharp defects lead to finite intervalley scattering time even in the cleanest samples [125]. Thus, the inclusion of intervalley processes in the collision integral [Eq. (6.46)] is crucial to understand the spin dynamics in realistic conditions. A similar procedure as outlined in Sec. 6 yields the spin Bloch equations

$$\begin{pmatrix} \partial_t & \lambda & 0 \\ -4\lambda & \partial_t + \frac{1}{\tau_+} & 2\lambda_{\rm sv} \\ 0 & -2\lambda_{\rm sv} & \partial_t + \frac{1}{\tau_-} \end{pmatrix} \begin{pmatrix} S_z \\ y \\ z \end{pmatrix} = \begin{pmatrix} 0 \\ 0 \\ 0 \end{pmatrix}, \tag{6.84}$$

with

$$\frac{1}{\tau_\pm} = \frac{1}{\tau} + \frac{1}{3} \times \frac{2 \pm 1}{\tau_{\rm iv}}. \tag{6.85}$$

We obtain the following asymptotic solutions for the out-of-plane spin polarisation density

$$S_z(t)|_{\lambda \gg \lambda_{\rm sv}} = \frac{1}{2} \begin{cases} \exp[-4\,\lambda^2\,\tau_+\,t\,(1 - 4\lambda_{\rm sv}^2\tau_+\tau_-)], & \lambda\tau \ll 1\,, \\ \cos\left[2\lambda\left(1 + \frac{\lambda_{\rm sv}^2}{\lambda^2}\right)t\right] e^{-t/2\tau_+}, & \lambda\tau \gg 1\,. \end{cases} \tag{6.86}$$

and

$$S_z(t)|_{\lambda \ll \lambda_{\rm sv}} = \frac{1}{2} \begin{cases} \exp[-4\,\lambda^2\,\tau_+\,t(1 - 4\lambda_{\rm sv}^2\tau_+\tau_-)], & \lambda_{\rm sv}\tau \ll 1\,, \\ e^{-\frac{t}{\tau_-}\frac{\lambda^2}{\lambda_{\rm sv}^2}}, & \lambda_{\rm sv}\tau \gg 1\,. \end{cases} \tag{6.87}$$

Note that as we are interested in the SRTA, in the small SO coupling cases $\lambda_{\rm SOC}\tau \ll 1$ we also took the limit $\lambda_{\rm SOC}\tau_{\rm iv} \ll 1$, where one can ignore the oscillating factors $\cos(2\lambda_{\rm sv}t)$ reported in the previous section, Eqs. (6.79) and (6.82). Considering the in-plane components, we reduce the set of coupled equations [Eqs. (6.59)-(6.64)] to only two independent equations coupling $S_x = S_x^0 + \bar{S}_x^0$ and $\tilde{S}_y = S_y^0 - \bar{S}_y^0$,

$$\begin{pmatrix} \partial_t^2 + 2\lambda^2 + \frac{\partial_t}{\tau_+} & 2\lambda_{\rm sv}(\partial_t + \frac{1}{\tau_+}) \\ -2\lambda_{\rm sv}(\partial_t + \frac{1}{\tau_-}) & \partial_t^2 + 2\tilde{\lambda}^2 + \frac{\partial_t}{\tau} + \frac{5}{3}\frac{\partial_t}{\tau_{\rm iv}} \end{pmatrix} \begin{pmatrix} S_x \\ \tilde{S}_y \end{pmatrix} = \begin{pmatrix} 0 \\ 0 \end{pmatrix}, \tag{6.88}$$

where we have defined

$$2\tilde{\lambda}^2 = 2\lambda^2 + \frac{4}{3}\frac{1}{\tau_{\rm iv}}\frac{1}{\tau_-}. \tag{6.89}$$

Solving Eq. (6.88) with the usual boundary conditions i.e., $S_x(t = 0) = 1/2$ and all the other functions being zero at the initial time, we find

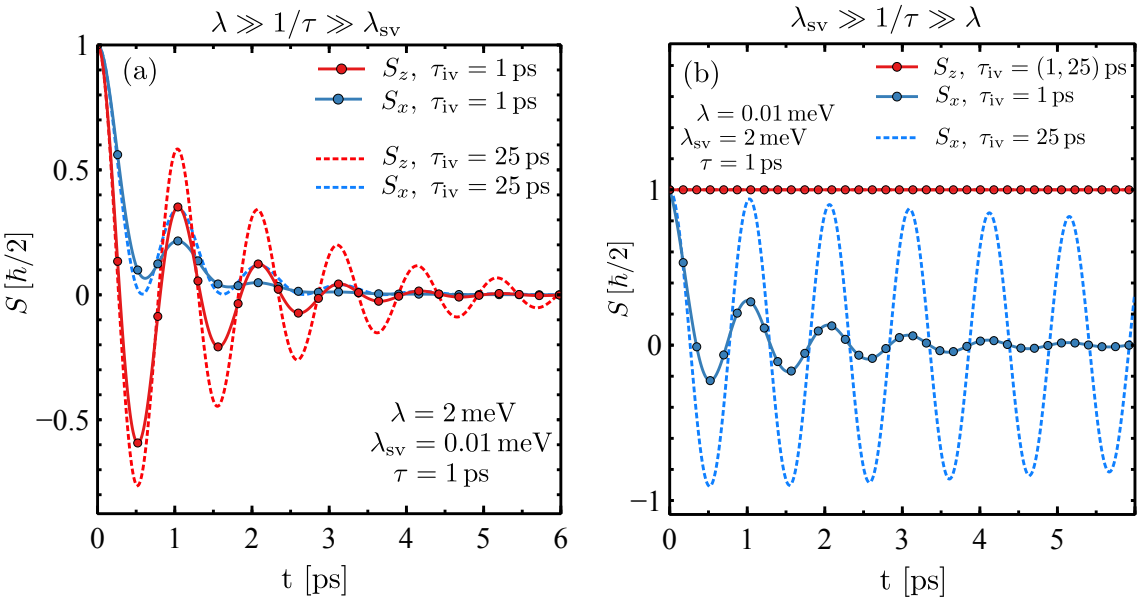

Figure 6.5: Spin dynamics for strong proximity-induced SO coupling ($\lambda_{SOC}\tau \gg 1$) in the presence of intervalley scattering. For dominant Rashba-type SO coupling (a), the spin dynamics display characteristic fast oscillations with lifetime set by the momentum scattering timescale, as discussed in the main text and illustrated in Fig. 6.4. For dominant spin-valley-type SO coupling (b) the out-of-plane component is weakly sensitive to the value of τ_{iv}. This is expected to hold in the highly-doped regime $\epsilon \gg \lambda_{sv}$, as discussed in the main text. In (a) the traces S_x are calculated including higher-order harmonics up to $m = \pm 2$.

$$S_x(t)|_{\lambda \gg \lambda_{sv}} = \frac{1}{2} \begin{cases} \exp[-(2\lambda^2\tau_+ + 3\lambda_{sv}^2\tau_{iv})t]\,, & \lambda\tau \ll 1\,, \\ \exp[-(1/2\tau_+ + 3\lambda_{sv}^2\tau_{iv})t] \times & \\ \times \cos(\lambda t)^2\,, & \lambda\tau \gg 1\,, \end{cases} \tag{6.90}$$

and

$$S_x(t)|_{\lambda \ll \lambda_{sv}} = \frac{1}{2} \begin{cases} \exp[-(2\lambda^2\tau_+ + 3\lambda_{sv}^2\tau_{iv})t]\,, & \lambda_{sv}\tau \ll 1\,, \\ \cos(2\lambda_{sv}t)\, e^{-\left(\frac{\lambda^2}{2\lambda_{sv}^2}\frac{1}{\tau} + \frac{2}{3}\frac{1}{\tau_{iv}}\right)t}\,, & \lambda_{sv}\tau \gg 1\,. \end{cases} \tag{6.91}$$

In Figs. 6.5 and 6.6, we show representative examples of the spin polarisation dynamics in the strong and weak SO coupling limits, respectively, according to our results.

Spin relaxation time anisotropy

The spin Bloch equations, Eqs. (6.59)-(6.64)—showing a crossover between overdamped (weak SO coupling) and oscillating damped modes (strong SO coupling)—are the most important result of this section. We now discuss in more detail how the SRTA evolves from weak interface-induced SO coupling ($\lambda_{SOC}\tau \ll 1$) to well-resolved SO coupling ($\lambda_{SOC}\tau \gtrsim 1$). We focus on the

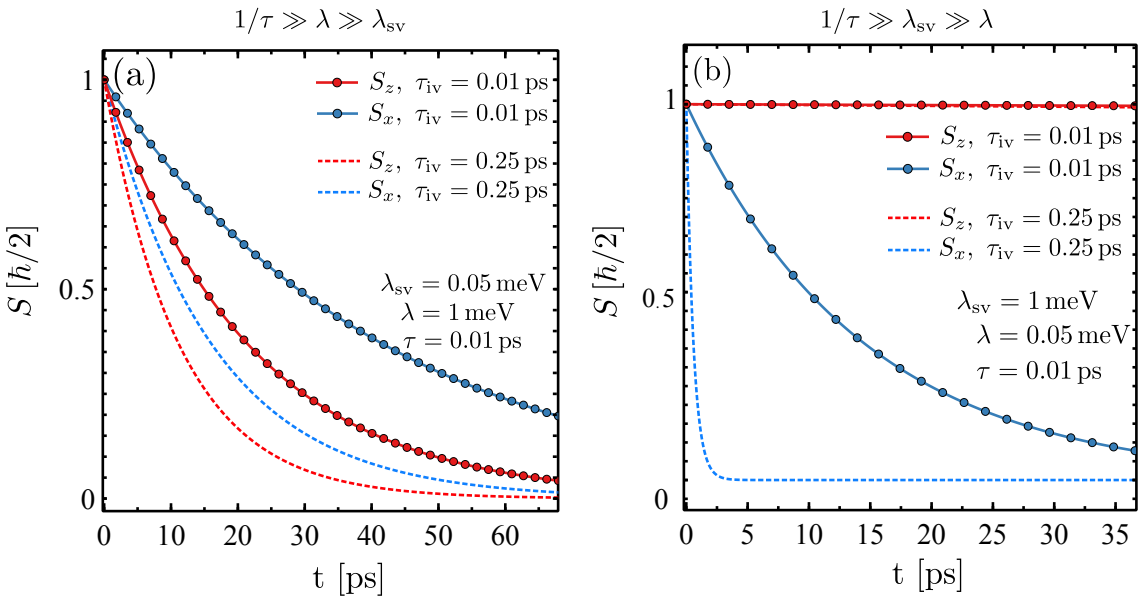

Figure 6.6: Spin dynamics for weak proximity-induced SO coupling ($\lambda_{SOC}\tau \ll 1$) in the presence of intervalley scattering, for $\lambda_{sv} \ll \lambda$ ($\lambda \ll \lambda_{sv}$) [panel (a), (b) respectively]. In (b), the in-plane spin polarisation is more sensitive to the value of τ_{iv}, whereas out-of-plane spins are virtually unaffected by a finite τ_{iv}. This is consistent with the findings in Ref. [243].

asymptotic regimes

$$\zeta = \begin{cases} \frac{1}{2} + \frac{3}{4}\frac{\lambda_{sv}^2}{\lambda^2}\left(1 + \frac{\tau_{iv}}{\tau}\right), & \lambda\tau, \lambda_{sv}\tau \ll 1, \\ 2 + O(\lambda_{sv}^2/\lambda^2), & \lambda\tau \gg 1 \gg \lambda_{sv}\tau, \\ \frac{1}{1+3\frac{\tau_{iv}}{\tau}}\left[\frac{2\lambda_{sv}^2}{\lambda^2} + \frac{3}{2}\frac{\tau_{iv}}{\tau}\right], & \lambda_{sv}\tau \gg 1 \gg \lambda\tau. \end{cases} \tag{6.92}$$

For the sake of clarity, we note that the first line in the expression for ζ is obtained by considering the first line of Eq. (6.91) [or equivalently Eq. (6.90)] together with the first line of Eq. (6.86) (or Eq. (6.87)). The second line of Eq. (6.92) is obtained using the second lines of Eq. (6.90) and Eq. (6.86). Finally the third line of Eq. (6.92) is a result of the second lines of Eq. (6.91) and Eq. (6.87).

The first important observation concerns the strong Rashba case with $\lambda\tau \gg 1 \gg \lambda_{sv}\tau$, which can in principle be achieved in clean graphene-based heterostructures, where also the lattice mismatch is sizable enough to produce $\lambda_{sv} \approx 0$. Contrary to the other two presented cases [first and third lines of Eq. (6.92)], in this limit a direct estimation of τ_{iv}/τ or λ_{sv}/λ from spin precession measurements alone is not possible. Hence, whenever $\zeta \approx 2$ is measured, the extraction of other parameters from spin precession data should be considered unfeasible.

We focus in the following on the two more interesting cases $\lambda\tau, \lambda_{sv}\tau \ll 1$ and $\lambda_{sv}\tau \gg 1 \gg \lambda\tau$. For the weak SO coupling case [first line of Eq. (6.92)] we report a visualisation of the obtained result in terms of contour lines for fixed ζ, see Fig. 6.7(a). Our results in this limit are in good qualitative agreement with the toy model of fluctuating spins put forward in Ref. [243],

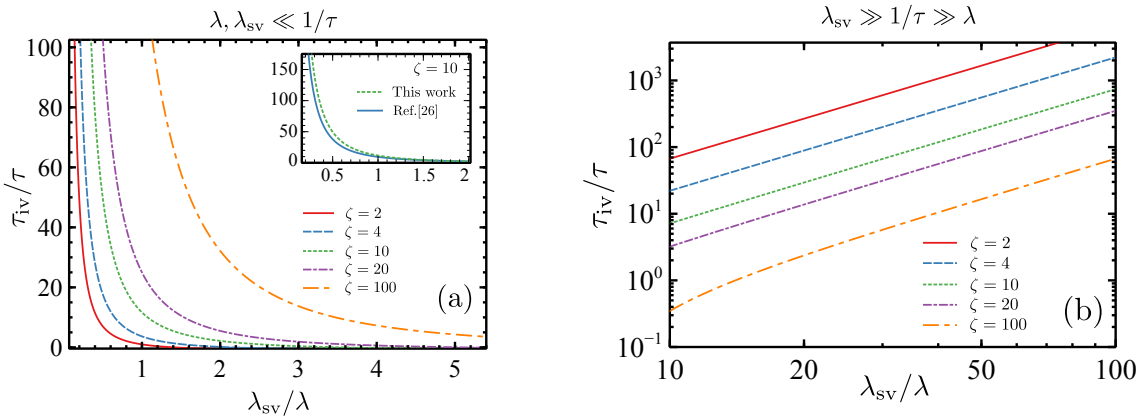

Figure 6.7: Traces of fixed SRTA for weak (a) and strong (b) proximity-induced SO coupling, Eq. (6.92). (a) The inset shows a comparison with the spin white-noise model in Ref. [243] for $\zeta = 10$. (b) Traces of fixed SRTA in the strong SO coupling regime, Eq. (6.92), third line. The typical ratio $\tau_{iv}/\tau \sim 25$ [254] is compatible with a broad range of SO couplings in the interval $\lambda_{sv}/\lambda = 14 - 80$ depending on the measured SRTA ratio.

i.e.

$$\zeta = \frac{1}{2} + \frac{\lambda_{sv}^2}{\lambda^2}\frac{\tau_{iv}}{\tau}\,, \quad \text{(Ref. [26])}\,, \tag{6.93}$$

$$\zeta = \frac{1}{2} + \frac{1}{4}\frac{\lambda_{sv}^2}{\lambda^2}\left(3 + \frac{\tau_{iv}}{\tau}\right), \quad \text{(this work)}. \tag{6.94}$$

where, for simplicity, we identified the ratio of intervalley to intravalley correlation time in Ref. [243] with the ratio τ_{iv}/τ. The inset of Fig. 6.7(a) shows a detailed comparison for the case $\zeta = 10$. Following the experiment in Ref. [242] ($\zeta = 11$), assuming $\lambda_{sv}/\lambda \sim 0.67$ for graphene/$MoSe_2$ [122], a $\tau_{iv}/\tau = 30$ is obtained, which for $\tau = 0.076$ ps gives $\tau_{iv} = 2.2$ ps (against $\tau_{iv} = 1.7$ ps following Ref. [243]). These estimates (obtained from modelling of spin precession data) agree qualitatively well with typical relaxation times extracted from magneto-transport measurements [125, 254]. We would like to point out that our Eq. (6.94) (and similarly Eq. (6.93)) gives a divergent SRTA in the limit of absence of intervalley scattering $\tau_{iv} \to \infty$, at first glance contradicting Eq. (6.83). The dilemma is solved by noticing that Eq. (6.94) is strictly valid for $\lambda_{sv}\tau \sim \lambda_{sv}\tau_{iv} \ll 1$. This particular case corresponds to the physical situation where the out-of-plane component of the "SO coupling field" is randomised on a time scale τ_{iv} (recall that $H_{sv}^{\kappa} = -H_{sv}^{\bar{\kappa}}$). This activates a dominant motional-narrowing channel for the in-plane spin component, which strongly impacts the spin dynamics as shown in Fig. 6.6.

A careful analysis of the crossover to the strong λ_{sv} regime allows one to conclude that the transition between the motional-narrowing (DP) regime $\lambda_{sv}\tau_{iv} \ll 1$ and the fast (oscillating) relaxation regime with $\lambda_{sv}\tau_{iv} \gg 1$ is achieved for $\lambda_{sv}\tau_{iv} \simeq 1/3$, assuming $\lambda \ll \lambda_{sv}$. We briefly discuss the experimental conditions for which the strong spin-valley case of Eq. (6.92) (third line) may be relevant. For instance, in Ref. [255], the authors estimate $\lambda_{sv} = 0.96\,\text{meV} \sim 32\,\lambda$, with $\tau \sim 12\,\text{ps}$ for a graphene/WS_2 heterostructure. Assuming a SRTA ratio $\zeta = 11$ (see above) and using Eq. (6.93) from Ref. [243] (or, equivalently, first line in Eq. (6.92)) one would obtain an unphysical result $\tau_{iv}/\tau \simeq 0.01 < 1$. The usage of Eq. (6.92) in the limit of strong spin-valley coupling then is required. Using this relation, we estimate $\tau_{iv}/\tau \approx 70$, which would suggest a dominant role of intravalley processes in the experiment of Ref. [255].

Conclusions

In this Chapter, we have presented a unified theory of spin and charge dynamics for 2D Dirac materials with strong proximity-induced SO coupling in generic nonstationary conditions; in particular we focused on the class of systems described by the point symmetry group C_{3v}.

Combining an evaluation of the associated WIs and explicit diagrammatic calculation, we have shown how the SHE, absent in the C_{6v} case, is restored in the presence of an out-of-plane component of the spin texture associated with the electronic bands. Being the WIs exact symmetry relations, they also provide a stringent test for real-space numerical approaches, for which the achievable energy resolutions still represent a major limiting factor.

Furthermore, we have introduced a proper figure of merit for the CSC associated with the ISGE, and shown it attains values close to unity at the minority spin band edge. The effect is robust against nonmagnetic disorder and remains large at room temperature. The ISGE is only limited by the electronic mobility, and thus it is expected to achieve unprecedentedly large values in ultraclean samples.

Finally we discussed the spin dynamics in the highly-doped regime of large Fermi energy, where the only role of the "SO coupling field" is to induce Larmor precession. We have devoted particular attention to the SRTA $\zeta = \tau_s^{\perp}/\tau_s^{\parallel}$, which is an experimentally accessible figure of merit [217]. The theoretical results reported in Ref. [243] for weak SO coupling are qualitatively reproduced by our microscopic theory. On the other hand, in ultra-clean samples with strong SO coupling on the order of (or larger than) the disorder-induced quasiparticle broadening, our microscopic theory uncovers a qualitatively different spin relaxation picture. Here, the spin polarisation density undergoes fast damped oscillations with spin lifetime set by the time scale of momentum scattering. If the Rashba interaction dominates ($\lambda \gg \lambda_{\rm sv}, 1/\tau$), our theory predicts $\tau_s^{\perp}/\tau_s^{\parallel} = 2$. For samples with dominant spin-valley interaction ($\lambda_{\rm sv} \gg \lambda, 1/\tau$), the spin relaxation anisotropy acquires a strong dependence on the relevant intravalley and intervalley scattering times. We note in passing that to incorporate the SO coupling at low electronic densities, a possibility is to adopt the self-consistent quantum diagrammatic formalism for 2D Dirac fermions recently presented in Chapter 5. This problem will be investigated in future publications.

Chapter 7

Magnetic Dirac Fermions with Spin–Orbit Interactions: Anomalous Hall and Magnetic Spin Hall Effect in 2D Dirac Materials

Overview

Ferromagnetic order in 2D crystals is of great significance for fundamental studies and applications in spintronics. Recent experiments have revealed that intrinsic ferromagnetism occurs in 2D crystals of $Cr_2Ge_2Te_6$ [256] and CrI_3 [257], while graphene and group-VI dichalcogenide monolayers acquire large exchange splitting when integrated with nanomagnets [128, 129, 258–262]. Different from bulk compounds, the electronic states of atomically thin layers can be dramatically affected by short-range magnetic interactions, opening up a new arena for studies of emergent spin-dependent phenomena [100, 263–266]. In this regard, graphene and other 2D Dirac materials with multiple internal DOFs offer particularly promising perspectives.

The AHE recently observed in graphene/YIG heterostructures indicates that the interface-induced MEC is accompanied by sizable Rashba effect [123, 129]. The breaking of inversion symmetry in a honeycomb layer couples different $SU(2)$ subspaces (spin and sublattice) [191] and can drive the ferromagnetic 2D Dirac system through a topological phase transition to a Chern insulator when the chemical potential is tuned inside the gap [100, 267]. This system is predicted to exhibit the QAH effect, with transverse conductivity $\sigma_{\mathrm{AH}} = 2e^2/h$ [52, 130, 131]. However, much less is known about the *nonquantised regime* at finite carrier density. The latter is the current experimental accessible regime [128, 129]. Beyond the nonquantised part of the intrinsic contribution, the presence of a Fermi surface makes the transverse (anomalous Hall) conductivity depend nontrivially on spin-dependent scattering due to pseudospin-spin coupling [159, 171, 172, 268]. Moreover, in ultraclean heterostructures, the MEC and SO coupling energy scales can easily reach the disorder-induced broadening [122, 123, 269], thus questioning the use of standard approaches where the SO coupling is treated as a weak perturbation.

In this Chapter we report an accurate theoretical study of charge and spin transport in magnetised 2D Dirac systems by treating the effects of strong MEC and SO coupling *nonperturbatively* in the presence of dilute random impurities. Our theory is valid for both weak (Born) and strong

(unitary) potential scattering and accounts for intervalley processes from point defects. We find that the out-of-plane component of the noncollinear spin texture $\mathbf{S}_{\mu\nu\mathbf{k}}$ [where we recall that $\nu(\mu) = \pm 1$ is associated to pseudospin (spin) chirality], see Fig. 7.1, activates a robust skew scattering mechanism, which determines the behaviour of leading Fermi surface contributions to the transverse transport coefficients. We predict that the $\mathbf{k}$ modulation of the spin polarisation manifests into a ubiquitous *change of sign* in the charge Hall conductivity as the Fermi level approaches the majority spin band edge, which, as we argue below, is a forerunner of the elusive QAH effect [128,129,258]. Second, we predict that scattered electron waves with opposite polarisation (e.g., from within the 'Mexican hat' with $S^z_{\mathbf{k}_\pm} \gtrless 0$; Fig. 7.1) have different transverse cross section leading to net spin Hall current in the bulk [30]. Such a magnetic spin Hall effect (MSHE) in a 2D Dirac system with broken time reversal symmetry can be seen as the reciprocal of the ISHE discovered recently in ferromagnets [270–272]. The common stem of AHE and MSHE implies the change of sign reveals likewise in the spin Hall response, unveiling the possibility of *reversing the spin accumulation at the sample boundaries by gate voltage*. Remarkably, the sign-change feature is found to be preserved when adding the Berry curvature-dependent contributions to the AHE and MSHE over a wide range of parameters in samples with high mobility.

Model

The low-energy Hamiltonian of graphene with proximity-induced Rashba and MEC interaction reads [in the basis used in Eq. (3.3)]

$$H = \int d\mathbf{x}\, \Psi^\dagger(\mathbf{x}) \{ v\, \tau_z\, \boldsymbol{\sigma}\cdot\mathbf{p} + \delta\, s_z + \lambda\, \tau_z \left(\sigma_x s_y - \sigma_y s_x\right) + V(\mathbf{x})\} \Psi(\mathbf{x})\,, \tag{7.1}$$

where δ is the MEC energy scale, and all the other parameters have been defined previously [see e.g. Eq. (3.3)]. This model describes magnetised graphene with C_{6v} point group symmetry and can be easily extended to other ferromagnetic 2D materials, such as $MoTe_2$/EuO [273–275]. We consider (nonmagnetic) matrix disorder with

$$V(\mathbf{x}) = \sum_{i=1}^{N_1} \left(u_0 1 + u_x \tau_x\right) \delta(\mathbf{x} - \mathbf{x}_i) \equiv \mathcal{V} \sum_{i=1}^{N_1} \delta(\mathbf{x} - \mathbf{x}_i)\,, \tag{7.2}$$

where $\{\mathbf{x}_i\}_{i=1\ldots N_i}$ are random impurity positions and $u_{0(x)}$ parameterises the intravalley (intervalley) scattering strength [171, 196]. This choice allows us to interpolate between "smooth" potentials in clean samples ($|u_x| \ll |u_0|$) and the "sharp defect" limit of enhanced backscattering processes ($u_x \approx u_0$). The energy-momentum dispersion relation associated to the clean system $\mathscr{H}_0 = \mathscr{H} - V(\mathbf{x})$ reads

$$\epsilon_{\mu\nu\mathbf{k}} = \nu \sqrt{v^2 k^2 + M_\mu^2\,(k)}\,, \tag{7.3}$$

where $M_\mu(k) = \sqrt{2\lambda^2 + \delta^2 + 2\mu\sqrt{\lambda^4 + v^2k^2(\lambda^2+\delta^2)}}$ is the SO coupling mass and $k = |\mathbf{k}|$ is the wavevector measured from a Dirac point. Indices $\{\mu,\nu\} = \pm 1$ define the spin winding direction and the carrier polarity (Fig. 7.1). In the absence of SO coupling, the Dirac cones are shifted vertically, resulting in mixed electron–hole states near the Dirac point. For $\lambda \neq 0$, $\delta = 0$ (no MEC), the spectrum admits a spin-gap or *pseudogap* region, within which the spin and momentum of quasiparticles are locked at right angles (Rashba spin texture) [170, 191]. The combination of SO coupling and MEC opens a gap and splits the Dirac spectrum into 3 branches: *regions I and III*, defined by $|\lambda\delta\,|\,/\sqrt{\lambda^2+\delta^2} \equiv \epsilon_{\rm I} < |\epsilon| < \epsilon_{\rm II} = |\delta\,|$ and $|\epsilon| > \sqrt{4\lambda^2+\delta^2} \equiv \epsilon_{\rm III}$;

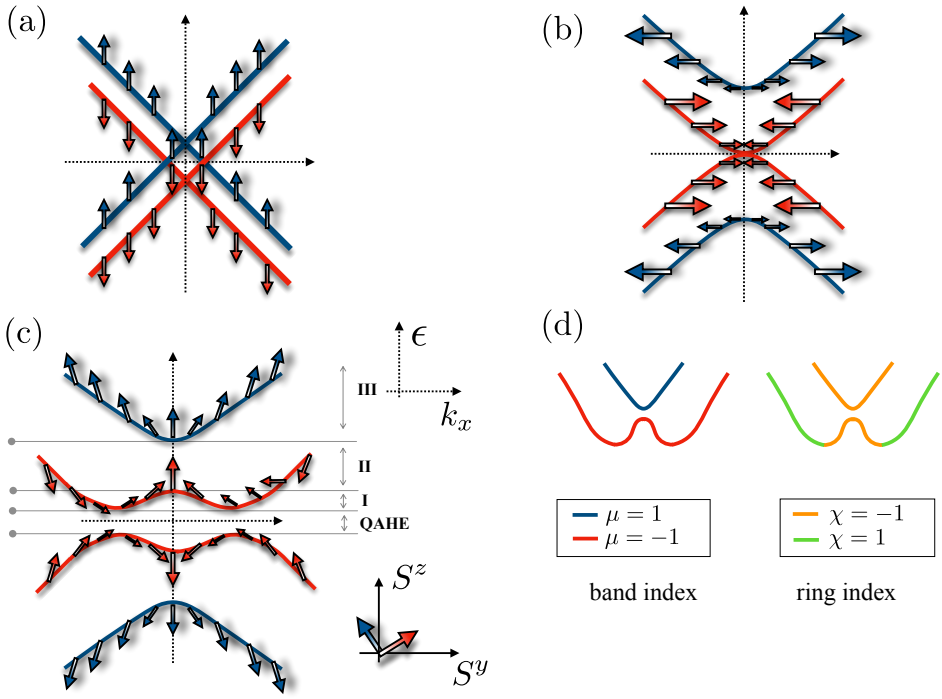

Figure 7.1: (a-c) Energy bands and spin texture in systems with (a) MEC (b) SO coupling and (c) MEC and SO coupling. For visualisation purposes, the bands are plotted along $\hat{k}_x$ (spins lie only in the yz plane). (d) Band classification using band (ring) index $\mu = \pm 1$ ($\chi = \pm 1$).

those energy regimes are characterised by a non-simply connected Fermi surface allowing for scattering between states with different Fermi momenta; and *region II*, $\epsilon_{\text{II}} < |\epsilon| < \epsilon_{\text{III}}$, with only one band intersecting the Fermi level. For brevity, all functions are projected onto valley $\tau_z = 1$ (K point). The Bloch eigenstates read as

$$\Psi_{0\mu\nu\mathbf{k}}(\mathbf{x}) \equiv \Phi_{0\mu\nu\mathbf{k}} e^{\imath \mathbf{k}\cdot\mathbf{x}} = \begin{pmatrix} e^{-\imath\phi_{\mathbf{k}}} \\ \imath \dfrac{\left(\epsilon_{\mu\nu}-\delta\right)^2 - v^2k^2}{2v k \lambda} \\ \dfrac{\epsilon_{\mu\nu}-\delta}{vk} \\ \imath \dfrac{\left(\epsilon_{\mu\nu}-\delta\right)^2 - v^2k^2}{2\lambda\left(\epsilon_{\mu\nu}+\delta\right)} e^{\imath\phi_{\mathbf{k}}} \end{pmatrix} e^{\imath \mathbf{k}\cdot\mathbf{x}}, \tag{7.4}$$

where $\phi_{\mathbf{k}}$ is the wavevector polar angle. The noncoplanar spin texture in momentum space these states are associated with, highlights the competition between different interactions: while the Rashba effect favours in-plane alignment, the exchange interaction tilts the spins out of the plane, leading to a noncoplanar band polarisation [Fig. 7.1 (c)]. The pronounced effects of symmetry breaking on the spin texture has been highlighted in other systems, e.g. surface states of Bi thin films [276]. We underline here its impact on relativistic transport: as shown below, the out-of-plane spin texture $S_{z,\mu\nu\mathbf{k}} \equiv \frac{1}{2}\langle s_z \rangle_{\mu\nu\mathbf{k}}$ modulates intrinsic and extrinsic transport contributions; even if the electronic states are not fully spin polarised, it will prove useful to refer to *effective* spin-up ($S_z > 0$) and spin-down ($S_z < 0$) states. We focus on positive energies, $\epsilon > 0$, and also $\lambda, \delta > 0$, thus fixing $\nu = 1$ and omitting this index from the expressions.

Transverse charge- and spin-current responses: solving the Boltzmann transport equations for the dominant extrinsic contribution

Spin texture-driven skew scattering

To assess the dominant extrinsic transport contributions in the metallic regime ($\epsilon > \epsilon_1$), we solve the BTEs for a spatially homogeneous system. The formalism allows for the inclusion of a nonquantised magnetic field and, more importantly, for a transparent physical interpretation of the scattering processes. The BTEs read as

$$\partial_t f_{\mathbf{k}\chi} - e\,(\boldsymbol{\mathcal{E}} + \mathbf{v}\times\boldsymbol{\mathcal{B}})\cdot\nabla_{\mathbf{k}} f_{\mathbf{k}\chi} = 2\pi n_i \sum_{\chi'=\pm1}\int \frac{S d^2\mathbf{k}'}{(2\pi)^2}\left(f_{\mathbf{k}'\chi'}\mathcal{T}_{\mathbf{k}'\chi',\mathbf{k}\chi} - f_{\mathbf{k}\chi}\mathcal{T}_{\mathbf{k}\chi\mathbf{k}'\chi'}\right)\delta(\epsilon_{\mathbf{k}\chi}-\epsilon_{\mathbf{k}'\chi'})\,, \tag{7.5}$$

where $f_{\mathbf{k}\chi} = f^0_{\mathbf{k}\chi} + \delta f_{\mathbf{k}\chi}$ is the sum of the Fermi-Dirac distribution function and $\delta f_{\mathbf{k}\chi}$, the deviation from equilibrium. Moreover, $\boldsymbol{\mathcal{E}}, \boldsymbol{\mathcal{B}}$ are external DC fields and S is the area. The RHS is the collision term describing single impurity scattering and n_i is the impurity areal density. Subscripts $\chi, \chi' = \pm1$ are *ring* indices for the *outer/inner* Fermi surfaces associated with Fermi momenta

$$k_\pm = \frac{\sqrt{\epsilon^2+\delta^2 \pm \sqrt{\epsilon^2\lambda^2 + (\epsilon^2-\lambda^2)\delta^2}}}{v}\,, \tag{7.6}$$

see Fig. 7.1(d). Accounting for possible scattering resonances due to the Dirac spectrum [171], transition rates are evaluated by means of the T-matrix approach i.e. the transition rate [Fermi golden rule, see Eq. (2.4)]

$$W_{\mathbf{k}\chi,\mathbf{k}'\chi'} = 2\pi n_i\,\mathcal{T}_{\mathbf{k}\chi\mathbf{k}'\chi'}\,\delta(\epsilon_{\mathbf{k}\chi}-\epsilon_{\mathbf{k}'\chi'}) = 2\pi n_i \left|\langle \mathbf{k}'_{\chi'}|\mathrm{T}^R|\mathbf{k}\chi\rangle\right|^2 \delta(\epsilon_{\mathbf{k}\chi}-\epsilon_{\mathbf{k}'\chi'})\,, \tag{7.7}$$

$$\mathrm{T}^R = \frac{\mathcal{V}}{1-g_0^R\mathcal{V}}\,, \tag{7.8}$$

where T^R is the retarded single-impurity T-matrix [cf. Eq. (3.20)]. Also $g_0^R = \int d^2\mathbf{k}/(4\pi^2)\,(\epsilon - H_{0\mathbf{k}} + \imath 0^+)^{-1}$ is the retarded momentum integrated propagator [see Eq. (3.22)]. In regime II, only intra-ring processes are allowed, whereas in regime I and III, one needs to take into account inter-ring transitions (see Fig. 7.2). We start by considering $u_x = 0$, for which electrons undergo *intra-* and *inter-ring* scattering processes in the same valley (see Fig. 7.2). Exploiting the Fermi surface isotropy, and momentarily setting $\boldsymbol{\mathcal{B}} = 0$, the exact solution to the linearised BTEs ($\nabla_{\mathbf{k}} f_{\mathbf{k}\chi} \to \nabla_{\mathbf{k}} f^0_{\mathbf{k}\chi}$) is [171]

$$\delta f_{\mathbf{k}\chi} = -e\left(\frac{\partial f^0_{\mathbf{k}\chi}}{\partial\epsilon}\right)\mathbf{v}_{\mathbf{k}\chi}\cdot\left(\tau^\parallel_\chi\,\boldsymbol{\mathcal{E}} + \tau^\perp_\chi\,\hat{z}\times\boldsymbol{\mathcal{E}}\right)\,, \tag{7.9}$$

with $\mathbf{v}_{\mathbf{k}\chi} = \nabla_{\mathbf{k}}\epsilon_\chi(\mathbf{k})$. In the above, $\tau^\varsigma_\chi = \tau^\varsigma_\chi(\epsilon,\lambda,\delta,u_0,n_i)$ are the longitudinal ($\varsigma = \parallel$) and transverse ($\varsigma = \perp$) transport times given by

$$\boldsymbol{\tau}^\parallel = -2\left(\hat{\Lambda} + \hat{\Upsilon}\hat{\Lambda}^{-1}\hat{\Upsilon}\right)^{-1}\mathbf{1}\,, \tag{7.10}$$

$$\boldsymbol{\tau}^\perp = \hat{\Lambda}^{-1}\hat{\Upsilon}\,\boldsymbol{\tau}^\parallel\,, \tag{7.11}$$

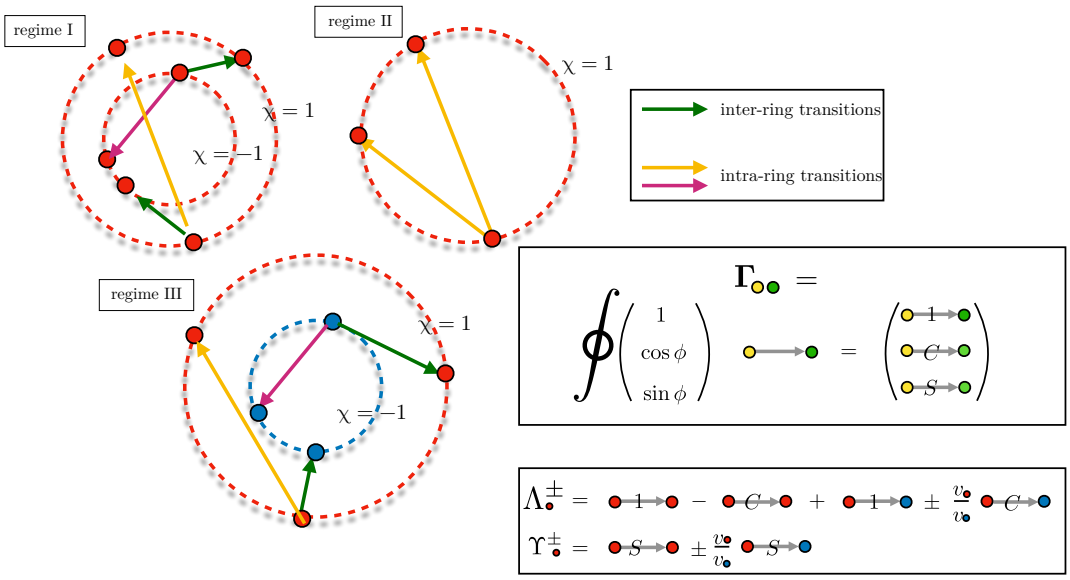

Figure 7.2: Graphic visualisation of the different impurity scattering processes in this model for the different Fermi energy ϵ regimes (I, II and III; see main text). Also we report graphically the different relaxation rates $\Lambda^{\pm}_{\chi}, \Upsilon^{\pm}_{\chi}$ mentioned in the main text. Colored dots are to be identified with the indices χ. When a generic scattering amplitude (grey segment connecting yellow and green dots) is integrated over the angle, it gives rise to different components of $\mathbf{\Gamma}_{\chi\chi'}$ depending to which trigonometric function it is contracted with. Combinations of the various components yield the different relaxation rates.

where $\boldsymbol{\tau}^{\varsigma} = (\tau^{\varsigma}_{\chi}, \tau^{\varsigma}_{\bar{\chi}})^{\mathrm{t}}$, $\hat{\Lambda} = ((\Lambda^{-}_{\chi}, \Lambda^{+}_{\chi})^{\mathrm{t}}, (\Lambda^{-}_{\bar{\chi}}, -\Lambda^{+}_{\bar{\chi}})^{\mathrm{t}})$, $\mathbf{1} = (1,0)^{\mathrm{t}}$ and $\bar{\chi} \equiv -\chi$ ($\hat{\Upsilon}$ is obtained from $\hat{\Lambda}$ via the substitution $\Lambda^{\pm}_{\chi} \to \Upsilon^{\mp}_{\chi}$). The kernels $\Lambda^{\pm}_{\chi}$ and $\Upsilon^{\pm}_{\chi}$ are cumbersome functions of symmetric and skew cross sections defined by $\mathbf{\Gamma}_{\chi\chi'} = \frac{n_i}{2\pi} \int S d^2\mathbf{k}' \, \mathcal{T}_{\mathbf{k}'_{\chi'}\mathbf{k}_{\chi}} \{1, \cos\phi, \sin\phi\}^{\mathrm{t}}$ with $\phi = \phi_{\mathbf{k}'} - \phi_{\mathbf{k}}$. We report the details of the calculation in Appendix E. Considering the two valleys, the general solution involves 16 cross sections. The exact form of the kernels is essential to correctly determine the energy dependence of the conductivity tensor. As shown in Appendix E, including a magnetic field $\boldsymbol{\mathcal{B}} = \mathcal{B}\hat{z}$ only requires the substitution $\Gamma^{\mathrm{sin}}_{\chi\chi} \to \Gamma^{\mathrm{sin}}_{\chi\chi} + \omega_{\chi}$, where $\omega_{\chi} = k_{\chi} v_{\chi}^{-1} \mathcal{B}$ is the cyclotron frequency associated with the ring states.

At $T = 0$, accounting for the valley degeneracy, we obtain the transverse response functions

$$\sigma^{c,s}_{\perp}(\mathcal{B}, \epsilon) = \frac{-e}{h} \sum_{\chi=\pm 1} k_{\chi}(\epsilon) \, \langle J_{c,s}(\epsilon) \rangle_{\chi} \, \tau^{\perp}_{\chi}(\epsilon, \mathcal{B}) \,, \tag{7.12}$$

where $\langle J_{c,s}(\epsilon) \rangle_{\chi} = -e \, \langle \{1, s_z/2\} \, \boldsymbol{\sigma} \cdot |\hat{z} \times \hat{\boldsymbol{\mathcal{E}}}| \rangle_{\chi}$ denotes the equilibrium transverse charge (spin) current of plane-wave states in the χ ring. The skew cross sections (and hence $\tau^{\perp}_{\chi}$) are found to be nonzero (except for isolated points) and thus, in the dilute regime, one has $\sigma^{c,s}_{\perp} \propto n_i^{-1}$, which is a signature of skew scattering [158]. As discussed below [cf. Fig. 7.3(a)], the energy dependence of the skew cross sections is very marked, reflecting the out-of-plane spin texture of conducting electrons. For simplicity, in what follows, we work at saturation field $\mathcal{B} \geq \mathcal{B}_{\mathrm{sat}}$ such that the transverse responses coincide with their "anomalous" parts, that is, $\sigma_{\mathrm{AH(SH)}}(\mathcal{B}_{\mathrm{sat}}, \epsilon)\big|_{\delta} \simeq \sigma_{\perp}(0, \epsilon)\big|_{\delta_{\mathrm{sat}}}$, where $\delta_{\mathrm{sat}} = \delta(M_z(\mathcal{B}_{\mathrm{sat}}))$ and M_z is the magnetisation.

The change of sign

Focusing on the regime $\lambda \lesssim \delta$, we show how, approaching low carrier density, electrons undergoing *spin-conserving* and *spin-flip* scattering processes determine a change of sign in $\sigma^{c,s}_{\perp}$. Let

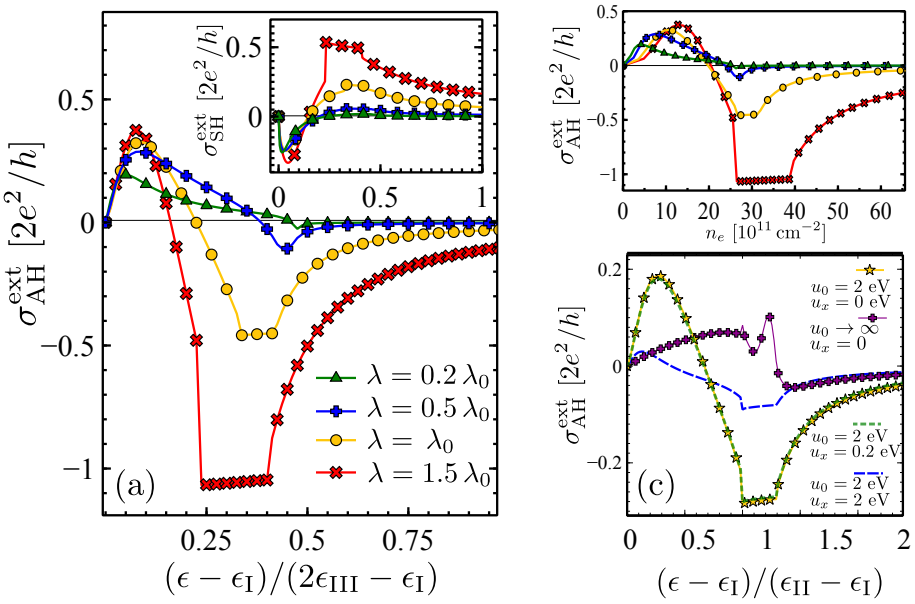

Figure 7.3: Energy dependence of AHE and MSHE. (a) $\sigma_\perp^{c,s}(\epsilon)$ is the result of the competing effective spin Lorentz forces as discussed in the main text [see also Fig. (7.1)(e)]. The *change of sign* is more prominent for large SO coupling. (b) $\sigma_\perp^c(n_e)$ where $n_e = \pi\{k_+^2 - k_-^2,\, k_+^2,\, k_+^2 + k_-^2\}$, respectively, in regions I, II, and III. (c) While less evident in the unitary limit, the change of sign is robust across all scattering regimes. $\delta = 30$ meV, $\lambda_0 = \delta/3$, $u_0 = 1\,\text{eV}\cdot\text{nm}^2$, $u_x = 0$ and $n_0 = 10^{12}\text{cm}^{-2}$.

us consider for simplicity the charge transverse response $\sigma_\perp^c \equiv \sigma_\perp$ and rewrite Eq. (7.12) in the following form

$$\sigma_\perp = \frac{e^2}{h}\sum_{\chi=\pm1} k_\chi v_\chi \tau_\chi^\perp\,. \tag{7.13}$$

Clearly, the peculiar sign-change must result from the energy dependence of transverse scattering times $\tau_\chi^\perp$. In Fig. 7.4 we show a comparison between the two $\tau_\chi^\perp$ where inter-ring transition are neglected. Both $\tau_\chi^\perp$ change sign, although $|\tau_+^\perp| > |\tau_-^\perp|$. The outer ring is also associated with a larger density of states $N_+ > N_-$, where $N_\chi = k_\chi|2\pi v_{k_\chi}|^{-1}$, as displayed in Fig. 7.4(b). The larger $\tau_+^\perp$ and $N_+^\perp$ as compared to their $\chi = -1$ counterparts suggest to focus our discussion concerning the change of sign of $\sigma_\perp$ on $\mathbf{k}_+ \to \mathbf{k}_+$ transitions, i.e. scattering transition happening in the outer ring $\chi = 1$. In addition, the out-of-plane spin polarisation S^z also changes sign within the $\chi = 1$ ring, as displayed in Fig. 7.4(c) and (d).

Having demonstrated the dominant role played by intra-ring χ=1 processes, we now discuss the physical picture behind the sign-change in $\sigma_\perp$ as the Fermi level approaches the spin majority band edge. The transverse relaxation time, in the absence of a magnetic field, is given by

$$\tau_+^\perp = \frac{\Gamma_{++}^{\rm sin}}{(\Gamma_{++}^0 - \Gamma_{++}^{\rm cos})^2 + (\Gamma_{++}^{\rm sin})^2}\,, \tag{7.14}$$

and hence the change of sign of $\tau_+^\perp$ is controlled by the antisymmetric part of $\mathcal{T}_{++}(\phi) = |\langle \mathbf{k}'_+|\mathrm{T}^R|\mathbf{k}_+\rangle|^2$. The single-impurity T-matrix can be decomposed according to the following form

$$\mathrm{T}^R = \mathrm{T}_0^R\gamma_0 + \mathrm{T}_{zz}^R\gamma_{zz} + \mathrm{T}_z^R s_z + \mathrm{T}_m^R\sigma_z + \mathrm{T}_r^R\gamma_r\,, \tag{7.15}$$

where we remind the matrix structures γ in our notation have the form $\gamma_0 \equiv \tau_0\sigma_0 s_0, \gamma_{zz} =$

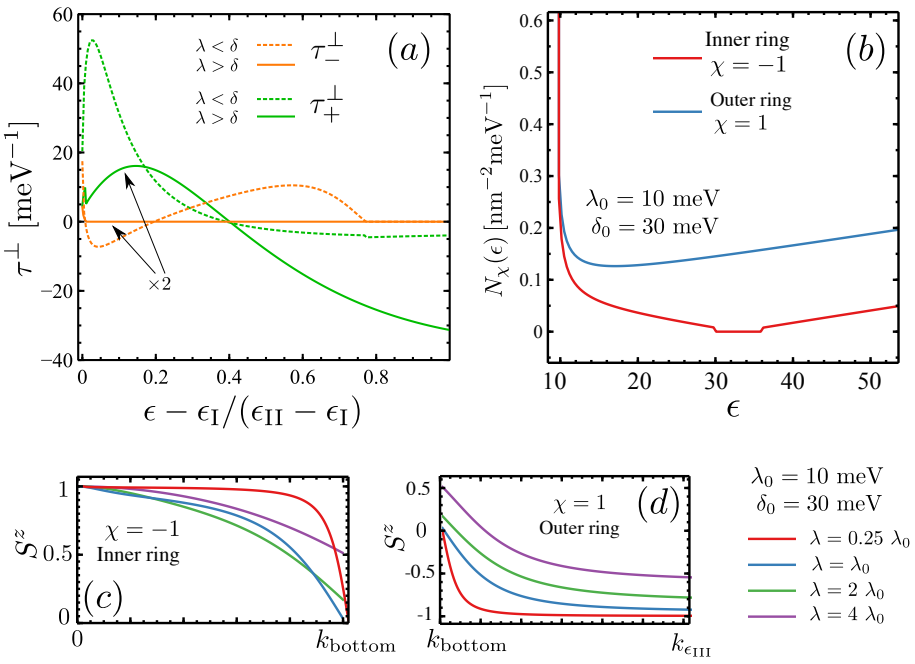

Figure 7.4: (a) Transverse scattering time in two cases of interest $\lambda \gtrless \delta$, where the larger and smaller energy scales are, respectively, 10 and 30 meV. The change of sign is clearer for $\tau^{\perp}_{+}$. (b) Also the density of states of the outer ring is generally larger (here $\lambda > \delta$). (c) Finally it is shown the sign change in the out-of-plane spin polarisation happens within the ring $\chi = 1$. Parameters: $u_0 = 0.36$ eV·nm^{-2} and $n_i = 10^{12}$ cm^{-2}.

$\sigma_z s_z, \gamma_r = \tau_z (\boldsymbol{\sigma} \times \mathbf{s})_z$. Importantly, all terms are associated with diagonal matrices in spin space, except the "Rashba term" $\mathrm{T}_r\gamma_r$. The latter is indeed what connects orthogonal spin states. Hence, the resulting terms in $\Gamma^{\rm sin}_{++}$ lead hence to effective *spin-flip* (Rashba term) and *spin-conserving* (all others) Lorentz forces. The change of sign can in fact be explained in terms of those two effective forces.

For the sake of illustration, we assume weak scatterers $|g_0 u_0| \ll 1$, also restricting the focus of the analysis to intra-ring transitions within the outer ring: $\mathbf{k}_+ \to \mathbf{k}'_+$ as mentioned above. A first scenario for the change of sign is as follows. First, we note that as k is increased from $k = 0$, electron states in the lower band $\mu = -1$ progressively change their spin orientation from effective spin-up to -down states (see Fig. 7.1). Starting from $\epsilon_{\rm I}$, varying ϵ instead, it can be verified that the same occurs within the outer ring, such that by tuning ϵ one can switch between states with opposite spin polarisation. As effective up/down states are associated with an opposite effective spin Lorentz force (i.e., skew cross sections with opposite signs), this also means conducting electrons can be selectively deflected towards opposite boundaries of the system. The associated anomalous Hall voltage and MSHE spin accumulation will then display the characteristic change of sign [Fig. 7.3(a)].

A second scenario involves the spin-flip force and does not require changing the polarisation of carriers. Instead, what changes when varying ϵ is the ratio of spin-flip to elastic skew cross sections. This also produces a change of sign as depicted in Fig. 7.1(e); the fate of the transverse conductivity will depend ultimately on the competition between the two effective spin Lorentz forces. In Fig. 7.5 we plot the modulus square of $\mathcal{T}_{++}(\phi)$ as a function of the scattering angle and for different values of the Fermi energy ϵ lying in region I or II. We also picked two exemplifying cases $\lambda, \delta = \{10, 30\}$ meV. The spin-conserving force is generally shown to be larger in magnitude.

The change of sign in $\sigma^{c,s}_{\perp}$ is a persistent feature as long as SO coupling and MEC are compar-

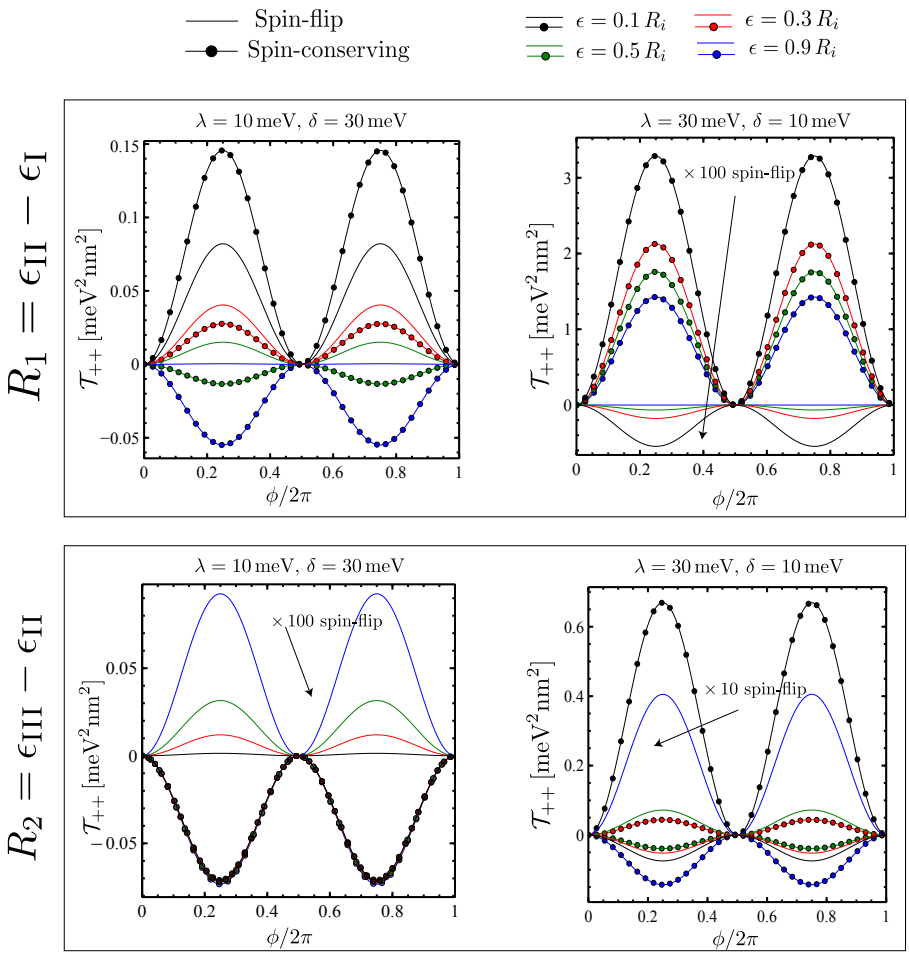

Figure 7.5: Competition of the effective spin-conserving and the spin-flip Lorentz forces. Depending on the Fermi-energy position (taken between regime I and II) different curves (in different colours) are obtained for two relevant cases $\lambda, \delta = \{10, 30\}$ meV. The spin-conserving force (dotted lines) is generally larger in magnitude with respect to the spin-flip one (solid lines) Parameters: $u_0 = 0.036$ eV nm^{-2} and $n_i = 10^{12}\,\mathrm{cm}^{-2}$.

able [Fig. 7.3(a)]. In that case, the noncollinear spin texture is well developed, such that, on one hand, it is possible to interchange between effective spin-up and -down states $"S" = "\uparrow, \downarrow" = -"\bar{S}"$ using a gate voltage, and, on the other, both spin-conserving $\langle "S"|V(\mathbf{x})|"S"\rangle$ and spin-flip $\langle "\bar{S}"|V(\mathbf{x})|"S"\rangle$ scattering matrix elements are non-zero. Asymptotically, $\epsilon \gg \delta, \lambda$, the AH signal must vanish due to the opposite spin orientation of electron states belonging to $\mu = \pm 1$ bands, which produce vanishing small total magnetisation $S_z(\epsilon) = \sum_\chi S_{z\chi} \ll 1$. In comparison, the staggered field experienced by charge carriers $S_z^{\mathrm{stag}}(\epsilon) = \sum_\chi \chi S_{z\chi}$ has slower asymptotic decay (for $\lambda \lesssim \delta$), implying that the MSHE is more robust than the AHE.

The robustness of the change of sign is to be tested against numerous factors. First, the system realises the QAH effect provided the gap remains robust against disorder, $\sigma_\perp^c(\epsilon < \epsilon_\mathrm{I}) = 2e^2/h$, $\sigma_\perp^s(\epsilon < \epsilon_\mathrm{I}) = 0$. In the metallic regime, the Berry curvature of occupied states also provides a (nonquantised) intrinsic contribution to the transverse conductivity, which can affect the change of sign. We discuss this point below.

Next, consider that in the strong scattering limit, $|g_0 u_0| \gg 1$, the rate of inter-ring transitions increases and the one-ring scenario presented above might break down. However, as shown in Fig. 7.3(c) the change of sign is still visible. In real samples, structural defects and short-range

impurities, such as hydrocarbons [277], induce scattering between inequivalent valleys, thereby opening the backscattering channel [196]. In fact, spin precession measurements in graphene with interface-induced SO coupling indicate that the in-plane spin dynamics is sensitive to intervalley scattering [241–243]. To determine the impact of intervalley processes on DC transport, we solved the BTEs for arbitrary ratio u_x/u_0. Fig. 7.3(c) shows the AH conductivity for selected values of u_x (dashed lines). $\sigma_\perp^c$ is strongly impacted showing a 50% reduction when intra- and intervalley scattering processes are equally likely ($u_x = u_0$). However, the sign change in $\sigma_\perp$, approaching the majority spin band edge $\epsilon \approx \epsilon_{\rm II}$ is still clearly visible.

Our thorough numerical analysis in the strong SO coupling regime provides an estimation for ϵ_0 defined as $\sigma_\perp(\epsilon_0) = 0$,

$$\epsilon_0 = a\,\epsilon_{\rm I} + b\,\epsilon_{\rm III}\,, \tag{7.16}$$

with $a \simeq 0.3$–0.4 and $b \simeq 0.6$–0.8. This relation shows that knowledge of δ (e.g., from the Curie temperature [128]) allows one to estimate the SO coupling strength directly from the gate voltage dependence of the anomalous Hall resistance. The values $\sigma_\perp \approx 0.1 - 1$ (e^2/h) are compatible with the measurements in Refs. [123, 129], for a reasonable choice of parameters, $0 \leq \lambda, \delta \leq 30\,$meV in the dirty regime with $n_i = 10^{12}\,\text{cm}^2$ and $u_0 \sim (0.1, 1)\,\text{eV}\cdot\text{nm}^2$. In high mobility samples, our theory predicts that the robust skew scattering contribution with $\sigma_\perp \propto n_i^{-1}$ results in much larger values $\sigma_\perp \approx 10 - 100$ (e^2/h).

Intrinsic contribution to the anomalous Hall effect

As discussed above, the system under consideration can be classified from a topological standpoint as a QAH insulator. In our unified picture of transport in magnetised graphene, it is a important point to address the calculation of the quantised part of the anomalous Hall response, and consequently of the transition from the nonquantised to the quantised regime.

Previous studies—where the topological nature of the model was also firstly pointed out [100]—tackled the problem numerically, also with a focus in the regime $\delta \gg \lambda$. Below we go beyond this limitation performing an exact analytic evaluation of the intrinsic anomalous Hall conductivity.

Berry-curvature calculation

Starting from the chiral eigenstates of Eq. (7.4), we obtain the Berry curvature of the bands as

$$\Omega_{\mathbf{k}}^n = (\nabla_{\mathbf{k}} \times \boldsymbol{\mathcal{A}}_{\mathbf{k}}^n)_z\,, \tag{7.17}$$

where $\boldsymbol{\mathcal{A}}_{\mathbf{k}}^n = -\imath\langle n\mathbf{k}|\nabla_{\mathbf{k}}|n\mathbf{k}\rangle$ and $n \equiv (\mu, \nu)$ is a combined band index; we choose to assign the label n in descending order, starting from the band of highest energy. Therefore our convention is such that $\nu, \mu = \pm(1,1) \to n = \pm 2$ and $\nu, \mu = \pm(1,-1) \to n = \pm 1$. The transverse conductivity is obtained via integration of the Berry curvatures [278–281]

$$\sigma_\perp^{\rm int} = \sum_n \sum_{\mathbf{k}} \Omega_{\mathbf{k}}^n\, f_{k_n}^0. \tag{7.18}$$

Note that $\sum_n \Omega_{\mathbf{k}}^n = 0$ and $\sum_{\mathbf{k}} \sum_{n<0} \Omega_{\mathbf{k}}^n = 2e^2/h$, which is the case when ϵ is tuned into the gap, with (according to our notation) bands $n = -2, -1$ filled: $f_{k_n}^0 = 1 \neq 0\,,\text{if } n < 0$. Working in radial components, we find the relevant Berry-connections $\boldsymbol{\mathcal{A}}_{\mathbf{k}}^{-1}, \boldsymbol{\mathcal{A}}_{\mathbf{k}}^{-2}$ only contains the angular

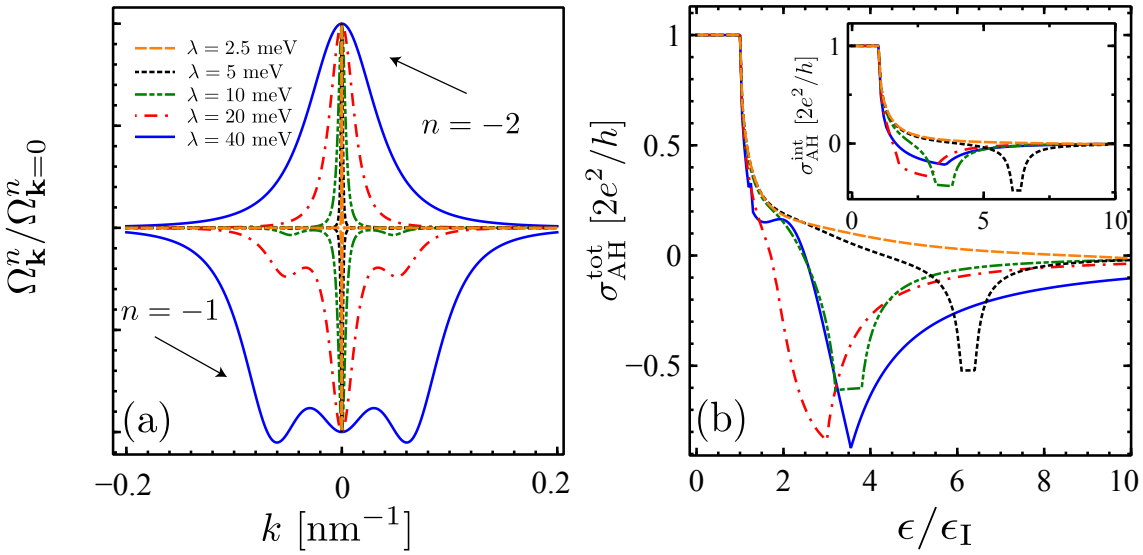

Figure 7.6: Intrinsic contribution and total anomalous Hall conductivity. (a) The Berry curvatures of hole bands $n = -1, -2$. Note that $\Omega_{n=-1}(\mathbf{k})$ develops additional "hot spots" as SO coupling is increased. (b) The total $\sigma_\perp^{\rm tot} = \sigma_\perp + \sigma_\perp^{\rm int}$ at selected values of λ; same legend as in (a). (b) Adding the intrinsic contribution (inset) to $\sigma_\perp$ leaves the estimate for ϵ_0 [Eq. (7.16)] virtually unaffected. Parameters: $u_0 = 10$ eV·nm^2, $n_i = 10^{12}$ cm^{-2} and $\delta = 30$ meV.

components:

$$\left(\boldsymbol{\mathcal{A}}_{\mathbf{k}}^{n=-1,2}\right)_\phi = \pm \frac{\lambda^2\delta\left(\delta^4 + 2\lambda^2(2v^2k^2 \pm 3S_k + 3\lambda^2) + \delta^2(3v^2k^2 \pm 3S_k + 4\lambda^2)\right)}{\left(S_k^2\left(v^2k^2 + 2S_k + \delta^2 + 2\lambda^2\right)\right)^{3/2}}\,, \tag{7.19}$$

with

$$S_k = \sqrt{\lambda^4 + v^2k^2(\lambda^2 + \delta^2)}\,. \tag{7.20}$$

The result is plotted in the inset of Fig. 7.6(b), while Fig. 7.6(a) shows the opposite-in-sign Berry curvatures for the bands $n = -1, -2$. We point out that this result can be equivalently obtained from the clean limit of the Kubo–Streda formula [53].

Similarly to the situation presented for the extrinsic contribution, we find the intrinsic term also presents a peculiar change of sign under the same condition $\lambda > \lambda_c \approx \delta/6$ [see Fig. 7.3 (a)], where λ_c is a critical value for the Rashba strength. The effect in this case is ascribed to the profile of the Berry curvatures; in particular, in the electron sector the change of sign happens for $\epsilon = \tilde{\epsilon}_0$ solution of the self-consistent equation

$$I_1|_{k_-}^{k_+}(\tilde{\epsilon}_0) + \theta_{\tilde{\epsilon}_0,\epsilon_{\rm II}}\, I_1|_0^{k_+}(\tilde{\epsilon}_0) + \theta_{\tilde{\epsilon}_0,\epsilon_{\rm III}}\, I_2|_0^{k_-}(\tilde{\epsilon}_0) = -\frac{2e^2}{h}\,, \tag{7.21}$$

where $I_i|_a^b(\epsilon) \equiv \int_{a(\epsilon)}^{b(\epsilon)} dk\, k\, \Omega_{\mathbf{k}}^i$ and $\theta_{\epsilon_a,\epsilon_b} = \theta(\epsilon_a - \epsilon_b)$ is the Heaviside step function. In Fig. 7.6(b) we show the total anomalous Hall conductivity, given by $\sigma_\perp^{\rm tot} = \sigma_\perp^{\rm int} + \sigma_\perp^c$. Remarkably, we find $\tilde{\epsilon}_0 \simeq \epsilon_0$, such that our estimate for the AHE reversal energy (ϵ_0) in Eq. (7.16) is still accurate when adding all contributions [cf. Fig. 7.6(b) and inset]. This robust energy dependence in the AHE/MSHE transverse response functions connects the skew scattering mechanism, unveiled in this work, to the intrinsic properties of magnetised 2D Dirac bands.

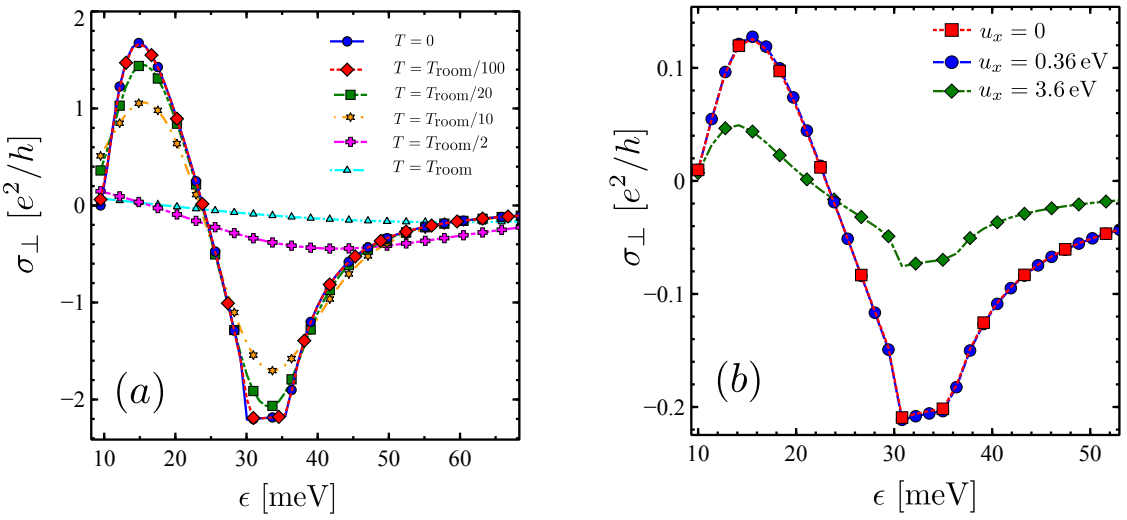

Figure 7.7: Effect of thermal fluctuations and intervalley scattering. (a) Change of sign in $\sigma_\perp$ is distinguishable for $T \lesssim T_{\rm room}/2$, where $T_{\rm room} = 300\,{\rm K}$. (b) In the less favourable scenario ($u_x = u_0$), the transport times $\tau^{\parallel,\perp}(\epsilon)$ are reduced by a factor ≈ 2. Parameters: $u_0 = 3.6$ eV·nm^{-2} and $n = 10^{12}\,{\rm cm}^{-2}$.

Thermal and quantum effects

We analyse the impact of thermal fluctuations on the change of sign. The finite temperature transverse response is obtained from

$$\sigma_\perp^T(\mu) = -\int_{-\infty}^{+\infty} d\epsilon \left(\frac{\partial f^0(\epsilon,\mu,T)}{\partial \epsilon}\right) \sigma_\perp^{T=0}(\epsilon)\,, \tag{7.22}$$

where $\sigma_\perp^{T=0}(\epsilon)$ is the zero-temperature response and $f^0(\epsilon,\mu,T) = (1+{\rm Exp}\left[(\epsilon-\mu)/k_BT\right])^{-1}$. Fig. 7.7 shows the temperature dependence of the anomalous Hall conductivity for typical parameters. The characteristic change of sign is visible up to temperatures $T \approx T_{\rm room}/2$. Another possible factor impacting the validity of the change of sign is the contribution of quantum (anomalous) processes to the transverse transport coefficients. We analyse here the role of the quantum side-jump contribution [134], showing it provides a small correction to the transverse response in clean samples with $k_F l \gg 1$. The side-jump contribution $\mathcal{Q}_{yx}$ is obtained by isolating the impurity concentration-independent term

$$\sigma_{yx}^I = \frac{\mathcal{S}_{yx}}{n_i} + \mathcal{Q}_{yx} + O(n_i)\,. \tag{7.23}$$

Within the rigorous diagrammatic formalism, this requires the calculation of the ladder series for the renormalised vertex (see Fig. 2.4). In Fig. 7.8 we plot the ratio $\mathcal{S}_{yx}/n_i\mathcal{Q}_{yx}$ at selected SO coupling values in a system with high mobility. The results show that the side-jump contribution is only sizable in a very narrow energy window, i.e. ~1-10% of the distance between the Rashba edge $\epsilon_{\rm III}$ and the bottom of the skyrmionic band $\epsilon_{\rm I}$. The side-jump part rapidly decays to zero, in the diffusive regime with $k_F l \gg 1$, thus justifying our approximation in the main text $\sigma_{yx}^I \simeq \mathcal{S}_{yx}/n_i$. We note that the anomalous term $\mathcal{Q}_{yx}$ also receives contributions from the so-called Ψ and X diagrams encoding quantum coherent skew scattering not evaluated here (see [159] for more details).

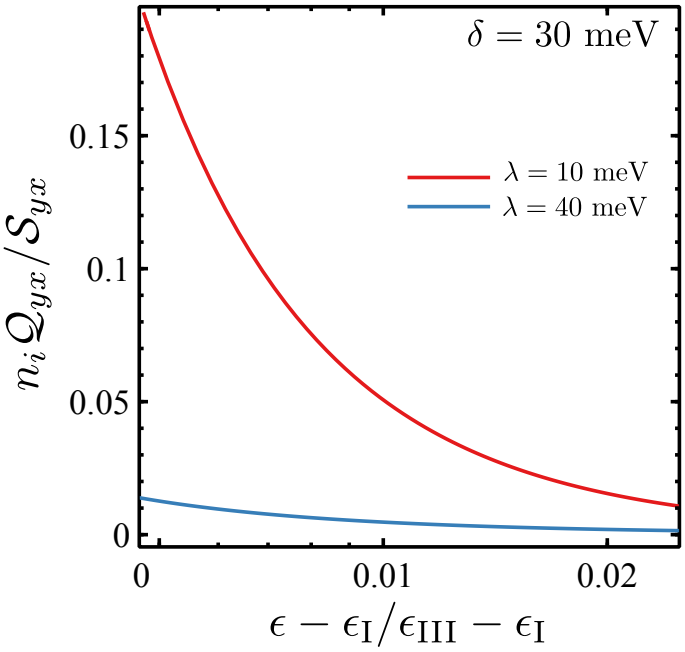

Figure 7.8: Ratio of the side-jump and skew scattering contribution to σ^I_{yx} in high mobility samples. The side-jump contribution is negligible away from the Dirac point $k_F l \gg 1$. Parameters: λ =10 meV (red line) and $\lambda = 40$ meV (blue line), $\delta = 30$ meV, $u_0 = 1$ eV nm^{-2} and $n_i = 10^{10}$ cm^{-2}.

Conclusions

In this Chapter we have outlined a unified theory—incorporating extrinsic and intrinsic contributions on equal footing—to describe the occurrence of the AHE, and the MSHE, in 2D Dirac systems with pseudospin-spin coupling. We identified a peculiar change of sign of the transverse responses as functions of the Fermi energy, which is connected to the peculiar skyrmionic spin texture of magnetised Dirac bands. The change of sign is more clearly visible at low temperature in systems with high mobility, but is robust against thermal and quantum effects, and hence can serve on-going experimental efforts, as a mean to estimate the size of the transferred Rashba SOC to the carbon layer simply from Hall measurements, but also as a precursor of the exotic QAH phase in these systems. In fact, predictions of rich electronic phases in 2D Dirac systems [99, 100, 282] have triggered numerous efforts aimed to realise topological fermions in graphene heterostructures. Our work presented in this Chapter is extremely relevant to guide such efforts and opens new perspective in the context of transport phenomena in 2D Dirac heterostructures with broken time reversal symmetry.

Chapter 8

Conclusions

2D Dirac systems are emerging as strong contenders for the next generation of spintronics devices. Their unique electronic properties (e.g., large spin diffusion length in graphene and spin-valley coupling in semiconducting TMDs) can be further enhanced by proximity to other 2D layered compounds, making them ideal playgrounds to harness the electrons' spin for applications. From a fundamental viewpoint, the multiple *spin-like* [SU(2)] DOFs in 2D honeycomb layers (pseudospin, spin and valley) offer unprecedented possibilities to explore unconventional spin dynamics and novel microscopic mechanisms for interconversion of charge and spin currents.

In this thesis we have studied coupled charge/spin dynamics in 2D honeycomb layers with strong proximity-induced interactions in the presence of static disorder (e.g., due to impurities). By combining a FQM approach, based on the diagrammatic expansion of the linear response functions to weak external perturbations, and SC transport theory generalised for 2D Dirac fermions, we have developed a unified theoretical framework, obtaining a number of major results.

First, we have developed a quantum theory of SO-coupled transport in graphene with Rashba spin–orbit interaction, arising from interfacial breaking of inversion symmetry about the 2D plane, and described by the C_{6v} point group of the honeycomb lattice. For this class of systems, we have concluded that CSC via the SHE is completely suppressed in the presence of an arbitrary small concentration of nonmagnetic impurities, but at the same time it is robustly enabled via the ISGE. Intuitively, this result can be understood in terms of the peculiar spin texture of Dirac–Rashba states. The locking of spin and momentum at right angles, while leading to a robust ISGE, implies that the transverse (skew) scattering cross section is vanishing. This absence of skew scattering in the C_{6v} model hints at the vanishing of SHE. We have confirmed this simple, yet remarkable result by direct calculation and by means of WIs underlying the $SU(2)$ invariance of the model. Here, the WIs for the four-point vertex function entirely fix the out-of-equilibrium spin response of the system.

We have extended our quantum diagrammatic analysis of the C_{6v} model to finite frequency. Equations of motion for spin observables have been obtained in the diffusive regime with large mean free path between impurity-scattering events, allowing for the determination of the in-plane and out-of-plane SRTs and charge-to-spin interconversion rates.

We examined a wider class of C_{3v}-invariant Hamiltonians, lacking sublattice symmetry (e.g., due the proximity to polyatomic 2D layers, such as TMDs). A relevant example of materials

falling under this class of models is represented by graphene on TMDs. Using our unified framework, we have discovered that a finite SHE emerges in these systems, due to 'transfer' of spin-valley coupling to the band structure of graphene, which leads to the out-of-plane tilting of the spin texture. Remarkably, the robust ISGE found in the C_{6v} model is only mildly affected by the introduction of additional terms in the Hamiltonian, being also robust against thermal fluctuations. We hence demonstrated that this particular CSC effect is potentially observable over a large window of parameters. Our results were confirmed by direct evaluation of the WIs in the C_{3v} model.

We have studied the spin dynamics of the C_{3v} model, focusing on the highly-doped regime where the Fermi energy is much larger than any of the present proximity-induced couplings. We have shown that the evolution of the spin polarisation vector as a function of time reveals a delicate competition between the Rashba and the spin-valley SO interactions. We derived analytic formulas for the SRTA in the motional narrowing (strong SO coupling) regime, where the disorder-induced broadening of electron states at the Fermi level is much larger (much smaller) than the spin splitting. Our results can be useful for Hanle precession experiments in oblique magnetic field, where the SRTA is used to estimate the magnitude of proximity-induced interactions.

Finally, we have explored the physics of 2D Dirac systems with strong SO interaction *and* MEC. Combining the SC Boltzmann and the FQM formalism, we have provided the first unified charge transport theory of magnetised 2D Dirac fermions, with intrinsic and extrinsic mechanisms considered on an equal footing and at all orders in the proximity-induced interactions. Motivated by recent experimental results in graphene/YIG heterostructures, we studied the crossover between the AHE and the *QAH* effect, predicted to take place in such systems. We identified a robust change of sign of the transverse responses—linked to the skyrmionic-like spin texture of the electronic bands in momentum space, which is a smoking gun of successful transfer of *both* SO and MEC to the carbon layer. The change of sign allows for an estimation of the proximity-induced SO coupling, but more importantly is a precursor of the quantum anomalous Hall effect.

Our results are of the utmost importance to interpret current experimental efforts in graphene-based vdW heterostructures, which have already successfully shown transport fingerprints of strong proximity-induced SO interactions, by using magneto-transport and spin precession measurements. On the other hand, our unified theoretical framework allows one to predict the realisation of relativistic transport phenomena—such as the emergence of the SHE in graphene on TMDs—elucidating the link between the equilibrium and nonequilibrium properties of 2D Dirac systems, which can also help to design novel platforms with on-demand characteristics.

We want to conclude by mentioning future perspectives and possible extensions of the work presented in this thesis. A first possible extension concerns the derivation of coupled charge/spin diffusion equations beyond the assumption of large Fermi energy (highly-doped regime). The strong entanglement of spin and orbital DOFs in this regime makes this task particularly challenging. Spin dynamics is expected to be strongly affected by such an entanglement, especially in ultra-clean samples, with spin relaxation length pushed towards its theoretical lower bound, where electrons' spin relaxes upon single impurity scattering (ultra-fast spin relaxation).

We have assessed here the impact of random SO fields only marginally. However, this aspect deserves to be explored in more detail. Random interactions in 2D materials, studied by SC methods, have been recently associated with a novel CSC effect dubbed *anisotropic spin precession* (C. Huang *et al.,* 2017). While this effect shares similarities with the ISGE studied in this thesis, describing its competition/interplay with ISGE and SHE within a self-consistent fully-quantum mechanical formalism remains an open problem.

Appendix A

The Tight-Binding Low-Energy Model of Graphene

Graphene is a 2D allotrope of carbon, with atoms arranged in a honeycomb-lattice configuration [Fig. A.1(a.1)]. This structure stems from the sp^2 hybridisation of the electron orbitals of carbon producing three new orbitals: $|sp_1^2\rangle = \frac{1}{\sqrt{3}}|2s\rangle + \sqrt{\frac{2}{3}}|2p_y\rangle$; $|sp_{2,3}^2\rangle = \pm\frac{1}{\sqrt{3}}|2s\rangle + \sqrt{\frac{2}{3}}\left(\frac{1}{2}|2p_y\rangle \pm \frac{\sqrt{3}}{2}|2p_x\rangle\right)$. In the binding process, three out of four valence electrons per carbon atom are involved in the formation of a strongly covalent σ-bond, determining the energetic stability and the elastic properties of graphene. The remaining electron is involved a π-bond. While σ-electrons form bands far away from the Fermi energy, π-electrons are responsible for the electronic properties at low energies [70].

The honeycomb structure can be seen as a bipartite lattice (sublattices A and B) spanned by the basis vectors

$$\mathbf{a}_1 = \sqrt{3}a\,\hat{x}, \;\; \mathbf{a}_2 = \frac{\sqrt{3}}{2}a\left(\hat{x} + \sqrt{3}\hat{y}\right), \tag{A.1}$$

with $a \simeq 0.142\,\text{nm}$. The inequality of the two sublattices is readily seen by looking at the position of the nearest neighbours for two inequivalent sites: while, say, a site on the A sublattice has nearest neighbours in the north, south-east and south-west directions, a site on the B sublattice has them in the south, north-east and north-west directions [see Fig. A.1(a.1)]. The reciprocal Bravais lattice [Fig. A.1(a.2)] is spanned by the vectors:

$$\mathbf{a}_1^* = \frac{2\pi}{\sqrt{3}a}\left(\hat{x} - \frac{\hat{y}}{\sqrt{3}}\right), \;\; \mathbf{a}_2^* = \frac{4\pi}{3a}\hat{y}\,. \tag{A.2}$$

The corners of the Brillouin zone consist of inequivalent K and $K' = -K$ (*Dirac points*), explicitly:

$$\pm K = \pm\frac{4\pi}{3\sqrt{3}a}\hat{x}\,. \tag{A.3}$$

To study the low-energy properties of graphene we take into account a tight-binding model for the π-electrons [283]. Restricting our focus to nearest-neighbours interaction only, the Hamiltonian reads

$$H_G = -t\sum_{\langle i,j\rangle}\left(a_i^\dagger b_j + h.c.\right), \tag{A.4}$$

where $a_i^\dagger$ (a_i) and $b_i^\dagger$ (b_i) creates (annihilates) a electron on a site i belonging to the A or the

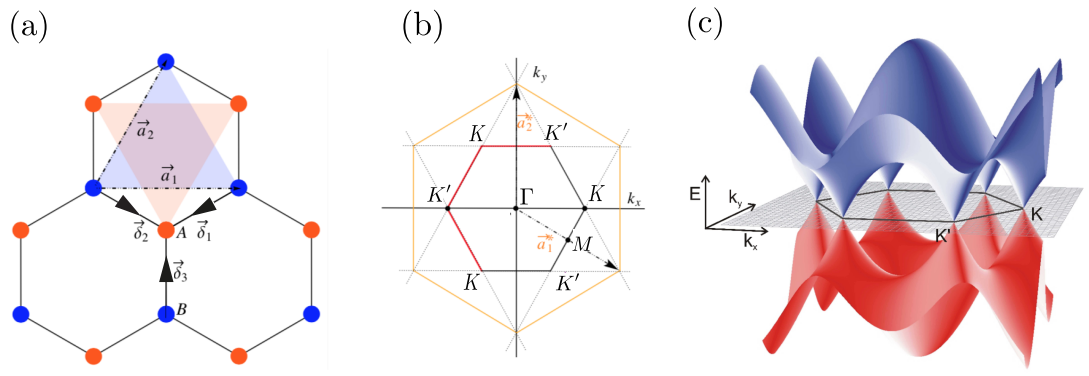

Figure A.1: Lattice structure and band dispersion of bare graphene. (a) The honeycomb structure with penetrating inequivalent Bravais lattices made up of A, B carbon atoms (red and blue respectively). (b) In reciprocal space, two inequivalent corners K, K' appear, with the low-energy physics of this material being descried by excitations around those points. (c) Visualisation of graphene band structure, where the linear dispersion (Dirac cone) in the vicinity of K, K' can be recognised.

B sublattice respectively, while $t \simeq 2.7\,\text{eV}$ is the nearest-neighbours hopping-integral energy between inequivalent sites[1]. Expressing the creation-annihilation operators into their Fourier components

$$(a_i, b_i) = \frac{1}{\sqrt{N_{A,B}}} \sum_{\mathbf{q}} e^{-\imath \mathbf{q} \mathbf{r}_i} (a_{\mathbf{q}}, b_{\mathbf{q}}) \,, \tag{A.5}$$

with $N_A + N_B = N$ is the total number of carbon atoms in the lattice, and substituting Eq. (A.5) into Eq. (A.4), we get

$$H_G = -t \sum_{\mathbf{q}} \sum_{\alpha=1,2,3} e^{-\imath \mathbf{q} \delta_\alpha} a^\dagger_{\mathbf{q}} b_{\mathbf{q}} + \text{h.c.} = \sum_{\mathbf{q}} F^\star_{\mathbf{q}} a^\dagger_{\mathbf{q}} b_{\mathbf{q}} + \text{h.c.} \,, \tag{A.6}$$

with

$$F_{\mathbf{q}} = -t \sum_{\alpha=1,2,3} e^{\imath \mathbf{q} \delta_\alpha} \,, \tag{A.7}$$

and [see Fig. A.1(a.1)]

$$\delta_1 = -\frac{a}{2}(\sqrt{3}, 1) \,, \tag{A.8}$$

$$\delta_2 = \frac{a}{2}(\sqrt{3}, -1) \,, \tag{A.9}$$

$$\delta_3 = a(0, 1) \,. \tag{A.10}$$

We can compact the notation by writing

$$H_G = \sum_{\mathbf{q}} (a^\dagger_{\mathbf{q}} \; b^\dagger_{\mathbf{q}}) \begin{pmatrix} 0 & F^\star_{\mathbf{q}} \\ F_{\mathbf{q}} & 0 \end{pmatrix} \begin{pmatrix} a_{\mathbf{q}} \\ b_{\mathbf{q}} \end{pmatrix} \,, \tag{A.11}$$

from which, by analysing the Schrödinger equation, the dispersion relation is found as

$$\epsilon_{\mathbf{q}} = \pm |F_{\mathbf{q}}| = \sigma t \sqrt{3 + \sum_{\alpha \neq b} \cos[\mathbf{q} \cdot (\delta_\alpha - \delta_\beta)]} \,, \tag{A.12}$$

where $\sigma = \pm 1$ is a band index denoting the positive and negative branch of the spectrum re-

[1] The on-site energy is conventionally set to zero, as it only contributes with an energy offset in the spectrum.

spectively. One can verify $\epsilon_{K,K'} = 0$. We can hence derive a low-energy continuum Hamiltonian describing excitations around these point. Note

$$F_{\pm\mathbf{k}} \equiv F_{\pm\mathbf{K}+\mathbf{q}} = -t\left[-\imath\, k_y a + \imath\frac{e^{\mp\imath 2\pi/3}}{2}\left(-\sqrt{3}\,k_x a + k_y a\right) + \imath\frac{e^{\pm\imath 2\pi/3}}{2}(\sqrt{3}\,k_x a + k_y a) + O(\mathbf{k}^2)\right] \tag{A.13}$$

$$\simeq \frac{3ta}{2}(\pm k_x + \imath k_y)\,, \tag{A.14}$$

where we have retained only linear terms in momentum. We arrive at

$$H_{\mathbf{G},\mathbf{k}} = \hbar v \begin{pmatrix} 0 & k_x - \imath k_y & 0 & 0 \\ k_x + \imath k_y & 0 & 0 & 0 \\ 0 & 0 & 0 & -k_x - \imath k_y \\ 0 & 0 & -k_x + \imath k_y & 0 \end{pmatrix}, \tag{A.15}$$

acting on the spinor $\Psi_{\mathbf{k}} = (\Psi_{KA\mathbf{k}}, \Psi_{KB\mathbf{k}}, \Psi_{K'A\mathbf{k}}, \Psi_{K'B\mathbf{k}})^{\mathrm{t}}$. Therefore we see in the low-energy continuum model, sublattices (A, B) and valleys (K, K') are treated as $SU(2)$ DOFs similar to electrons' spin. Being H_G diagonal in the valley DOF, we introduce a valley index $\kappa = \pm 1$ for the K, K' valley respectively, writing

$$H_{\mathrm{G},\kappa\mathbf{k}} = \hbar\, v\,(\kappa\,\sigma_x k_x + \sigma_y k_y)\,, \tag{A.16}$$

with $\boldsymbol{\sigma} = (\sigma_x, \sigma_y)$ being x, y Pauli matrices associated the sublattice two-fold space and with the Fermi velocity of graphene $v = 3at/2\hbar \simeq 10^6$ m/s. The respective eigenvalues are obtainable by expanding Eq. (A.12) around band edges

$$\epsilon_{\sigma\kappa\mathbf{k}} = \sigma\, v\, \hbar|\mathbf{k}|\,, \tag{A.17}$$

so that a linear dispersion for massless particles is obtained. The Hamiltonian Eq. (A.16) takes a more compact form by rotating it to the so-called *magic* basis[2] $\Psi_{\mathbf{k}} = (\Psi_{KA\mathbf{k}}, \Psi_{KB\mathbf{k}}, \Psi_{K'B\mathbf{k}}, \Psi_{K'A\mathbf{k}})^{\mathrm{t}}$, which swaps sublattices A, B at K'. In matrix form we have

$$H_{G,\mathbf{k}} = \hbar\, v\, \tau_z \otimes \boldsymbol{\sigma}\cdot\mathbf{k}\,, \tag{A.18}$$

where $\boldsymbol{\tau}$ are introduced as Pauli matrix for the valley DOF. The Bloch eigenstates associated to Eq. (A.18) read as

$$\Psi_{\kappa\sigma s\mathbf{k}}(\mathbf{x}) = \frac{e^{\imath\mathbf{k}\cdot\mathbf{x}}}{\sqrt{2}}\begin{pmatrix} \kappa\,\sigma \\ e^{\imath\phi_{\mathbf{k}}} \end{pmatrix} \otimes |\kappa\rangle \otimes |s\rangle\,, \tag{A.19}$$

where $s = \uparrow, \downarrow \equiv \pm 1$ denotes real spin and $\phi_{\mathbf{k}} = \angle(\hat{k}_x, \mathbf{k})$. Note the eigenvectors are spin degenerate as real spin is absent from Eq. (A.18).

Spin–orbit interaction in Dirac materials

We now discuss the inclusion of the SO interaction in 2D honeycomb layers following the approach in Ref. [284]. The starting point is the SO Hamiltonian in Eq. (1.7). As discussed in

[2]When including the spin DOF, one has the 2^3 =8-dimensional spinor $\Psi_{\mathbf{k}}$ with components $\{\Psi_{\varsigma\mathbf{k}}\}$ where ς a shorthand notation for the set of indices $\kappa, \sigma = \pm 1$ and $s = \uparrow, \downarrow$.

Chapter 1, the possible spin-dependent hoppings according to Eq. (1.7) can be obtained by leveraging time-reversal (in the magic basis) $\Theta = \imath\,\tau_x\sigma_x s_y C$, where C is the complex conjugation, and the lattice symmetry point group. On-site spin-dependent terms change sign under Θ and hence are not generated by the SO Hamiltonian $H_{\rm SOC}$. Restricting the attention to nearest- and next nearest-neighbour hoppings, on general grounds we can write

$$H_{\rm SOC} = \sum_{\langle i,.j\rangle} a_i^\dagger X_{ij}^{AB} b_j + \sum_{\langle\langle i,j\rangle\rangle} a_i^\dagger X_{ij}^{AA} a_j + b_i^\dagger X_{ij}^{BB} b_j\,, \tag{A.20}$$

where $X_{ij}^{SS'}$ are 2×2 matrices in spin space denoting hopping from sublattice $S \to S'$ and $a_i, a_i^\dagger, b_i, b_i^\dagger$ are meant as spinors. Omitting sublattice superscripts for simplicity, one can expand X_{ij} onto the Pauli matrices

$$X_{ij} = \omega_{ij}^x s_x + \omega_{ij}^y s_y + \omega_{ij}^z s_z\,. \tag{A.21}$$

Imposing time reversal invariance $X_{ij} = \Theta^{-1} X_{ij}\Theta$ leads to the constraints $\omega_{ij}^\alpha = -(\omega_{ij}^\alpha)^*$, $\alpha = x,y,z$. This implies that spin-conserving hoppings mediated by the SO interaction are purely imaginary.

Let us now consider directly the most general case of our interest, i.e. the C_{3v} point symmetry group [see also Fig. 3.1(c)]

$$C_{3v} = \{E, R^z_{\pm\pi/3}, 3\Sigma_v^{yz}\}\,, \tag{A.22}$$

where E is the identity, $R^z_{\pm\pi/3}$ are rotations of angles $\pm\pi/3$ about the $\hat{z}$-axis and $3\Sigma_v^{yz}$ represent 3 vertical reflections with mirror plane passing through the vertices of the honeycomb lattice. By imposing these symmetries, one finds the most general SO Hamiltonian as

$$H_{\rm SOC}^{C_{3v}} = \frac{\imath}{3\sqrt{3}} \sum_{\langle\langle i,j\rangle\rangle} \nu_{ij}(\lambda_A^{sc} a_i^\dagger s_z a_j - \lambda_B^{sc} b_i^\dagger s_z b_j) + \frac{2\imath}{3}\sum_{\langle i,j\rangle} \lambda\,[a^\dagger(\mathbf{s}\times\mathbf{d}_{ij})_z b_j + (b \longleftrightarrow a)] \tag{A.23}$$

$$+ \frac{2\imath}{3\sqrt{3}} \sum_{\langle\langle i,j\rangle\rangle} [\lambda_A^{sf} a_i^\dagger(\mathbf{s}\times\mathbf{d}_{ij})_z a_j + \lambda_B^{sf} b_i^\dagger(\mathbf{s}\times\mathbf{d}_{ij})_z b_j]\,. \tag{A.24}$$

Above, $\mathbf{d}_{ij}$ is the unit vector connecting the line segment between sites i,j and $\nu_{ij} = \pm 1$ for (anti)clockwise hopping. This Hamiltonian admits both spin-flipping ($\lambda_{A,B}^{sf}$) and spin-conserving ($\lambda_{A,B}^{sc}$) hoppings between nearest neighbours. The spin-conserving part is a fingerprint of 2D materials. The term proportional to λ is the Bychkov-Rashba SO coupling due to the breaking of mirror symmetry about the 2D plane.

To derive to continuum-limit form of Eqs. (3.52)-(3.54), similarly to what done above, we can switch to Fourier space and expand around the low-energy points K, K'. It can be shown that one arrives at the form reported in Eq. (3.52).

Appendix B

Details on the electronic properties of 2D Dirac-Rashba models

C_{6v} model

The momentum propagators of the minimal 2D Dirac-Rashba model, presented in Chapter 3 read as

$$G^a_{0\mathbf{k}}(\epsilon) = \sum_{\mu,\nu=\pm1} \frac{P_{\mu\nu\mathbf{k}}}{\epsilon - \epsilon_{\mu\nu\mathbf{k}} + \imath\, a\, 0^+} \tag{B.1}$$

$$= -\frac{1}{2}\sum_{\mu=\pm1} L^a_{0\mu}\left[(\lambda+\mu\epsilon)\gamma_0 + v\,\mu\,\tau_z\,\boldsymbol{\sigma}\cdot\mathbf{k} - \frac{\epsilon}{2}\,\gamma_r + v\,(\mathbf{s}\times\mathbf{k})_z + \lambda\gamma_{zz} + \delta M_{2\phi_\mathbf{k}}\right], \tag{B.2}$$

where, expressing the formula in the full 8×8 representation (i.e. re-instating the valley quantum DOF), $\gamma_0 \equiv \tau_0\sigma_0 s_0$ is the 8×8 identity matrix, $\gamma_{zz} = \sigma_z s_z$, $\gamma_r = \tau_z\,(\boldsymbol{\sigma}\times\mathbf{s})_z$ we have

$$L^{A(R)}_{0\mu} = \frac{\mu}{v^2k^2 - \epsilon^2 - 2\mu\lambda\epsilon \pm \imath\, 0^+\mathrm{sign}(\epsilon-\mu\lambda)}, \tag{B.3}$$

$$\delta M_{2\phi_\mathbf{k}} = -\frac{1}{2}(\epsilon+2\mu\lambda)\,\tau_z\left[(\sigma_y s_y - \sigma_x s_x)\sin 2\phi_\mathbf{k} + (\sigma_x s_y + \sigma_y s_x)\cos 2\phi_\mathbf{k}\right], \tag{B.4}$$

and $\phi_\mathbf{k}$ is the angle formed by the wavevector with $\hat{k}_x$.

The disorder-averaged Green's functions in the presence of scalar impurities, as described in Chapter 3 are obtained in two steps. First, we calculate the bare Green's functions $G^{a,\mathrm{eff}}_{0\mathbf{k}}$ of the effective model in Eq. (3.44)

$$G^{a,\mathrm{eff}}_{0\mathbf{k}}(\epsilon,\lambda,\lambda_{zz}) = -\frac{1}{2}\sum_{\mu=\pm1} L^{a,\mathrm{efff}}_{0\mu}\left[(\lambda+\mu\epsilon)\gamma_0 + v\,\mu\,\tau_z\,\boldsymbol{\sigma}\cdot\mathbf{k} - \frac{\epsilon-\lambda_{zz}}{2}\,\gamma_r + v\,(\mathbf{s}\times\mathbf{k})_z\right. \tag{B.5}$$

$$\left. +(\lambda+\mu\,\lambda_{zz})\gamma_{zz} + \delta M^{\mathrm{eff}}_{2\phi_\mathbf{k}}\right], \tag{B.6}$$

with

$$L^{A(R),\mathrm{eff}}_{0\mu} = \frac{\mu}{v^2k^2 - (\epsilon-\lambda_{zz})(\epsilon+\lambda_{zz}\pm2\lambda)}, \tag{B.7}$$

$$\delta M^{\mathrm{eff}}_{2\phi_\mathbf{k}} = -\frac{1}{2}(\epsilon+\lambda_{zz}+2\mu\lambda)\tau_z\left[(\sigma_y s_y - \sigma_x s_x)\sin 2\phi_\mathbf{k} + (\sigma_x s_y + \sigma_y s_x)\cos 2\phi_\mathbf{k}\right]. \tag{B.8}$$

Then, the connection to the disordered averaged propagators of the original C_{3v} Dirac-Rashba model is obtained by performing an analytical continuation of the parameters in Eq. (B.5)

$$\epsilon \to \epsilon^a = \epsilon + \imath\, a\, n_i\, \eta_0, \tag{B.9}$$

$$\lambda \to \lambda^a = \lambda - \imath\, a\, n\, \eta_r, \tag{B.10}$$

$$\lambda_{zz} \to \lambda^a_{zz} = \imath\, a\, n\, \eta_{zz}\,, \tag{B.11}$$

i.e.

$$\mathcal{G}^a_{\mathbf{k}}(\epsilon,\lambda) = G^{a,\text{eff}}_{0\mathbf{k}}(\epsilon + \imath\, a\, n_i\, \eta_0, \lambda - \imath\, a\, n\, \eta_r, -\imath\, a\, n\, \eta_{zz}) \tag{B.12}$$

where we have neglected the associated real parts as they are not important in determining the leading-order terms of the transport coefficients we are interested in.

C_{3v} model

To write the bare and disorder-averaged propagators associated to Eq. (3.54) we adopt a similar strategy leading us to Eqs. (3.14),(B.12). First, the bare propagators can be found as

$$\begin{aligned} G^a_{0\mathbf{k}} = &-\frac{1}{2}\sum_{\zeta=\pm1} L^a_{0\mu}\,\big[(f_0+\zeta\epsilon)\gamma_0 + v\,\zeta\,\tau_z\boldsymbol{\sigma}\cdot\mathbf{k} - f_r\gamma_r + \\ &\frac{v\,\lambda}{2\tilde{\Gamma}}\,(\epsilon - \lambda_{zz} + \tau_z\sigma_z\,(\Delta+\lambda_{\text{sv}}))\,(\mathbf{s}\times\mathbf{k})_z \\ &+(f_{zz}+\zeta\,\lambda_{zz})\gamma_{zz} + (f_{\text{sv}}-\zeta\lambda_{\text{sv}})\tau_z s_z + (\zeta\Delta+f_{0z})\tau_z\sigma_z - v\,(\lambda_{zz}\Delta+\epsilon\lambda_{\text{sv}})\,\boldsymbol{\sigma}\cdot\mathbf{k}s_z + \delta M_{2\phi_{\mathbf{k}}}\Big]\,, \end{aligned} \tag{B.13}$$

with

$$\delta M_{2\phi_{\mathbf{k}}} = -\frac{1}{2}(f_M + 2\zeta\lambda)\tau_z\left[(\sigma_y s_y - \sigma_x s_x)\sin 2\phi_{\mathbf{k}} + (\sigma_x s_y + \sigma_y s_x)\cos 2\phi_{\mathbf{k}}\right]\,, \tag{B.14}$$

and

$$f_0 = \epsilon(\lambda^2 + \lambda^2_{\text{sv}}) + \lambda_{zz}(\Delta\lambda_{\text{sv}} - \lambda^2)\,, \tag{B.15}$$

$$f_r = \frac{\lambda}{2\tilde{\Gamma}}[(\Delta+\lambda_{\text{sv}})^2 - (\epsilon-\lambda_{zz})^2\,, \tag{B.16}$$

$$f_{zz} = \frac{\epsilon(\lambda^2 - \lambda_{\text{sv}}\Delta) - \lambda_{zz}(\lambda^2+\Delta^2)}{2\tilde{\Gamma}}\,, \tag{B.17}$$

$$f_{\text{sv}} = \frac{\lambda^2(\Delta+\lambda_{\text{sv}}) - \epsilon(\Delta\lambda_{zz} + \epsilon\lambda_{\text{sv}})}{2\tilde{\Gamma}}\,, \tag{B.18}$$

$$f_{0z} = \frac{\lambda^2(\Delta+\lambda_{\text{sv}}) - \lambda_{zz}(\Delta\lambda_{zz} + \epsilon\lambda_{\text{sv}})}{2\tilde{\Gamma}}\,, \tag{B.19}$$

$$f_M = \frac{\lambda\left(\epsilon^2 + \lambda^2_{\text{sv}} - \lambda^2_{zz} - \Delta^2\right)}{2\tilde{\Gamma}}\,, \tag{B.20}$$

$$\tilde{\Gamma} = \sqrt{\lambda^2[(\epsilon-\lambda_{zz})^2 - (\Delta+\lambda_{\text{sv}})^2] + (\lambda_{zz}\Delta + \epsilon\lambda_{\text{sv}})^2} \tag{B.21}$$

$$L^a_{0\pm} = \left[v^2k^2 - \left(\epsilon^2 + \lambda^2_{\text{sv}} - \lambda^2_{zz} - \Delta^2 \pm 2\tilde{\Gamma}\right) + \imath\, a\, 0\right]^{-1}\,. \tag{B.22}$$

Due to the fact that the matrix structures in Eq. (3.52) form a closed Clifford algebra, contrarily to what was done for the minimal model, no effective Hamiltonian is required for the disorder-

averaged propagators, simply obtained by performing analytical continuation

$$\mathcal{G}^a_{\mathbf{k}}(\epsilon,\lambda,\lambda_{\rm sv},\Delta,\lambda_{zz}) = G^a_{0\mathbf{k}}(\epsilon+\imath\, n_i\, a\,\eta_0,\lambda-\imath\, n_i\, a\,\eta_r,\lambda_{\rm sv}-\imath\, n_i\, a\,\eta_{\rm sv},\Delta-\imath\, n_i\, a\,\eta_\Delta,\lambda_{zz}-\imath\, n_i\, a\,\eta_{zz})\,. \tag{B.23}$$

Appendix C

Vanishing of the Anomalous Commutator in the 2D Dirac-Rashba Model

Here we show that the anomalous commutator introduced in Eq. (4.6)

$$C = \int dy [J_0^a(x), J_\mu(y)] A^\mu(y)\,, \tag{C.1}$$

due to the joint effect of an infinite Dirac sea of filled electron states and an external field is identically zero.

Using the definition of the spin and current densities Eqs. (4.3)-(4.4), we can manipulate the commutator as:

$$\begin{aligned}
\left[J_0^a(\mathbf{x}), J_\mu(\mathbf{y})\right] &= \frac{1}{2}\left[\Psi_0^\dagger(\mathbf{x})\,\sigma_0\,s_a\,\Psi_0(\mathbf{x}), \Psi_0^\dagger(\mathbf{y})\sigma_\mu\,\Psi_0(\mathbf{y})\right] && \text{(C.2)}\\
&= \frac{1}{2}\Big(\Psi_0^\dagger(\mathbf{x})\,\sigma_0\,s_a\left\{\Psi_0(\mathbf{x}), \Psi_0^\dagger(\mathbf{y})\right\}\sigma_\mu\,\Psi_0(\mathbf{y}) && \text{(C.3)}\\
&- \Psi_0^\dagger(\mathbf{y})\,\sigma_\mu\,\left\{\Psi_0^\dagger(\mathbf{x}), \Psi_0(\mathbf{y})\right\}\sigma_0\,s_a\,\Psi_0(\mathbf{x}) && \text{(C.4)}\\
&- \Psi_0^\dagger(\mathbf{y})\,\sigma_\mu\,\left\{\Psi_0^\dagger(\mathbf{x}), \Psi_0(\mathbf{y})\right\}\sigma_0\,s_a\,\Psi_0(\mathbf{x})\Big) && \text{(C.5)}\\
&= \frac{1}{2}\Big(\Psi_0^\dagger(\mathbf{x})\,s_a\,\sigma_\mu\,\Psi_0(\mathbf{y})\delta(\mathbf{x}-\mathbf{y}) - \Psi_0^\dagger(\mathbf{y})\,\sigma_\mu\,s_a\,\Psi_0(\mathbf{x})\,\delta(\mathbf{y}-\mathbf{x})\Big)\,. && \text{(C.6)}
\end{aligned}$$

At equal position, the above object is in principle singular as we are effectively subtracting two infinite quantities [88]. In order to be sure that this term is zero, we need first to regularise it and then evaluate it explicitly. As a regularisation scheme we choose point splitting with two infinitesimal quantities η and η' [88] and use the normal ordering definition $A\,B = :A\,B: + \langle A\,B\rangle$

$$\begin{aligned}
\left[J_0^a(\mathbf{x}), J_\mu(\mathbf{y})\right] = \lim_{\boldsymbol{\eta},\boldsymbol{\eta}'\to 0}\frac{1}{2}\Big(&: \Psi_0^\dagger(\mathbf{x}+\boldsymbol{\eta})\,s_a\,\sigma_\mu\,\Psi_0(\mathbf{y}-\boldsymbol{\eta}'): \delta(\mathbf{x}-\mathbf{y}-\boldsymbol{\eta}-\boldsymbol{\eta}') && \text{(C.7)}\\
&- : \Psi_0^\dagger(\mathbf{y}+\boldsymbol{\eta}')\,\sigma_\mu\,s_a\,\Psi_0(\mathbf{x}-\boldsymbol{\eta}): \delta(\mathbf{y}-\mathbf{x}-\boldsymbol{\eta}-\boldsymbol{\eta}') && \text{(C.8)}\\
&+ \langle\Psi_0^\dagger(\mathbf{x}+\boldsymbol{\eta})\,s_a\,\sigma_\mu\,\Psi_0(\mathbf{y}-\boldsymbol{\eta}')\rangle\,\delta(\mathbf{x}-\mathbf{y}-\boldsymbol{\eta}-\boldsymbol{\eta}') && \text{(C.9)}\\
&- \langle\Psi_0^\dagger(\mathbf{y}+\boldsymbol{\eta}')\,\sigma_\mu\,s_a\,\Psi_0(\mathbf{x}-\boldsymbol{\eta})\rangle\,\delta(\mathbf{y}-\mathbf{x}-\boldsymbol{\eta}-\boldsymbol{\eta}')\Big) && \text{(C.10)}
\end{aligned}$$

where the expectation value is taken with respect to the filled Dirac sea. Since the normal ordered terms are finite, we can now take their difference and so we are left with the expectation values only. Let us now fix $a = y$ and choose the gauge such as $E = \partial_t A_0$ [1]. It is also convenient to move to momentum and imaginary frequency space, from which we arrive at the Matsubara sum [$q = (\imath\omega_m, \mathbf{q})$ and $p = (\imath\nu_n, \mathbf{p})$]

$$\langle [J_0^y(q), J_0(-q)] \rangle = -\frac{1}{k_B T} \sum_n \int \frac{d^2p}{(2\pi)^2} \left\{ G^y_{0\mathbf{p}+\mathbf{q}}(\imath\omega_m + \imath\nu_n) - G^y_{0\mathbf{p}}(\imath\nu_n) \right\}, \tag{C.11}$$

where $G^p_{0\mathbf{p}} = \mathrm{tr}[G_{0\mathbf{p}}\sigma_0 s_y/4]$. At this point we can safely shift the momentum in the first Green's function as $\mathbf{p} + \mathbf{q} \to \mathbf{p}$ to obtain the cancellation. A longer but equivalent way consists in performing the integrals explicitly. In this case it is easy to see that the second integrand (Green's function not depending on q) is zero after angular average, whereas for the first integrand, one can expand for small q and perform the integral explicitly, finding again zero.

[1] It can be checked explicitly that this choice does not affect the final result.

Appendix D

Details on the Derivation of the Spin-Bloch Equations

Simple scattering model

The collision integral [Eq. (D.1)] is diagonal in valley space, $\langle \mathbf{k}\kappa|I|\mathbf{k}'\bar{\kappa}\rangle = 0$, which was justified in the main text,

$$\partial_t \mathbf{S}^{\kappa}_{\mathbf{k}}|_{\text{scatt}} = \langle \mathbf{k}\kappa|I|\mathbf{k}\kappa\rangle \equiv I[\mathbf{S}^{\kappa}_{\mathbf{k}}] \tag{D.1}$$

$$= -\pi \sum_{\mathbf{k}'\kappa'} \delta(\epsilon_{\mathbf{k}} - \epsilon_{\mathbf{k}'}) \langle \mathbf{S}^{\kappa}_{\mathbf{k}} V^{\kappa\kappa'}_{\mathbf{k}\mathbf{k}'} U^{\kappa'\kappa}_{\mathbf{k}'\mathbf{k}} + V^{\kappa\kappa'}_{\mathbf{k}\mathbf{k}'} V^{\kappa'\kappa}_{\mathbf{k}'\mathbf{k}} \mathbf{S}^{\kappa}_{\mathbf{k}} - 2\, V^{\kappa\kappa'}_{\mathbf{k}\mathbf{k}'} \mathbf{S}^{\kappa'}_{\mathbf{k}'} V^{\kappa'\kappa}_{\mathbf{k}'\mathbf{k}} \rangle_{\text{dis}}\,. \tag{D.2}$$

Intervalley processes are still taken into account *internally* to the collision integral, i.e. by considering transitions of the type $K \to K' \to K$ where electrons initially at $K(K')$ are scattered at $K'(K)$ and then scattered back to $K(K')$. Inserting the disorder correlator

$$\langle |V^{\kappa\kappa'}_{\mathbf{k}\mathbf{k}'}|^2 \rangle_{\text{dis}} = u^2\, \delta_{\kappa\kappa'} \cos^2\theta + w^2 \delta_{\kappa\bar{\kappa}'} \sin^2\theta\,, \tag{D.3}$$

$$\theta \equiv \frac{\phi_{\mathbf{k}'} - \phi_{\mathbf{k}}}{2}, \tag{D.4}$$

into Eq. (D.1) gives Eqs. (6.56)-(6.57) in main text. Using the notation in the main text and the relation

$$2\pi\, u^2 \int_0^{\infty} \frac{dk'}{2\pi} k' \delta(\epsilon_{\mathbf{k}} - \epsilon_{\mathbf{k}'}) = \frac{u^2 \epsilon}{v^2} \equiv \frac{4}{\tau}\,, \tag{D.5}$$

where the intravalley transport time τ has been defined, yields, after simple algebra

$$I^{\text{intra}} = -\frac{4}{\tau} \sum_m e^{\imath\, m\phi_{\mathbf{k}}} \int_0^{2\pi} \frac{d\phi_{\mathbf{k}'}}{2\pi} \cos^2\left(\frac{\phi_{\mathbf{k}} - \phi_{\mathbf{k}'}}{2}\right) \left[1 - e^{-\imath\, 2m \left(\frac{\phi_{\mathbf{k}} - \phi_{\mathbf{k}'}}{2}\right)}\right] S^m_i \tag{D.6}$$

$$= -\frac{4}{\tau} \sum_m e^{\imath\, m\, \phi_{\mathbf{k}}} S^m_i \int_0^{2\pi} \frac{d\theta}{2\pi} \cos^2\theta\, (1 - \cos 2\, m\, \theta) \tag{D.7}$$

$$\equiv -\sum_{m\neq 0} e^{\imath\, m\, \phi_{\mathbf{k}}} \frac{S^m_i}{\tau^A_m}\,, \tag{D.8}$$

with

$$\frac{1}{\tau^A_m} = \frac{4}{\tau} \int_0^{2\pi} \frac{d\theta}{2\pi} \cos^2\theta\, [1 - \cos(2\, m\, \theta)]\,. \tag{D.9}$$

The intervalley part reads

$$I^{\text{inter}} = -\frac{4}{\tau} r^2 \left\{ \sum_m e^{\imath\, m\, \phi_{\mathbf{k}}} \int_0^{2\pi} \frac{d\phi_{\mathbf{k}'}}{2\pi} \sin^2\left(\frac{\phi_{\mathbf{k}} - \phi_{\mathbf{k}'}}{2}\right) \left[S_i^m - \bar{S}_i^m e^{-\imath\, 2m \left(\frac{\phi_{\mathbf{k}} - \phi_{\mathbf{k}'}}{2}\right)} \right] \right\} \tag{D.10}$$

$$= -\frac{4}{\tau} r^2 \left(\sum_m e^{\imath\, m\, \phi_{\mathbf{k}}} \frac{S_i^m}{2} - \bar{S}_i^m \int_0^{2\pi} \frac{d\theta}{2\pi} \sin^2\theta\, \cos 2\, m\, \theta \right) \tag{D.11}$$

$$= -\, r^2 \sum_m e^{\imath\, m\, \phi_{\mathbf{k}}} \left(\frac{2 S_i^m}{\tau} - \frac{\bar{S}_i^m}{\tau_m^B} \right) , \tag{D.12}$$

with

$$\frac{1}{\tau_m^B} = \frac{4}{\tau} \int_0^{2\pi} \frac{d\theta}{2\pi} \sin^2\theta \cos(2\, m\, \theta) \, . \tag{D.13}$$

It is instructive to consider the system *without* SO coupling, for which the various harmonics are decoupled

$$\partial_t S_i^m = -\left(\frac{1}{\tau_m^A} + \frac{2r^2}{\tau} \right) S_i^m + \frac{r^2}{\tau_m^B} \bar{S}_i^m \, , \tag{D.14}$$

$$\partial_t \bar{S}_i^m = -\left(\frac{1}{\tau_m^A} + \frac{2r^2}{\tau} \right) \bar{S}_i^m + \frac{r^2}{\tau_m^B} S_i^m \, , \tag{D.15}$$

and the corresponding expression at K', obtainable by $S \to \bar{S}$. Solving these equations, we obtain

$$\begin{pmatrix} S_i^m(t) \\ \bar{S}_i^m(t) \end{pmatrix} = e^{-\left(\frac{1}{\tau_m^A} + 2r^2 \frac{t}{\tau}\right)} \begin{pmatrix} \cosh\left(t \frac{r^2}{\tau_m^B}\right) & \sinh\left(t \frac{r^2}{\tau_m^B}\right) \\ \sinh\left(t \frac{r^2}{\tau_m^B}\right) & \cosh\left(t \frac{r^2}{\tau_m^B}\right) \end{pmatrix} . \begin{pmatrix} S_i^m(0) \\ \bar{S}_i^m(0) \end{pmatrix} . \tag{D.16}$$

For $m = 0$, we have $\tau_0^A \to \infty$ and $\tau_0^B \to \tau/2$, so that the solution for the total spin polarization is found as $S_i(t) = S_i^0(t) + \bar{S}_i^0(t) = S_i(t=0)$, which is simply a statement of spin conservation. Note that the uniform oscillation (zeroth harmonic) of the Fermi surface is associated with the charge density. Restoring SO coupling, and defining $\tau_{\pm 1}^A = \tau = -\tau_{\pm 1}^B$ we find Eqs. (6.59)-(6.64) of the main text for the harmonics $m = 0, \pm 1$.

General nonmagnetic disorder

The correlator for generic non-magnetic disorder reads as

$$\langle |U_{\mathbf{k}\mathbf{k}'}^{\kappa\kappa'}|^2 \rangle_{\text{dis}} = \sum_{p=\pm} \left[\left(u_p^2\, \delta_{\kappa\kappa'} + \tilde{w}_p^2 \delta_{\kappa\bar{\kappa}\prime} \right) \cos^2\theta_p + \left(w_p^2 \delta_{\kappa\bar{\kappa}\prime} + \tilde{u}_p^2\, \delta_{\kappa\kappa'} \right) \sin^2\theta_p \right] , \tag{D.17}$$

$$\theta_\pm \equiv \frac{\phi_{\mathbf{k}'} \pm \phi_{\mathbf{k}}}{2} \, . \tag{D.18}$$

It is convenient to define the relaxation rates [see main text, Eqs. (6.50)-(6.53)],

$$\frac{1}{\tau_u^p} = \frac{u_p^2 \epsilon}{4v^2} \, , \quad \frac{1}{\tau_{\tilde{u}}^p} = \frac{\tilde{u}_p^2 \epsilon}{4v^2} \, , \quad \frac{1}{\tau_w^p} = \frac{w_p^2 \epsilon}{4v^2} \, , \quad \frac{1}{\tau_{\tilde{w}}^p} = \frac{\tilde{w}_p^2 \epsilon}{4v^2} \, . \tag{D.19}$$

Following the same steps as in Appendix A, we find

$$I^{\text{intra}} = -4\sum_m e^{\imath\, m\phi_{\mathbf{k}}} \int_0^{2\pi} \frac{d\phi_{\mathbf{k}'}}{2\pi} \left(\frac{1}{\tau_u^-}\cos^2\theta_- + \frac{1}{\tau_u^+}\cos^2\theta_+ + \frac{1}{\tau_{\tilde{u}}^-}\sin^2\theta_- + \frac{1}{\tau_{\tilde{u}}^-}\sin^2\theta_+ \right) \tag{D.20}$$

$$\times \left(1 - e^{-\imath\, 2m\,\theta_-}\right) S_i^m \tag{D.21}$$

$$= -\sum_{m\neq 0} e^{\imath\, m\,\phi_{\mathbf{k}}} \frac{S_i^m}{\tau_{KK}} + \left(\frac{1}{\tau_u^+} - \frac{1}{\tau_{\tilde{u}}^+}\right)\left(e^{5\imath\phi_{\mathbf{k}}} S_i^1 + e^{-5\imath\phi_{\mathbf{k}}} S_i^{-1}\right), \tag{D.22}$$

where

$$\frac{1}{\tau_{KK}} = \frac{1}{\tau_u^-} + \frac{3}{\tau_{\tilde{u}}^-} + \frac{2}{\tau_u^+} + \frac{2}{\tau_{\tilde{u}}^+}. \tag{D.23}$$

The intervalley part of the collision integral reads

$$I^{\text{inter}} = -4\sum_m e^{\imath\, m\phi_{\mathbf{k}}} \int_0^{2\pi} \frac{d\phi_{\mathbf{k}'}}{2\pi} \left(\frac{1}{\tau_{\tilde{w}}^-}\cos^2\theta_- + \frac{1}{\tau_{\tilde{w}}^+}\cos^2\theta_+ + \frac{1}{\tau_w^-}\sin^2\theta_- + \frac{1}{\tau_w^+}\sin^2\theta_+ \right) \tag{D.24}$$

$$\times \left(S_i^m - \bar{S}_i^m e^{-\imath\, 2m\,\theta_-}\right) \tag{D.25}$$

$$= -\sum_m e^{\imath\, m\,\phi_{\mathbf{k}}} \left(\frac{S_i^m}{\tau_{KK'}} + \frac{\bar{S}_i^m}{\tau_m^{\text{iv}}}\right) - \left(\frac{1}{\tau_w^+} - \frac{1}{\tau_{\tilde{w}}^+}\right)\left(e^{-3\imath\phi_{\mathbf{k}}} S_i^1 + e^{3\imath\phi_{\mathbf{k}}} S_i^{-1}\right), \tag{D.26}$$

where

$$\frac{1}{\tau_{KK'}} = 2\left(\frac{1}{\tau_w^-} + \frac{1}{\tau_{\tilde{w}}^-} + \frac{1}{\tau_w^+} + \frac{1}{\tau_{\tilde{w}}^+}\right), \qquad \frac{1}{\tau_0^{\text{iv}}} = \frac{1}{\tau_{KK'}}, \qquad \frac{1}{\tau_{\pm 1}^{\text{iv}}} = \frac{1}{\tau_w^-} - \frac{1}{\tau_{\tilde{w}}^-}. \tag{D.27}$$

The general Bloch equations are thus obtained from Eqs. (6.59)-(6.64) in main text via the following mapping

$$\frac{2r^2}{\tau} \to \frac{1}{\tau_{KK'}}, \qquad h(S_i^{\pm}, \bar{S}_i^{\pm}) \to \left(\frac{1}{\tau_{KK}} + \frac{1}{\tau_{KK'}}\right) S_i^{\pm 1} + \left(\frac{1}{\tau_w^-} - \frac{1}{\tau_{\tilde{w}}^-}\right) \bar{S}_i^{\pm 1}. \tag{D.28}$$

Appendix E

Magnetised Graphene: Details on the Solution of the Boltzmann Transport Equations

In what follows, we derive the analytical form of the nonequilibrium distribution function for intravalley scattering potentials. For brevity, we work at fixed Fermi energy, $\epsilon > 0$. The scattering probability is given by

$$W_{\mathbf{k}_\chi,\mathbf{k}'_{\chi'}} = 2\pi n_i \, \mathcal{T}_{\mathbf{k}_\chi \mathbf{k}'_{\chi'}} \, \delta(\epsilon_{\mathbf{k}_\chi} - \epsilon_{\mathbf{k}'_{\chi'}}) = 2\pi n_i \left| \langle \mathbf{k}'_{\chi'} | \mathrm{T} | \mathbf{k}_\chi \rangle \right|^2 \delta(\epsilon_{\mathbf{k}_\chi} - \epsilon_{\mathbf{k}'_{\chi'}}) \,, \tag{E.1}$$

where all the quantities appearing in the last equation are defined in the main text. Throughout this Appendix, we also employ the short-hand notation $(d\mathbf{k}) = d^2\mathbf{k}/4\pi^2$. The wavefunctions are expressed in the basis:

$$(A^\uparrow K,\, A^\downarrow K,\, B^\uparrow K,\, B^\downarrow K,\, B^\uparrow K',\, B^\downarrow K',\, A^\uparrow K',\, A^\downarrow K')^{\mathrm{t}} \,. \tag{E.2}$$

Exact solution in zero magnetic field

Without loss of generality, we take the electric field oriented along the $\hat{x}$ direction. In the steady state of the linear response regime, the left-hand side of the BTEs [Eq. (7.5)] reads as

$$-\boldsymbol{\mathcal{E}} \cdot \nabla_{\mathbf{k}} f^0_{\mathbf{k}_\chi} = -\boldsymbol{\mathcal{E}} \cdot \mathbf{v}_{\mathbf{k}_\chi} \left(\frac{\partial f^0_{\mathbf{k}_\chi}}{\partial \epsilon} \right) = -\varsigma_v \, |\boldsymbol{\mathcal{E}}| \, v_{k_\chi} \cos\phi_{\mathbf{k}} \left(\frac{\partial f^0_{\mathbf{k}_\chi}}{\partial \epsilon} \right) \,, \tag{E.3}$$

where v_{k_χ} is the band velocity of the χ Fermi ring and ς_v is its sign, $\cos\phi_{\mathbf{k}} = k_x/k$ and $f^0_{\mathbf{k}_\chi} = (1 + \mathrm{Exp}[(\epsilon_{\mathbf{k}_\chi} - \epsilon)/k_B T])^{-1}$. To solve the BTEs, we make use of the ansatz [cf. Eq. (7.9)]

$$\delta f_{\mathbf{k}\chi} = -\left(\frac{\partial f^0_{\mathbf{k}_\chi}}{\partial \epsilon} \right) \left(\tau^{\parallel}_\chi \boldsymbol{\mathcal{E}} + \tau^{\perp}_\chi \, \hat{z} \times \boldsymbol{\mathcal{E}} \right) \cdot \mathbf{v}_{\mathbf{k}_\chi} \tag{E.4}$$

$$= -\varsigma_v \, \mathcal{E} \left(\frac{\partial f^0_{\mathbf{k}_\chi}}{\partial \epsilon} \right) v_{k_\chi} \left(\tau^{\parallel}_\chi \cos\phi_{\mathbf{k}_\chi} + \tau^{\perp}_\chi \, \sin\phi_{\mathbf{k}_\chi} \right) \,. \tag{E.5}$$

In regime II, only intra-ring processes are allowed, whereas in regime I and III, one needs to take into account inter-ring transitions. For fixed index χ, we separate intra-ring $(\chi\chi)$ and inter-ring $(\chi\bar{\chi})$ processes

$$S\left[f_{\mathbf{k}_\chi}\right] = S^{\text{intra}}\left[f_{\mathbf{k}_\chi}\right] + S^{\text{inter}}\left[f_{\mathbf{k}_\chi}\right], \tag{E.6}$$

$$S^{\text{intra}}\left[f_{\mathbf{k}_\chi}\right] = -\int (d^2\mathbf{k}')\left(f_{\mathbf{k}_\chi} W_{\mathbf{k}_\chi,\mathbf{k}'_\chi} - f_{\mathbf{k}'_\chi} W_{\mathbf{k}'_\chi,\mathbf{k}_\chi}\right), \tag{E.7}$$

$$S^{\text{inter}}\left[f_{\mathbf{k}_\chi}\right] = -\int (d^2\mathbf{k}')\left(f_{\mathbf{k}_\chi} W_{\mathbf{k}_\chi,\mathbf{k}'_{\bar{\chi}}} - f_{\mathbf{k}'_{\bar{\chi}}} W_{\mathbf{k}_{\bar{\chi}},\mathbf{k}'_\chi}\right). \tag{E.8}$$

The different scattering probabilities are

$$W_{\mathbf{k}_\chi,\mathbf{k}'_\chi} = 2\pi n_i\, \delta(\epsilon_{\mathbf{k}_\chi} - \epsilon_{\mathbf{k}'_\chi})\, \mathcal{T}_{\chi\chi}(\phi), \tag{E.9}$$

$$W_{\mathbf{k}_\chi,\mathbf{k}'_{\bar{\chi}}} = 2\pi n_i\, \delta(\epsilon_{\mathbf{k}_\chi} - \epsilon_{\mathbf{k}'_{\bar{\chi}}})\, \mathcal{T}_{\chi\bar{\chi}}(\phi), \tag{E.10}$$

$$W_{\mathbf{k}'_\chi,\mathbf{k}_\chi} = 2\pi n_i\, \delta(\epsilon_{\mathbf{k}'_\chi} - \epsilon_{\mathbf{k}_\chi})\, \mathcal{T}_{\chi\chi}(-\phi), \tag{E.11}$$

$$W_{\mathbf{k}'_{\bar{\chi}},\mathbf{k}_\chi} = 2\pi n_i\, \delta(\epsilon_{\mathbf{k}'_{\bar{\chi}}} - \epsilon_{\mathbf{k}_\chi})\, \mathcal{T}_{\bar{\chi}\chi}(-\phi). \tag{E.12}$$

It will be useful in the following to work with the symmetric and antisymmetric components

$$\mathcal{T}_{\chi\chi'}(\pm\phi) = \mathcal{T}^s_{\chi\chi'} \pm \mathcal{T}^a_{\chi\chi'}, \tag{E.13}$$

along with the trigonometric relations

$$\cos(\alpha+\beta) = \cos\alpha\cos\beta - \sin\alpha\sin\beta, \tag{E.14}$$

$$\sin(\alpha+\beta) = \sin\alpha\cos\beta + \sin\beta\cos\alpha, \tag{E.15}$$

to recast Eq. (E.4) into the form

$$f_{\mathbf{k}'_\chi} = -\varsigma_v\, \mathcal{E}\, v_{k_\chi} \frac{\partial f^0_{\mathbf{k}'_\chi}}{\partial\epsilon}\left[\cos\phi_{\mathbf{k}_\chi}\left(\tau^{\parallel}_\chi\cos\phi + \tau^{\perp}_\chi\sin\phi\right) + \sin\phi_{\mathbf{k}_\chi}\left(\tau^{\perp}_\chi\cos\phi - \tau^{\parallel}_\chi\sin\phi\right)\right]. \tag{E.16}$$

The intra-ring integrals now reduce to

$$I_1^{\text{intra}} \equiv \int (d^2\mathbf{k}') f_{\mathbf{k}_\chi} W_{\mathbf{k}_\chi,\mathbf{k}'_\chi} = 2\pi n_i\, f_{\mathbf{k}_\chi} N(\epsilon_{\mathbf{k}_\chi}) \int \frac{d\phi}{2\pi} \mathcal{T}_{\chi\chi}(\phi), \tag{E.17}$$

$$I_2^{\text{intra}} \equiv \int (d^2\mathbf{k}') f_{\mathbf{k}'_\chi} W_{\mathbf{k}'_\chi,\mathbf{k}_\chi} \tag{E.18}$$

$$= 2\pi n_i\, F_\chi\, v_{k_\chi}\, N(\epsilon_{\mathbf{k}_\chi})\left\{c_{1,\mathbf{k}_\chi}\int\frac{d\phi}{2\pi}\cos\phi\,\mathcal{T}_{\chi\chi}(-\phi) + c_{2,\mathbf{k}_\chi}\int\frac{d\phi}{2\pi}\sin\phi\,\mathcal{T}_{\chi\chi}(-\phi)\right\}, \tag{E.19}$$

where $N(\epsilon_{\mathbf{k}}) = \frac{1}{2\pi}\frac{k}{v_k}$ is the density of states and

$$\{c_{1,\mathbf{k_\emptyset}},\, c_{2,\mathbf{k}_\chi}\} = \{\cos\phi_{\mathbf{k}_\chi}\tau^{\parallel}_\chi + \sin\phi_{\mathbf{k}_\chi}\tau^{\perp}_\chi,\, \cos\phi_{\mathbf{k}_\chi}\tau^{\perp}_\chi - \sin\phi_{\mathbf{k}_\chi}\tau^{\parallel}_\chi\}, \quad \text{and} \quad F_\chi = -\varsigma_v\,\mathcal{E}\,\frac{\partial f^0_{\mathbf{k}_\chi}}{\partial\epsilon}. \tag{E.20}$$

The inter-ring integrals are obtained via the a similar procedure. In the following, we define $(\tau^{\parallel}_{\chi}, \tau^{\parallel}_{\bar{\chi}}) = (\tau^{\parallel}, \bar{\tau}^{\parallel})$ and equally for $\tau^{\perp}_{\chi}, v_{\chi}, N(\epsilon_{k_\chi}), F_{\chi}$. The full scattering operator is thus

$$S^{\text{intra}}\left[f_{\mathbf{k}_\chi}\right] = -2\pi n_i F_\chi N v \left[\cos\phi_{\mathbf{k}_\chi}\left(\tau^{\parallel}\int\frac{d\phi}{2\pi}\mathcal{T}^s_{\chi\chi} - \tau^{\parallel}\int\frac{d\phi}{2\pi}\cos\phi\,\mathcal{T}^s_{\chi\chi} - \tau^{\perp}\int\frac{d\phi}{2\pi}\sin\phi\,\mathcal{T}^a_{\chi\chi}\right)\right. \tag{E.21}$$

$$\left. + \sin\phi_{\mathbf{k}_\chi}\left(\tau^{\perp}\int\frac{d\phi}{2\pi}\mathcal{T}^s_{\chi\chi} - \tau^{\perp}\int\frac{d\phi}{2\pi}\cos\phi\mathcal{T}^s_{\chi\chi} + \tau^{\parallel}\int\frac{d\phi}{2\pi}\sin\phi\mathcal{T}^a_{\chi\chi}\right)\right] \tag{E.22}$$

$$S^{\text{inter}}\left[f_{\mathbf{k}_\chi}\right] = -2\pi n_i F_\chi v \left[\cos\phi_{\mathbf{k}_\chi}\left(\tau^{\parallel} N\int\frac{d\phi}{2\pi}\mathcal{T}^s_{\chi\bar{\chi}} - \bar{\tau}^{\parallel}\bar{N}\frac{\bar{v}}{v}\int\frac{d\phi}{2\pi}\cos\phi\mathcal{T}^a_{\bar{\chi}\chi} - \bar{\tau}^{\perp}\bar{N}\frac{\bar{v}}{v}\int\frac{d\phi}{2\pi}\sin\phi\,\mathcal{T}^a_{\bar{\chi}\chi}\right)\right. \tag{E.23}$$

$$\left. - \sin\phi_{\mathbf{k}_\chi}\left(\tau^{\perp} N\int\frac{d\phi}{2\pi}\mathcal{T}^s_{\chi\bar{\chi}} - \bar{\tau}^{\perp}\bar{N}\frac{\bar{v}}{v}\int\frac{d\phi}{2\pi}\cos\phi\mathcal{T}^s_{\bar{\chi}\chi} + \bar{\tau}^{\parallel}\bar{N}\frac{\bar{v}}{v}\int\frac{d\phi}{2\pi}\sin\phi\mathcal{T}^a_{\bar{\chi}\chi}\right)\right]. \tag{E.24}$$

Equating the coefficients of $\cos\phi_{\mathbf{k}}$, $\sin\phi_{\mathbf{k}}$ on the LHS and RHS of the linearized BTEs, we obtain for the steady state:

$$-1 = \tau^{\parallel}\left(\Gamma^0_{\chi\chi} - \Gamma^{\cos}_{\chi\chi} + \Gamma^0_{\chi\bar{\chi}}\right) + \tau^{\perp}\Gamma^{\sin}_{\chi\chi} - \bar{\tau}^{\parallel}\frac{\bar{v}}{v}\Gamma^{\cos}_{\bar{\chi}\chi} + \bar{\tau}^{\perp}\frac{\bar{v}}{v}\Gamma^{\sin}_{\bar{\chi}\chi}, \tag{E.25}$$

$$0 = \tau^{\perp}\left(\Gamma^0_{\chi\chi} - \Gamma^{\cos}_{\chi\chi} + \Gamma^0_{\chi\bar{\chi}}\right) - \tau^{\parallel}\Gamma^{\sin}_{\chi\chi} - \bar{\tau}^{\perp}\frac{\bar{v}}{v}\Gamma^{\cos}_{\bar{\chi}\chi} - \bar{\tau}^{\parallel}\frac{\bar{v}}{v}\Gamma^{\sin}_{\bar{\chi}\chi}, \tag{E.26}$$

where, as defined already in the main text,

$$\Gamma^{(0,\cos,\sin)}_{\chi\bar{\chi}} = 2\pi n_i N_\chi \int\frac{d\phi}{2\pi}\{1,\cos\phi,\sin\phi\}\left(\mathcal{T}^s_{\chi\bar{\chi}}(\phi) + \mathcal{T}^a_{\chi\bar{\chi}}(\phi)\right). \tag{E.27}$$

The system of equations can now be closed considering the respective equations for the other channel $\bar{\chi}$, *i.e.*,

$$-1 = \bar{\tau}^{\parallel}\left(\Gamma^0_{\bar{\chi}\bar{\chi}} - \Gamma^{\cos}_{\bar{\chi}\bar{\chi}} + \Gamma^0_{\bar{\chi}\chi}\right) + \bar{\tau}^{\perp}\Gamma^{\sin}_{\bar{\chi}\bar{\chi}} - \tau^{\parallel}\frac{v}{\bar{v}}\Gamma^{\cos}_{\chi\bar{\chi}} + \tau^{\perp}\frac{v}{\bar{v}}\Gamma^{\sin}_{\chi\bar{\chi}}, \tag{E.28}$$

$$0 = \bar{\tau}^{\perp}\left(\Gamma^0_{\bar{\chi}\bar{\chi}} - \Gamma^{\cos}_{\bar{\chi}\bar{\chi}} + \Gamma^0_{\bar{\chi}\chi}\right) - \bar{\tau}^{\parallel}\Gamma^{\sin}_{\bar{\chi}\bar{\chi}} - \tau^{\perp}\frac{v}{\bar{v}}\Gamma^{\cos}_{\chi\bar{\chi}} - \tau^{\parallel}\frac{v}{\bar{v}}\Gamma^{\sin}_{\chi\bar{\chi}}. \tag{E.29}$$

The four equations above can be manipulated by summing and subtracting them to identify some common coefficient:

$$-2 = \tau^{\parallel}\Lambda_- + \bar{\tau}^{\parallel}\bar{\Lambda}_- + \tau^{\perp}\mathrm{Y}_+ + \bar{\tau}^{\perp}\bar{\mathrm{Y}}_+, \tag{E.30}$$

$$0 = \tau^{\parallel}\Lambda_+ - \bar{\tau}^{\parallel}\bar{\Lambda}_+ + \tau^{\perp}\mathrm{Y}_- - \bar{\tau}^{\perp}\bar{\mathrm{Y}}_-, \tag{E.31}$$

$$0 = \tau^{\perp}\Lambda_- + \bar{\tau}^{\perp}\bar{\Lambda}_- - \tau^{\parallel}\mathrm{Y}_+ - \bar{\tau}^{\parallel}\bar{\mathrm{Y}}_+, \tag{E.32}$$

$$0 = \tau^{\perp}\Lambda_+ - \bar{\tau}^{\perp}\bar{\Lambda}_+ - \tau^{\parallel}\mathrm{Y}_- + \bar{\tau}^{\parallel}\bar{\mathrm{Y}}_-, \tag{E.33}$$

or in matrix form

$$\begin{pmatrix} \Lambda_- & \bar{\Lambda}_- & \mathrm{Y}_+ & \bar{\mathrm{Y}}_+ \\ \Lambda_+ & -\bar{\Lambda}_+ & \mathrm{Y}_- & -\bar{\mathrm{Y}}_- \\ -\mathrm{Y}_+ & -\bar{\mathrm{Y}}_+ & \Lambda_- & \bar{\Lambda}_- \\ -\mathrm{Y}_- & \bar{\mathrm{Y}}_- & \Lambda_+ & -\bar{\Lambda}_+ \end{pmatrix}\begin{pmatrix} \tau^{\parallel} \\ \bar{\tau}^{\parallel} \\ \tau^{\perp} \\ \bar{\tau}^{\perp} \end{pmatrix} = \begin{pmatrix} -2 \\ 0 \\ 0 \\ 0 \end{pmatrix} \tag{E.34}$$

$$\iff \begin{pmatrix} \hat{\Lambda} & \hat{\mathrm{Y}} \\ -\hat{\mathrm{Y}} & \hat{\Lambda} \end{pmatrix}\begin{pmatrix} \boldsymbol{\tau}^{\parallel} \\ \boldsymbol{\tau}^{\perp} \end{pmatrix} = -2\begin{pmatrix} \mathbf{1} \\ \mathbf{0} \end{pmatrix}, \tag{E.35}$$

where we have defined

$$\Lambda_{\pm} = \Gamma^{0}_{\chi\chi} - \Gamma^{\cos}_{\chi\chi} + \Gamma^{0}_{\chi\bar{\chi}} \pm \frac{v}{\bar{v}}\Gamma^{\cos}_{\chi\bar{\chi}}\,, \tag{E.36}$$

$$\Upsilon_{\pm} = \Gamma^{\sin}_{\chi\chi} \pm \frac{v}{\bar{v}}\Gamma^{\sin}_{\chi\bar{\chi}}\,, \tag{E.37}$$

and analogously for their barred version, obtained from the last two equations by replacing $\chi \to \bar{\chi}$. In our compact notation we have $\left(\boldsymbol{\tau}^{\parallel}, \boldsymbol{\tau}^{\perp}\right)^{\mathsf{t}} = (\tau^{\parallel}, \bar{\tau}^{\parallel}, \tau^{\perp}, \bar{\tau}^{\perp})^{\mathsf{t}}$, and $(\mathbf{1}, \mathbf{0})^{\mathsf{t}} = (1,0,0,0)^{\mathsf{t}}$. Together with the corresponding system at K' valley we thus identify 16 relaxation rates.

The formal solution of the linear system Eq. (E.35) gives

$$\boldsymbol{\tau}^{\parallel} = -2\left(\hat{\Lambda} + \hat{\Upsilon}\hat{\Lambda}^{-1}\hat{\Upsilon}\right)^{-1}\mathbf{1}\,, \tag{E.38}$$

$$\boldsymbol{\tau}^{\perp} = \hat{\Lambda}^{-1}\hat{\Upsilon}\boldsymbol{\tau}^{\parallel}\,, \tag{E.39}$$

as reported in Eq. (6) of the main text.

Finite magnetic field

In the presence of an external magnetic field, the LHS of the BTEs reads as

$$\dot{\mathbf{k}}\cdot\nabla_{\mathbf{k}} f_{\mathbf{k}_\chi} = -\left(\boldsymbol{\mathcal{E}} + \mathbf{v}_{\mathbf{k}}\times\boldsymbol{\mathcal{B}}\right)\cdot\nabla_{\mathbf{k}}\left(f^{0}_{\mathbf{k}_\chi} + \delta f_{\mathbf{k}_\chi}\right)\,. \tag{E.40}$$

In the linear response regime, the contraction with the electric field only selects the equilibrium part $f^{0}_{\mathbf{k}_\chi}$, as seen above. On the other hand, the contraction with the magnetic field selects the non-equilibrium part since

$$\left(\mathbf{v}_k\times\boldsymbol{\mathcal{B}}\right)\cdot\mathbf{v}_k = 0\,. \tag{E.41}$$

It is thus convenient to use the following generalised ansatz:

$$\delta f_{\mathbf{k}_\chi} = v_{\mathbf{k}_\chi}\left(\tau^{\parallel}_{\chi}\cos\phi_{\mathbf{k}} + \tau^{\perp}_{\chi}\sin\phi_{\mathbf{k}}\right)\,. \tag{E.42}$$

In evaluating the term $\nabla_{\mathbf{k}}\delta f_{\mathbf{k}_\chi}$, we use the relations between cartesian and polar derivates

$$\frac{\partial}{\partial k_x} = \cos\phi_{\mathbf{k}}\frac{\partial}{\partial k} - \frac{\sin\phi_{\mathbf{k}}}{k}\frac{\partial}{\partial\phi_{\mathbf{k}}}\,, \tag{E.43}$$

$$\frac{\partial}{\partial k_y} = \sin\phi_{\mathbf{k}}\frac{\partial}{\partial k} + \frac{\cos\phi_{\mathbf{k}}}{k}\frac{\partial}{\partial\phi_{\mathbf{k}}}\,. \tag{E.44}$$

We thus have (omitting the index χ in the intermediate steps)

$$\left(\mathbf{v}_{\mathbf{k}}\times\boldsymbol{\mathcal{B}}\right)\cdot\nabla_{\mathbf{k}}\delta f_{\mathbf{k}} = \epsilon_{abc}v^{a}_{\mathbf{k}}\mathcal{B}_b\,\partial_c\left[v_{\mathbf{k}}\left(\tau^{\parallel}\cos\phi_{\mathbf{k}} + \tau^{\perp}\sin\phi_{\mathbf{k}}\right)\right]\,, \tag{E.45}$$

where ϵ_{abc} is the Levi-Civita symbol. Expanding the derivatives (and using $\partial_{k_i}\to\partial_i$ for brevity), we obtain

1. $$\partial_x\left[v_{\mathbf{k}}\left(\tau^{\parallel}\cos\phi_{\mathbf{k}} + \tau^{\perp}_{\chi}\sin\phi_{\mathbf{k}}\right)\right] = \cos^2\phi_{\mathbf{k}}\,\partial_k\left(v_{\mathbf{k}}\tau^{\parallel}\right) + \cos\phi_{\mathbf{k}}\sin\phi_{\mathbf{k}}\partial_k\left(v_{\mathbf{k}}\tau^{\perp}\right) + \\ + \tau^{\parallel}\,v_{\mathbf{k}}\,\partial_x\cos\phi_{\mathbf{k}} + \tau^{\perp}v_{\mathbf{k}}\,\partial_x\sin\phi_{\mathbf{k}}\,, \tag{E.46}$$
2. $$\partial_y\left[v_{\mathbf{k}}\left(\tau^{\parallel}\cos\phi_{\mathbf{k}} + \tau^{\perp}_{\chi}\sin\phi_{\mathbf{k}}\right)\right] = \sin\phi_{\mathbf{k}}\cos\phi_{\mathbf{k}}\,\partial_k\left(v_{\mathbf{k}}\tau^{\parallel}\right) + \sin^2\phi_{\mathbf{k}}\,\partial_y\left(v_{\mathbf{k}}\tau^{\perp}\right) + \\ + \tau^{\parallel}v_{\mathbf{k}}\,\partial_y\cos\phi_{\mathbf{k}} + \tau^{\perp}v_{\mathbf{k}}\,\partial_y\sin\phi_{\mathbf{k}}\,, \tag{E.47}$$

where we assumed an isotropic Fermi surface $\mathbf{k} \parallel \mathbf{v}$. These expressions, using Eqs. (E.43)-(E.44), can be rewritten as

1. $\cos^2\phi_{\mathbf{k}}\,\partial_k\left(v_{\mathbf{k}}\tau^{\parallel}\right)+\cos\phi_{\mathbf{k}}\sin\phi_{\mathbf{k}}\,\partial_k\left(v_{\mathbf{k}}\tau^{\perp}\right)+v_{\mathbf{k}}\dfrac{\tau^{\parallel}}{k}\sin^2\phi_k-v_{\mathbf{k}}\dfrac{\tau^{\perp}}{k}\sin\phi_{\mathbf{k}}\cos\phi_{\mathbf{k}}\,,$ (E.48)
2. $\sin\phi_{\mathbf{k}}\cos\phi_{\mathbf{k}}\,\partial_k\left(v_{\mathbf{k}}\tau^{\parallel}\right)+\sin^2\phi_{\mathbf{k}}\,\partial_k\left(v_{\mathbf{k}}\tau^{\perp}\right)-v_{\mathbf{k}}\dfrac{\tau^{\parallel}}{k}\sin\phi_{\mathbf{k}}\cos\phi_{\mathbf{k}}+v_{\mathbf{k}}\dfrac{\tau^{\perp}}{k}\cos^2\phi_{\mathbf{k}}\,.$ (E.49)

Taking a perpendicular magnetic field $\boldsymbol{\mathcal{B}}=\mathcal{B}\,\hat{z}$, one obtains after standard algebraic manipulations

$$\left(\mathbf{v}_{\mathbf{k}_\chi}\times\boldsymbol{\mathcal{B}}\right)\cdot\nabla_{\mathbf{k}}\delta f_{\mathbf{k}_\chi}=v_{\mathbf{k}_\chi}\omega^{\chi}_{\mathcal{B}}\left(\tau^{\parallel}_{\chi}\sin\phi_{\mathbf{k}_\chi}-\tau^{\perp}_{\chi}\cos\phi_{\mathbf{k}_\chi}\right)\,, \tag{E.50}$$

where we reinstated the index χ and defined the cyclotronic frequency of the χ-ring

$$\omega^{\chi}_{\mathcal{B}}=\frac{v_{\mathbf{k}_\chi}}{k_\chi}\mathcal{B}\,. \tag{E.51}$$

It is clear from Eq. (E.28)-(E.29), that $\omega^{\chi}_{\mathcal{B}}$ can be reabsorbed in the definition of the skew cross sections:

$$\Gamma^{\text{sin}}_{\chi\chi}\to\Gamma^{\text{sin}}_{\chi\chi}+\omega^{\chi}_{B}\,, \tag{E.52}$$

to which the trivial generalisation of Eqs. (E.35) follows. Note however, due to the slight different ansatz we have used, the column of the know terms $-2(\mathbf{1},\mathbf{0})^{\text{t}}$ has to be generalised to $-2F_\chi\,(\mathbf{1},\mathbf{0})^{\text{t}}$.

Nomenclature

2DEG	Two-dimensional electron gas
BA	Born approximation
BS	Bethe Salpeter
BTE	Boltzmann transport equation
CSC	Charge-to-spin conversion
DOF	Degree of freedom
DP	Dyakonov-Perel
FQM	Fully quantum mechanical
ISGE	Inverse spin-Galvanic effect
ISHE	Inverse spin Hall effect
LHS	Left-hand side
MEC	Magnetic exchange coupling
MSHE	Magnetic spin Hall effect
QAH	Quantum anomalous Hall
QSH	Quantum spin Hall
R/A	Retarded/Advanced
RHS	Right-hand side
SC	Semiclassical
SCBA	Self-consistent Born approximation
SCTM	Self-consistent T-matrix
SGE	Spin Galvanic effect
SHE	Spin Hall effect
SO	Spin-orbit
SOT	Spin orbit torque
SRT	Spin-relaxation time

SRTA Spin-relaxation time anisotropy

STT Spin transfer torque

TI Topological insulators

TMD Transition metal dichalcogenide

vdW Van der Waals

WI Ward identity

Bibliography

[1] A. H. Compton, *The magnetic electron,* Journal of the Franklin Institute, **192**, 145 (1921).

[2] R. de L. Kronig, *Spinning Electrons and the Structure of Spectra*, Nature **117**, 550 (1926).

[3] G. E. Uhlenbeck, and S. A. Goudsmit, *Ersetzung der Hypothese vom unmechanischen Zwang durch eine Forderung bezüglich des inneren Verhaltens jedes einzelnen Elektrons,* **13**, 953-954 (1925).

[4] L. H. Thomas, *The motion of the Spinning Electron,* Nature **117**, 514 (1926);

[5] J. Schwinger, *On Quantum-Electrodynamics and the Magnetic Moment of the Electron,* Phys. Rev. **73**, 416 (1948).

[6] J. D. Jackson, *Classical Electrodynamics*, 548–53, 563–64, New York, Wiley, 3rd ed. (1998).

[7] Report of the International Technology Roadmap of Semiconductors, (2015).

[8] R. R. Schaller, *Moore's law: past, present and future,* IEEE Spectrum **34**, 6 (1997).

[9] P. Upadhyaya, *Spin-orbitronics: Electrical control of magnets via spin-orbit interaction,* PhD Thesis, California Digital Library, University of California (2015).

[10] E. Chen, D. Apalkov, Z. Diao, A. Driskill-Smith, D. Druist, D. Lottis, V. Nikitin, X. Tang, S. Watts, S. Wang, S. A. Wolf, A. W. Ghosh, J. W. Lu, S. J. Poon, M. Stan, W. H. Butler, S. Gupta, C. K. Mewes, T. Mewes, , and P. B. Visscher, *Advances and Future Prospects of Spin-Transfer Torque Random Access Memory*, IEEE Transactions on Magnetics **46**, 6 (2010).

[11] M. N. Baibich, J. M. Broto, A. Fert, F. Nguyen Van Dau, F. Petroff, P. Etienne, G. Creuzet, A. Friederich, and J. Chazelas, *Giant Magnetoresistance of (001)Fe/(001)Cr Magnetic Superlattices,* Phys. Rev. Lett. **61**, 2472 (1988).

[12] G. Binasch, P. Grünberg, F. Saurenbach, and W. Zinn, *Enhanced magnetoresistence in layered magnetic structures with antiferromagnetic interlayer exchange,* Phys. Rev B **39**, 4828(R) (1989).

[13] S. Yuasa, T. Nagahama, A. Fukushima, Y. Suzuki, and K. Ando, *Giant room-temperature magnetoresistance in single-crystal Fe/MgO/Fe magnetic tunnel junctions*, Nature Materials **3**, 868–871 (2004); D.D. Djayaprawiraa, K. Tsunekawa, M. Nagai, H. Maehara, S. Yamagata, N. Watanabe, S. Yuasa, T. Suzuki, and K. Ando, *230% room-temperature magnetoresistance in CoFeB/MgO/CoFeB magnetic tunnel junctions*, Appl. Phys. Lett. **86**, 092502 (2005).

[14] J. C. Sankey, Y. T. Cui, J. Z. Sun, J. C. Slonczewski, R. A. Buhrman, and Daniel C. Ralph, *Measurement of the spin-transfer-torque vector in magnetic tunnel junctions,* Nature Physics **4**, 67-71 (2008); Z. Diao, Z. Li, S. Wang, Y. Ding, A. Panchula, E. Chen, L. C. Wang, and Y. Huai, *Spin-transfer torque switching in magnetic tunnel junctions and spin-transfer torque random access memory*, Journal of Physics Condensed Matter **19**, 16 (2007).

[15] S. A. Wolf, D. D. Awschalom, R. A. Buhrman, J. M. Daughton, S. von Molnar, M. L. Roukes, A. Y. Chtchelkanova, D. M. Treger, *Spintronics: A Spin-Based Electronics Vision for the Future,* Science **294**, 1488-1495 (2001).

[16] R. Winkler, *Spin–Orbit Coupling Effects in Two-Dimensional Electron and Hole Systems,* Springer-Verlag Berlin Heidelberg (2003).

[17] K.V. Samokhin, *Spin–orbit coupling and semiclassical electron dynamics in noncentrosymmetric metals,* Annals of Physics **324**, 2385-2407 (2009).

[18] M. I. Dyakonov, and V. I. Perel, *Possibility of Orienting Electron Spins with Current*, Soviet Journal of Experimental and Theoretical Physics Letters **13**, 467 (1971); M. I. Dyakonov, and V. I. Perel, *Current-induced spin orientation of electrons in semiconductors*, Phys. Lett. A **35**, 459 (1971);

[19] J. E. Hirsch, *Spin Hall Effect,* Phys. Rev. Lett. **83**, 9 (1999).

[20] E. Hall, *On a New Action of the Magnet on Electric Currents,* American J. of Mathematics **2**, 287-292 (1879).

[21] N. F. Mott, *The scattering of fast electrons by atomic nuclei,* Proceeding of the Royal Society A **124**, 794 (1929).

[22] Y. K. Kato, R. C. Myers, A. C. Gossard, and D. D. Awschalom, *Observation of the Spin Hall effect in Semiconductors,* Science **306**, 1910 (2004).

[23] J. Wunderlich, B. Kaestner, J. Sinova, and T. Jungwirth, *Experimental Observation of the Spin-Hall Effect in a Two-Dimensional Spin-Orbit Coupled Semiconductor System*, Phys. Rev. Lett. **94**, 047204 (2005).

[24] L. Onsager, *Reciprocal Relations in Irreversible Processes*, Phys. Rev. **37**, 405–426 (1931).

[25] E. Saitoh, M. Ueda, H. Miyajima, and G. Tatara, *Conversion of spin current into charge current at room temperature: Inverse spin-Hall effect,* Appl. Phys. Lett. **88**, 182509 (2006).

[26] S. O. Valenzuela, and M. Tinkham, *Direct electronic measurement of the spin Hall effect*, Nature **13**, 442 (2006).

[27] H. Zhao, E. J. Loren, H. M. van Driel, and A, L. Smirl, *Coherence Control of Hall Charge and Spin Currents*, Phys. Rev. Lett. **96**, 246601 (2006).

[28] E. M. Hankiewicz, L. W. Molenkamp, T. Jungwirth, and J. Sinova, *Manifestation of the spin Hall effect through charge-transport in the mesoscopic regime*, Phys. Rev. B **70**, 241301 (2004).

[29] A. L. Friedman, O. M. J. van 't Erve, C. H. Li, J. T. Robinson, and B. T. Jonker, *Homoepitaxial tunnel barriers with funcionalized graphene-on-graphene for charge and spin transport,* Nature Comm. **5**, 3161 (2014).

[30] J. Sinova, S. O. Valenzuela, J. Wunderlich, C. H. Back, and T. Jungwirth, *Spin Hall effects,* Reviews of Modern Physics **87**, 1213 (2015).

[31] C. Brüne, A. Roth, E. G. Novik, M. König, H. Buhmann, E. M. Hankiewicz, W. Hanke, J. Sinova, and L. W. Molenkamp, *Evidence for the ballistic intrinsic spin Hall effect in HgTe nanostructures*, Nature Physics **6**, 448 (2010).

[32] M. Johnson, and R. H. Silsbee, *Interfacial charge-spin coupling: Injection and detection of spin magnetization in metals,* Phys. Rev. Lett. **55**, 1790 (1985).

[33] S. O. Valenzuela, and M. Tinkham, *Electrical detection of spin currents: The spin-current induced Hall effect,* Journal of Applied Physics **101**, 09B103 (2007).

[34] W. Hanle, *Über magnetische Beeinflussung der Polarisation der Resonanzfluoreszenz*, Zeitschrift für Physik **30**(1), 93–105 (1924).

[35] A. Bakun, B. Zakharchenya, A. Rogachev, M. Tkachuk, and V. Fleisher, *Observation of a surface photocurrent caused by optical orientation of electrons in a semiconductor,* JETP Letters. **40**, 464 (1984).

[36] C. Huang, Y. D. Chong, and Miguel A. Cazalilla, *Anomalous Nonlocal Resistance and Spin-Charge Conversion Mechanisms in Two-Dimensional Metals*, Phys. Rev. Lett. **119**, 136804 (2017).

[37] E. Ivchenko, and G. Pikus, N*ew photogalvanic effect in gyrotropic crystals*, Soviet Journal of Experimental and Theoretical Physics Letters **27**, 604–608 (1978).

[38] L. E. Vorobev, E. L. Ivchenko, G. E. Pikus, I. I. Farbshtein, V. A. Shalygin, and V. A. Shturbin, *Optical activity in tellurium induced by a current*, Soviet Journal of Experimental and Theoretical Physics Letters **29**, 441 (1979).

[39] A. Aronov, and Y. B. Lyanda-Geller, *Nuclear electric resonance and orientation of carrier spins by an electric field*, Soviet Journal of Experimental and Theoretical Physics Letters **50**, 431 (1989).

[40] V. Edelstein, *Spin polarization of conduction electrons induced by electric current in two-dimensional asymmetric electron systems,* Solid State Communications **73**, 3 (1990).

[41] S. D. Ganichev, E. L. Ivchenko, V. V. Belkov, S. A. Tarasenko, M. Sollinger, D. Weiss, W. Wegscheider, and W. Prettl, *Spin-galvanic effect*, Nature **417**, 153–156 (2002).

[42] J. R. Sánchez, L. Vila, G. Desfonds, S. Gambarelli, J. P. Attané, J.M. De Teresa, C. Magén, and A. Fert, *Spin-to-charge conversion using Rashba coupling at the interface between non-magnetic materials,* Nature Communications **4**, 2944 (2013).

[43] J. C. Rojas-Sanchez, S. Oyarzun, Y. Fu, A. Marty, C. Vergnaud, S. Gambarelli, L. Vila, M. Jamet, Y. Ohtsubo, A. Taleb-Ibrahimi, P. LeFevre, F. Bertran, N. Reyren, J. M. George, and A. Fert, *Spin to Charge Conversion at Room Temperature by Spin Pumping into a New Type of Topological Insulator: α -Sn Films,* Phys. Rev. Letters **116**, 096602 (2016).

[44] E. Lesne, Y. Fu, S. Oyarzun, J. C. Rojas-Sánchez, D. C. Vaz, H. Naganuma, G. Sicoli, J. P. Attané, M. Jamet, E. Jacquet, J. M. George, A. Barthélémy, H. Jaffrès, A. Fert, M. Bibes, L. Vila, *Highly efficient and tunable spin-to-charge conversion through Rashba coupling at oxide interfaces*, Nature Materials **15**, 1261 (2016).

[45] A. Maleki, and R. Raimondi, *Inverse spin galvanic effect in the presence of impurity spin-orbit scattering: a diagrammatic approach,* MDPI Condensed Matter **2**, 17 (2017).

[46] A. Soumyanarayanan, N. Reyren, A. Fert, and C. Panagopoulos, *Emergent phenomena induced by spin– orbit coupling at surfaces and interfaces,* Nature **539**, 509-517 (2016).

[47] I. Dzyaloshinsky, *A thermodynamic theory of 'weak' ferromagnetism of antiferromagnetics*, Journal Phys. Chem. Solids **4**, 241–255 (1958).

[48] T. Moriya, *Anisotropic superexchange interaction and weak ferromagnetism*, Phys. Rev. **120**, 91–98 (1960).

[49] M. Heide, G. Bihlmayer, and S. Blügel, *Dzyaloshinskii–Moriya interaction accounting for the orientation of magnetic domains in ultrathin films: Fe/W(110)*, Phys. Rev. B **78**, 140403 (2008).

[50] C. Moreau-Luchaire, C. Moutafis, N. Reyren, J. Sampaio, C. A. F. Vaz, N. Van Horne, K. Bouzehouane, K. Garcia, C. Deranlot, P. Warnicke, P. Wohlhüter, J. M. George, M. Weigand, J. Raabe, V. Cros, and A. Fert, *Additive interfacial chiral interaction in multilayers for stabilization of small individual skyrmions at room temperature,* Nature Nanotechnology **11**, 444-448 (2016).

[51] N. Nagaosa, and Y. Tokura, *Topological properties and dynamics of magnetic skyrmions*, Nature Nanotechnology **8**, 899–911 (2013).

[52] Z. Qiao, H. Jiang, X. Li, Y. Yao and Q. Niu, *Microscopic theory of quantum anomalous Hall effect in graphene,* Phys. Rev. B **85**, 115439 (2012).

[53] M. Offidani, and A. Ferreira, *Anomalous Hall Effect in 2D Dirac Materials,* Phys. Rev. Lett. **121**, 126802 (2018).

[54] N. D. Mermin, *Crystalline order in two dimensions*, Phys. Rev. **176**, 250-254 (1968).

[55] S. Iijima, *Helical microtubes of graphitic carbon,* Nature **354**, 56-58 (1991).

[56] A. J Huh, and Y. J. Kwon, *"Nanoantibiotics": A new paradigm for treating infectious diseases using nanomaterials in the antibiotics resistant era,* Journal of Controlled Release **156**, 2 (2011).

[57] A. Schindler, J. Brill, N. Fruehauf, J. P. Novak, Z. Yaniv, *Solution-deposited carbon nanotube layers for flexible display applications,* Physica E **37**, 119-123 (2007).

[58] Y. Kim, S. Cook, S. M. Tuladhar, S. A. Choulis, J. Nelsnon, J. R. Durrant, D. D. C. Bradley M. Giles, I. McCulloch, C. Ha and, M. Ree, *A strong regioregularity effect in self-organizing conjugated polymer films and high-efficiency polythiophene: fullerene solar cells,* Nature Materials **5**, 197-2013 (2006).

[59] K. S. Novoselov, A. K. Geim, S. V. Morozov, D. Jiang, Y. Zhang, S. V. Dubonos, I. V. Grigorieva, and A. A. Firsov, *Electric field effect in atomically thin carbon films,* Science **306**, 666–669 (2004).

[60] M. I. Katsnelson, *Graphene: carbon in two dimensions*, Materials today **10**, 20-27 (2007).

[61] R. Mas-Balleste, C. Gomez-Navarro, J. Gomez-Herrero, and F. Zamora, *2D materials: to graphene and beyond,* Nanoscale **3**, 20 (2011).

[62] R. Feynman, *There is Plenty of Room at the Bottom,* Lecture APS meeting at CalTech University (1959).

[63] J. N. Coleman, M. Lotya, A. O'Neill, S. D. Bergin, P. J. King, U. Khan, K. Young, A. Gaucher, S. De, R. J. Smith, I. V. Shvets, K. Arora, G. Stanton, H.-Y. Kim, K. Lee, G. T. Kim, G. S. Duesberg, T. Hallam, J. J. Boland, J. J. Wang, J. F. Donegan, J. C. Grunlan, G. Moriarty, A. Shmeliov, R. J. Nicholls, J. M. Perkins, E. M. Grieveson, K. Theuwissen, D. W. McComb, P. D. Nellist, and V. Nicolosi, *Two-Dimensional Nanosheets Produced by Liquid Exfoliation of Layered Materials*, Science **331**, 568–571 (2011).

[64] V. Nicolosi, M. Chhowalla, M. G. Kanatzidis, M. S. Strano, and J. N. Coleman, *Liquid exfoliation of layered materials,* Science **340**, 1226419 (2013).

[65] P. Mirò, M. Audiffred, and T. Heine, *An atlas of two-dimensional materials,* Chem. Soc. Rev. **43**, 6537 (2014).

[66] Y. Zhang, L. Zhang, and C. Zhou, *Review of Chemical Vapor Deposition of Graphene and Related Applications*, Acc. Chem. Res. **46**, 2329–2339 (2013).

[67] S. Datta, and B. Das, *Electronic analog of the electro-optic modulator,* Appl. Phys. Lett. **56**, 665 (1990).

[68] Y. G. Semenov, K. W. Kim, and J. M. Zavada, *Spin field effect transistor with a graphene channel,* Appl. Phys. Lett. **91**, 153107 (2007).

[69] A. K. Geim and K. S. Novoselov, *The rise of graphene,* Nature Materials **6**, 183 (2007).

[70] A. H. Castro Neto, F. Guinea, N. M. R. Peres, K. S. Novoselov, and A. K. Geim, *The electronic properties of graphene,* Rev. Mod. Phys. **81**, 109 (2009).

[71] D. Huertas-Hernando, F. Guinea, A. Brataas, *Spin-orbit coupling in curved graphene, fullerenes, nanotubes, and nanotube,* Phys. Rev. B **74,** 155426 (2006).

[72] S. Konschuh, M. Gmitra, J. Fabian, *Tight-binding theory of the spin-orbit coupling in graphene*, Phys. Rev. B **82**, 245412 (2010).

[73] H. Min, J. E. Hill, N. A. Sinitsyn, B. R. Sahu, L. Kleinman, and A. H. MacDonald, *Intrinsic and Rashba spin–orbit interactions in graphene sheets,* Phys. Rev. B **74**, 165310 (2006).

[74] W. Han, *Perspectives for spintronics in 2D materials*, APL Materials **4**, 032401 (2016).

[75] M. Drögeler, F. Volmer, M. Wolter, B. Terrés, K. Watanabe, T. Taniguchi, G. Güntherodt, C. Stampfer, and B. Beschoten, *Nanosecond Spin Lifetimes in Single- and Few-Layer Graphene–hBN Heterostructures at Room Temperature*, Nano Lett. **14**, 6050 (2014).

[76] S. M. Marie Dubois, X. Declerck, J. C. Charlier, and M. C. Payne, *Spin Filtering and Magneto-Resistive Effect at the Graphene/h-BN Ribbon Interface*, ACS Nano **7**(5), 4578-4585 (2013).

[77] A. Geim, and I. Grigorieva, *Van der Waals heterostructures,* Nature **499**, 419-425 (2013).

[78] K. S. Novoselov, A. Mischenko, A. Carvalho, and A. H. Castro Neto, *2D materials and van der Waals heterostructures,* Science **353**, 6298 (2016).

[79] M. Yankowitz, J. Xue, D. Cormode, J. D. Sanchez-Yamagishi, K. Watanabe, T. Taniguchi, P. Jarillo-Herrero, P. Jacquod, and B. J. LeRoy, *Emergence of superlattice Dirac points in graphene on hexagonal boron nitride*, Nature Physics **8**, 382–386 (2012).

[80] C. R. Woods, L. Britnell, A. Eckmann, R. S. Ma, J. C. Lu, H. M. Guo, X. Lin, G. L. Yu, Y. Cao, R. V. Gorbachev, A. V. Kretinin, J. Park, L. A. Ponomarenko, M. I. Katsnelson, Yu. N. Gornostyrev, K. Watanabe, T. Taniguchi, C. Casiraghi, H-J. Gao, A. K. Geim, and K. S. Novoselov, *Commensurate–incommensurate transition in graphene on hexagonal boron nitride,* Nature Physics **10**, 451-456 (2014).

[81] B. Hunt, J. D. Sanchez-Yamagishi, , A. F. Young, , M. Yankowitz, B. J. LeRoy, K. Watanabe, T. Taniguchi, P. Moon, M. Koshino, P. Jarillo-Herrero, and R. C. Ashoori, *Massive Dirac Fermions and Hofstadter Butterfly in a van der Waals Heterostructure,* Science **340**, 6139 (2013).

[82] T. Kuschel, and G. Reiss, *Spin orbitronics: Charges ride the spin wave,* Nature Nanotech. **10**, 22–24 (2015).

[83] K. Roy, M. Padmanabhan, S. Goswami, T. P. Sai, G. Ramalingam, S. Raghavan, A. Ghosh, *Graphene–MoS_2 hybrid structures for multifunctional photoresponsive memory devices,* Nature Nanotech. **8**, 826–830 (2013).

[84] M. Gmitra, and J. Fabian, *Graphene on transition-metal dichalcogenides: A platform for proximity spin-orbit physics and optospintronics,* Phys. Rev. B **92**, 155403 (2015).

[85] H. Fang, C. Battaglia, C. Carraro, S. Nemsak, B. Ozdol, J. S. Kang, H. A. Bechtel, S. B. Desai, F. Kronast, A. A. Unal, G. Conti, C. Conlon, G. K. Palsson, M. C. Martin, A. M. Minor, C. S. Fadley, E. Yablonovitch, R. Maboudian, and A. Javey, *Strong interlayer coupling in van der Waals heterostructures built from single-layer chalcogenides,* PNAS **111**, 6198-6202 (2014).

[86] V. W. Brar, M. S. Jang, M. Sherrott, S. Kim, J. J. Lopez, L. B. Kim, M. Choi, H. Atwater, *Hybrid surface-phonon-plasmon polariton modes in graphene/monolayer h-BN heterostructures,* ACS Nano Lett. **14**, 3876-3880 (2014).

[87] H. Nielsen, and M. Ninomiya, *Absence of neutrinos on a lattice: (I). Proof by homotopy theory*, Nucl. Phys. B **185**, 20 (1981); H. Nielsen and M. Ninomiya, *Absence of neutrinos on a lattice: (II). Intuitive topological proof*, Nucl. Phys. B **193**, 173 (1981).

[88] E. Fradkin, *Field Theories of Condensed Matter Physics*, Cambridge University Press, second edition (2013).

[89] E. McCann, *Staying or going? Chirality decides!*, Physics **2**, 98 (2009).

[90] V. V. Cheianov, and V. I. Falko, *Selective transmission of Dirac electrons and ballistic magnetoresistance of n-p junctions in graphene,* Phys. Rev. B **74**, 041403 (2006).

[91] M. I. Katsnelson, K. S. Novoselov, and A. K. Geim, *Chiral tunnelling and the Klein paradox in graphene,* Nature Phys. **2**, 620 (2006).

[92] C. W. J. Beenakker, *Colloquium: Andreev reflection and Klein tunneling in graphene,* Rev. Mod. Phys. **80**, 1337 (2008).

[93] V. I. Falko, K. Kechedzhi, E. McCann, B. L. Altshuler, H. Suzuura, and T. Ando, *Weak localization in graphene,* Science Direct **142**, 33-38 (2007).

[94] K. Kechedzhi, E. McCann, V. I. Falko, H. Suzuura, T. Ando, and B. L. Altshuler, *Weak localization in monolayer and bilayer graphene,* The European Physical Journal Special Topics **148**, 39-54 (2007).

[95] K. S. Novoselov, A. K. Geim, S. V. Morozov, D. Jiang, M. I. Katsnelson, I. V. Grigorieva, S. V. Dubonos, and A. A. Firsov, *Two-dimensional gas of massless Dirac fermions in graphene,* Nature **438**, 197–200 (2005).

[96] Y. Zhang, Y. W. Tan, H. L. Stormer, and P. Kim, *Experimental observation of the quantum Hall effect and Berry's phase in graphene,* Nature **438**, 201-2014 (2005).

[97] S. Gattenlöhner, W. R. Hannes, P. M. Ostrovsky, I. V. Gornyi, A. D. Mirlin, and M. Titov, *Quantum Hall Criticality and Localization in Graphene with Short-Range Impurities at the Dirac Point,* Phys. Rev. Lett. **112**, 026801 (2014).

[98] A. Ferreira, and E. R. Mucciolo, *Critical Delocalization of Chiral Zero Energy Modes in Graphene,* Phys. Rev. Lett. **115**, 106601 (2015).

[99] C. L. Kane, and E. J. Mele, *Quantum Spin Hall Effect in Graphene*, Phys. Rev. Lett. **95**, 226801 (2005).

[100] Z. Qiao, S. A. Yang, W. Feng, W. K. Tse, J. Ding, Y. Yao, J. Wang, and Q. Niu, *Quantum anomalous Hall effect in graphene from Rashba and exchange effects*, Phys. Rev. B **82**, 161414(R) (2010).

[101] J. W. McClure, and Y. Yafet, *Proceedings of the Fifth Conference on Carbon,* Pergamon, New York, **1**, 22–28 (1962).

[102] Y. Yao, F. Ye, X.-L. Qi, S.-C. Zhang, and Z. Fang, *Spin-orbit gap of graphene: First-principles calculations,* Phys. Rev. B **75**, 041401 (2007).

[103] J. C. Boettger, and S. B. Trickey, *First-principles calculation of the spin-orbit splitting in graphene,* Phys. Rev. B **75**, 121402(R) (2007).

[104] M. Gmitra, S. Konschuh, C. Ertler, C. Ambrosch-Draxl, and J. Fabian, *Band-structure topologies of graphene: Spin-orbit coupling effects from first principles*, Phys. Rev. B **80**, 235431 (2009).

[105] A. H. Castro Neto, and F. Guinea, *Impurity-induced spin–orbit coupling in graphene*, Phys. Rev. Lett. **103**, 026804 (2009).

[106] C. Weeks, J. Hu, J. Alicea, M. Franz, and R. Wu, *Engineering a Robust Quantum Spin Hall State in Graphene via Adatom Deposition,* Phys. Rev. X **1**, 021001 (2011).

[107] H. Zhang, C. Lazo, S. Blügel, S. Heinze, and Y. Mokrousov, *Electrically tunable quantum anomalous Hall effect in graphene decorated by 5d transition-metal adatoms*, Phys. Rev. Lett. **108**, 056802 (2012).

[108] U. Chandni, E. A. Henriksen, and J. P. Eisenstein, *Transport in indium-decorated graphene,* Phys. Rev. B **91**, 245402 (2015).

[109] Y. Wang, S. Xiao, X. Cai, W. Bao, J. R. Robey, and M. S. Fuhrer, *Electronic transport properties of Ir-decorated graphene,* Scientific Rep. **5**, 15764 (2015).

[110] Z. Jia, B. Yan, J. Niu, Q. Han, R. Zhu, D. Yu, and X. Wu, *Transport study of graphene adsorbed with indium adatoms*, Phys. Rev. B **91**, 085411 (2015).

[111] Y. Wang, X. Cai, J. Reutt-Robey, and M. S. Fuhrer, *Neutral-current Hall effects in disordered graphene*, Phys. Rev. B **92**, 161411(R) (2015).

[112] J. A. Elias, and E. A. Henriksen, *Electronic transport and scattering times in tungsten-decorated graphene*, Phys. Rev. B **95**, 075405 (2017).

[113] F. J. dos Santos, D. A. Bahamon, R. B. Muniz, K. McKenna, E. V. Castro, J. Lischner, and A. Ferreira, *Impact of complex adatom-induced interactions on quantum spin Hall phases*, Phys. Rev. B **98**, 081407(R) (2018).

[114] M. Chhowalla, H. S. Shin, G. Eda, L. Li, K. Ping, and H. Zhang, *The chemistry of two-dimensional layered transition metal dichalcogenide nanosheets*, Nature Chemistry **5**, 263-275 (2013).

[115] S. Manzeli, D. Ovchinnikov, D. Pasquier, O. V. Yazyev, and A. Kis, *2D transition metal dichalcogenides,* Nature Rev. Mat. **2**, 17033 (2017).

[116] L. Ruitao, J. A. Robinson, R. E. Schaak, D. Sun, Y. Sun, T. E. Mallouk, and M. Terrones, *Transition Metal Dichalcogenides and Beyond: Synthesis, Properties, and Applications of Single- and Few-Layer Nanosheets,* Accounts of Chemical Research **48**, 1 (2014).

[117] Z. Y. Zhu, Y.C. Cheng, and U. Schwingenschlögl, *Giant spin–orbit-induced spin splitting in two-dimensional transition-metal dichalcogenide semiconductors*, Phys. Rev. B **84**, 153402 (2011).

[118] D. Xiao, G. B. Liu, W. Feng, X. Xu, and W. Yao, *Coupled Spin and Valley Physics in Monolayers of MoS_2 and Other Group-VI Dichalcogenides,* Phys. Rev. Lett. **108**, 196802 (2012).

[119] W. Yao, D. Xiao, and Q. Niu, *Valley-dependent optoelectronics from inversion symmetry breaking*, Phys. Rev. B **77**, 235406 (2008).

[120] K. F. Mak, K. He, J. Shan, and T. F. Heinz, *Control of valley polarization in monolayer MoS_2 by optical helicity*, Nature Nanotechnology **7**, 494-498 (2012).

[121] T. Cao, G. Wang, W. Han, H. Ye, C. Zhu, J. Shi, Q. Niu, P. Tan, E. Wang, B Liu, and J. Feng, *Valley-selective circular dichroism of monolayer molybdenum disulphide,* Nature Communications **3**, 887 (2012).

[122] M. Gmitra, D. Kochan, P. Hogl, and J. Fabian, *Trivial and inverted Dirac bands and the emergence of quantum spin Hall states in graphene on transition-metal dichalcogenides,* Phys. Rev. B **93**, 155104 (2016).

[123] Z. Wang, D. K. Ki, H. Chen, H. Berger, A. H. MacDonald, and A. F. Morpurgo, *Strong interface-induced spin–orbit interaction in graphene on WS_2*, Nature Communications **6**, 8339 (2015).

[124] A. Avsar, J. Y. Tan, T. Taychatanapat, J. Balakrishnan, G.K.W. Koon, Y. Yeo, J. Lahiri, A. Carvalho, A. S. Rodin, E.C.T. O'Farrell, G. Eda, A. H. Castro Neto, and B. Özyilmaz, *Spin-orbit proximity effect in graphene,* Nature Communications **5**, 4875 (2014).

[125] Z. Wang, D. K. Ki, J. Y. Khoo, D. Mauro, H. Berger, L. S. Levitov, and A. F. Morpurgo, *Origin and Magnitude of 'Designer' Spin-Orbit Interaction in Graphene on Semiconducting Transition Metal Dichalcogenides*, Phys. Rev. X **6**, 041020 (2016).

[126] T. Völkl, T. Rockinger, M. Drienovsky, K. Watanabe, T. Taniguchi, D. Weiss, and J. Eroms, *Magnetotransport in heterostructures of transition metal dichalcogenides,* Phys. Rev. B **96**, 125405 (2017).

[127] Y. K. Luo, J. Xu, T. Zhu, G. Wu, E. J. McCormick, W. Zhan, M. R. Neupane, and R. K. Kawakami, *Opto-Valleytronic Spin Injection in Monolayer MoS2/Few-Layer Graphene Hybrid Spin Valves,* ACS Nano Letters **17**, 6 (2017).

[128] Z. Wang, C. Tang, R. Sachs, Y. Barlas, and J. Shi, *Proximity-Induced Ferromagnetism in Graphene Revealed by the Anomalous Hall Effect,* Phys. Rev. Letters **114**, 016603 (2015).

[129] C. Tang, B. Cheng, M. Aldosary, Z. Wang, Z. Jiang, K. Watanabe, T. Taniguchi, M. Bockrath, and J. Shi, *Approaching quantum anomalous Hall effect in proximity-coupled YIG/graphene/h-BN sandwich structure*, APL Materials **6**, 026401 (2018).

[130] Z. Qiao, W. Ren, H. Chen, L. Bellaiche, Z. Zhang, A. H. MacDonald, and Qian Niu, *Quantum Anomalous Hall Effect in Graphene Proximity Coupled to an Antiferromagnetic Insulator*, Phys. Rev. Lett. **112**, 116404 (2014).

[131] J. Zhang, B. Zhao, Y. Yao, and Z. Yang, *Robust quantum anomalous Hall effect in graphene-based van der Waals heterostructures,* Phys. Rev. B **92**, 165418 (2015).

[132] M. Ben Shalom, M. J. Zhu, V. I. Falko, A. Mishchenko, A. V. Kretinin, K. S. Novoselov, C. R. Woods, K. Watanabe, T. Taniguchi, A. K. Geim, and J. R. Prance, *Quantum oscillations of the critical current and high-field superconducting proximity in ballistic graphene,* Nature Physics **12**, 318-322 (2016).

[133] D. Culcer, Y. Yao, and Q. Niu, *Coherent wave-packet evolution in coupled bands,* Phys. Rev. B **72**, 085110 (2005).

[134] N. A. Sinitsyn, A. H. MacDonald, T. Jungwirth, V. K. Dugaev, and Jairo Sinova, *Anomalous Hall effect in a two-dimensional Dirac band: The link between the Kubo-Streda formula and the semiclassical Boltzmann equation approach,* Phys. Rev. B **75**, 045315 (2007).

[135] H. J. W. Haug, and A. P. Jahuo, *Quantum Kinetics in Transport and Optics of Semiconductors, 2nd Edition*, Springer-Verlag Berlin Heidelberg (2008).

[136] J. Rammer, *Quantum Transport Theory*, Taylor & Francis Inc., Abingdon, UK (1998).

[137] J. M. Ziman, *Principles of the Theory of Solids,* Cambridge University Press (1972).

[138] E. Fermi, *Nuclear Physics*, University of Chicago Press ISBN 978-0226243658, (1950).

[139] L. E. Ballentine, *Quantum Mechanics: A Modern Development Second Edition*, World Scientific Publishing Company (2014).

[140] E. Adams, and E. Blount, *Energy bands in the presence of an external force field,* J. Phys. Chem. Solids **10**, 286 (1959).

[141] N. A. Sinitsyn, Q. Niu, J. Sinova, and Kentaro Nomura, *Disorder effects in the anomalous Hall effect induced by Berry curvature,* Phys. Rev. B **72**, 045346 (2005).

[142] N. A. Sinitsyn, Q. Niu, and A. H. MacDonald, *Coordinate shift in the semiclassical Boltzmann equation and the anomalous Hall effect,* Phys. Rev. B **73**, 075318 (2006).

[143] N. D. Mermin, *Lindhard Dielectric Function in the Relaxation-Time Approximation*, Phys. Rev. B **1**, 2362 (1970).

[144] R. Kragler and H. Thomas, *Dielectric Function in the Relaxation-Time Approximation Generalized to Electronic Multiple-Band Systems,* Z. Phys. B **39**, 99 (1980).

[145] C. Huang, Y. D. Chong, G. Vignale, and M. A. Cazalilla, *Graphene electrodynamics in the presence of the extrinsic spin Hall effect*, Phys. Rev. B **93**, 165429 (2016).

[146] H. P. Breuer, and F. Petruccione, *The theory of open quantum systems*, Oxford University Press on Demand (2002).

[147] D. Culcer, and R. Winkler, *Steady states of spin distributions in the presence of spin-orbit interactions,* Phys. Rev. B **76**, 245322 (2007).

[148] D. Culcer, and R. Winkler, *Weak momentum scattering and the conductivity of graphene,* Phys. Rev. B **78**, 235417 (2008).

[149] S. A. Tarasenko, *Scattering Induced Spin Orientation and Spin Currents in Gyrotropic Structures*, Journal of Experimental and Theoretical Physics Letters **84**, 4 (2006).

[150] M. W. Wu, J. H. Jiang, M. Q.Weng, *Spin dynamics in semiconductors*, Physics Reports **493**, 2-4 (2010).

[151] R. Kubo, *Statistical-Mechanical Theory of Irreversible Processes. I. General Theory and Simple Applications to Magnetic and Conduction Problems,* Journal of Japanese Phys. Soc. **12**, 570-586 (1957).

[152] G. D. Mahan, *Many-particle physics,* Springer Science & Business Media (2013).

[153] A. Crépieux, and P. Bruno, *Theory of the anomalous Hall effect from the Kubo formula and the Dirac equation*, Phys. Rev. B **64**, 014416 (2001).

[154] P. Streda, *Theory of quantised Hall conductivity in two dimensions* J. Phys. C **15**, L717 (1982).

[155] C. Di Castro and R. Raimondi, *Statistical Mechanics and Applications in Condensed Matter*, Cambridge University Press (2015).

[156] H. Bruus, and K. Flensberg, *Many-body quantum theory in condensed matter physics,* Oxford University Press (2004).

[157] A. F. Ioffe and A. R. Regel, *Non-crystalline, amorphous and liquid electronic semiconductors,* Prog. Semicond. **4**, 237 (1960).

[158] M. Milletarì, and A. Ferreira, *Quantum diagrammatic theory of the extrinsic spin Hall effect in graphene,* Phys. Rev. B **94**, 134202 (2016).

[159] M. Milletarì, and A. Ferreira, *Crossover to the anomalous quantum regime in the extrinsic spin Hall effect of graphene,* Phys. Rev. B **94**, 201402(R) (2016).

[160] A. Ferreira, J. Viana-Gomes, Johan Nilsson, E. R. Mucciolo, N. M. R. Peres, and A. H. Castro Neto, *Unified description of the dc conductivity of monolayer and bilayer graphene at finite densities based on resonant scatterers*, Phys. Rev. B **83**, 165402 (2011).

[161] E. Noether, *Invariante Variationsprobleme*, Nachr. D. König. Gesellsch. D. Wiss. Zu Göttingen Math-Phys. Klasse **18**, 235–257 (1918).

[162] I. V. Tokatly, *Equilibrium Spin Currents: Non-Abelian Gauge Invariance and Color Diamagnetism in Condensed Matter,* Phys. Rev. Lett. **101**, 106601 (2008).

[163] D. Kochan, S. Irmer, and J. Fabian, *Model spin–orbit coupling Hamiltonians for graphene systems,* Phys. Rev. B **95**, 165415 (2017).

[164] M. Gmitra, D. Kochan, and J. Fabian, *Spin-Orbit Coupling in Hydrogenated Graphene,* Phys. Rev. Lett. **110**, 246602 (2013).

[165] Y. A. Bychkov, and E. I. Rashba, *Properties of a 2D electron gas with lifted spectral degeneracy,* Soviet Journal of Experimental and Theoretical Physics Letters **39**, 71 (1984).

[166] P. Schwab, R. Raimondi, and C. Gorini, *Spin-charge locking and tunneling into a helical metal*, EPL **93**, 67004 (2011).

[167] D. Hsieh, Y. Xia, D. Qian, L. Wray, J. H. Dil, F. Meier, J. Osterwalder, L. Patthey, J. G. Checkelsky, N. P. Ong, A. V. Fedorov, H. Lin, A. Bansil, D. Grauer, Y. S. Hor, R. J. Cava, and M. Z. Hasan, *A tunable topological insulator in the spin helical Dirac transport regime*, Nature **460**, 1101 (2009).

[168] V. Brosco, L. Benfatto, E. Cappelluti, and C. Grimaldi, *Unconventional dc Transport in Rashba Electron Gases,* Phys. Rev. Lett. **116**, 166602 (2016).

[169] M. Milletarì, M. Offidani, A. Ferreira, and R. Raimondi, *Covariant conservation laws and the spin Hall effect in Dirac-Rashba systems,* Phys. Rev. Lett. **119**, 246801 (2017).

[170] M. Offidani, M. Milletarì, R. Raimondi, and A. Ferreira, *Optimal Charge-to-Spin Conversion in Graphene on Transition-Metal Dichalcogenide,* Phys. Rev. Lett. **119**, 196801 (2017).

[171] A. Ferreira, T. G, Rappoport, M. A. Cazalilla, and A. H. Castro Neto, *Extrinsic Spin Hall Effect Induced by Resonant Skew Scattering in Graphene*, Phys. Rev. Lett. **112**, 066601 (2014).

[172] C. Huang, Y. D. Chong, and M. A. Cazalilla, *Direct coupling between charge current and spin polarization by extrinsic mechanisms in graphene*, Phys. Rev. B **94**, 085414 (2016).

[173] P. M. Ostrovsky, I. V. Gornyi, and A. D. Mirlin, *Electron transport in disordered graphene,* Phys. Rev. B **74**, 235443 (2006).

[174] J. I. Inoue, G. E. W. Bauer, and L. W. Molenkamp, *Suppression of the persistent spin Hall current by defect scattering*, Phys. Rev. B **70**, 041303 (R) (2004).

[175] E. G. Mishchenko, A. V. Shytov, and B. I. Halperin, *Spin Current and Polarization in Impure Two-Dimensional Electron Systems with Spin-Orbit Coupling*, Phys. Rev. Lett. **93**, 226602 (2004).

[176] R. Raimondi, and P. Schwab, *Spin-Hall effect in a disordered two-dimensional electron system*, Phys. Rev. B **71**, 033311 (2005).

[177] O. V. Dimitrova, *Spin-Hall conductivity in a two-dimensional Rashba electron gas*, Phys. Rev. B **71**, 245327 (2005).

[178] A. Khaetskii, *Nonexistence of Intrinsic Spin Currents,* Phys. Rev. Lett. **96**, 056602 (2006).

[179] R. Raimondi, P. Schwab, C. Gorini, and G. Vignale, *Spin-orbit interaction in a two-dimensional electron gas: a SU(2) formulation,* Annalen der Physik **524**, 3-4 (2012).

[180] M. Milletarì, R. Raimondi, and P. Schwab, *Magneto-spin Hall conductivity of a two-dimensional electron gas,* Europhys. Lett. **82**, 67005 (2008).

[181] C. Gorini, P. Schwab, M. Dzierzawa, and R. Raimondi, *Spin polarizations and spin Hall currents in a two-dimensional electron gas with magnetic impurities*, Phys. Rev. B **78**, 12 125327 (2008).

[182] E. Frantzeskakis, S. Pons, H. Mirhosseini, J. Henk, C. R. Ast, and M. Grioni, *Tunable Spin Gaps in a Quantum-Confined Geometry,* Phys. Rev. Lett. **101**, 196805 (2008).

[183] K. He, T. Hirahara, T. Okuda, S. Hasegawa, A. Kakizaki, and I. Matsuda, *Spin Polarization of Quantum Well States in Ag Films Induced by the Rashba Effect at the Surface,* Phys. Rev. Lett. **101**, 107604 (2008).

[184] J. H. Dil, F. Meier, J. Lobo-Checa, L. Patthey, G. Bihlmayer, and J. Osterwalder, *Rashba-Type Spin-Orbit Splitting of Quantum Well States in Ultrathin Pb Films,* Phys. Rev. Lett. **101**, 266802 (2008).

[185] S. Mathias, A. Ruffing, F. Deicke, M. Wiesenmayer, I. Sakar, G. Bihlmayer, E. V. Chulkov, Y. M. Koroteev, P. M. Echenique, M. Bauer, and M. Aeschlimann, *Quantum-Well-Induced Giant Spin-Orbit Splitting,* Phys. Rev. Lett. **104**, 066802 (2010).

[186] P. D. C. King, R. C. Hatch, M. Bianchi, R. Ovsyannikov, C. Lupulescu, G. Landolt, B. Slomski, J. H. Dil, D. Guan, J. L. Mi, E. D. L. Rienks, J. Fink, A. Lindblad, S. Svensson, S. Bao, G. Balakrishnan, B. B. Iversen, J. Osterwalder, W. Eberhardt, F. Baumberger, and P. Hofmann, *Large Tunable Rashba Spin Splitting of a Two-Dimensional Electron Gas in Bi_2Se_3,* Phys. Rev. Lett. **107**, 096802 (2011).

[187] Z. H. Zhu, G. Levy, B. Ludbrook, C. N. Veenstra, J. A. Rosen, R. Comin, D. Wong, P. Dosanjh, A. Ubaldini, P. Syers, N. P. Butch, J. Paglione, I. S. Elfimov, and A. Damascelli, *Rashba Spin-Splitting Control at the Surface of the Topological Insulator Bi_2Se_3,* Phys. Rev. Lett. **107**, 186405 (2011).

[188] S. V. Eremeev, I. A. Nechaev, Yu. M. Koroteev, P. M. Echenique, and E. V. Chulkov, *Ideal Two-Dimensional Electron Systems with a Giant Rashba-Type Spin Splitting in Real Materials: Surfaces of Bismuth Tellurohalides*, Phys. Rev. Lett. **108**, 246802 (2012).

[189] D. Marchenko, A. Varykhalov, M. R. Scholz, G. Bihlmayer, E. I. Rashba, A. Rybkin, A.M. Shikin, and O. Rader, *Giant Rashba splitting in graphene due to hybridization with gold,* Nat. Commun. **3**, 1232 (2012).

[190] B. Yang, M. Lohmann, D. Barroso, I. Liao, Z. Lin, Y. Liu, L. Bartels, K. Watanabe, T. Taniguchi, and J. Shi, *Strong electron-hole symmetric Rashba spin-orbit coupling in graphene/monolayer transition metal dichalcogenide heterostructures*, Phys. Rev. B **96**, 041409(R) (2017).

[191] E. I. Rashba, *Graphene with structure-induced spin-orbit coupling: Spin-polarized states, spin zero modes, and quantum Hall effect*, Phys. Rev. B **79**, 161409(R) (2009).

[192] J. Sinova, D. Culcer, Q. Niu, N. A. Sinitsyn, T. Jungwirth, and A. H. MacDonald, *Universal Intrinsic Spin-Hall Effect,* Phys. Rev. Lett. **92**, 126603 (2004).

[193] R. A. Bertlmann, Anomalies in Quantum Field Theory, Oxford University Press (1996).

[194] A. Dyrdal, V. K. Dugaev, and J. Barnas, *Spin Hall effect in a system of Dirac fermions in the honeycomb lattice with intrinsic and Rashba spin-orbit interaction*, Phys. Rev. B **80**, 155444 (2009).

[195] N. A. Sinitsyn, *Semiclassical theories of the anomalous Hall effect*, J. Phys. Condens. Matter **20**, 023201 (2008).

[196] N. M. R. Peres, *Colloquium: The transport properties of graphene: An introduction,* Rev. Mod. Phys. **82**, 2673 (2010).

[197] C. Grimaldi, E. Cappelluti, and F. Marsiglio, *Off-Fermi surface cancellation effects in spin-Hall conductivity of a two-dimensional Rashba electron gas*, Phys. Rev. B **73**, 081303(R) (2006).

[198] V. K. Dugaev, M. Inglot, E. Ya. Sherman, and J. Barnaś, *Robust impurity-scattering spin Hall effect in a two-dimensional electron gas*, Phys. Rev. B **82**, 121310(R) (2010);

[199] A. Dyrdał and J. Barnaś, *Spin Hall effect in graphene due to random Rashba field,* Phys. Rev. B **86**, 161401(R) (2012).

[200] M. Rodriguez-Vega, G. Schwiete, J. Sinova, and E. Rossi, *Giant Edelstein effect in topological-insulator–graphene heterostructures*, Phys. Rev. B **96**, 235419 (2016).

[201] X. Li, H. Chen, and Q. Niu, *Out-of-plane carrier spin in transition-metal dichalcogenides under electric current*, pre-print: arXiv:1707.04548 (2017).

[202] P. Schwab and R. Raimondi, *Magnetoconductance of a two-dimensional metal in the presence of spin-orbit coupling*, EPJ B **25**, 483 (2002).

[203] M. B. Lundeberg, R. Yang, J. Renard, and J. A. Folk, *Defect-Mediated Spin Relaxation and Dephasing in Graphene*, Phys. Rev. Lett. **110,** 156601 (2013).

[204] V. K. Dugaev, E. Y. Sherman, and J. Barnaś, *Spin dephasing and pumping in graphene due to random spin-orbit interaction,* Phys. Rev. B **83**, 085306 (2011).

[205] I. M. Vicent, H. Ochoa, and F. Guinea, *Spin relaxation in corrugated graphene,* Phys. Rev. B **95,** 195402 (2017).

[206] S. Roche, and S. O Valenzuela, *Graphene spintronics: puzzling controversies and challenges for spin manipulation*, Journal of Physics D: Applied Physics **47**, 094011 (2014).

[207] N. Tombros, C. Jozsa, M. Popinciuc, H. T. Jonkman, and B. J. van Wees, *Electronic spin transport and spin precession in single graphene layers at room temperature,* Nature **448**, 571-574 (2007).

[208] C. Józsa, T. Maassen, M. Popinciuc, P. J. Zomer, A. Veligura, H. T. Jonkman, and B. J. van Wees, *Linear scaling between momentum and spin scattering in graphene*, Phys. Rev. B **80**, 241403(R) (2009).

[209] M. Popinciuc, C. Józsa, P. J. Zomer, N. Tombros, A. Veligura, H. T. Jonkman, and B. J. van Wees, *Electronic spin transport in graphene field-effect transistors*, Phys. Rev. B **80**, 214427 (2009).

[210] W. Han, K. Pi, K. M. McCreary, Yan Li, Jared J. I. Wong, A. G. Swartz, and R. K. Kawakami, *Tunneling Spin Injection into Single Layer Graphene*, Phys. Rev. Lett. **105**, 167202 (2010).

[211] T. Y. Yang, J. Balakrishnan, F. Volmer, A. Avsar, M. Jaiswal, J. Samm, S. R. Ali, A. Pachoud, M. Zeng, M. Popinciuc, G. Güntherodt, B. Beschoten, and B. Özyilmaz, *Observation of Long Spin-Relaxation Times in Bilayer Graphene at Room Temperature*, Phys. Rev. Lett. **107**, 047206 (2011).

[212] W. Han, and R. Kawakami, *Spin Relaxation in Single-Layer and Bilayer Graphene*, Phys. Rev. Lett. **107**, 047207 (2011).

[213] K. Pi, W. Han, K. M. McCreary, A. G. Swartz, Yan Li, and R. K. Kawakami, *Manipulation of Spin Transport in Graphene by Surface Chemical Doping*, Phys. Rev. Lett. **104**, 187201 (2011).

[214] S. Jo, D. K. Ki, D. Jeong, H. J. Lee, and S. Kettemann, *Spin relaxation properties in graphene due to its linear dispersion*, Phys. Rev. B **84**, 075453 (2011).

[215] P. J. Zomer, M. H. D. Guimaraes, N. Tombros, and B. J. Van Wees, *Long-distance spin transport in high-mobility graphene on hexagonal boron nitride*, Phys. Rev. B **86**, 161416 (2012).

[216] M. Drögeler, C. Franzen, F. Volmer, T. Pohlmann, L. Banszerus, M. Wolter,, K. Watanabe, T. Taniguchi, C. Stampfer, and B. Beschoten, *Spin Lifetimes Exceeding 12 ns in Graphene Nonlocal Spin Valve Devices*, Nano Lett. **16**, 3533 (2016).

[217] B. Raes, J. E. Scheerder, M. V. Costache, F. Bonell, J. F. Sierra, J. Cuppens, J. Van de Vondel, and S. O. Valenzuela, *Determination of the spin-lifetime anisotropy in graphene using oblique spin precession*, Nat. Comm. **7**, 11444 (2016).

[218] W. Han, R. Kawakami, M. Gmitra, and J. Fabian, *Graphene Spintronics,* Nature Nanotechnology **9**, 794-807 (2014).

[219] D. Huertas-Hernando, F. Guinea, and A. Brataas, *Spin-Orbit-Mediated Spin Relaxation in Graphene*, Phys. Lett **103**, 075453 (2009).

[220] C. Ertler, S. Konschuh, M. Gmitra, and J. Fabian, *Electron spin relaxation in graphene: The role of the substrate,* Phys. Rev. B **80**, 041405(R) (2009).

[221] D. Kochan, M. Gmitra, and J. Fabian, *Spin Relaxation Mechanism in Graphene: Resonant Scattering by Magnetic Impurities*, Phys. Rev. Lett. **112**, 116602 (2014).

[222] T. Maassen, F. K. Dejene, M. H. D. Guimarães, C. Józsa, and B. J. van Wees, *Comparison between charge and spin transport in few-layer graphene,* Phys. Rev. B **83**, 115410 (2011).

[223] F. Volmer, M. Drögeler, E. Maynicke, N. von den Driesch, M. L. Boschen, G. Güntherodt, and B. Beschoten, *Role of MgO barriers for spin and charge transport in Co/MgO/graphene nonlocal spin-valve devices,* Phys. Rev. B **88**, 161405(R) (2013).

[224] D. V. Fedorov, M. Gradhand, S. Ostanin, I. V. Maznichenko, A. Ernst, J. Fabian, and I. Mertig, *Impact of Electron-Impurity Scattering on the Spin Relaxation Time in Graphene: A First-Principles Study*, Phys. Rev. Lett. **110**, 156602 (2013).

[225] D. Soriano, D. V. Tuan, S. M. M. Dubois, M. Gmitra, A. W. Cummings, D. Kochan, F. Ortmann, J. C. Charlier, J. Fabian, and S. Roche, *Spin transport in hydrogenated graphene*, 2D Materials **2**, 022002 (2015).

[226] D. V. Tuan, F. Ortmann, D. Soriano, S. O. Valenzuela, and S. Roche, *Pseudospin-driven spin relaxation mechanism in graphene,* Nat. Physics **10**, 857-863 (2014).

[227] D. V. Tuan, F. Ortmann, A. W. Cummings, D. Soriano, and S. Roche, *Spin dynamics and relaxation in graphene dictated by electron-hole puddles*, Scientific Reports **6**, 21046 (2016).

[228] P. Zhang, and M. W. Wu, *Electron spin relaxation in graphene with random Rashba field: comparison of the D'yakonov–Perel' and Elliott–Yafet-like mechanisms*, New Journal of Physics **14**, 033015 (2015).

[229] H. Ochoa, A. H. Castro Neto, and F. Guinea, *Elliott-Yafet Mechanism in Graphene,* Phys. Rev. Lett. **108**, 206808 (2012).

[230] C. Gorini, A. Maleki, K. Shen, I. V. Tokatly, G. Vignale, and R. Raimondi, *Theory of current-induced spin polarization in an electron gas*, Phys. Rev. B **95**, 205424 (2017).

[231] A. A. Burkov, A. S. Nunez, and A. H. MacDonald, *Theory of spin-charge-coupled transport in a two-dimensional electron gas with Rashba spin-orbit interactions,* Phys. Rev. B **70**, 155308 (2004).

[232] A. A. Burkov, and L. Balents, *Spin relaxation in a two-dimensional electron gas in a perpendicular magnetic field*, Phys. Rev. **B** 69, 245312 (2004).

[233] K. Shen, G. Vignale, and R. Raimondi, *Microscopic Theory of the Inverse Edelstein Effect*, Phys. Rev. Lett. **112**, 096601 (2014).

[234] E. McCann, K. Kechedzhi, Vladimir I. Fal'ko, H. Suzuura, T. Ando, and B. L. Altshuler, *Weak-Localization Magnetoresistance and Valley Symmetry in Graphene,* Phys. Rev. Lett. **97**, 146805 (2006).

[235] D. A. Abanin, A. V. Shytov, L. S. Levitov, and B. I. Halperin, *Nonlocal charge transport mediated by spin diffusion in the spin Hall effect regime*, Phys. Rev. B **79**, 03504 (2009).

[236] M. Offidani, R. Raimondi, and A. Ferreira, *Microscopic Linear Response Theory of Spin Relaxation and Relativistic Transport Phenomena in Graphene,* MDPI Condensed Matter **3**(2), 18 (2018).

[237] T. Ando, T. Nakanishi, and R. Saito, *Berry's Phase and Absence of Back Scattering in Carbon Nanotubes,* J. Phys. Soc. Jpn. **67**, 2857-2862 (1998).

[238] P. L. McEuen, M. Bockrath, D. H. Cobden, Y. G. Yoon, and S. G. Louie, *Disorder, Pseudospins, and Backscattering in Carbon Nanotubes*, Phys. Rev. Lett. **83**, 5098 (1999).

[239] A. W. Cummings, and S. Roche, *Effects of Dephasing on Spin Lifetime in Ballistic Spin-Orbit Materials,* Phys. Rev. Lett. **116**, 086602 (2016).

[240] E. McCann, and V. Falko, $z \rightarrow -z$ *Symmetry of Spin-Orbit Coupling and Weak Localization in Graphene*, Phys. Rev. Lett **108**, 166606 (2012).

[241] L. A. Benítez, J. F. Sierra, W. S. Torres, A. Arrighi, F. Bonell, M. V. Costache, and Sergio O. Valenzuela, *Strongly anisotropic spin relaxation in graphene–transition metal dichalcogenide heterostructures at room temperature*, Nature Physics **14**, 303 (2017).

[242] T. S. Ghiasi, J. Ingla-Aynes, A. A. Kaverzin, and B. J. Van Wees, *Large Proximity-Induced Spin Lifetime Anisotropy in Transition-Metal Dichalcogenide/Graphene Heterostructures,* Nano Lett. **17**, 7528-7532 (2017).

[243] A. W. Cummings, J. H. Garcia, J. Fabian, and S. Roche, *Giant Spin Lifetime Anisotropy in Graphene Induced by Proximity Effects*, Phys. Rev. Lett. **119**, 206601 (2017).

[244] J.H. Garcia, L. Covaci, and T.G. Rappoport, *Real-Space Calculation of the Conductivity Tensor for Disordered Topological Matter*, Phys. Rev. Lett. **114**, 116602 (2015).

[245] F. Ortmann, N. Leconte, and S. Roche, *Efficient linear scaling approach for computing the Kubo Hall conductivity,* Phys. Rev. B **91**, 165117 (2015).

[246] J. Fabian, A. Matos-Abiage, C. Ertler, P. Stano, and I. Zutic, Acta Phys. Slovaca, *Semiconductor spintronics*, **4**(5), 565-907 (2007).

[247] S. Zihlmann, A. W. Cummings, J. H. Garcia, M. Kedves, K. Watanabe, T. Taniguchi, C. Schönenberger, and P. Makk, *Large spin relaxation anisotropy and valley-Zeeman spin-orbit coupling in WSe_2 /graphene/ h -BN heterostructures*, Phys. Rev. B **97**, 075434 (2018).

[248] V. K. Dugaev, E. Ya. Sherman, V. I. Ivanov, and J. Barnaś, *Spin relaxation and combined resonance in two-dimensional electron systems with spin-orbit disorder*, Phys. Rev. B **80**, 081301(R) (2009).

[249] K. Hao, G. Moody, F. Wu, C. K. Dass, L. Xu, C. H. Chen, L. Sun, M. Y. Li, L. J. Li, A. H. MacDonald, and X. Li, *Direct measurement of exciton valley coherence in monolayer WSe_2*, Nature Physics **12**, 677-682 (2016).

[250] A. Pachoud, A. Ferreira, B. Özyilmaz, and A. H. Castro Neto, *Scattering theory of spin-orbit active adatoms on graphene,* Phys. Rev. B **90**, 035444 (2015).

[251] V. N. Gridnev, *Theory of Faraday rotation beats in quantum wells with large spin splitting,* Journal of Experimental and Theor. Phys. Letters **74**, 380 (2001).

[252] P. Schwab, M. Dzierzawa, C. Gorini, and R. Raimondi, *Quasiclassical approach to the spin Hall effect in the two-dimensional electron gas,* Phys. Rev. B **74**, 155316 (2006).

[253] C. C. Liu, H. Jiang, and Y. Yao, *Low-energy effective Hamiltonian involving spin-orbit coupling in silicene and two-dimensional germanium and tin*, Phys. Rev. **B** 84, 195430 (2011).

[254] F. V. Tikhonenko, D. W. Horsell, R. V. Gorbachev, and A. K. Savchenko, *Weak Localization in Graphene Flakes*, Phys. Rev. Lett. **100**, 056802 (2008).

[255] B. Yang, M. F. Tu, J. Kim, Y. Wu, H. Wang, J. Alicea, , R. Wu, M. Bockrath, and J. Shi, *Tunable spin–orbit coupling and symmetry-protected edge states in graphene/WS_2*, 2D Materials **3**, 031012 (2016).

[256] C. Gong, L. Li, Z. Li, H. Ji, A. Stern, Y. Xia, T. Cao, W. Bao, C. Wang, Y. Wang, Z. Q. Qiu, R. J. Cava, S. G. Louie, J. Xia, and X. Zhang, *Discovery of intrinsic ferromagnetism in two-dimensional van der Waals crystals*, Nature **546**, 265 (2017).

[257] B. Huang, G. Clark, E. Navarro-Moratalla, D. R. Klein, R. Cheng, K. L. Seyler, D. Zhong, E. Schmidgall, M. A. McGuire, D. H. Cobden, W. Yao, D. Xiao, P. Jarillo-Herrero, and X. Xu, *Layer-dependent ferromagnetism in a van der Waals crystal down to the monolayer limit,* Nature **546**, 270 (2017).

[258] J. C. Leutenantsmeyer, A. A. Kaverzin, M. Wojtaszek, B. J. van Wees, *Proximity induced room-temperature ferromagnetism in graphene probed with spin currents,* 2D Materials **4**, 014001 (2017).

[259] A. G. Swartz, P. M. Odenthal , Y. Hao , R. S. Ruoff, and R. K. Kawakami, *Electric field induced spin and valley polarization within a magnetically confined silicene channel*, ACS Nano **6**, 10063 (2012).

[260] P. Wei, S. Lee, F. Lemaitre, L. Pinel, D. Cutaia, W. Cha, F. Katmis, Y. Zhu, D. Heiman, J. Hone, J. S. Moodera, C. T. Chen, *Strong interfacial exchange field in the graphene/EuS heterostructure,* Nature Materials **15**, 711 (2016).

[261] Y. F. Wu, H. D. Song, L. Zhang, X. Yang, Z. Ren, D. Liu, H. C. Wu, J. Wu, J. G. Li, Z. Jia, B. Yan, X. Wu, C. G. Duan, G. Han, Z. M. Liao, and D. Yu, *Magnetic proximity effect in graphene coupled to a $BiFeO_3$ nanoplate,* Phys. Rev. B **95**, 195426 (2017).

[262] D. Zhong, K. L. Seyler, X. Linpeng, R. Cheng, N. Sivadas, B. Huang, E. Schmidgall, T. Taniguchi, K. Watanabe, M. A. McGuire, W. Yao, D. Xiao, K. M. C. Fu, and X. Xu, *Van der Waals engineering of ferromagnetic semiconductor heterostructures for spin and valleytronics*, Science Advances **31**, 1603113 (2017).

[263] H. Haugen, D. Huertas-Hernando and A. Braatas, *Spin transport in proximity-induced ferromagnetic graphene,* Phys. Rev B **77**, 115406 (2008).

[264] Q. Sun, Z. Jiang, Y. Yu and X.C. Xie, *Spin superconductor in ferromagnetic graphene,* Phys. Rev. B **84**, 214501 (2011).

[265] H. X. Yang, A. Hallal, D. Terrade, X. Waintal, S. Roche, and M. Chshiev, *Proximity Effects Induced in Graphene by Magnetic Insulators: First-Principles Calculations on Spin Filtering and Exchange-Splitting Gaps,* Phys. Rev. Lett. **110**, 046603 (2013).

[266] D. Marchenko, A. Varykhalov, J. S.-Barriga, O. Rader, C. Carbone, and G. Bihlmayer, *Highly spin-polarized Dirac fermions at the graphene/Co interface*, Phys. Rev. B **91**, 235431 (2015).

[267] T.-Wei Chen, Z.-R. Xiao, D.-Wei Chiou, and G.-Y. Guo, *High Chern number quantum anomalous Hall phases in single-layer graphene with Haldane orbital coupling,* Phys. Rev. B **84**, 165453 (2011).

[268] D. V. Tuan, J. M. Marmolejo-Tejada, X. Waintal, B. K. Nikolić, S. O. Valenzuela, and S. Roche, *Spin Hall Effect and Origins of Nonlocal Resistance in Adatom-Decorated Graphene*, Phys. Rev. Lett. **117**, 176602 (2016).

[269] K. Zollner, M. Gmitra, T. Frank, and J. Fabian, *Theory of proximity-induced exchange coupling in graphene on hBN/(Co, Ni)*, Phys. Rev. B **94**, 155441 (2016).

[270] B. F. Miao, S. Y. Huang, D. Qu, and C. L. Chen, *Inverse Spin Hall Effect in a Ferromagnetic Metal,* Phys. Rev. Lett. **111**, 066602 (2013).

[271] K. S. Das, W. Y. Schoemaker, B. J. van Wees, and I. J. Vera-Marun, *Spin injection and detection via the anomalous spin Hall effect of a ferromagnetic metal*, Phys. Rev. B **96**, 220408(R) (2017).

[272] S. Iihama, Y. Otani and S. Maekawa, *Spin-transfer torque induced by the spin anomalous Hall effect,* Nature Electronics **1**, 120 (2018).

[273] J. Qi, X. Li, Q. Niu and J. Feng, *Giant and tunable valley degeneracy splitting in $MoTe_2$,* Phys. Rev. B **92**, 121403(R) (2015).

[274] C. Cheng, J.-T. Sun, X.-R. Chen, H.-X. Fua and S. Meng, *Nonlinear Rashba spin splitting in transition metal dichalcogenide monolayers*, Nanoscale **8**, 17854 (2016).

[275] Q.-F. Yao, J. Cai, W.-Y. Tong, S.-J. Gong, J.-Q. Wang, X. Wan, C.-G. Duan, and J. H. Chu, *Manipulation of the large Rashba spin splitting in polar two-dimensional transition-metal dichalcogenides*, Phys. Rev. B **95**, 165401 (2017).

[276] A. Takayama, T. Saro, S. Souma, and T. Takahashi, *Giant Out-of-Plane Spin Component and the Asymmetry of Spin Polarization in Surface Rashba States of Bismuth Thin Film,* Phys. Rev. Lett. **106**, 166401 (2011).

[277] Z. H. Ni, L. A. Ponomarenko, R. R. Nair, R. Yang, S. Anissimova, I. V. Grigorieva, F. Schedin, P. Blake, Z. X. Shen, E. H. Hill, K. S. Novoselov, and A. K. Geim, *On Resonant Scatterers As a Factor Limiting Carrier Mobility in Graphene*, Nano Lett. **10**, 3868 (2010).

[278] D. J. Thouless, M. Kohmoto, M. P. Nightingale and M. den Nijs, *Quantized Hall Conductance in a Two-Dimensional Periodic Potential,* Phys. Rev. Lett. **49**, 405 (1982);

[279] N. P. Ong and W. L. Lee, *Geometry and the Anomalous Hall Effect in Ferromagnets*, Foundations of Quantum Mechanics in the Light of New Technologies **121** (2006);

[280] N. Nagaosa, J. Sinova, S. Onoda, A. H. MacDonald and N. P. Ong, *Anomalous Hall effect,* Rev. Mod. Physics **82**, 1539 (2010).

[281] F. D. M. Haldane, *Nobel Lecture: Topological quantum matter*, Rev. Mod. Phys. **89**, 040502 (2017).

[282] F. D. M. Haldane, *Model for a Quantum Hall Effect without Landau Levels: Condensed-Matter Realization of the "Parity Anomaly",* Phys. Rev. Lett. **81**, 2015 (1988).

[283] P. R. Wallace, *The Band Theory of Graphite,* Phys. Rev. **71**, 622 (1947).

[284] A. Ferreira, in preparation.